University *of*
Leicester

Gamma Ray Bursts:
Selected results from the *Swift* mission.

Cheryl Pauline Hurkett

Supervisors:
Paul O'Brien
Julian Osborne

Thesis to be submitted for the degree of
Doctor of Philosophy
at the University of Leicester.

X-Ray & Observational Astronomy Group
Department of Physics and Astronomy
University of Leicester

December 12, 2008

Declaration

I hereby declare that no part of this thesis has been previously submitted to this or any other University as part of the requirement for a higher degree. The work described herein was conducted by the undersigned, except for contributions from colleagues as acknowledged in the text.

Cheryl Hurkett.

December 12, 2008

Gamma Ray Bursts: Selected results from the *Swift* mission.

Cheryl Pauline Hurkett

Abstract

Gamma Ray Bursts (GRBs) are short, energetic events that mark the most violent explosions in the Universe. Current hypotheses associated them with the births of stellar-sized black holes or rapidly spinning, highly magnetized stars. The introduction to this work places GRBs in their historical and theoretical context and provides a description of the current models describing them. This study makes use of data from the *Swift* satellite. Chapter two is a multi-wavelength study of the high redshift GRB 050505, which indicates that this burst has properties consistent with the general lower z GRB sample. Furthermore there is evidence for a 'jet-break' in the X-ray light curve; a phenomena rarely seen in *Swift* era bursts. The next two chapters investigate the presence of X-ray emission lines in GRB spectra. Chapter three provides a discussion of the pre-*Swift* observations and a comparison of three methods already extant in the literature for assessing the significance of such spectral features. The detection limits for each method were determined for emission line strengths in bursts with spectral parameters typical of the *Swift* era sample. Chapter four applies these methods to a sample of 40 *Swift* bursts; no strong evidence was found for emission lines in early time X-ray spectra once host galaxy absorption was accurately modelled. Chapter five investigates the phenomena of 'precursors' and 'quiescent intervals', indicating a common origin for events normally ascribed to 'prompt emission' and 'flares', in line with previous studies, and extending it to cover 'precursor' emission. Evidence was also found to reinforce (anti-)correlations seen between pulse temporal and energetic properties also seen in previous studies. The final chapter summarises the important results for each section and proposes future studies that could be conducted in each field.

Publications

Refereed

Hurkett, C.P. et al. 2008. **"Line Searches in Swift X-Ray Spectra"**, *ApJ*, 679, 587-606.

Hurkett, C.P. et al. 2006. **"GRB 050505: a high-redshift burst discovered by Swift"**, *MNRAS*, 368, 1101-1109.

Levan, A.J. et al. 2007. **"A case of mistaken identity? GRB060912A and the nature of the long-short GRB divide"**, *MNRAS*, 378, 1439-1446.

Curran, P.A. et al. 2007. **"The prompt to late-time multiwavelength analysis of GRB 060210"**, *A&A*, 467, 1049-1055.

Burleigh, M.R. et al. 2006. **"The nature of the close magnetic white dwarf + probable brown dwarf binary SDSSJ121209.31+013627.7"**, *MNRAS*, 373, 1416-1422.

Krimm, H.A. 2006. **"GRB 050717: A Long, Short-Lag, High-Peak Energy Burst Observed by Swift and Konus"**, *ApJ*, 648, 1117-1124.

O'Brien, P.T. et al. 2006. **"The Early X-Ray Emission from GRBs"**, *ApJ*, 647, 1213-1237.

Nousek, J.A. et al. 2006. **"Evidence for a Canonical Gamma-Ray Burst Afterglow Light Curve in the Swift XRT Data"**, *ApJ*, 642, 389-400.

Gehrels, N. et al. 2005. **"A short γ-ray burst apparently associated with an elliptical galaxy at redshift z = 0.225"**, *Nature*, 437, 851-854.

Un-refereed

Hurkett, C.P. et al. 2006. **"GRB 050505: A High Redshift Burst Discovered by Swift"**, *Proceedings of the The X-ray Universe 2005 (ESA SP-604)*, 604, 885.

Burleigh, M.R. et al. 2007. **"The Nature of the Close Magnetic White Dwarf + Probable Brown Dwarf SDSS J121209.31+013627.7"**, *Fifteenth European Workshop on White Dwarfs ASP Conference Series*, 372, 477.

Krimm, H.A. et al. 2006. **"GRB 050717: A Long, Short-Lag Burst Observed by Swift and Konus"**, *Gamma-Ray Bursts in the Swift Era, Sixteenth Maryland Astrophysics Conference*, 836, 141-144.

Acknowledgements

I would like to thank everyone who helped me to get this far, especially my parents; without your support and encouragement this thesis would not have become a reality.

A big thank you to the teachers and lecturers that inspired me during my studies. A special mention must go out to Mrs Probert and Dr Clarke (Highsted Grammar School), Dr Gurman, Professor Raine and Dr Symons (University of Leicester), and Professor Ward (Durham University). Also my supervisors: the last few years would not have been the same without your help.

Thanks to everyone I have worked with in the *Swift* team: there are so many that it would be hard to list you all. To the local *Swift* team: you are all stars! Kim, Andy, Phil, Rhaana, Evert, Mike, Klaas and Nial. To the Penn State team: thank you all for being so welcoming, I had a great time studying with you. It was a real shame I could only budget for one visit. Simon Vaughan: thanks for helping me to get my head around the statistics and for always pushing me to make sure I understood the details.

And last, but not least, my friends. Thank you for keeping me sane - kinda.

And now for something completely different - the legalese: *this research has made use of data obtained through the UK Swift Data Archive, provided by the University of Leicester.*

CONTENTS

LIST OF FIGURES

LIST OF TABLES

Chapter 1

Introduction

The history of gamma ray bursts has been likened to a bunch of 6 year olds playing soccer. They don't play positions, they just all run around following the ball. Then mainly by accident the ball pops out and they all run that way. That's kind of what gamma ray bursts theorists have done over the past few years. They were always sure they knew what caused them, but what the cause was has changed over time. – Anon.

Gamma Ray Bursts (henceforth, GRBs) are short (lasting from a fraction of a second up to several hundreds of seconds in the observer's reference frame), energetic events that mark the most violent explosions in the Universe. Current hypotheses associate them with the births of stellar-sized black holes or rapidly spinning, highly magnetized stars. The isotropic luminosity of a typical GRB is $\sim 10^{51}$-10^{52} ergs s^{-1}, making them the most luminous objects in the sky. Assuming a representative burst duration of 100 s indicates that these events release $\sim 10^{53}$-10^{54} ergs of energy isotropically (Frail et al., 2001). However, GRBs are thought to be beamed, thus the total energy released is $\sim 10^{51}$ ergs (Frail et al., 2001; Panaitescu & Kumar, 2001; Piran et al., 2001; Berger et al., 2003b), which is comparable to the total electromagnetic energy released in a supernova (Woosley & Weaver, 1986). Whilst the 'prompt' emission comprises primarily of high energy radiation, hence their name, their long lasting 'afterglows' are visible over essentially all electromagnetic wavelengths. They are also potential emission sources of ultra-high energy cosmic rays, high energy neutrinos and gravitational waves.

The field of GRB research has undergone many changes during its history and over 7,000 refereed works have been published on this subject to date. Thus a full review of the theoretical and observational developments is beyond the scope of this work. In this introductory section I aim to place GRBs in their historical (observational) context whilst briefly describing some of the notable satellites used to observe GRBs before discussing current theoretical models for these phenomena in light of the most recent observations.

1.1 Missions observing GRBs: Historical to present day

In the late 1960s Colgate (Colgate, 1968, 1970, 1974) predicted that supernovae (SNe) could emit γ- and X-rays from accelerated particles at the breakout of a shock front from a SN progenitor's photosphere and urged observatories of the time to look for correlations between SNe and high energy photons.

1.1.1 *Vela* satellites

The *Vela* series of classified satellites (Dickinson & Tamarkin, 1965; Singer, 1965) were run jointly by the Advanced Research Projects of the US Department of Defense and the US Atomic Energy Commission, managed by the US Air Force. They were designed to monitor international compliance with the Nuclear Test Ban Treaty (1963), wherein the signatory countries agreed not to test nuclear devices in the atmosphere, under water or in space. These satellites, launched in pairs for full sky coverage[1], carried a basic instrumentation complement of X-ray, γ-ray and neutron detectors, that were supplemented by various optical and EMP instruments, with which to detect the expected signature of a space detonation. They were not intended for astronomical studies but did provide a significant amount of useful celestial data.

During the mission lifetimes of *Vela* 3 & 4 high energy trigger events that were clearly not the signatures of nuclear detonations were logged but remained unidentified. With the launch of the later satellites (*Vela* 5A,B and 6A,B), with improved timing accuracy, members of the Los Alamos Scientific Laboratory (Klebesadel et al., 1973) were able to rule out the Earth, Moon and the Sun as sources

[1] *Vela* 1 & 2, 16^{th} October 1963; *Vela* 3 & 4, 17^{th} July 1964; and, *Vela* 5 & 6 20^{th} July 1965.

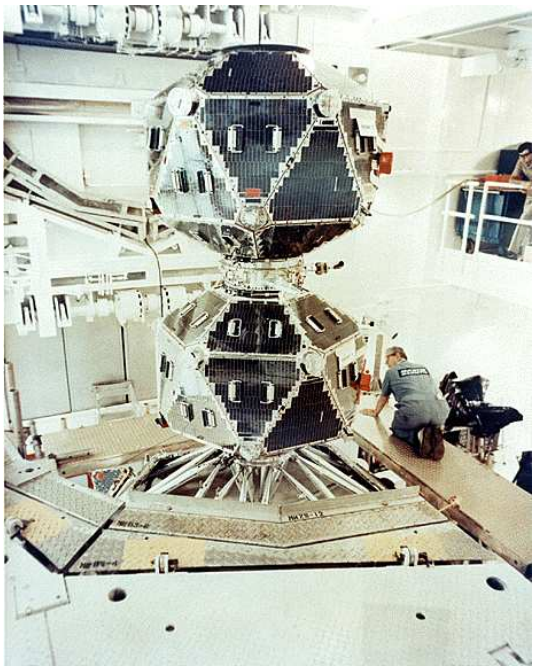

Figure 1.1: The *Vela* 5 satellite. Amongst the instrumental payload were six 10 cm^3 CsI scintillation γ-ray detectors (0.2-1.0 MeV, Vela 5; 0.3-1.5 MeV Vela 6) and a NaI(Ti) scintillation X-ray detector (3-12 keV, Vela 5 & 6). Image courtesy of http://heasarc.gsfc.nasa.gov/docs/heasarc/missions/.

for these unique events, concluding that the γ-ray events were of "cosmic origin". None, however, were associated with SN events, though Klebesadel et al. (1973) point out that this does not necessarily argue against a GRB-SN association, since it is possible that the SNe were merely not bright enough to be detected.

Klebesadel et al. (1973) report on 16 GRB events discovered in the *Vela* data between July 1969 and July 1972[2] stating;

> "*These bursts display a wide variety of characteristics. Time durations range from less than a second to about 30 s. Some count-rate records have a number of clearly resolved peaks whilst others do not appear to display any significant structure.*"

Figure 1.2 shows two such examples of these early GRB detections. Figure 1.2(a) is a reproduction

[2]A total of 73 GRBs were recorded during the mission lifetimes (July 1969 to April 1979) of *Vela* 5 and 6: http://heasarc.gsfc.nasa.gov/docs/heasarc/missions/vela5a.html

Instrument	Energy range (MeV)	Source position localisation†
OSSE	$0.06 \rightarrow 10.0$	10 arc min^2 box
COMPTEL	$0.80 \rightarrow 30.0$	$0.5 \rightarrow 1.0$ degrees
EGRET	$20.00 \rightarrow 3\times10^4$	$5 \rightarrow 10$ arc min
BATSE (large area)	$0.03 \rightarrow 1.90$	3 degrees‡
BATSE (spectroscopy)	$0.015 \rightarrow 110.00$	-

Table 1.1: Summary of *CGRO* instrumental capabilities. † 'Best case' scenario assuming a bright burst. ‡ The localisation accuracy evolved throughout the mission, see Pendleton et al. (1999) for details.

of figure 1 from Klebesadel et al. (1973) showing the typical structure of a GRB detected by *Vela* 5 & 6. Figure 1.2(b) is an event that triggered *Vela* 3 & 4; the satellites in question did not have sufficient timing resolution to make a determination of the location of the burst source[3], however, the event time-history is similar in appearance to the bursts reported in Klebesadel et al. (1973). As such it may represent the first recorded GRB.

1.1.2 *CGRO* -BATSE

The Compton Gamma-Ray Observatory (*CGRO*) was launched on the 5^{th} April 1991 and was decommissioned on the 4^{th} June 2000, detecting $\sim$2700 GRBs over that time period. It carried four instruments[4]: the Burst And Transient Source Experiment (BATSE); the Orientated Scintillation Spectrometer Experiment (OSSE); the Imaging Compton Telescope (COMPTEL); and the Energetic Gamma Ray Experiment Telescope (EGRET). These instruments were much larger and more sensitive than any γ-ray telescope previously flown in space. Table 1.1 summarises the various instrumental capabilities.

The large positional errors associated with *CGRO* -BATSE GRBs hindered efforts to identify counter-

[3]For later versions of the *Vela* satellites the direction angle to the GRB, with respect to the line between the pair of satellites, could be calculated (to an accuracy of $\sim 10^o$) from the difference in burst trigger times. The light travel time from one satellite to another, across the orbital diameter was $\sim$ 1 s, which was greater than the event resolution time ($\sim$ 0.2 s). If an event was observed by multiple pairs of satellites then these direction angles were combined to determine one or two possible directions for the burst.

[4]http://cossc.gsfc.nasa.gov/docs/cgro/cgro/

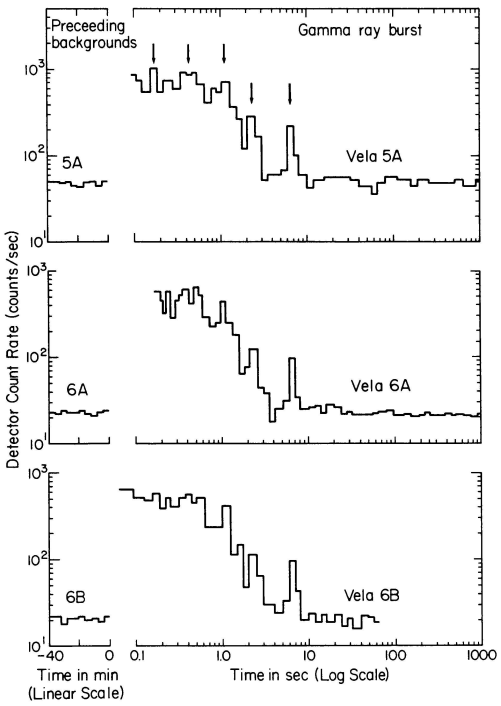

(a)

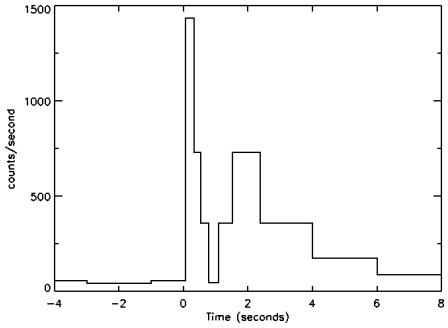

(b)

Figure 1.2: *Vela* GRB countrate light curves. (a) Copy of figure 1 from Klebesadel et al. (1973) showing the light curve of a GRB event detected on the 22^{nd} August 1970 as recorded by 3 *Vela* satellites. The lefthand sections (plotted with a linear timescale) indicate the background countrate prior to the event, whilst the righthand sections (logarithmic scale) show the events. *Vela* 5A count rates have been reduced by 100 counts s^{-1} (a major fraction of the background) to emphasise structure. Arrows indicate some of the common structure. (b) Event recorded by *Vela* 4A,B on 2^{nd} July 1967 (taken from http://antwrp.gsfc.nasa.gov/htmltest/jbonnell/www/grbhist.html).

Figure 1.3: The Compton Gamma-Ray Observatory (*CGRO*). Image courtesy of http://heasarc.gsfc.nasa.gov/docs/heasarc/missions/.

parts in other wavelengths. However, the large GRB sample did produce some important results;

- Previous hints of a bimodality in burst duration distribution put forward by Klebesadel (1992a,b), from a limited set of burst data (derived over an eight year period from a variety of spacecraft) was confirmed. The duration distribution, measured from T_{90} values[5], consisted of two populations; 'short-hard' bursts (T_{90}: fractions of a second $\rightarrow$ 2 s) and 'long-soft' bursts (T_{90}: 10 $\rightarrow$ several hundred s) (Kouveliotou et al., 1993; Norris et al., 1993).

- The distribution of GRBs across the sky was shown to be isotropic (Hartmann et al., 1992; Meegan et al., 1992) indicating that the progenitors of these events were either extremely close to our Sun within the galaxy (i.e. less than the galactic disk scale height), in an extended galactic halo, or were cosmological in origin.

- GRB continua spectra were shown to be non-thermal over the *CGRO* bandpass, being well fit by a single power law (over a narrow energy range), or by broken power law or Band function[6]

[5] T_{90} is the time period over which 90% of the total GRB fluence is detected, i.e. from 5% to 95%.

[6] The Band function (Band et al., 1993) is defined as;

$$N(E) = \begin{array}{ll} K\left(\frac{E}{100}\right)^{\alpha_1} exp\left(\frac{-E}{E_0}\right), & E < (\alpha_1 - \alpha_2)E_0, \\ K\left[\frac{(\alpha_1-\alpha_2)E_0}{100}\right]^{(\alpha_1-\alpha_2)}\left(\frac{E}{100}\right)^{\alpha_2} exp[-(\alpha_1 - \alpha_2)], & E > (\alpha_1 - \alpha_2)E_0, \end{array} \quad (1.1)$$

(over the full energy range). See Fishman & Meegan (1995) and references therein.

- A bright, prompt optical flash and radio flare were discovered in association with the very bright GRB 990123. Optical observations were started 22 s after the BATSE trigger by ROTSE-I and peaked at a V equivalent magnitude of 8.86 ± 0.02 (from table 1 of Akerlof et al., 1999). A short lived radio flare, occuring $\sim$ 1 day after the burst, which rapidly faded away, was reported by Kulkarni et al. (1999b).

Before the launch of *CGRO* one theory proposed that GRB progenitors were Galactic neutron stars (henceforth NSs), distributed primarily in the Galactic plane e.g. Higdon & Lingenfelter (1990). This distribution was later ruled out by Mao & Paczynski (1992). A simple Galactic halo model (extending out to between 125 and 400 kpc) was found to be an acceptable fit to the observed distribution of bursts by Hakkila et al. (1994a,b), however, Fishman & Meegan (1995) point out that there was no direct physical or observational evidence for such an extended halo and that its existance was postulated purely to solve the GRB problem. A cosmological origin for GRBs was first postulated by Usov & Chibisov (1975). Such distributions were fit by numerous groups in the *CGRO* era (see § 5.4 of Fishman & Meegan (1995) and references therein) with the conclusion that a satisfactory fit to the observations could be made if GRBs were considered to be 'standard candles' (with luminosities of the order 10^{51} ergs s^{-1}), with standard cosmologies and no source evolution (though models including source evolution were starting to be considered). Whilst many theorists adopted the cosmological distance paradigm the BATSE data were unable to provide conclusive evidence for the distance scale; the isotropy and inhomogeneity of bursts only showed that we were at the centre of the apparent burst distribution. Final confirmation would require observations at additional wavelengths.

The *CGRO* spectra were shown to be non-thermal over the entire bandpass, with the COMPTEL experiment observing the peak power from many bursts to be in the MeV energy range (e.g. Winkler et al., 1992; Hanlon et al., 1994). A comprehensive study of BATSE spectra was conducted by Band et al. (1993) by modelling the low energy continuum as a power law with an exponential cutoff and by a steeper power law at higher energies. This spectral form was found to fit the data well over the entire *CGRO* energy range, however, the model parameters showed a wide diversity in values. The break energy, E_0, in particular varied from 100 keV to over 1 MeV.

where α_1 is the low energy power law index, α_2 is the high energy power law index, E_0 is the characteristic (or break) energy of the spectrum in keV and K is a normalisation constant.

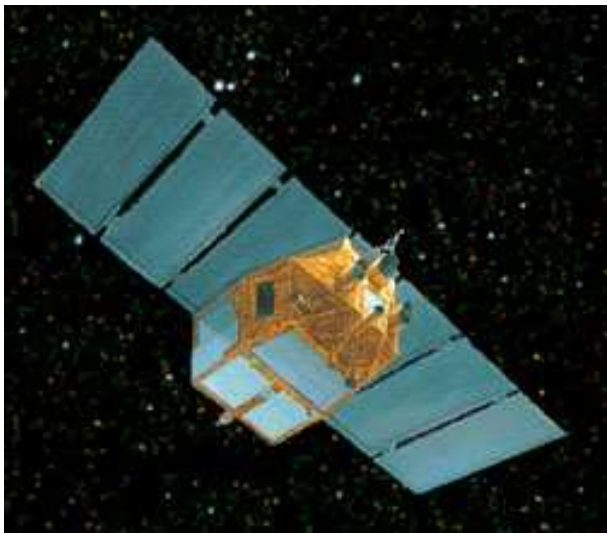

Figure 1.4: The *BeppoSAX* observatory. Image courtesy of http://heasarc.gsfc.nasa.gov/docs/heasarc/missions/.

Prior to *CGRO* 's launch the canonical view of GRB spectra was that there should be spectral line features superimposed over the continuum of these bursts, mostly likely cyclotron lines produced in the intense magnetic fields of NSs. Fishman & Meegan (1995) reported that up to the date of their review paper that no emission or absorption line features had been conclusively proved. (Further discussion on this topic will be covered in chapters 3 and 4 of this work.)

1.1.3 *BeppoSAX*

The *BeppoSAX* observatory was launched on the 30^{th} April 1996 by the Italian Space agency (ASI), with participation of the Netherlands Agency for Aerospace programs (NIVR). All in-orbit operations of the mission were ended on 30^{th} April 2002 due to degrading spacecraft conditions and rapid orbital decay. It carried both Narrow Field Instruments (NFI) and Wide Field Cameras.

The NFI (Boella et al., 1997) consisted of: three identical Medium Energy Concentrator Spectrometers (MECS); a Low Energy Concentration Spectrometer (LECS); a collimated High Pressure Gas Scintillation Proportional Counter (HPGSPC); and a collimated Phoswich Detector System (PDS). The four lateral active shields of the PDS were used as GRB monitors with a temporal resolution of $\sim$ 1 ms, provided the burst had a fluence of $\geq 10^{-6}$ ergs cm^{-2} in the 60 $\rightarrow$ 600 keV energy range. In addition,

Instrument	Energy range (keV)	Field of view (^{o} FWHM)
MECS	1.3 $\rightarrow$ 10.0	0.5
LECS	0.1 $\rightarrow$ 10.0	0.5
HPGSPC	4.0 $\rightarrow$ 120.0	1.1
PDS	15.0 $\rightarrow$ 300.0	1.3
WFC†	2.0 $\rightarrow$ 30.0	20 $\times$ 20

Table 1.2: Summary of *BeppoSAX* instrumental capabilities (see Boella et al., 1997, and references therein). †Per unit through the mask.

perpendicular to the axis of the NFI and pointed in opposite directions, were two coded mask proportional counters (Wide Field Cameras, WFC). One of the scientific aims of this mission was to provide not only well resolved (1 ms) high energy GRB light curves but also to detect X-ray counterparts with a positional accuracy of $\sim 5'$ (Boella et al., 1997). Table 1.2 summarises the various instrumental capabilities.

The following lists some of the prominent results found during the *BeppoSAX* mission;

- The first X-ray afterglow was discovered in GRB 970228 (Costa et al., 1997). This in turn facilitated optical (van Paradijs et al., 1997) and radio (Frail et al., 1997) detections of the same GRB.
- The first GRB redshift measurement was made from the *BeppoSAX* trigger of GRB 970508 with z $= 0.8349 \pm 0.002$ from a metal line absorption system and an approximate upper limit of z < 2.3 from a Lyman-α absorption system (Metzger et al., 1997, and references therein). The measured fluence in the 20 $\rightarrow$ 1000 keV energy range was 3×10^{-6} ergs cm^{-2}. Assuming isotropic emission this burst had a total γ-ray energy, E_γ, of 7×10^{51} ergs.
- *BeppoSAX* was the first mission to show that virtually all ($\sim$90%) 'long' GRBs have fading X-ray counterparts, which remain detectable for days or weeks after the initial GRB (De Pasquale et al., 2003). The same study reported that only 50% of the GRBs had Optical Transients (OTs) associated with them. The authors stated this could be because optical observations were delayed

or were not deep enough, the bursts could be at high redshift or the OTs could be affected by high absorption columns.

- The discovery of a class of events called X-Ray Flashes (XRFs) that appear to be closely related to GRBs (Heise et al., 2001; Kippen et al., 2003).

- An achromatic steepening break in afterglow light curves was found in several bursts, hinting that at least some GRB emission is likely to be collimated (Kulkarni et al., 1999a; Harrison et al., 1999, see also § 1.3.2 of this work).

- A 'possible' GRB-SN association was put forward linking GRB 980425 with SN1998bw (Galama et al., 1998; Kulkarni et al., 1998b, see also § 1.2.1 of this work). *BeppoSAX* was the first mission to trigger on this burst but it was also detected by other missions such as *CGRO* -BATSE.

Heise et al. (2001) identified a class of transient objects called XRFs in data from the WFC, with durations of the order of minutes. Whilst being bright in X-rays these events did not trigger the GRB Monitor on *BeppoSAX* . Their properties are very similiar to the X-ray counterparts of GRBs, with peak energies in the $2 \rightarrow 10$ keV range; the flux in this energy range was up to a factor of 100 larger than the flux in the $50 \rightarrow 300$ keV γ-ray range. Heise et al. (2001) state that the properties of XRFs display an extension of GRB properties and are therefore probably a result of a continuation of the physical circumstances which lead to the formation of GRBs. *HETE-2* (see § 1.1.4) was to later confirm that burst spectra form a continuum from events in which the peak energy is < 10 keV (XRFs) with no measurable γ-ray emission, through 'X-ray Rich' events that have some γ-ray emission, to the 'classical' GRBs with peak energies of the order 100 keV (Hurley, 2006), in roughly equal numbers (Sakamoto et al., 2005).

An OT was discovered in the error box of GRB 980425 (a weak but otherwise unremarkable GRB; Galama et al., 1998), however, its optical light curve was unusual compared to those seen in other GRBs, showing clear evidence of a SN profile. The spectrum of the OT and its location in the spiral arm of the galaxy ESO184-G82 indicated that it was a very luminous SN (SN 1998bw) that exploded at roughly the same time as the GRB. In addition, at its peak, the radio light curve of this SN was unusually luminous, a fact which Kulkarni et al. (1998b) interpreted as the source expanding with an apparent velocity of at least twice the speed of light. Therefore the SN must have produced a relativistic shock wave (whereas SN ejecta are typically characterized by non-relativistic velocities). Kulkarni

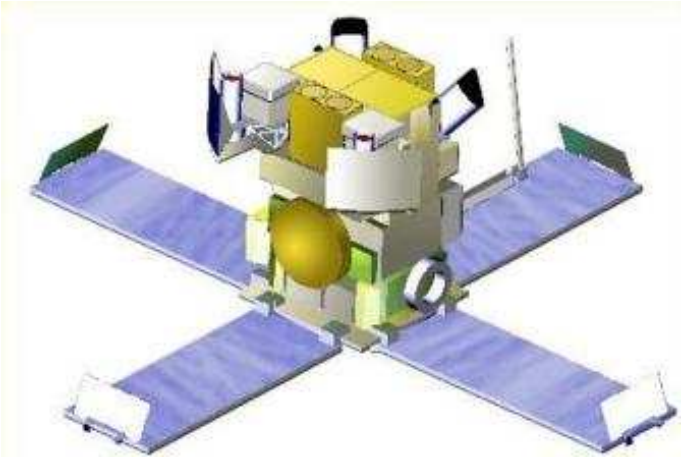

Figure 1.5: The *HETE-2* observatory. Image courtesy of http://heasarc.gsfc.nasa.gov/docs/heasarc/missions/.

et al. (1998b) further inferred that this shock wave produced the burst of γ-rays that formed the GRB signature. However, for this burst, the positional accuracy of the GRB was insufficient to conclusively prove that the two events were directly connected. For further discussion on the GRB-SN connection see § 1.2.1.

1.1.4 *HETE-2*

The original *HETE* mission was launched on the 4^{th} November 1996, however, the failure of several explosive bolts prevented its separation from another satellite (Argentina's *SAC-B*) and from its Dual Payload Attachment Fairing (DPAF) envelope. As a result *HETE-1* was unable to function correctly and suffered a critical failure due to a lack of solar power within a day of the launch[7]. A second mission, *HETE-2* , was launched on the 9^{th} October 2000 and declared fully operational on the 6^{th} February 2001. This mission was a collaboration between the USA, Japan, France and Italy, led by the Center for Space Research at MIT.

The primary aims of the mission[8] were: to provide precise ($10'$) localization of GRBs within 10-100 s of the burst onset; to transmit these coordinates in 'near real time' (< 10 s) to the Gamma ray burst

[7] http://space.mit.edu/HETE/history.html

[8] http://space.mit.edu/HETE/mission_goals.html

Instrument	Energy range (keV)	Field of view (steradians)
FREGATE	$6.0 \rightarrow 400.0$	3.00
WXM	$2.0 \rightarrow 25.0$	1.60
SXC	$0.5 \rightarrow 14.0$	0.91

Table 1.3: Summary of *HETE-2* instrumental capabilities (see the *HETE-2* mission instrument page at http://space.mit.edu/HETE/Instruments.html and attendant links).

Coordinates Network (GCN)[9]; to perform spectroscopy and provide time histories of these bursts over the $1 \rightarrow 400$ keV energy range.

HETE-2 carried three instruments: a set of wide-field γ-ray spectrometers (the French Gamma Telescope, FREGATE), a Wide field X-ray Monitor (WXM) and a set of Soft X-ray Cameras (SXC).

The most important results to come out of this mission were;

- A selection of so called 'dark' bursts, or GRBs previously thought to have no optical counterparts, were found to have faint optical emission. Their previous classification as 'dark' may have been the result of several observational effects: some GRBs fade rapidly in the optical domain, thus are undetectable by delayed observations; others are merely too faint to been seen by all but the largest telescopes; whilst the rest may be affected large absorption columns in their host galaxies.
- The confirmation of the *BeppoSAX* result of another subclass of GRBs called XRFs (see §1.1.3).
- The discovery of GRB 030329, a widely observed, nearby GRB (z = 0.169), which provided the first firm evidence for a direct link between GRBs and SN (in this case SN 2003dh). See for example Stanek et al. (2003), Hjorth et al. (2003) and § 1.2.1 of this work.
- The localisation of GRB 050709 (Butler et al., 2005a), which was the first short burst observed to have an optical counterpart. This led to the firm establishment of the cosmological (z =0.16) origin of this class of GRBs (see Hjorth et al., 2005; Villasenor et al., 2005; Covino et al., 2006, and references therein). Optical observations were also able to place stringent constraints on the

[9] http://gcn.gsfc.nasa.gov/gcn/

presence of a SN signature: a SN, if present, would be $\geq$ 100 times fainter than a typical type Ia supernova or a bright hypernova like SN 1998bw. See § 1.2.2 of this work for a discussion of short GRB progenitors.

Whilst previous GRBs had been linked to SN (e.g. GRB 980425/SN 1998bw, GRB 011121/SN 2001ke) GRB 030329 was the first burst with a confirmed spectroscopic detection of a SN signature in its afterglow. Stanek et al. (2003) found that, after correcting for the standard afterglow emission, the spectrum of the supernova was remarkably similar to the type Ic "hypernova" SN 1998bw. Broadband observations collated by Berger et al. (2003c) also suggested that the central engine of the GRB may have emitted a structured jet, with a narrow (5^o opening angle) relativistic core and a wider (17^o), mildly relativistic jet. This theory was backed up by millimetre data presented by Sheth et al. (2003), which also ruled out a competing 'refreshed shock' model for the broad band behaviour of GRB 030329 proposed by Granot et al. (2003). Whilst GRB 030329 (and other bursts like it) are sub-energetic in the γ-ray band ($E_{030329,\gamma} \sim 5 \times 10^{49}$ ergs) the energy carried by lower wavelengths, typically radio, in the theorised mildly relativistic jet brings the total energy yield of the GRB upto the standard reservoir of $\sim 10^{51}$ ergs (Frail et al., 2001; Panaitescu & Kumar, 2001; Piran et al., 2001; Berger et al., 2003b).

1.1.5 *Swift*

Swift is a NASA Medium-Class Explorer (MIDEX) mission, developed and built in collaboration with UK and Italian institutes. Thus far it is a unique multi-wavelength mission that is able to automatically slew rapidly (typically within 100s of the trigger; Gehrels et al., 2007) to and observe GRBs in γ-ray, X-ray and optical wavelengths: a time frame which has previously remained unexplored at lower energies. *Swift* is able to determine GRB positions to arcsecond accuracy within minutes of the trigger event, which are then disseminated via the GCN system, allowing for rapid ground-based follow-up[10]. It was launched on the 20^{th} November 2004 and was brought online over a period of 8 weeks. *Swift* started detecting GRBs in December 2004 and began actively following afterglows in February 2005. Normal, i.e. fully automated, operations commenced on the 5^{th} April 2005. Between December 2004 and the end of June 2008 *Swift* detected 340 GRBs and nearly all have been followed up with the onboard NFIs.

[10]A team of observers affiliated with *Swift* represent over 40 telescopes world wide and can be found at http://heasarc.gsfc.nasa.gov/docs/swift/about_swift/participants/teamlist.html

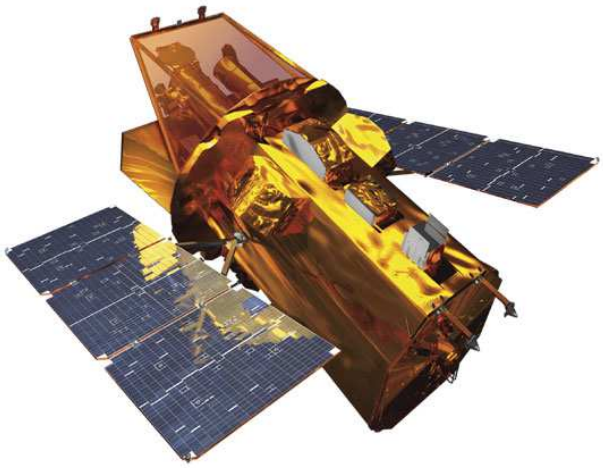

Figure 1.6: Computer rendering of the *Swift* satellite. Image courtesy of http://heasarc.gsfc.nasa.gov/docs/heasarc/missions/.

Instrument	Energy/wavelength range	Field of view	Source position localisation
BAT	$15.0 \rightarrow 150.0$ keV	1.4 steradians (half coded)	1-4 $'$
XRT	$0.2 \rightarrow 10.0$ keV	$23.6\,' \times 23.6\,'$	5 $''$
UVOT	$170 \rightarrow 650$ nm	$17.0\,' \times 17.0\,'$	few $\frac{1}{10}$ $''$

Table 1.4: Summary of *Swift* instrumental capabilities.

The three instruments providing broadband coverage are: a wide field of view, coded aperature mask Burst Alert Telescope (BAT; Barthelmy et al., 2005a); an imaging X-Ray Telescope (XRT; Burrows et al., 2005a) utilizing flight spares from JET-X (Wolter 1 grazing incidence mirrors) and XMM-Newton (CCD detector); and a modified Ritchey-Chretien telescope with six colour filters and two grisms, the Ultra-Violet/Optical Telescope (UVOT; Roming et al., 2005). Table 1.4 summarises the various instrumental capabilities.

Swift has two main observation types[11]: Automatic target (AT), when a new GRB is detected the satellite autonomously slews to the new position; and Pre-Planned Target (PPT), where observations are planned on the ground and telemetered to the satellite. The XRT can operate in two states: Auto,

[11] http://swift.gsfc.nasa.gov/docs/swift/analysis/xrt_swguide_v1_2.pdf

the normal operating mode, where the XRT automatically selects the science mode according to the source count rate; and Manual, where the science mode is predetermined for each observation.

The science modes available in both states ares are: Image (Im) long or short; Photodiode, either Piled-up (PU) or Low Rate (LR); Windowed Timing (WT); and Photon Counting (PC). Im has a readout time of 0.1 s (short) or 2.5 s (long) when the source has a flux of 25 mCrab to 45 Crab. The image produced is highly piled up and produces no spectroscopic data. It is primarily used to derive accurate X-ray positions and flux estimates (see chapter 2 for a discussion of pile up and analysis methods to counter it in other modes). The XRT switches to Photodiode mode when the incidence flux is $0.6 - 60$ Crab; this produces a high resolution (0.14 ms) light curve and spectrum but does not produce any spatial information. Unfortunately a micrometeorite impacted the XRT CCD at the end of May 2005 producing a number of hot columns (Abbey et al., 2006). The readout method for the Photodiode mode means that this mode has currently been disabled as a result of this damage. The final two modes, WT and PC, have remained operational by vetoing the hot columns to prevent saturation of the telemetry. WT mode becomes active for incident fluxes of $1 - 600$ mCrab producing 1-D images, spectral data and light curves with 1.7 ms resolution. As the source becomes fainter, i.e. < 1 mCrab, the XRT switches to PC mode, producing 2-D images, spectral data and light curves with 2.5 s resolution.

To eliminate the effect of charged particles incident on the XRT CCD X-ray event patterns from each readout mode are identified and classified. For PC mode the distribution of charge, for a single event, in a 3×3 matrix is classified according to a library of 32 grades, of which grades $0 - 12$ are considered to be good (see figure 1.7(a)). It is not possible to use a 3×3 matrix to define the grades for the WT or Photodiode modes, instead a 7×1 matrix is used (see figure 1.7(b)). Grades $0 - 2$ are considered good for WT mode and $0 - 5$ for Photodiode mode.

The primary objectives[12] of the *Swift* mission are to: rapidly disseminate GRB positions to the community; determine the origins of GRBs; classify GRBs and search for new types; determine how the blastwave evolves and interacts with its surroundings; use GRBs to study the early universe and preform a sensitive ($\sim$1 mCrab in the 15-150 keV band over two years, decreasing to $\sim$3 mCrab in crowded fields of view) hard X-ray survey of the sky. Under normal operational conditions priority is given to GRB observations ($\sim$56% of the total observing time thus far, Gehrels et al. 2007), whilst the remaining time is shared between non-GRB planned targets, Target of Opportunity (ToO) observations (submitted

[12] http://swift.gsfc.nasa.gov/docs/swift/about_swift/

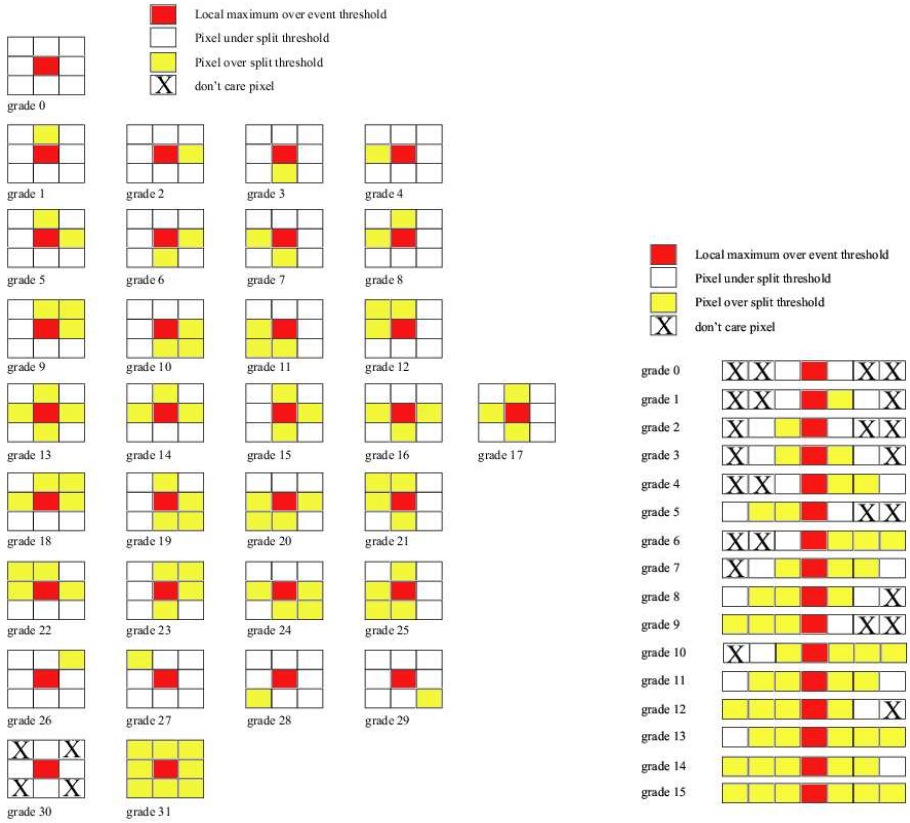

(a) Definition of the XRT grades for Photon Counting (PC) mode.

(b) Definition of the XRT grades for Timing modes.

Figure 1.7: Definition of the XRT grades, taken from figures 2.2 and 2.3 respectively of The *Swift* XRT Data Reduction Guide (http://swift.gsfc.nasa.gov/docs/swift/analysis/xrt_swguide_v1_2.pdf).

via http://www.swift.psu.edu/too.html) of non-GRB transients, and calibration sources.

As a result of *Swift* 's ability to rapidly slew to detected events, there has been unprecedented coverage of early time X-ray afterglows of GRBs and other transient high energy events. The following are some highlights of the mission thus far;

- Nearly all of the GRBs observed promptly by *Swift* have an X-ray afterglow; a canonical light curve has emerged from these observations as described by Nousek et al. (2006) and Zhang et al. (2006), which differs from pre-launch expectations (see § 1.3.3 for a more detailed description).
- Early time observations have revealed that the prompt γ- and X-ray emission smoothly transitions

into the afterglow (O'Brien et al., 2006; Zhang et al., 2006).

- The early optical afterglows of most *Swift* -era GRBs are dimmer than expected (Roming et al., 2006). The fraction of promptly observed GRBs with a UVOT detection is $\sim$30%; if ground based observations are also included then the detection rate increases to $\sim$50%.

- Contrary to pre-*Swift* expectations there is a notable lack of confirmed achromatic jet breaks in the *Swift* sample (Willingale et al., 2007; Sato et al., 2007). It is unclear at this stage if these results will invalidate the standard theoretical GRB model (see § 1.3.3 'Phase IV' for further discussion on this topic).

- The average redshift of the *Swift* mission, $< z > \cong 2.7$, is higher than that of previous missions, $< z > \cong 1.5$ (Le & Dermer, 2007). This is a consequence of improved trigger sensitivity and rapid afterglow observations.

- On the 27^{th} December 2004 a giant flare (total isotropic energy 2×10^{46} ergs) from Soft Gamma-ray Repeater (SGR) 1806-20 was detected (Palmer et al., 2005). This energetic event also triggered several other high energy detectors, see e.g. Hurley et al. (2005), Terasawa et al. (2005) and Boggs et al. (2007). If the flare had occurred further away, but within 40 Mpcs, it would have resembled a short hard GRB. This suggests that flares from extragalactic SGRs may form a subclass of short GRBs. The transient was not produced by the formation of a compact stellar body but is thought to be the result of a catastrophic reconfiguration of a neutron star's magnetic field.

- Early *Swift* GRBs, notably GRB 050126 and 050219A, were found to have unexpectedly steep decay sections in their early time X-ray afterglows (Goad et al., 2006). This steep decay phase was later found to present in virtually all *Swift* GRBs that had prompt observations (Nousek et al., 2006, see also § 1.3.3 of this work).

- Bright X-ray flares were seen in GRB/XRF 050406 and GRB 050502B. The fluence of the flare in GRB 050502B was comparable to that seen in the prompt γ-rays (Burrows et al., 2005b; Falcone et al., 2006). It has been discovered that flaring events occur in $\sim 50\%$ of afterglows with prompt follow up observations, with fluences ranging from a few percent to $\sim$100% of the fluence of the burst emission (Burrows et al., 2007).

- Two candidate "naked" GRBs were detected; GRB 050421 (Godet et al., 2006) and GRB 050911 (Page et al., 2006). These bursts, which had rapidly decaying afterglows with a temporal decay

index of $\sim$ 3, are thought to occur in extremely low density environments, leading to a weak, or non-existant, forward shock. Thus the observed decay comes from high latitude emission (Kumar & Panaitescu, 2000, see §1.3.3 for further discussion of afterglow phases).

- GRB 050509B marked the first *Swift* X-ray afterglow from a short GRB (Gehrels et al., 2005). It was located near a luminous, non-star forming elliptical galaxay with a redshift of 0.225; a location that provided support for the theory that short GRBs are formed by the merger of two compact objects (see § 1.2.2 for more details). The X-ray afterglow of GRB 050509B faded below the *Swift* detection limit within a few hours and no optical afterglow was detected, explaining the past difficulty in localising this type of event.

- GRB 050904 is the highest redshift burst detected by the *Swift* mission thus far with z = 6.29 (Kawai et al., 2005). Higher redshifts have been claimed for other bursts but as yet have not been confirmed spectroscopically. Studies indicate that GRB 050904 is phenomenologically similiar to lower redshift bursts but may be more energetic (Cusumano et al., 2007; Gou et al., 2007).

- A GRB-SN association between XRF/GRB 060218/SN 2006aj was detected at z = 0.0331 (Campana et al., 2006b, and references therein). The rapid slew preformed by *Swift* ensured that the NFI were able to observe the SN at the time of the initial core collapse and shock breakout. In addition to the classical non-thermal emission a thermal component was also detected and observed to evolve over time (Campana et al., 2006b).

- GRB 060614 threw the previous long/short classification of bursts into doubt. It was a nearby burst (z = 0.125) with a T_{90} duration (15-350 keV) of 102 s but with no detected SN signature (Gehrels et al., 2006). In addition GRB 060614's afterglow is located a significant distance from the center of the star forming region in its host galaxy; a location more commonly associated with short GRBs (Gal-Yam et al., 2006). Further inspection of the GRB's prompt light curve shows early hard spikes (duration $\sim$ 5 s) followed by a long, soft emission tail (see the discussion in § 1.2.2).

- The bright (in X-rays and optical wavelengths) burst GRB 060729 was observed by *Swift* and *XMM* -Newton for 125 days with no confirmed jet break. The longterm visibility of the afterglow was partly due to an extended (53 ks) shallow (temporal decay index, $\alpha = 0.14 \pm 0.02$) period of decay (Grupe et al., 2007), which implies a much larger energy injection than seen in any other GRB afterglow.

- GRB 070125 was the first long GRB to be detected in a halo environment (Cenko et al., 2008), $\sim$ 27 kpc away from the nearest host galaxy, a position normally associated with short GRBs. The combined measured values for duration, energy release and large local density for GRB 070125 all point to this being a long burst. For the progenitor to have travelled that far from its host it would have to have a pecular velocity of $\sim 10^4$ km s^{-1} (assuming a lifetime of 20 Myr), an order of magnitude higher than the fastest known object in our galaxy, the Guitar pulsar (v = 1600 km s^{-1}, Cordes et al. 1993). Cenko et al. (2008) state that it is much more likely that the GRB progenitor was formed in situ and is either part of an extended UV disk from the host galaxy or was formed in a tidal tail from interacting galaxies.

- The most distant spectroscopically confirmed short burst, GRB 070714B, at z = 0.92 (Graham et al., 2007) was detected, exceeding the previous record of z = 0.55 for GRB 051221 (Berger & Soderberg, 2005). This moves back the time at which we know short bursts were being formed, suggesting that the present evidence for an old progenitor population may be observationally biased.

1.2 Classes and their Progenitors

As discussed in § 1.1 there appear to be two distinct classes of GRBs based on temporal and spectral behaviour. Kouveliotou et al. (1993) assigned a separation point at T_{90} = 2 s in the bimodal distribution producing 'long' (LGRB; typical T_{90} of the order few 100 s) and 'short' (SGRB; T_{90} of the order milliseconds) duration categories. These classifications are supported by the spectral properties; SGRBs typically have harder spectra than LGRBs. The spectral lag (the delay of arrival time between lower energy band emission to high energy band emission) has been found to be much smaller in SGRBs than LGRBs (Yi et al., 2006; Norris & Bonnell, 2006; Gehrels et al., 2006) and is consistent with being zero.

A third class has been proposed by several authors (Mukherjee et al., 1998; Horváth, 1998) with an intermediate duration (2.5 s $< T_{90} <$ 7 s) and spectra that are similiar to the classical 'long' duration bursts. At the present time this class has not been widely accepted by the GRB community.

1.2.1 LGRBs

The host galaxies of LGRBs are early type, predominantly irregular dwarf galaxies (Fruchter et al., 2006), with star formation rates of $\sim 1 \rightarrow 10$ $M_{\odot}$ yr^{-1}, (Berger et al., 2003a; Christensen et al., 2004; Tanvir et al., 2004). The metallicities of the regions around LGRBs have been shown to be low (Vreeswijk et al., 2001; Savaglio et al., 2003; Prochaska et al., 2004; Vreeswijk et al., 2004). Le Floc'h et al. (2003) asserts that the host galaxies, as a whole, have metallicities that are generally lower than average massive star forming galaxies; in contrast Christensen et al. (2004) found that LGRB host galaxies are similar to field galaxies with the largest specific star formation rates. LGRBs are concentrated in the very brightest regions of their host galaxies (Fruchter et al., 2006; Kelly et al., 2008), more so than core-collapse SNe, in hosts that are significantly fainter than the hosts of core-collapse SNe. All such observational evidence strongly suggests that LGRBs are associated with extremely massive, but short lived, stars and may be restricted to galaxies of limited chemical evolution.

The strongest support for the massive star progenitor scenario comes from the identification of SN Ib/c light curves that are seen to peak weeks after the burst in GRB afterglows. The first 'potential' GRB-SN association was GRB 980425/ SN 1998bw (Galama et al., 1998; Kulkarni et al., 1998a, see also § 1.1.3), though the accuracy of the localisations of the GRB and SN were insufficient to prove a firm connection. The first confirmed association was GRB 030329/ SN 2003dh (Hjorth et al., 2003; Stanek et al., 2003, see also § 1.1.4). Since then many GRB-SN associations have been studied, e.g. : GRB 011121/ SN 2001ke (Bloom et al., 2002b; Price et al., 2002; Stanek et al., 2002; Garnavich et al., 2003, candidate); GRB 021211/ SN 2001lt (Della Valle et al., 2003a,b, 2004, candidate); GRB 031203/ SN 2003lw (Malesani et al., 2004; Gal-Yam et al., 2004; Soderberg et al., 2004, confirmed); GRB 050525A/ SN 2005nc (Della Valle et al., 2006b, confirmed); and GRB 060218/ SN 2006aj (Campana et al., 2006b; Ferrero et al., 2006; Mirabal et al., 2006; Sollerman et al., 2006; Gehrels, 2008, confirmed)

Woosley & Bloom (2006) state that the observations thus far, taking into account limited follow-up programs etc, are consistent with all LGRBs being accompanied by SNe of Type Ic, even though there is considerable diversity in rise times, brightness and evolution. In addition well studied GRB/SN show evidence for broad lines in their spectra (indicative of high velocity ejecta), leading to a suggestion by Woosley & Bloom (2006) that a subclassification of Type Ic-BL should be used. This subclassification is based purely on observational signatures and makes no reference to progenitor models; as such it may be a less contentious nomenclature than the previous 'hypernova' classification used in the literature

(see below).

One of the early models proposed for LGRB progenitors was the 'supranova' model (Vietri & Stella, 1998); a massive star undergoes a SN event to form a rapidly rotating, 'hypermassive' NS (a NS with a mass above the critical value for a slowly rotating NS) whilst ejecting its outer layers. Dipole radiation eventually slows the NS down and it collapses to form a BH. During this collapse $\sim 10 - 20\%$ of the NS material forms a disk/torus around the BH, which subsequently accretes onto the BH causing jets to be launched by a process that is currently poorly defined (see § 1.3.2). The delay between the SN and the GRB can range between weeks to months (or even years in the original incarnation of the model). However, this model was ruled out during the analysis of the GRB 030329/ SN 2003dh association (and subsequent events) as the GRB was observed to occur within 2 days of SN 2003dh (though the observations were also compatable with the simultaneous occurance of both events).

One of the current theories postulates that LGRBs are the result of the core collapse of a massive star progenitor (Main Sequence mass of $25 \rightarrow 30$ $M_{\odot}$; Woosley & Bloom 2006 and references therein), mostly likely a Wolf Rayet star (Woosley, 1993; Paczynski, 1998b,a), with an extremely luminous event (many orders of magnitude brighter than classical SNe events) called a 'hypernova' or 'Type Ic-BL' SN. The outer material of this star, the H and He envelope, is thrown off during the explosion. The inner core of the star collapses directly into a ~ 10 $M_{\odot}$ Kerr BH whilst the outer core forms a massive accretion torus. Accretion of this torus into the BH is thought to launch and sustain relativistic jets along the BH's rotation axis, though the precise details of this mechanism are not currently known. It is also thought that the progress of the ejecta through the stellar envelope aids the collimation of the jets into narrow opening angles (θ_j of the order a few degrees), as may the presence of magnetic fields surrounding the BH-torus system. LGRBs derive their energy from either the gravitational energy liberated by accretion of matter from the torus, or by the extraction of rotational energy from the central BH, mediated by the presence of the torus, or from a combination of these mechanisms (see § 1.3.2). The duration of the burst is set by the fall back timescale of the stellar material rather than the accretion timescale (MacFadyen & Woosley, 1999), which gives the typical duration of the 'prompt' emission of a LGRB.

The interaction of the relativistic jets with the stellar envelope as they break out of the surface of the progenitor should produce unique observational 'precursor' signatures, which could consist of: a brief non-thermal γ-/X-ray transient; a longer lasting (few hours to days) UV/X-ray thermal pulse whose

energy is a few percent of the total burst energy; and potential Fe K_α line emission with $I_{Fe} \sim 10^{45}$ ergs s^{-1} (Mészáros & Rees, 2001; Ramirez-Ruiz et al., 2002a; Waxman & Mészáros, 2003). For further discussion on the 'precursor' phenomenum see chapter 5 of this work.

In addition to this model various groups have suggested that millisecond magnetars could provide the GRB central engine (e.g. Usov, 1992; Thompson, 1994; Wheeler et al., 2000; Drenkhahn & Spruit, 2002). In particular Thompson et al. (2004) state that large energies, up to 10^{52} ergs s^{-1}, can be extracted from the coupling between the neutrino-powered wind of the newly formed NS with the strong magnetic field of the millisecond magnetar. The fields required ($> 10^{15}$ G) are large, but no larger than in other LGRB progenitor models. However, all of the models constructed so far ignore the accretion of material, > 0.1 $M_\odot$ s^{-1}, onto the proto-NS for several seconds before it contracts to its final state of a millisecond magnetar. This accretion must be halted in some way to prevent a further collapse to a BH.

Several models invoking binary channels have been put forward for the production of LGRBs. Some, like the merger (by common envelope) of two massive stars that burn He in their centers result in Wolf Rayet stars similar to the single star model above (Fryer & Heger, 2005). Other models, such as the merger of a BH with the He core of a massive star (Fryer & Woosley, 1998; Zhang & Fryer, 2001) or the merger of a BH and White Dwarf (WD) (Fryer et al., 1999), produce long bursts, which are probably longer than typical GRBs.

1.2.2 SGRBs

SGRBs are typically located on the outskirts of elliptical galaxies (Bloom & Prochaska, 2006) in which the star formation rate is generally very low. Some authors have cited star formation rates of the order < 0.02 $M_\odot$ yr^{-1} (Berger et al., 2005b; Berger, 2006), whilst others have quoted a higher value of the order < 0.2 $M_\odot$ yr^{-1} for such hosts (Fox et al., 2005; Prochaska et al., 2006a; Berger, 2006). A limited number of SGRBs have been associated with star forming galaxies (GRB 050709, Fox et al. 2005; GRB 051221A, Soderberg et al. 2006) but they are located a significant distance away from star forming regions. Deep SN searches have been conducted but have yielded negative results (see § 2.1 of Zhang, 2007, and references therein). The combination of these results rules out massive star death as the origin of SGRBs. Instead the progenitors are thought to consist of binary systems that merge

to form a BH-torus system or magnetars undergoing catastrophic reconfigurations of their magnetic fields.

The proposed merger models all involve systems where both objects are compact bodies (either a WD, NS or BH); NS-NS, NS-BH, WD-BH or WD-WD (see e.g. Paczynski 1986; Goodman 1986; Paczynski 1991; Eichler et al. 1989; Narayan et al. 1992; Mészáros & Rees 1992a,b; Rosswog et al. 2003; King et al. 2007 or Lee & Ramirez-Ruiz 2007 and references therein). The final states of these systems, much like the LGRB progenitors discussed in the previous section, produce a central BH surrounded by an accretion torus.

As the binary system revolves, gravitational waves carry away its energy and angular momentum. The loss rates depend on the system mass, semi-major axis and eccentricity, and rapidly increases as orbital decay progresses. In the last minutes before coalescence the gravitational wave signal should sweep through the frequency range that is accessible to ground based gravitational wave detectors such as LIGO (Abramovici et al., 1992; Frey, 2007) and VIRGO (Acernese et al., 2007). The detection of a gravitational wave signal coincident with a SGRB would allow the determination of the distance to the source and its beaming angle (Kobayashi & Mészáros, 2003). The dynamics of the merger process are sensitive to the mass ratio of the two bodies in the system, thus the signal from a NS-NS event (with a mass ratio close to unity) would be very different to the signal from a NS-BH event (where the BH can potentially be much more massive than the NS). The coalescence signal of these systems can be divided into three phases; (1) the inspiral due to gravitational wave emission, (2) the actual merger, and (3) the 'ring-down' of the remnant once its settles into its final state of a BH. Examples of the expected signals for different binary pairs can be seen in Rosswog (2007).

There is a significant delay between the formation of the compact objects and their subsequent coalescence, thus the system travels a large distance from the birth site of the original Main Sequence stars due to the large natal kicks received upon the compact object formation. Therefore such merger events should occur on the outskirts of the host galaxies (as observed) where the ambient medium will be tenuous. This is borne out by afterglow modelling of SGRBs, which indicate the surrounding medium is indeed sparse. However, novel channels for compact star mergers on relatively short timescales have been put forward by Belczynski et al. (2002, 2006). This invokes tight binary systems to produce merger events on timescales of 0.001-0.2 Myr, as opposed to the normal wide binary systems with merger times of the order 100-15,000 Myr.

A subset of SGRBs may also be the result of SGR giant flares in nearby galaxies, similar to the event observed by *Swift* on the 27^{th} December 2004 (SGR 1806-20; Palmer et al., 2005; Tanvir et al., 2005; Chapman et al., 2008, see also § 1.1.5 of this work). The central engine of such an event is a rapidly rotating NS with a large magnetic field (B $\approx 10^{15}$ G), which undergoes a catastrophic reconfiguration of its magnetic field (Palmer et al., 2005). All of the magnetar giant flares observed thus far (Palmer et al., 2005, and references therein) show very similar light curves; all start with a very short (a few s) and spectrally hard main spike, followed by an extended softer tail that is highly modulated at the NS's spin period. In the case of SGR 1806-20 the extended emission lasted for ~ 50 cycles of the spin period, or ~ 380 s. If this flare had occured further away, but within 40 Mpc (encompassing even the Virgo cluster), it would have resembled a SGRB. A search for associations of well localized SGRBs with nearby galaxies, conducted by Nakar et al. (2006), produced an upper limit on the SGR fraction of SGRBs to be $\sim 15\%$. Lazzati et al. (2005) conducted a search of the BATSE data looking for SGRBs with spectral characteristics analogous to the SGR flare (i.e. a thermal spectrum with kT ~ 100 keV) and concluded that $< 4\%$ of SGRBs are SGR flares.

Both types of SGRB central engine can also be formed by Accretion Induced Collapse (AIC) models (Lee & Ramirez-Ruiz, 2007). A BH-torus engine can be created from a close binary system consisting of a NS and another companion, most likely a WD (Vietri & Stella, 1998, 1999; MacFadyen et al., 2005), in a Low Mass X-ray Binary. As the binary separation decreases the NS accretes material from its companion, causing it to spin up and form a rapidly rotating Super Massive NS (SMNS). The SMNS subsequently loses angular momentum via magnetic dipole radiation until it becomes destablized; the inner regions collapse to form a BH, whilst the equatorial matter (which is close to centrifugal equilibrium) form a torus. If the binary system consists of two WDs the binary system collapses, as in the previous case, until the less massive WD fills it Roche lobe and begins mass transfer (King et al., 2001; Levan et al., 2006; Dessart et al., 2007). It is possible that such a scenario could lead to a quiet AIC, forming a NS remnant (see § 1 of King et al., 2001, and references therein), though King et al. (2001) and Dessart et al. (2007) argue that it is more likely to produce a Type I SN and a magnetar. Such magnetars then give rise to SGRBs in the same manner as SGRs as described in the previous paragraphs.

Another potential subset of SGRBs may be mistaken for LGRBs, such GRB 060614 (see § 1.1.5 above). Deep searches have confirmed that any underlying SN associated with GRB 060614 is more than 100 times fainter than any other SNe associated with LGRBs (Gal-Yam et al., 2006; Fynbo et al., 2006;

Della Valle et al., 2006a). Further inspection of the GRB's prompt light curve shows early hard spikes (duration ~ 5 s) followed by a long, soft emission tail. The temporal analysis of the lags between light curve features in the first 5 s is 3 ± 6 ms, falling in the range of values typically associated with short bursts (Norris et al., 2000; Norris & Bonnell, 2006). The type of extended emission following these spikes has been seen in about $1/3$ of the sample of bursts in table 1 of Norris & Bonnell (2006); there has also been evidence of such emission in pre-*Swift* bursts (Norris & Bonnell, 2006; Norris & Gehrels, 2008).

Furthermore the total energy of GRB 060614 is ~ 8 times greater than GRB 050724 (a confirmed, 'classic' short burst). By assuming an empirical relation between isotropic energy and spectral peak energy (the 'Amati relation', Amati et al. 2002; Amati 2006) Zhang et al. (2007a) were able to 'scale down' GRB 060614's light curve. They found that the modified burst had a T_{90} of 4.4 s in the BATSE band and that the long, soft tail was shifted into the X-ray band as flares; forming a carbon-copy of GRB 050724. This suggests that GRB 060614 is likely to be a more energetic version of the comparison 'classic' short burst, and should therefore belong to merger-type short GRBs. However, this does not entirely rule out the possibility that GRB 060614 is a third type of GRBs (e.g. collapsars without a SN signature, Woosley 1993).

Troja et al. (2008) carried out an evaluation of SGRB (including those bursts with long soft emission tails) offsets from their host galaxies. They found that the bursts with extended ($\sim 100 - 200$ s) soft emission tended to be clustered very close to their host galaxies (< 5 kpc), whilst the shortest duration bursts appeared to have much larger offsets (up to 70 kpc), compared to the average LGRB offset of ~ 1.3 kpc (Bloom et al., 2002a). Thus SGRBs showing extended emission could be close NS-NS binaries as their shorter coalescence times would naturally lead to lower offsets. Furthermore Troja et al. (2008) found that those bursts with small offsets had, on average, more energetic afterglows and a higher chance of being detected at optical wavelengths. This is probably a result of the properties of their environment; bursts that occur closer to their host galaxies are presumably located in denser interstellar environments.

1.3 GRB emission: 'Prompt' and 'afterglow' behaviours

The initial γ-ray emission from GRBs can be highly variable. Some have single spikes with a Fast Rise, Exponential Decay (FRED) profile, whilst others consist of multiple, potentially overlapping pulses. Some bursts have extended periods of 'spikey' emission; if the individual peaks are sufficiently well resolved then they are usually well fit by FRED profiles. The initial spike of a subset of short bursts ($\sim$33%) is followed by a smooth, extended emission period (Gehrels et al., 2006). Rarer GRBs show an underlying, broad thermal component (GRB 060218, Campana et al. 2006b) in their early light curves. If rapid observations are available it can be shown that the behaviour of the X-ray light curve mirrors that of the γ-ray light curve at early times.

Traditionally 'prompt' emission refers to the emission component detected by the γ-ray detector whilst all of the remaining (lower energy) emission detected by other instruments at later times has been termed as the 'afterglow' emission. However, *Swift* observations suggest that this definition scheme is not physical, as early observations show that there are contemperaneous detections of X-rays that mirror the γ-ray emission. Furthermore late-time X-ray flares, if strong and hard enough, should also be included as part of the classical 'prompt' emission period. Zhang (2007) suggests that it would be much more appropriate to define emission components as either being of 'internal' or 'external' origin, mediated by the central engine or the external medium respectively. Using such a definition means that central engine related emission likely extends to much later epochs than have been previously considered, thus it can no longer be accurately called 'prompt'. The current theoretical models for the 'internal' emission component is described in §1.3.1 and the full light curve behaviour, including the 'external' component, is elaborated upon in §1.3.3.

1.3.1 GRB Fireball: Simplified model

The fireball model for GRBs was first proposed by Cavallo & Rees (1978). After three decades of refinement it is still the leading theoretical model to explain the GRB phenomenon and has been extensively reviewed (see e.g. Piran, 1999; Mészáros, 2002; Zhang & Mészáros, 2004; Piran, 2005; Mészáros, 2006, and references therein). The majority of the energy released during the formation of the BH-torus system and subsequent accretion processes is converted into neutrinos (initially in thermal equilibrium) and gravitational waves, whilst a significantly smaller fraction goes into a high

temperature fireball containing electron-positron pairs ($e^{\pm}$), γ-rays and baryons. The fireball, whose initial energy is greater than its rest mass, expands at relativistic speeds; the ultimate velocity of which depends upon the baryon load[13] (Paczynski, 1990). It is expected that the baryonic density in the region where the fireball forms will be low due to accretion processes (Mészáros, 2006, and references therein).

We infer that the fireball expansion must be relativistic from a consideration of the "Compactness problem" (e.g. Ruderman, 1975; Schmidt, 1978; Piran, 1999; Zhang & Mészáros, 2004). If the fireball were to expand at sub-relativistic speeds then a proportion of the observed high energy photons will be above the pair production ($\gamma\gamma \rightarrow e^{\pm}$) threshold. By approximating the pair production cross section to be of the order of the Thomson scattering cross section, $\sigma_{\rm T}$, this results in a huge pair production optical depth, $\tau_{\gamma\gamma}$. Thus the high energy γ-rays should be completely attenuated before they reach the observer. The only way to avoid this paradox is to invoke bulk relativistic motion, which alleviates this problem in two ways. Firstly, this motion means that the observed γ-ray photon energy is blue shifted by a factor of Γ (the Lorentz factor of the outflow); thus in the rest frame of the ejecta the photons are emitted in the X-ray range and are therefore below the pair production threshold. Secondly, the scale of the emission area increases from $c\delta t$ (where δt is the observed timescale) to $\Gamma^2 c\delta t$, which also acts to decrease $\tau_{\gamma\gamma}$. Therefore to resolve the "Compactness problem" and observe γ-ray radiation (i.e. to have an optically thin case, $\tau_{\gamma\gamma} < 1$) typically requires $\Gamma \sim 100$. There is further evidence of relativistic motion from observations of radio afterglows. At early times radio data are affected by diffractive scintillation by the Interstellar Medium (ISM), which is quenched at later times. The source sized implied by this quenching and the time at which it occurs after the GRB indicates that the expansion speed must be superluminal (Waxman et al., 1998).

Fireball scenarios where the total energy is released instantaneously in an explosion (Goodman, 1986) or steadily as a radiation/$e^{\pm}$ plasma wind over longer timescales of central engine activity (Paczynski, 1986) have been studied. Despite the seemingly large phenomenological differences between the two models it has been shown that they both have the same qualitative behaviour (Piran, 1999). In these cases the energy released is converted into the bulk kinetic energy of the baryonic matter within the fireball by adiabatic expansion. As the fireball expands it sweeps up material from the external medium, creating a highly relativistic shock that moves into the external medium and backwards into the fireball, decelerating the material. This 'external' shock accelerates the electrons to large Lorentz factors; this

[13] If the fireball contains a large baryonic mass, of the order several $M_{\odot}$, then the expansion will be sub-relativistic.

energy is then converted into γ-rays through synchrotron emission and inverse-Compton scattering (Paczynski & Xu, 1994, and references therein). However, these models cannot directly account for the rapid time variability within the GRB signal, but instead rely on inhomogenities in the external medium (density or magnetic) to produce them (Rees & Meszaros, 1992).

Current theoretical models expand upon these basic ideas and invoke a situation whereby the radiation/$e^{\pm}$ plasma is ejected intermittantly from the central engine and therefore forms many 'mini-shells' with a wide range of bulk Lorentz factors (Rees & Meszaros, 1994; Zhang, 2007, and references therein). Faster ejecta emitted at later times are able to catch up with slower material that was ejected earlier, producing relativistic 'internal' shocks (see also Paczynski & Xu, 1994). These shocks are collisionless, i.e. mediated by chaotic electric and magnetic fields rather than by binary particle interactions. As with the previous models the shocks accelerate the electrons to relativisitic energies, whereby non-thermal radiation is created via synchrotron and inverse-Compton processes. Such 'internal' collisions are thought to produce the early GRB signal (historically defined as the 'prompt' emission). As before a relativistic shock is formed as the fireball collides with the external medium (either the ISM or a pre-ejected stellar wind generated by the progenitor before collapse), which forms the 'afterglow' of the GRB.

In this model it is assumed that the fireball's behaviour is essentially hydrodynamical in nature. Magnetic fields are considered when discussing synchrotron radiation from the outflow, via the parameterization[14] ε_B, but are otherwise essentially neglected when considering bulk dynamics. The formation of the central engine BH naturally creates a large magnetic field, of the order $10^{12} \rightarrow 10^{13}$ G, via magnetic flux conservation during collapse. This may be further enhanced to $\sim 10^{15}$ G by dynamo effects. Such magnetic fields can allow energy to be extracted from the gravitational energy of the torus as well as the rotational energy of the BH. The electromagnetic forces also strongly collimate the flow, giving rise to an asymptotically cylindrical structure (Vlahakis & Königl, 2003a,b, see also § 1.3.2).

Strong internal shocks cannot develop in the outflow if it is Poynting flux dominated, i.e. if the magnetic field is large. Therefore the emission process that produces the burst signal is replaced by non-thermal emission from the dissipation of internal energy during reconnection (Spruit et al., 2001; Drenkhahn & Spruit, 2002). If the burst signature is a result of local magnetic dissipation events then the minimum timescales of the emission could be smaller than the timescales of the central engine. Magnetic

[14] ε_B is the energy fraction in the magnetic field, whilst ε_e is the energy fraction in the electrons.

reconnection processes convert the total burst energy into 'prompt' radiation at an efficiency of 10-50% (compared to an efficiency of 1-5% for internal shocks). In the Poynting flux dominated models the fireball evolution is assumed to be converted back to a hydrodynamical process in the deceleration phase in order to match the late time afterglow theories and observations. Such a transition is reasonable given that a similar transition is seen in pulsar wind nebula.

1.3.2 GRB Jets

Once redshifts became available for GRBs the isotropic energy, E_γ , released by these events could be calculated. The energy of the first burst with a redshift measurement, GRB 970508 (Metzger et al., 1997), was 7×10^{51} ergs. However, subsequent GRBs yielded increasingly large values, e.g GRB 990123 with $E_\gamma = 3.4 \times 10^{54}$ ergs, or $\approx 1.9 M_\odot c^2$, which is more than the rest mass of a NS (Kulkarni et al., 1999a). The energy budget problem can be alleviated if GRBs emit a collimated outflow (a cone with opening angle θ_j, with either a uniform or angular dependant structure; Rhoads, 1999; Sari et al., 1999), an assertation that was backed up by early radio observations (see e.g. Kulkarni et al., 1999b; Harrison et al., 1999). Further evidence for such beaming is supplied by the empirical relation that that geometrically corrected γ-ray energy is quasi-standard (Frail et al., 2001), assuming that certain optical temporal jet breaks are associated with 'jet breaks' when $\Gamma^{-1} = \theta_j$ (Rhoads, 1999; Sari et al., 1999).

Since the GRB ejecta are emitted at highly relativistic velocities the γ-rays observed therefore originate from material moving within an angle Γ^{-1} to our line of sight. Consequently the emission offers no straight forward way of determining whether the bursts are isotropic emitters or are beamed into a small angle at early times, as long as $\Gamma^{-1} < \theta_j$. A detectable signature can be observed once the ejecta decelerates, through interactions with the external medium, so that $\Gamma^{-1} > \theta_j$. This results in an achromatic break in the light curve leading to a steeper rate of decay (see Phase IV in § 1.3.3 for further details). Beamed outflows are remarkably common in astrophysical sources, being seen at both small (protostars) and large (Active Galactic Nuclei) scales.

Unlike other astrophysical jets, GRB outflows are non-steady-state and generally the width of a discrete period of emission, in a direction parallel to its motion, is orders of magnitude smaller than its radius. Thus individual 'sub shells' of emission are better described by a 'flying pancake' structure (Piran, 2005). An illustration of the generic GRB jet/fireball model is shown in fig 1.8.

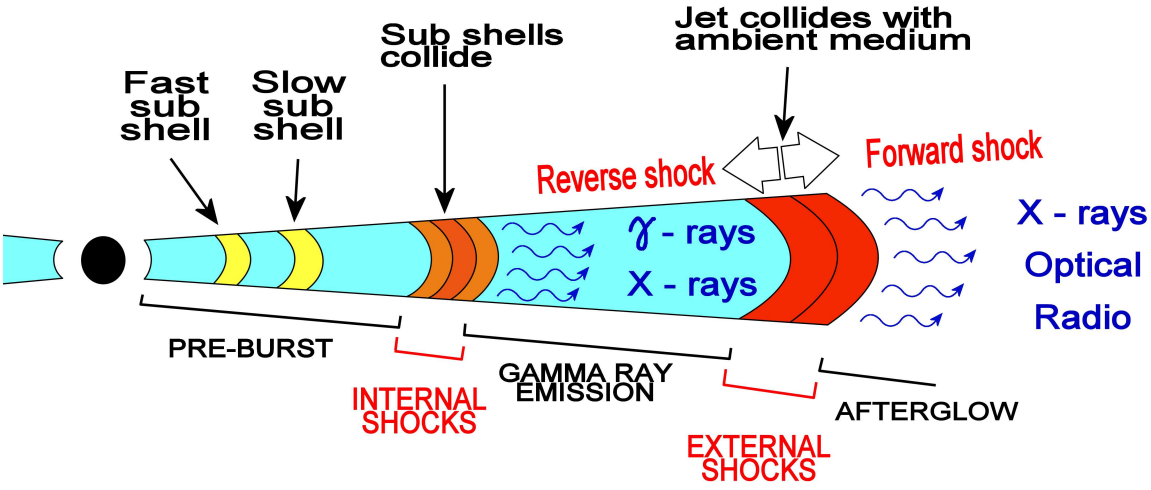

Figure 1.8: Schematic diagram of the generic model of GRB jet outflow, showing the location of shocks (internal and external).

As stated in the previous two sections it is unclear, at the present time, exactly how the highly relativistic jets are launched from the GRB central engine. Several different mechanisms have been proposed: neutrino cooling of the accretion disk, leading to $\nu\bar{\nu}$ annihilation; magnetic instabilities within the accretion disk; and Magnetohydrodynamical (MHD) extraction of the rotational energy of the BH energy.

The model proposed by Woosley (1993) and expanded upon by Popham et al. (1999) and Narayan et al. (2001) states that the accretion disk surrounding the central BH is hot and that the accretion flow is a Neutrino Dominated Accretion Flow (NDAF). Neutrino pairs are thus generated all around the BH and disk but are concentrated in the equatorial plane. The net momentum of the $e^{\pm}$ pairs produced by the annihilation of these neutrino pairs ($\nu + \bar{\nu} \rightarrow e^{+} + e^{-}$) is directed outward along the angular momentum axis, forming hot, high entropy jets containing $\sim 10^{51}$ ergs (see also Woosley & Bloom, 2006). This model assumes that the neutrinos do not interact with any other matter in the accretion disk. Di Matteo et al. (2002) built upon this work, adding the effects of neutrino transfer and opacity. They found that the region of the NDAFs are typically opaque, causing the emitted neutrinos to become trapped. Di Matteo et al. (2002) state that energy advection is therefore the dominant cooling mechanism in the accretion flow and that $\nu\bar{\nu}$ annihilation in hyperaccreting BHs is an inefficient mechanism to liberate

the amount of energy required for GRB jets.

Blandford & Payne (1982) advocated a mechanism whereby magnetic field lines threading the accretion disk, and that extend outwards to large distances, are able to extract energy and angular momentum from the accreting material. Blandford & Payne (1982) show that a centrifugally driven outflow of matter is possible if the poloidal component of the magnetic field makes an angle less than 60^o with the disk surface. At large distances from the disk the toroidal component of the magnetic field becomes important, causing the outflow to become collimated. This model was taken further by Proga et al. (2003), showing that the initial magnetic field in the disk very quickly deviates from a purely radial state because of magnetorotational instabilities (MRI) and shear effects; furthermore the toroidal field grows rapidly as field lines within the accretion disk wind up due to disk rotation. Material was found to accrete onto the BH via a magnetic polar funnel, however, the strength of the toroidal disk field was sufficient to drive a polar outflow along its gradient against the polar inflow. Such polar outflows were found to be narrow (half opening angle $\sim 5^o$) and Poynting flux dominated. However, Proga et al. (2003) did not taken into account neutrino interactions with the accreting gas, or neutrino annihilation. The authors state that further large scale simulations need to be carried out to prove whether this mechanism is powerful enough to produce GRB jets, however, recent work by Rothstein & Lovelace (2008) indicates that this mechanism is capable of producing them.

The BZ model for jet production was first proposed by Blandford & Znajek (1977) to explain Active Galactic Nuclei jets and has been discussed widely in the literature (see for example; Usov, 1992; Thompson, 1994; Mészáros & Rees, 1997; Mizuno et al., 2004; Levinson, 2006, and references therein). The model states that a relativistic MHD, Poynting flux dominated, outflow can be launched along the rotational axis by extracting angular momentum from the central rotating BH via electromagnetic torques (Blandford & Znajek, 1977). The original conceptualisation considered a rotating BH in the midst of an open magnetic field system (i.e. some magnetic fields lines extending to infinity) where there was no direct link between the BH event horizon and the disk/torus. Wald (1974) argued that such a system causes an electric field to be induced, the lowest energy state of which has a finite charge on the BH. The electric field of the BH generally has a non-zero component parallel to the externally supported magnetic field. If the magnetic field and the angular momentum of the BH are large enough any charged particles near the BH would be electrostatically accelerated; if the magnetic field is paraboloidal in shape then the energy will be beamed along antiparallel directions. The accelerated charged particles would then radiate and this radiation would produce further charged particles in the

form of $e^{\pm}$ pairs. When charges are produced so freely the electromagnetic field in the vicinity of the BH becomes approximately force free[15]. Thus the energy extracted from the BH is transported outward along the axis field lines in the form of a Poynting flux flow. One caveat to this model is that the current closure path of the system is not well understood. Levinson (2006, and references therein) suggest that a current sheet may form in the equatorial plane, thereby providing a return path. If that is the case then a torque may be excerted on the inner parts of the disk/torus by the cross-field currents.

A further refinement was later made to the model whereby a closed magnetic field system is considered instead (see Levinson, 2006, and references therein). At large radii the magnetic field quickly approaches a dipole solution; in the inner region the magnetic fields lines intersect the BH event horizon and the disk/torus, giving rise to a strong coupling between the BH and the disk/torus. In this case the magnetic field inside the disk/torus cannot be purely poloidal, as purely poloidal fields are unstable in such situations and tend to decay rapidly (compared to the dynamical timescale of the GRB; Eichler, 1982, and references therein). The interaction of the BH-torus system causes some magnetic field lines to twist. By conservation of helicity a twisted magnetic field does not decay to zero (in the limits of MHD) and thus evolves into a new, stable configuration wherein an open magnetic flux tube (extending from the BH to infinity) forms along the rotation axis. The outflow along the magnetic flux tube follows the arguments above for the open magnetic field case and are also expected to be relativistic.

Such jets, once launched, are expected to be potentially collimated by the surrounding magnetic fields, neutrino or baryon rich winds from the accretion disk (Levinson, 2006), or by the transverse containing pressure of the stellar envelope in the massive star progenitor scenario (e.g. MacFadyen & Woosley, 1999; Aloy et al., 2000; MacFadyen et al., 2001; Mészáros & Rees, 2001).

1.3.3 The canonical light curve

One of the major discoveries of the *Swift* mission is the identification of a canonical X-ray afterglow light curve (Nousek et al., 2006; Zhang et al., 2006; O'Brien et al., 2006; Zhang, 2007), which is illustrated in figure 1.9. Besides the classically defined 'prompt' or, more accurately, 'internal' emission (denoted as phase 0, discussed in §1.3.1), are a total of five phases in the light curve. These are the;

[15] In the force free approximation the charge density $\rho_{\rm e}$ and the current density $\mathbf{J}$ satisfy $\rho_e \mathbf{E} + \mathbf{J} \wedge \mathbf{B} = 0$, which is equivalent to ignoring the inertial terms in the particle's equation of motion.

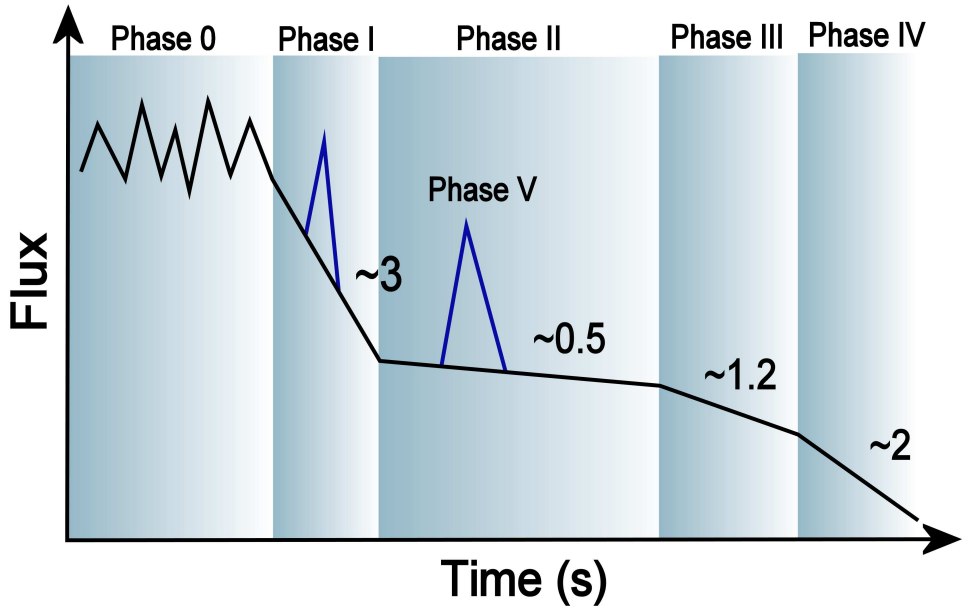

Figure 1.9: Schematic of the log flux-log time relation of cannonical GRB light curve as discovered by *Swift* (adapted from figure 1) of Zhang et al. 2006). Phase 0, I and V mostly likely originate from 'internal' mechanisms, whilst the remaining phases arise from 'external' mechanisms (see text for details). Phase I ends at $10^2 \rightarrow 10^3$ s, phases II at $10^3 \rightarrow 10^4$ s and phase III at $10^4 \rightarrow 10^5$ s.

Steep (I), Shallow (II), Normal (III) and Post jet break (IV) decay phases, on top of which Flares (V) can be superimposed. A potential sixth phase (Subrelativistic) may be observed if the afterglow is followed for extended periods of time. However, not all bursts show every phase of the canonical light curve; e.g. "naked" GRB (Godet et al., 2006; Page et al., 2006) light curves consist of phase 0 and Steep (I) emission only. In the pre-*Swift* era only the Normal and Post jet break afterglow phases had been observed/predicted. The remaining three components were not anticipated, though flare signatures had been detected by *BeppoSAX* . Piro et al. (2005) interpreted the flare as the onset of the afterglow, however, subsequent calculations strongly suggest that this cannot produce a feature with a sharp flare-like temporal profile (Lazzati & Begelman, 2006; Kobayashi & Zhang, 2007).

Throughout this section, and for the rest of the paper, I adopt the convention of describing the afterglow fluence as $F_\nu \propto t^{-\alpha}\nu^{-\beta}$.

Phase I: Steep Decay

Emission during this phase typically connects smoothly to the phase 0 emission if observed directly, or extrapolates back to the same if not directly observed (Tagliaferri et al., 2005b; Barthelmy et al., 2005b). The temporal decay index of this period is ~ 3, though steeper values are not unusual (occasionally up to 10, Vaughan et al., 2006; Cusumano et al., 2006a; O'Brien et al., 2006), continuing until $\sim 10^2 \rightarrow 10^3$ s. Phase I decay usually has a different spectral slope to the subsequent phase II emission.

The most widely accepted theory for the temporal behaviour during this phase is due to emission from the 'curvature effect' (Kumar & Panaitescu, 2000). It is assumed that the emission region producing the GRB signal (internal collsions), is disconnected from the region producing the afterglow (external collision) and that this internal emission stops abruptly. It is generally assumed that the ejecta from the GRB has a conical geometry (with an half opening angle of θ_j). During the burst radiation is received from a region of the fireball with an angular size Γ^{-1}. The curvature of the radiation front is such that it creates a propagation delay for high latitude (compared to the line of sight) emission. After the emission process ceases, radiation from these high latitudes, $\theta > \Gamma^{-1}$, continues to propagate towards the observer. Combining this effect with the variation of the Doppler factor at different latitudes results in a prediction of $\alpha = 2 + \beta$.

Both α and β are directly measureable from the observational data. However, a decay with an α steeper than 2 + β will be acquired if two caveats are not taken into account;

1. For internal emissions the start time, t_0, must be reset for every emission episode. If not, in a log-log light curve, this introduces an artificially steep decay if the GRB trigger time, t_{trig}, significantly leads t_0.

2. The observed decay is the superposition of the curvature effect decay and the underlying external shock afterglow. Thus the underlying afterglow component must be subtracted from the light curve before the $\alpha = 2 + \beta$ relation can be confirmed.

In some bursts (e.g. GRB 050421, Godet et al. 2006; GRB 050911, Page et al. 2006) the X-ray afterglow appears to be dominated by the curvature effect in addition to several flare events. In these cases it is assumed that the surrounding medium is so tenuous that no external shock is formed (or is

extremely faint), thus they are likely to be 'naked' GRBs.

Other interpretations have been put forward in the literature to explain this phenomenology. Tagliaferri et al. (2005a) and Yamazaki et al. (2006) both expand on earlier work by Kumar & Piran (2000) suggesting that the fireball is inhomogeneous, i.e. it is comprised of many 'mini-jets'. They found that the decay tail of such jets are generally smooth and are also able to reproduce the small scale structure seen in some decay tails. The decay is due to a jet break as a mini-jet is decelerated by the external medium, giving $\alpha \leq p \sim 2$ - 2.5 (where p is the power law index of the electron energy distribution), which is significantly lower than the decay indices observed. Kobayashi et al. (2007) propose that this decay phase is due to the emission from large angles, relative to our line of sight, from the reverse external shock. The radiation is emitted either by the synchrotron or sychrotron self-Compton mechanisms. The latter could suppress the optical flux relative to that in the X-ray band, which supports the prompt upper limits given by UVOT (Roming et al., 2006). However, this interpretation requires a large Compton y-parameter[16] and, in turn, a very low magnetization of the outflow.

Another possible model relies upon photospheric emission as the ejecta becomes optically thin (Rees & Mészáros, 2005; Ramirez-Ruiz, 2005). This produces the observed non-thermal spectrum but it is not clear at the present time how this emission could last longer than the initial bursts and on into phase I timescales. Several authors (Mészáros & Rees, 2001; Ramirez-Ruiz et al., 2002a; Pe'er et al., 2006) suggest the source of the steeply decaying emission is the hot cocoon of material that potentially surrounds the jet as it breaks out of the progenitor in the collapsar model. This might provide the correct flux decay index but would result in a quasi-thermal spectrum, which is not observed.

At this point in time the curvature effect appears to provide the most convincing, basic explanation of phase I. For decay behaviour that is shallower than 2 + β it has been suggested that the emission in the shock region may not cease abruptly but instead diminishes with time gradually, which leads to a decaying internal shock afterglow (Fan & Wei, 2005; Zhang, 2006). Zhang et al. (2007b), motivated by the detection of spectrally evolving emission tails, have performed a systematic spectral analysis of 17 bright, steep decay tails and discovered that the curvature effect alone cannot explain all of the GRBs. They show that phase I decay in some GRBs may be due to the superposition of the curvature

[16]The Compton y-parameter is defined as the typical fractional gain in energy per scattering event times the typical number of scatterings.

effect and an underlying central engine afterglow. However, the strong spectral evolution seen in GRBs 057024, 060218 and 060614 cannot be adequately explained by such a superposition of components. Instead Zhang et al. (2007b) suggest that the underlying component is due to the cooling of the internal shocked region, which causes a spectral break to move through the observed energy band producing the observed spectral evolution.

The first break, defining the start of phase II, is generally interpreted as the time at which the slowly decaying emission from the forward shock becomes dominant over the rapidly decaying emission from phase I. The reason for this domination may be due to internal shock emission radiating most of the initial energy in the outflow, leaving a much smaller energy reservoir in the external shock. Alternatively the energy dissipated in the internal shocks is comparable to that dissipated in the external shock but the fraction of the energy radiated in the observed (X-ray) band is much larger for internal shocks.

The break at this time may also be accompanied by a change in spectral index if the emission processes from the internal and external emission regions are different (Butler & Kocevski, 2007b), though $|\Delta\beta|$ can be rather modest and may be small enough that it is not detectable within the limits of the avavilable spectra. If there is a change in β then the break will be chromatic.

Phase II: Shallow Decay

Phase II decay extends to $\sim 10^3 \rightarrow 10^4$ s (or up to $\sim 6 \times 10^4$ s in exceptional cases such as GRB 060729, Grupe et al. 2007), with no spectral evolution across the following break. The typical value of the temporal decay index seen during this phase, ~ 0.5 (though values as low as ~ 0.2 have been reported; Nousek et al. 2006), is too small to be reasonably accounted for by the adiabatic evolution of the forward shock with a constant energy (Nousek et al., 2006, and references therein). Including radiative losses would steepen the decay further. In most cases the shallow decay behaviour is seen in the optical band as well as the X-ray (Mason et al., 2006).

At the present time the Shallow decay phase is still an enigma. Several models have been suggested in the literature, which broadly fall into the catergories of energy injection, geometrical effects or evolving microphysical parameters.

•**Ejecta with a wide Γ distribution:** towards the end of the burst the central engine may produce

ejecta with Lorentz factor, Γ(t), that decreases with time. This material collides with the external shock when the earlier, high-Γ part is decelerated thus injecting eneregy into the external shock. In order to produce a smooth power law decay the ejected mass-distribution, M, needs to be close to a power law with $M(>\Gamma) \propto \Gamma^{-s}$ and therefore $E(>\Gamma) \propto \Gamma^{1-s}$. The requirement for significant energy injection implies that $s > 1$. The temporal break at $\sim 10^3 \rightarrow 10^4$ s suggests a cutoff, Γ_{min}, of several tens.

It is possible to constrain the value of s directly from the observed data, using equation 3 of Nousek et al. (2006, repeated here for clarity):

$$s = 1 + \frac{2(4-k)\Delta\alpha}{(3-k)b(\beta) - \Delta\alpha}, \tag{1.2}$$

where k refers to the density profile of the external medium ($\rho_{ext} = Ar^{-k}$)[17], $\Delta\alpha$ is the magnitude of the temporal break at the end of the Shallow decay period and $b(\beta)$ is a function of the observed spectrum given by equation 2) of Nousek et al. (2006, also repeated here for clarity):

$$b(\beta) = \begin{cases} 3/4 = 3\beta/2 & \nu_c < \nu < \nu_m \quad (k < 3), \\ (3+p)/4 = (\beta+2)/2 & \nu_m < \nu < \nu_c \quad (k = 0), \\ (1+p)/4 = (\beta+1)/2 & \nu_m < \nu < \nu_c \quad (k = 2), \\ (2+p)/4 = (\beta+1)/2 & \nu > max(\nu_m, \nu_c) \quad (k < 3), \end{cases} \tag{1.3}$$

where ν_c is the synchrotron cooling frequency and ν_m the synchrotron frequency associated with the minimum electron injection energy (where generally the broadband flux peaks). The requirement of $s > 1$ places a further constraint on $\Delta\alpha$ for this scenario:

$$0 < \Delta\alpha < \Delta\alpha_{max} = (3-k)b(\beta), \tag{1.4}$$

where $\Delta\alpha$ approaches $\Delta\alpha_{max}$ for $s \gg 1$.

In this scenario the reverse shock is typically non-relativistic as the difference between the Lorentz factors of the blastwave and the injection shell, $\Delta\Gamma$, is always low. This model assumes that the X-ray emission is dominated by the forward, rather than the reverse, shock.

[17] A constant density profile corresponds to $k = 0$ and a 'wind' profile to $k = 2$.

• **Long term central engine activity:** this scenario requires the long-term continuous, smooth energy injection from the central engine. To reproduce the shallow decay behaviour the (kinetic) luminosity of the central engine should be a power law in the observer's reference frame, $L \propto t^q$, where q is again given by observables (using the same definition of $b(\beta)$ as before, equation 1.3; Nousek et al., 2006):

$$q = \frac{\Delta\alpha}{b(\beta)} - 1. \tag{1.5}$$

This model places no upper bounds on $\Delta\alpha$ and only a trivial lower limit of $\Delta\alpha > 0$. Therefore this scenario can be distinguished from the previous one if $\Delta\alpha > (3-k)b(\beta)$. Another distinguishing signature is that it can produce a relativistic reverse shock, provided that the σ-parameter (the ratio between Poynting flux and the kinetic flux) is < 1 at the shock interacting region (Dai, 2004). Alternatively if the σ-parameter is initially high it will produce a weak reverse shock, which will become relativistic over time provided the central engine remains active for long enough (Zhang, 2007).

• **Central engine afterglow:** this scenario proposes that the shallow phase is not related to the external shock. Again the central engine remains active for a long period of time, producing an afterglow which is responsible for this phase (Katz et al., 1998; Fan et al., 2008). As a result the X-ray and optical emission during phase II are the result of two distinct components.

• **Delayed energy transfer to forward shock:** numerical calculations suggest that the timescale before entering the Blandford-McKee self-similiar deceleration phase is long, $\sim 10^3$ s, which in turn indicates that it takes time to transfer the kinetic energy of the fireball into the external medium. Thus phase II may simply reflect the slow energy transfer process. However, this model (Kobayashi & Zhang, 2007) predicts a significant curvature of the X-ray light curve, which is consistent with some light curves that show an early "dip" before phase II (e.g. 060206; Monfardini et al., 2006). For cases with a uniform shallow decay this model requires that the rising light curve of the delayed transfer is superimposed on the steep decay tail of phase I.

• **The precursor model:** Ioka et al. (2006) suggests that if a weak relativistic explosion occurs $10^3 \rightarrow 10^6$ s prior to the 'main' burst, i.e. a 'precursor' event, a shallow decay phase can be produced as the fireball sweeps up the remnants of the precursor.

• **Off-beam jet:** Eichler & Granot (2006) propose that, similiarly to the 'delayed energy transfer

to the forward shock' model, the phase II decay may be the result of the combination of two decay components. In this scenario the afterglow onset delay is instead due to the geometric effect of viewing the burst from an angle just outside of the jet opening angle. However, the expectation of this model for correlations between the shallow decay index, 'hump' luminosity and its epoch have not been confirmed observationally (Panaitescu, 2007).

• **Two component jet model:** a model invoking a jet with two components would produce a two-component afterglow. In this context an inner, highly relativistic, narrow ($\theta = 1^o$) jet produces the emission seen in phase 0 & I, whilst a much wider, less relativistic outflow produces the shallow component seen in phase II (Granot et al., 2006; Panaitescu, 2007).

• **Dust scattering:** Shao & Dai (2007) suggest that the entire X-ray light curve, from phase II onwards, can be explained as an echo of phase 0 & I emission. This echo is produced by the small-angle scattering of the X-rays off dust grains located at a distance of ∼tens of parsecs from the GRB source. Since the standard external shock model usually generates shocks at $\sim 10^{17}$ cm Shao & Dai (2007) state that the echo scenario does not rule out the existence of emission from external shocks in the X-ray or optical bands. However, recent work by Shen et al. (2008) indicates that such scattering should produce a strong spectral softening throughout phase II, which is not supported by the spectral observations at these times.

• **Varying microphysics:** Several different authors have invoked the evolution of the microphysical shock parameters, ε_e and ε_B, to reproduce the decay behaviour seen in this phase (Ioka et al., 2006; Granot et al., 2006; Panaitescu, 2007).

Phase III: Normal decay

The second break begins at $\sim 10^3 \rightarrow 10^4$ s. Generally the spectral index does not change across this break (Zhang, 2007), though Willingale et al. (2007) suggest that a slight change does occur in some bursts. The lack of spectral evolution across this break rules out any models for this phase that invoke the crossing of a spectral break across the observed energy band. Thus the nature of this break should be either hydrodynamical or geometrical.

Typically with a temporal decay slope of ∼1.2, this phase usually follows the predictions of the standard

afterglow model for the adiabatic expansion of the forward shock and was the afterglow emission component normally observed in the pre-*Swift* era (Sari et al., 1998; Chevalier & Li, 2000). However, a systematic test of the afterglow closure relations (e.g. table 1 of Zhang & Mészáros 2004) suggests that a fraction of bursts do not satisfy any afterglow model (Willingale et al., 2007).

Phase IV: Post jet break decay

This afterglow phase will only be seen if the GRB outflow is collimated. Assuming a uniform jet profile (or 'top hat' profile) the break occurs when the fireball is decelerated sufficiently so that the relativistic beaming angle, Γ^{-1}, becomes larger than the half opening angle, θ_j, of the jet. At this point two effects come into play. Firstly, the observer begins to become aware of an energy deficit outside of the jet. Secondly, the jet starts to expand sideways as a result of a horizontally propagating sound wave. Both effects act to steepen the light curve; their combined effect produces a temporal break with a magnitude, $|\Delta\alpha| \sim 1$ (Rhoads, 1999; Sari et al., 1999) and result in a post decay temporal index of p (the power law index of the electron energy distribution). The same behaviour is expected from a structured jet provided that the jet opening angle is replaced by the observer's viewing angle (Zhang & Mészáros, 2002a; Rossi et al., 2002). Since the jet break is a purely hydrodynamical effect the break must occur simultaneously across all wavelengths i.e. it must be achromatic. Furthermore the hydrodynamical nature of the break should not affect the microscopic shock physics, ε_e and ε_B. Thus there should be no change in the energy index of the shock accelerated electrons and therefore no change in spectral index across the break.

Another important feature of the post jet break evolution is that ν_c becomes constant in time, therefore the X-ray and optical spectra do not vary after this break. However, the radio spectrum continues to vary providing additional observational confirmation of the nature of such a break as the jet expands sideways (Harrison et al., 1999).

Since the launch of *Swift* a very large sample of GRBs with well sampled X-ray light curves have been accumulated, but relatively few, $< 10\%$ (Mészáros, 2006), show evidence of a jet break despite their long-term observations (Liang et al., 2008; Burrows & Racusin, 2007; Willingale et al., 2007). The lack of confirmed, well constrained, achromatic jet breaks in the *Swift* -era has resulted in an increasing feeling amongst the GRB community that the pre-*Swift* era breaks seen at optical wavelengths may

not be jet breaks and that the optical and X-ray afterglows may be generated by different mechanisms. Thus the standard fireball model may need to be reconsidered, possibly by placing more emphasis on structured jets.

Other temporal breaks in the X-ray light curves may be the result of spectral energy breaks crossing the observed band, such as ν_m, the synchrotron frequency associated with the minimum electron injection energy (where generally the broadband flux peaks), or ν_c, the cooling frequency (Sari et al., 1998). Alternatively, the electrons may have an intrinsic break in their energy spectrum (Li & Chevalier, 2001; Wei & Lu, 2002), which would give rise to a distinct temporal break as it crosses the observed band. This type of break has two features which distinguish it from the jet break discussed above: 1) the break typically rolls from high energies to lower ones, producing a chromatic break, and 2) there should be a distinct change in spectral properties across the break. Such breaks have been reported in e.g. Sato et al. (2003); Lipkin et al. (2004); Starling et al. (2007).

Phase V: Flares

Flare events occur in $\sim 50\%$ of *Swift* GRB afterglows, often with more than one flare per burst; they are superimposed on either (or both) phase I and phase II decay periods (Burrows et al., 2005b; Falcone et al., 2006; Chincarini et al., 2007). They typically have rapid rise and fall times with $\delta t/t << 1$, with weaker fluences occuring at later times. There are rare occurances (e.g. GRB 050502B) where the flare fluence is comparable to that of the phase 0 emission. Flares soften spectrally as they progress and generally later flares are less energetic and broader than early flares. They occur in both long and short GRB and XRF afterglows. These properties are all strongly indicative that the flares originate from internal shocks at late times rather than from the external shock. The internal shock origin has two advantages: 1) the clock needs to be reset each time the central engine restarts providing an easy way to explain the very sharp rising and falling light curve profiles, and 2) energetically the late internal dissipation model is very economical. If we were to consider the refreshed external shock as the site of the flare production then a large energy budget is required to reproduce the observed flares, as the injection energy must be comparable to that already in the blastwave to produce a noticable injection signature (Zhang & Mészáros, 2002b).

The late internal shocks could be a result of a collision between a slow shell ejected at early times and a

faster shell ejected later or between two shells of similar Lorentz factor ejected at late times. The latter case is not currently favoured as both shells must have a small Lorentz factor at the time of impact to avoid colliding with the decelerating blastwave. In addition, to avoid a collision with each other at early times their relative Lorentz factor, $\Delta\Gamma$, must be very small. The small Γ factors and $\Delta\Gamma$ result in a collision with an internal energy that is normally insufficient to produce a noticeable signature in the light curve.

Generally, the internal shock model requires that the central engine restarts, or remains active, for long periods of time, up to $\sim 10^5$ s. Strong evidence for the internal shock model has been provided by Liang et al. (2006). However, prior to the *Swift* observations no central engine model had specifically predicted such extended activity. Several suggestions have been put forward in the literature but as yet none has been proven by robust numerical simulations;

• **Fragmentation of progenitors leading to late time accretion:** it has been suggested that during either the collapse of a supermassive progenitor, or the collision of two compact bodies, that fragments of material are launched into eccentric orbits. The subsequent fallback and accretion of these materials at later times, up to several hours after the burst, could produce flares (King et al., 2005).

Alternatively, since flaring is seen in both long and short bursts, Perna et al. (2006) suggest that this behaviour must originate from a region that is common to both classes of GRBs: the hyperaccreting accretion disk around the central BH. Their work showed that the observed flare properties are consistent with viscous disk evolution, given that the disk fragments at large radii or otherwise suffers from large amplitude variability. They conclude that gravitational instability, possibly followed by fragmentation, is the most likely candidate for this variability.

• **Magnetic barriers in the accretion disk:** other authors suggest that the magnetic field near the BH may modulate the accretion flow from the disk to such an extent that accretion may be prevented altogether for extended periods of time (Proga & Begelman, 2003; Proga & Zhang, 2006). This model does not require the accretion flow to be 'chopped' by other means, e.g. fragmentation or gravitational instabilities, however these processes may occur simultaneously.

• **NS-NS merger leading to the formation of a massive NS:** Numerical simulations of NS-NS mergers have shown that the resultant object may not be a BH but a differentially rotating massive NS (Shibata et al., 2005), provided the NS equation of state is stiff. If the magnetic field of the newly created NS is

weak then dynamo action would induce magnetic explosions that give rise to late internal shocks; these could occur up to $\sim$ few 10^3 s after the burst (Dai et al., 2006).

Beyond Phase IV: Subrelativistic break

A further temporal break is expected at late times as the external shock transitions from the highly relativistic phase to the non-relativistic phase (§3.3 of Zhang, 2007, and references therein). If this transition occurs after the jet break Livio & Waxman (2000) hypothesise that the light curve would become flatter. It has been suggested that such a break has been observed at radio wavelengths (e.g. Frail et al., 2003), however, this has not been confirmed in optical or X-ray light curves; GRB 060729 (Grupe et al., 2007) was observed for more than 125 days with no evidence of such a break. This does not preclude the potential to observe such a light curve feature but indicates that searches may need to be carried out at extremely late times.

Chapter 2

GRB 050505: A high redshift burst detected by *Swift*[1]

This chapter discusses the discovery and subsequent multi-wavelength afterglow behaviour of the high redshift ($z = 4.27$; Berger et al., 2005a) GRB 050505; the third most distant burst, confirmed by spectroscopic measurement, to date. GRB 050505 is a long GRB with a multipeaked γ-ray light curve, a duration of $T_{90} = 63 \pm 2$ s and an inferred isotropic energy release in γ-rays of $\sim 4.44 \times 10^{53}$ ergs in the $1 - 10^4$ keV rest frame energy range. The Swift *X-Ray Telescope started observations ∼47 minutes after the burst trigger and followed the afterglow for 14 days. Two breaks were detected in the light curve at $1.4^{+0.3}_{-0.3}$ ks and $11.0^{+1.9}_{-2.9}$ ks in the rest frame of the burst. The power law decay slopes before, between and after these breaks were $0.25^{+0.16}_{-0.17}$, $1.17^{+0.08}_{-0.09}$ and $1.97^{+0.27}_{-0.28}$ respectively. The X-ray afterglow shows no spectral variation over the course of the* Swift *observations, being well fit with a single power law of photon index ∼2.0. This behaviour is consistent with cessation of continued energisation of the external shock followed by a potential jet break. Neither break is consistent with a cooling break. The light curve can also be fit with a 'smoothly broken' power law model but it was rejected as it was inconsistent with all the afterglow models considered. The spectral energy distribution shows the cooling frequency to be between the optical and X-ray bands. The optical – X-ray spectrum also shows that there is significant X-ray absorption in excess of that due to our Galaxy but very little optical/UV extinction intrinsic to the host galaxy, with $E(B-V) \approx 0.10$ for a SMC-like*

[1] Adapted from "GRB 050505: a high-redshift burst discovered by *Swift* ", Hurkett et al. (2006).

extinction curve. Interestingly the $N_{\rm H}$ column density inferred from the optical spectrum (Berger et al., 2006) differs significantly from that measured from the X-ray spectra; the reason for this discrepancy is, as yet, unresolved.

2.1 Introduction

Gamma Ray Bursts (GRBs) are expected to be visible over a large range of redshifts with a potential upper limit of $z \sim 15 - 20$ (Lamb & Reichart, 2000). The lowest recorded GRB redshift to date is GRB 980425 with $z = 0.0085 \pm 0.0002$ (Tinney et al., 1998), whilst the highest is GRB 050904 at $z = 6.29 \pm 0.01$ (Kawai et al., 2005)[2]. Bursts at high redshift are potentially important since they can be powerful probes of the early Universe and of the intervening matter between the observer and GRB (particularly the conditions of their host galaxies, e.g. Vreeswijk et al. 2004).

So far ~ 140 bursts have a firm redshift determination, mostly obtained through spectroscopy of their optical afterglow. The record holder is GRB 050904 (z = 6.29; Kawai et al., 2005); see e.g. Tagliaferri et al. (2005a), Cusumano et al. (2006b), Watson et al. (2006), Cusumano et al. (2007) and Gou et al. (2007) for more details. That burst was observed by *Swift's* NFIs 161 seconds post trigger in the observer's reference frame (which equates to 22 seconds in the rest frame of the burst) overlapping the end of the phase 0 emission. The long-term X-ray light curve was highly irregular with flaring activity that appeared to last up to 2 hours in the burst reference frame. Cusumano et al. (2007) conjecture that *Swift's* instruments recorded a single continuous period of internal emission that dominated the barely detectable standard X-ray afterglow component. Tagliaferri et al. (2005a) report a break in the optical and infrared afterglows at 2.6 ± 1.0 days, which they associated with a jet break. Assuming this to be the case Tagliaferri et al. (2005a) infer a jet opening angle of 2^o to 4^o, assuming that the efficiency of the fireball in converting the energy of the ejecta into γ-rays is 0.2 and that the circumburst density, n, is ~ 3 cm^{-3}.

Previously the highest redshift burst was GRB 000131 (z = 4.50; Andersen et al., 2000). Unfortunately *BATSE* detected GRB 000131 during a partial data gap (Kippen, 2000) so its position was not localised until 56 hours after the trigger, thus its early time behaviour is unknown. No breaks were directly

[2]We also note that a photometric redshift of ~ 6.6 has been reported for GRB 060116 (Malesani et al., 2006; Grazian et al., 2006; Piranomonte et al., 2006; Tanvir et al., 2006) but this was not confirmed spectroscopically.

observed in the light curve for GRB 000131 but, based on the spectral index, an upper limit on the jet break time of < 3.5 days has been hypothesised (Andersen et al., 2000). In contrast, the rapid position dissemination for GRB 050505 allowed a rapid spectroscopic redshift determination (Berger et al., 2005a), and its automated follow-up program provided a well-covered X-ray afterglow light curve.

In addition to GRB 050505's importance as a high redshift burst it also occurred during the first seven months of *Swift's* operations. At that stage of the mission each individual burst was capable of providing new insights into the underlying theory of GRB physics or confirming, with more detail, previously held theories and as such merited careful individual study.

Here I present the results from *Swift* on GRB 050505. Two breaks were detected in the X-ray light curve, the first of which I consider to be due to the cessation of continued energisation of the ISM shock and the second is a jet break, caused by either a structured or uniform jet. Both breaks are inconsistent with a cooling break passing through the X-ray band (see § 2.4.1).

2.2 *Swift* observations of GRB 050505.

At 23:22:21 UT on the $5^{\rm th}$ of May 2005, the *Swift* Burst Alert Telescope (BAT; Barthelmy et al., 2005a), triggered and located GRB 050505 on-board (trigger ID 117504; Hurkett et al., 2005). The BAT mask-weighted light curve (see figure 2.1) shows a multi-peaked structure with a $\rm T_{90}$ ($15-350$ keV) [3] of 63 ± 2 seconds. The initial peak began ~ 15 seconds before the trigger and extended to 10 seconds after the trigger. There were three further short spikes with peaks at $T + 22.3$, $T + 30.4$ and $T + 50.4$ seconds, where T is the trigger time.

The $\rm T_{90}$ $15-150$ keV BAT spectrum (in the observer's reference frame) was adequately fit by a single power law with a photon index $= 1.56 \pm 0.12$ ($\chi^2/\nu = 48/56$) and a mean flux over $\rm T_{90}$ of $6.44^{+0.42}_{-1.54}$ $\times 10^{-8}$ ergs cm^{-2} s^{-1} in the $15-350$ keV energy range and $3.76^{+0.21}_{-0.69}$ $\times 10^{-8}$ ergs cm^{-2} s^{-1} in the $15-150$ keV energy range. Whilst fitting a cutoff power law only provides a marginal improvement to the fit ($\chi^2/\nu = 45/55$) it does provide an indication of the $E_{\rm peak}$ for this burst. I found a photon index $= 1.02^{+0.51}_{-0.57}$ and a lower limit of $E_{\rm peak,obs} > 52$ keV, which is consistent with the peak energies found for BATSE bursts (Band et al., 1993, see also § 1.1.2). All errors and limits in this chapter are quoted

[3] $\rm T_{90}$ is the time period over which 90% of the total GRB fluence is detected, i.e. from 5% to 95%.

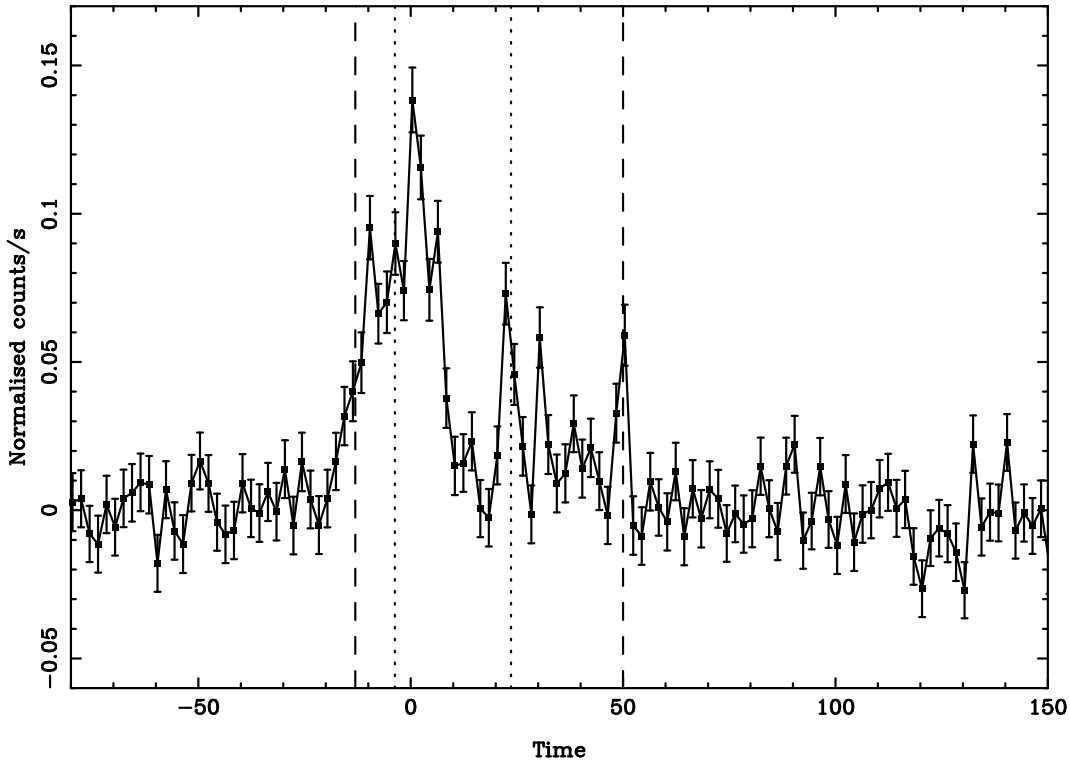

Figure 2.1: The BAT mask weighted light curve ($15 - 350$ keV) in the observer's rest frame, where $T = 0$ is the trigger time. The dashed lines indicate the T_{90} interval and the dotted lines indicate the T_{50} interval.

---

at 90% confidence unless otherwise stated.

The burst was detected in each of the four standard BAT energy bands[4] and had a ratio of fluence in the $50 - 100$ keV energy band to that in the $25 - 50$ keV energy band of 1.37 ± 0.14, close to the mean ratio of the *BATSE* catalogue[5]. The total fluence in the $15 - 350$ keV energy band is $(4.1 \pm 0.4) \times 10^{-6}$ ergs cm^{-2} (Hullinger et al., 2005), which was slightly higher than the average fluence detected up to that stage of the *Swift* mission.

Swift executed an automated slew to the BAT-detected position and the X-Ray Telescope (XRT; Burrows et al., 2005a) began taking data at 00:09:23 UT on $6^{\rm th}$ May 2005, ~ 47 minutes after the burst trigger. The delay in the spacecraft slew was due to an Earth limb observing constraint. The XRT was in Auto state, where autonomous data mode switching was enabled (see § 1.1.5), but the on-board

[4]The four standard BAT energy bands are; $15 - 25$, $25 - 50$, $50 - 100$ and $100 - 350$ keV.

[5]http://cossc.gsfc.nasa.gov/docs/cgro/batse/4Bcatalog/index.html

software did not automatically locate a position due to low source brightness. Ground processing revealed an uncatalogued X-ray source within the BAT error circle located at RA = 09:27:03.2, Dec = +30:16:21.5 (J2000) with an estimated uncertainty of 6 arcseconds radius (90% containment; Kennea et al., 2005). The astrometrically corrected X-ray position (using the XRT-UVOT alignment and matching UVOT field sources to the USNO-B1 catalogue)[6] for this burst was RA = 09:27:03.3, Dec = +30:16:24.2 with an estimated uncertainty of 1.4 arcseconds (also 90% containment). See figure 2.2 for a three colour X-ray image of the region surrounding GRB 050505. No data were obtained in Window Timing (WT) mode due to the delayed slew, since this mode is only used for sources brighter than 1 mCrab (see § 1.1.5).

Observations continued over the next 14 days, though the X-ray afterglow was not detected after the $6^{\rm th}$ day. Co-adding the final 8 days of observations produced a total of 58 ks of data providing an upper limit of $\sim 3.5 \times 10^{-4}$ counts s^{-1}, consistent with the extrapolated decay (see § 2.2.1).

The *Swift* Ultra-Violet/Optical Telescope (UVOT; Roming et al., 2005) observed the field starting at 00:09:08 UT on the $6^{\rm th}$ May 2005, ~ 47 minutes after the burst trigger. The initial data were limited to one 100 second exposure in each of the four filters. No new sources were found in the XRT error circle to limiting magnitudes (5σ in 6 arcsecond radius apertures) of V > 17.7, U > 18.4, UVW1 > 18.9 and UVM2 > 19.7. Additional co-added, deeper exposures (~ 2000 seconds) with the UVOT also failed to detect an optical counterpart at the location of the GRB (Rosen et al., 2005a,b). The deeper exposure in V placed a limiting magnitude for the source at > 20.35 (3σ confidence level) for a total exposure of 2527 seconds co-added from a series of short exposures over the time span of 2807 to 28543 seconds after the trigger. Due to the delayed slew of the satellite I cannot confirm whether this burst was intrinsically subluminous or had faded below the detection level of the UVOT. However, the optical counterpart for this burst was detected by several other facilities (see Table 2.2), which argues for the case that it was merely too faint to be detected by the UVOT ~ 47 minutes post-burst.

2.2.1 X-ray light curve and spectral analysis.

CCD detectors, such as the XRT, are prone to an effect called 'pile up' (Ballet, 1999), which occurs when more than one X-ray photon is incident on a given detector pixel in a single readout frame. The

[6] http://www.swift.ac.uk/xrt_positions/docs.php, see also Goad et al. (2007).

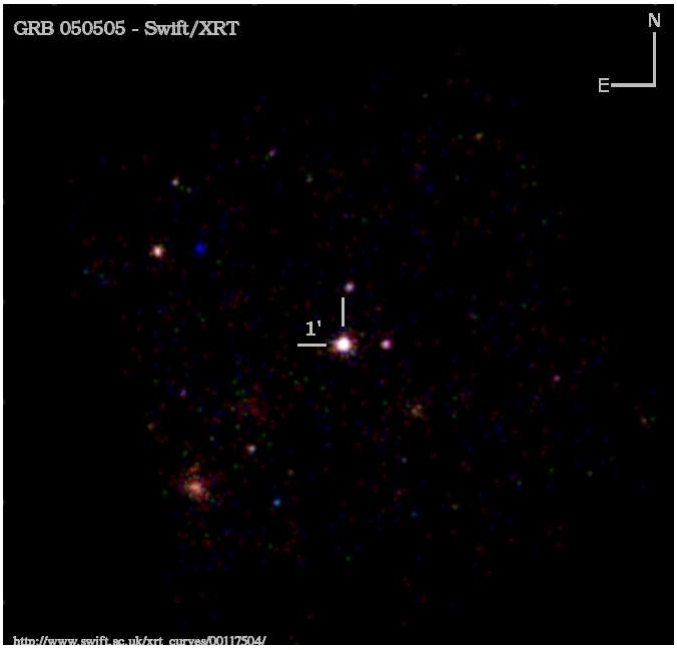

Figure 2.2: Three color X-ray image of GRB 050505, courtesy of the *Swift* /XRT GRB lightcurve repository (Evans et al., 2007). The colour image was created by splitting the data (total exposure 168.77 ks) into three energy bands: 0.3-1.2 keV, 1.2-1.8 keV and 1.8-10 keV. These were treated as red, green and blue channels respectively and combined to give the colour image, which was then smoothed. The energy bands used were chosen based on the spectra of the GRBs observed by *Swift* to date, so that a typical GRB will have equal numbers of counts in the three channels. Thus a comparatively soft burst will appear redder, and a hard burst bluer, in these images. Note that there are no nearby bright X-ray sources and therefore no contamination of the X-ray spectra or lightcurve.

---

two separate monopixel, relatively low energy events are recorded as a single higher energy event. If two monopixel, or multipixel, events occur adjacent to each other then they may be recorded as a single multipixel event of higher grade (see § 1.1.5). Pile-up therefore results in an apparent loss of flux (particularly from the center of the Point Spread Function; hereafter PSF), a change in the grade distribution and a distortion (hardening of the spectral slope, which corresponds to a decrease in the measured photon index) of the observed spectrum at high incident fluxes.

The XRT suffers from pile-up in Photon Counting (PC) mode when the count rate is ≥ 0.6 counts s^{-1} (Vaughan et al., 2006). There are several methods to evaluate the degree of pile-up in a spectrum, one

of which is to investigate the level of spectral distortion i.e. if the data are piled-up then the spectrum will be harder than expected. A series of grade $0-12$ spectra were extracted from the first 23 ks of data using annuli of varying inner radii. These background corrected spectra were then fitted in *XSPEC* with an absorbed power law. The point at which pile-up no longer affects the results was deemed to be when the power law index did not vary when the inner radius of the annulus was increased. Another method involves comparing the observed Point Spread Function (PSF) to the known un-piled-up PSF. In the absence of pile-up effects the *Swift* PSF can be modelled as a King function:

$$PSF(r) = \left[1 + \left(\frac{r}{r_c}\right)^2\right]^{-\beta}, \tag{2.1}$$

where, for *Swift*, $r_c \sim 5.8$ and $\beta \sim 1.55$ (Moretti et al., 2005). An image covering the timespan of interest was extracted from the PC mode data event files using *XSELECT* and then read into *XIMAGE*. Once the relevant image had been displayed the `psf` command was run. The PSF profile produced was then fitted using data in the 'wings' (> 15 arcsec from the center, where pile-up has no effect) with the King function given in equation 2.1. The fit was then extrapolated back into the central region of the PSF. The region where the PSF lies below the extrapolation of the King function was then excluded to avoid pile-up (see also § 2.1 of Evans et al. 2007). For GRB 050505 both methods of pile-up evaluation indicated that the inner 8 pixels (radius) should be excluded. Data after $T + 23$ ks were not piled up and therefore required no correction.

The X-ray light curve of GRB 050505 is shown in figures 2.3 and 2.4, with observations starting at $T+3$ ks after the trigger time and extending to $T+1.05\times10^3$ ks. The temporal and spectral behaviour of the XRT flux was characterised by $F_\nu \propto t^{-\alpha}\nu^{-\beta}$, where both standard power law indices may vary with time (see § 1.3.3). A series of models were fit to the light curve data. The simplest model considered was a single power law of decay index α. This model was rejected for GRB 050505 as it gave an unacceptable value of $\chi^2/\nu = 122.5/46$.

'Broken' and 'doubly broken' power laws were also fitted to the data. These models consist of two or three (respectively) power law sections whose slopes join but change instantaneously (sharply) from α_i to α_{i+1} at the break times. A 'broken' power law model was also a poor description of the light curve ($\alpha_1 = 0.90^{+0.05}_{-0.05}, \alpha_2 = 1.80^{+0.18}_{-0.15}, t_{\rm break} = 42^{+6.7}_{-7.3}$ ks) with $\chi^2/\nu = 58.0/44$. A 'doubly broken' power law provided a much better statistical fit to the data with $\chi^2/\nu = 38.7/42$ ($> 99.9\%$ improvement over

both the simple and the broken power law). The model consisted of a shallow decay, $\alpha_1 = 0.25^{+0.16}_{-0.17}$, which broke at $t_1 = 7.4^{+1.5}_{-1.5}$ ks to a steeper decay of $\alpha_2 = 1.17^{+0.08}_{-0.09}$. The steeper decay broke again at $t_2 = 58^{+9.9}_{-15.4}$ ks into a yet more rapidly decaying index of $\alpha_3 = 1.97^{+0.27}_{-0.28}$ (see figure 2.3).

A 'smoothly broken' power law was also fit to the data. This model consisted of two power law sections; the transition between these slopes was not instantaneous, but may spread over several decades in time:

$$F_\nu(t) \quad = \quad K \left(\left(\frac{t}{t_b} \right)^{-\alpha_1 S} + \left(\frac{t}{t_b} \right)^{-\alpha_2 S} \right)^{1/S}, \tag{2.2}$$

where S is the smoothing parameter, t_b is the break time and K is a normalisation constant. This produces a smooth break rather than a sharp break as in the previous models. Typically the values of the smoothing parameter, S, reported in the literature range between $0.5-10$, with a value of ~ 1 being favoured both observationally and theoretically (Stanek et al., 2005; Beuermann et al., 1999). A larger value of the smoothing parameter gives a sharper break. The light curve of GRB 050505 was well fit by a smoothly broken power law with $\chi^2/\nu \sim 1.0$. Unfortunately there was degeneracy between the smoothing factor and the initial decay index, with any value of S between 0.5 and 3 producing a good fit to the data (limit of $\chi^2/\nu = 1.16$). However, if the model parameters were constrained so that α_1 must have a positive value and that α_2 equals p, the electron spectral index (calculated from our spectral index, β, see below; Zhang & Mészáros 2004), then a smoothing parameter in the range of $0.5 - 2$ was allowed. This range of smoothing factors produced $\alpha_1 \sim 0.5$. Restricting S to 1.0 yielded $\alpha_1 = 0.37^{+0.13}_{-0.15}$, $\alpha_2 = 1.80^{+0.16}_{-0.16}$, $t_\mathrm{break} = 18.5^{+4.4}_{-3.2}$ ks and $\chi^2/\nu = 46.9/45$ (see figure 2.4).

Spectral fits were performed over $0.3 - 10.0$ keV using grade $0 - 12$ events (as selected for the light curve analysis), binned to 20 counts per data point, individually for co-added data encompassing $T + 3$ to $T + 17$ ks and $T + 26$ to $T + 138$ ks, as well as the summed spectra for both intervals combined. At the time of the initial analysis only version 007 of the calibration database (CALDB) was available and the spectra were fitted using *XSPEC* 11. Additional spectral fits were carried out using the updated version 008 CALDB[7] and *XSPEC* 12.3.1x. Both sets of spectral parameter values are reported in Table 2.1; the version 007 CALDB results are in the second column and the version 008 CALDB results are in the third column. Both sets of results are consistent and hereafter only version 008 CALDB results are reported.

[7]Version 008 of the CALDB is a marked improvement over the previous release (Campana et al., 2006a, see also http://heasarc.nasa.gov/docs/heasarc/caldb/swift/docs/xrt/SWIFT-XRT-CALDB-09.pdf.)

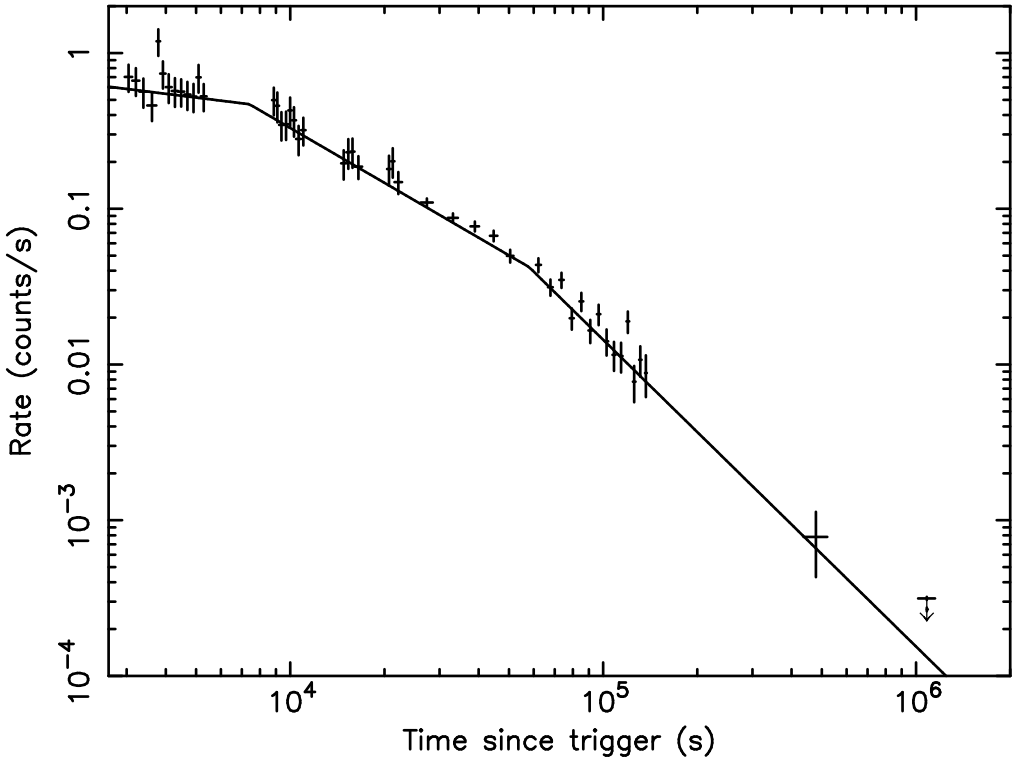

Figure 2.3: The $0.3-10.0$ keV X-ray light curve of GRB 050505 fit to a doubly broken power law (see § 2.2.1). The first decay slope, $\alpha_1 = 0.25^{+0.16}_{-0.17}$, which breaks sharply at $t_1 = 7.4^{+1.5}_{-1.5}$ ks (observer's frame) to second decay slope of $\alpha_2 = 1.17^{+0.08}_{-0.09}$. A second break occurs at $t_2 = 58^{+9.9}_{-15.4}$ ks into a third decay slope of $\alpha_3 = 1.97^{+0.27}_{-0.28}$. The final point on the light curve is the 3σ upper limit to the detection of the afterglow at that time.

The spectra were fit with a power law model (see figure 2.5) with the absorption, $N_{\rm H}$, set at the Galactic column density (2.1×10^{20} cm^{-2}, Dickey & Lockman, 1990), and with power law models with excess absorption (either in our Galaxy or the GRB host galaxy). During my analysis both Wisconsin and Tübingen-Boulder ISM absorption models (Arnaud, 1996a) were used; there was no significant difference in either the statistical quality of the fit or in the resulting derived parameters between the two. The results presented here were obtained using the Tübingen-Boulder model and the local interstellar medium abundances of Anders & Grevesse (1989)[8].

It is clear from Table 2.1 that there was no evidence, from either set of fits, for spectral change over

[8]Spectral fits were also preformed using the abundances of Wilms et al. (2000), it was found that they produced $N_{\rm H}$ values that agreed, within errors, to those given by the Anders & Grevesse (1989) abundances.

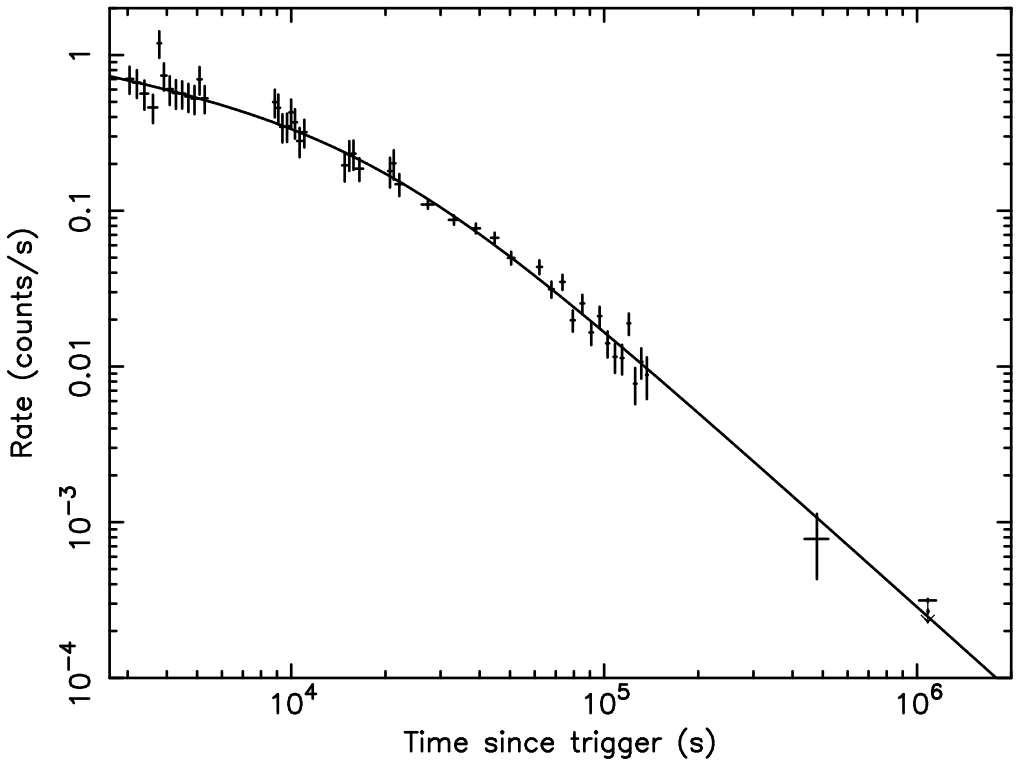

Figure 2.4: As figure 2.3, but fit with a smoothly broken power law (see § 2.2.1). The first decay slope, $\alpha_1 = 0.37^{+0.13}_{-0.15}$, which breaks at $t = 18.5^{+4.4}_{-3.2}$ ks (observer's frame), with a smoothing parameter $S = 1.0$, to second decay slope of $\alpha_2 = 1.80^{+0.16}_{-0.16}$.

---

the duration of the observations. This was confirmed by making a hardness ratio time series in the energy bands $0.3 - 1.5$ keV and $1.5 - 10.0$ keV; no variation was apparent (see figure 2.6). The fit to the total data-set reported in Table 2.1 also shows that there was significant excess absorption in this spectrum (at $> 99.99\%$ confidence). Statistically both Galactic and extra-galactic absorption fits appeared equally likely, however, if the absorption were to be due to gas in our Galaxy alone then the value of the excess absorption is almost twice the column density quoted by Dickey & Lockman (1990). Therefore, I conclude that the bulk component of excess absorption must come from the host galaxy with a value of $N_{\rm H} = 1.63^{+0.63}_{-0.58} \times 10^{22}{\rm cm}^{-2}$, using version 008 CALDB files, assuming local ISM abundances in the GRB rest frame.

The photon index $= \beta+1 = 2.01^{+0.08}_{-0.08}$ (version 008), is typical of the photon indices seen in other GRB afterglows (Nousek et al., 2006), even though a higher range of spectral energies are being sampled due to the high redshift of this burst. With a redshift of 4.27 (Berger et al., 2005a) the XRT spectrum was

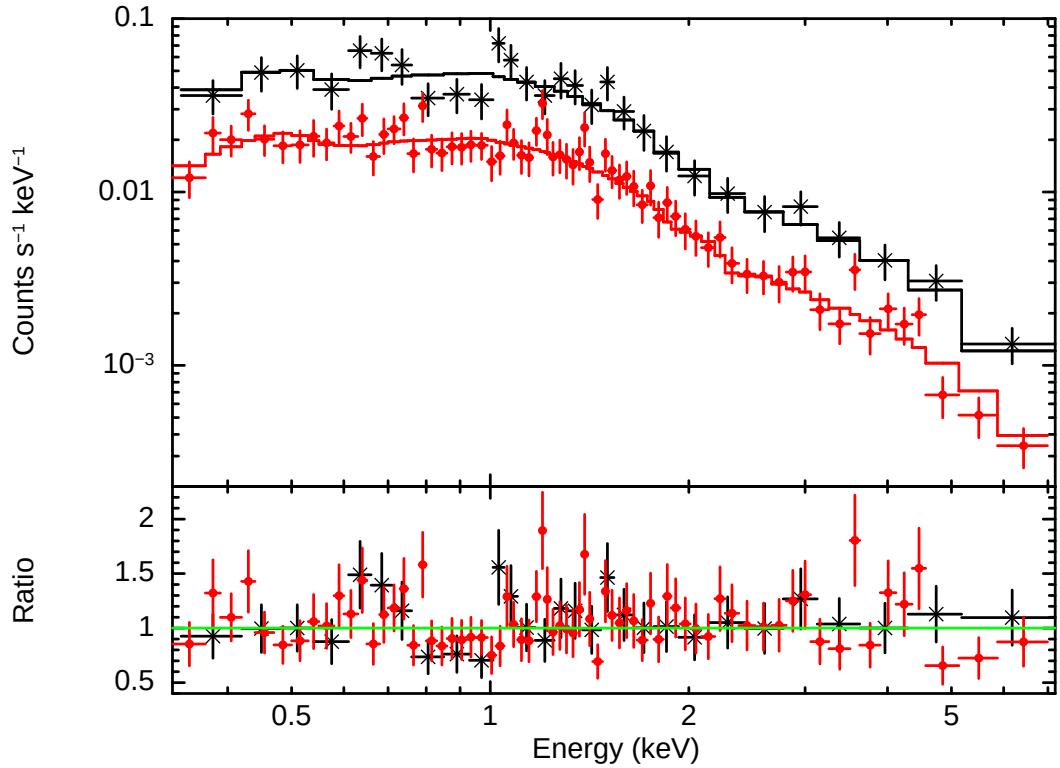

Figure 2.5: The summed $0.3 - 10.0$ keV spectrum of GRB 050505 from 'piled up' (black crosses) and 'non piled up' (red solid circles) data, which are consistent with a photon index of ~ 2.0, Galactic absorption (2.1×10^{20} cm^{-2}) plus an excess absorption component from the host galaxy ($163^{+63}_{-58} \times 10^{20}$ cm^{-2}). See Table 2.1 for a summary of spectral models.

---

measured over a rest-frame range of $1.6 - 53$ keV. The spectrum was well modelled up to such high energies in the rest-frame of the GRB, and the photon index is comparable to the values found from low redshift bursts.

2.3 Follow-up detections of GRB 050505

The first reported detection of an optical counterpart for GRB 050505 was made by Cenko et al. (2005) observing from the Keck I telescope, quickly followed by a measurement of the redshift by the same collaboration (Berger et al., 2005a). See Table 2.2 for a summary of all of the optical observations reported on the GCN system as well as data from Faulkes Telescope North, reported in Hurkett et al. (2006).

Model[a]	CALDB v007			CALDB v008		
	Photon index	Excess $N_{\rm H}$ ($\times 10^{20}{\rm cm}^{-2}$)	χ^2 (DOF)	Photon index	Excess $N_{\rm H}$ ($\times 10^{20}{\rm cm}^{-2}$)	χ^2 (DOF)
Co-added data for $T+3$ - $T+17$ ks						
PL+Gal	$1.76^{+0.09}_{-0.09}$	-	27 (27)	$1.78^{+0.09}_{-0.09}$	-	26 (27)
PL+Gal+Abs	$1.91^{+0.19}_{-0.18}$	< 7.74	24 (26)	$1.98^{+0.20}_{-0.18}$	$4.81^{+4.30}_{-3.77}$	21 (26)
PL+Gal+ZAbs	$1.87^{+0.15}_{-0.14}$	113^{+123}_{-107}	24 (26)	$1.92^{+0.15}_{-0.14}$	135^{+124}_{-108}	22 (26)
Co-added data for $T+26$ - $T+138$ ks						
PL+Gal	$1.77^{+0.06}_{-0.06}$	-	86 (69)	$1.86^{+0.06}_{-0.05}$	-	85 (69)
PL+Gal+Abs	$1.94^{+0.12}_{-0.11}$	$3.91^{+2.43}_{-2.14}$	77 (68)	$2.11^{+0.12}_{-0.11}$	$6.02^{+2.58}_{-2.29}$	65 (68)
PL+Gal+ZAbs	$1.91^{+0.10}_{-0.09}$	133^{+73}_{-65}	75 (68)	$2.04^{+0.09}_{-0.09}$	173^{+75}_{-66}	65 (68)
All data co-added						
PL+Gal	$1.76^{+0.05}_{-0.05}$	-	133 (97)	$1.84^{+0.05}_{-0.05}$	-	112 (97)
PL+Gal+Abs	$1.93^{+0.10}_{-0.10}$	$3.81^{+2.09}_{-1.93}$	102 (96)	$2.08^{+0.10}_{-0.10}$	$5.71^{+2.17}_{-2.02}$	88 (96)
PL+Gal+ZAbs	$1.90^{+0.08}_{-0.08}$	128^{+61}_{-58}	99 (96)	$2.01^{+0.08}_{-0.08}$	163^{+63}_{-58}	88 (96)

Table 2.1: XRT spectral fits for GRB 050505. The spectra show no variation in photon index between the two time spans, within the error limits. Whilst an absorbed power law was sufficient to model the data it can be seen that an additional absorption component provided a better fit, particularly at the redshift of the host galaxy. Version 008 CALDB files gave a better statistical fit to the data and yielded slightly larger excess absorption columns, which were consistent with the values given by the version 007 CALDB fits within the error limits. [a] Spectral models: power-law (PL), Galactic absorption (Gal), which has been assumed to be 2.1×10^{20} cm^{-2} (Dickey & Lockman 1990), excess Galactic absorption (Abs) and excess absorption in the host galaxy (ZAbs).

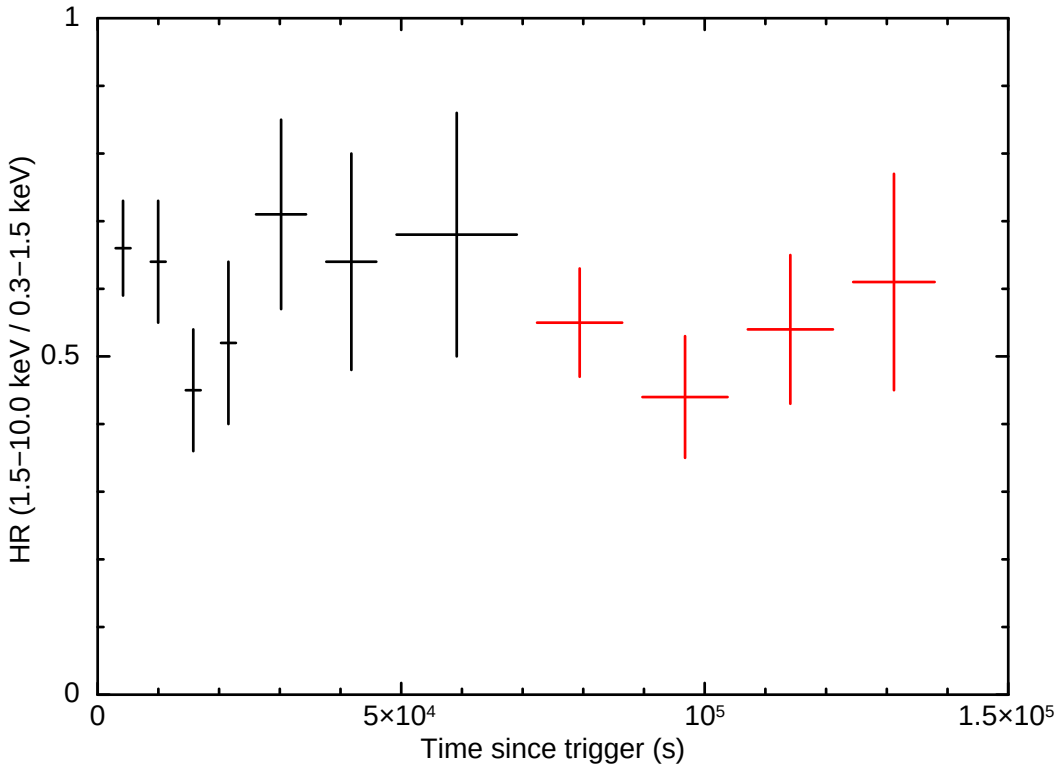

Figure 2.6: A hardness ratio plot between the $1.5 - 10.0$ keV and $0.3 - 1.5$ keV energy bands. Ratios calculated using an annular region to account for pile-up (inner radius 8 pixels, outer radius 30 pixels) are plotted in black and those calculated using a circular region (radius 30 pixels) are plotted in red. The data are consistent with a constant HR value of $0.57^{+0.05}_{-0.05}$ ($\chi^2/\nu = 8/10$), indicating that there is no spectral change at either of the possible break times. No additional Point Spread Function (PSF) correction was required when using an annular region as the *Swift* PSF function does not have a strong energy dependance (Moretti et al., 2005).

The BOOTES very wide field camera was observing the region of the sky containing the GRB position at the time of the burst as part of its routine observing schedule. A 30 s observation began at 23:22:00 UT, 21 s before the burst trigger. Jelinek et al. (2005) derived a limiting magnitude of $R > 9.2$ for any prompt flash arising from the GRB. A further 30 s exposure was started at 23:23:00 UT, providing the same limit. Unfortunately the initial spacecraft message sent to the GCN erronously flagged this event as not a GRB, which consequently meant that the majority of robotic follow-up missions did not observe GRB 050505 promptly. The sparse nature of this combined data-set naturally limits the knowledge that can be obtained.

Filter	Limiting mag.	Detected mag.	Duration (s)	Mid-point time (s)	Observatory	References
R	9.2		30	-6	BOOTES[a]	Jelinek et al. (2005)
R	9.2		30	54	BOOTES[a]	Jelinek et al. (2005)
I		18.2 ± 0.2	456	796	TAROT	Klotz et al. (2005)
I		18.4 ± 0.2	456	1259	TAROT	Klotz et al. (2005)
I	18.8		584	1946	TAROT	Klotz et al. (2005)
R	18.5		1680	2398	AAVSO	Hohman et al. (2005)
R	19.0		3600	2799	BOOTES[b]	de Ugarte Postigo et al. (2005)
R	19.7		2100	14326	SARA	Homewood et al. (2005)
I		20.51 ± 0.05	-	23006	Keck	Berger et al. (2006)
g		23.67 ± 0.12	-	23006	Keck	Berger et al. (2006)
K		18.1 ± 0.2	-	24552	UKIRT WFCAM	Rol et al. (2005)
R		21.8 ± 0.1	540	29894	FTN	Hurkett et al. (2006)
i'		21.0 ± 0.2	520	30154	FTN	Hurkett et al. (2006)
B	21.9		640	30154	FTN	Hurkett et al. (2006)

Table 2.2: Optical follow-up of GRB 050505. Mid-point times are given in seconds after the Trigger time. BOOTES - [a] Very Wide Field Camera, [b] IR. FTN[c] - Faulkes Telescope North.

2.4 Discussion

2.4.1 Physical origin of the X-ray light curve break

A doubly broken power law fit contains breaks at $7.4^{+1.5}_{-1.5}$ ks and $58.0^{+9.9}_{-15.4}$ ks in the observer's frame, which translate to $T + 1.4^{+0.3}_{-0.3}$ ks and $T + 11.0^{+1.9}_{-2.9}$ ks in the rest frame of the burst. The amplitudes of these temporal breaks are $\Delta\alpha_{1-2} = 0.92 \pm 0.19$ and $\Delta\alpha_{2-3} = 0.80 \pm 0.29$.

The combined BAT and XRT light curve (shown in figure 2.7) is consistent with the schematic diagram of the canonical behaviour of *Swift* XRT early light curves (see figure 1.9 of this work; alternatively fig 3 of Nousek et al., 2006). For GRB 050505 there is necessarily a steep decline from the bulk of the BAT emission to the early XRT emission, which would comprise the first power law segment (phase I emission) identified by Nousek et al. (2006), the early flat slope of the XRT decay (α_1) would comprise the phase II emission of canonical decay and the second slope of the doubly broken power law fit (α_2) would comprise the phase III emission. Whilst the BAT and XRT light curves are consistent with this

Afterglow model	$\nu > \nu_c$		$\nu < \nu_c$		$\lvert\Delta\beta\rvert$	$\lvert\Delta\alpha\rvert$
	β	α	β	α		
ISM, slow cooling	$\frac{p}{2}$	$-\frac{2-3p}{4}$	$\frac{p-1}{2}$	$-\frac{3(1-p)}{4}$	0.50	0.25
ISM, fast cooling	$\frac{1}{2}$	$\frac{1}{4}$	$-\frac{1}{3}$	$-\frac{1}{6}$	0.83	0.42
WIND, slow cooling	$\frac{p}{2}$	$-\frac{2-3p}{4}$	$\frac{p-1}{2}$	$-\frac{1-3p}{4}$	0.50	0.25
WIND, fast cooling	$\frac{1}{2}$	$\frac{1}{4}$	$-\frac{1}{3}$	$\frac{2}{3}$	0.83	0.42

Table 2.3: Temporal index α and spectral index β in various afterglow models, for cases where ν_c, the synchrotron cooling frequency, is below and above the observed frequency ν. The expected change in both indices is reported for a cooling break passing through the observed band. Adapted from Zhang & Mészáros (2004) and references therein.

canonical decay pattern, joining in the ~ 47 minute gap that separates them (following the trend seen in O'Brien et al., 2006), this behaviour cannot be confirmed with the data available.

Light curve breaks can be caused by the passage through the X-ray band of the cooling frequency (ν_c), the ending of continued shock energization, the presence of a structured jet or jet deceleration causing the relativistic beaming to become broader than the jet angle. The possibilities are examined here.

The passage of a cooling break through the X-ray band would result in $|\Delta\alpha| = 0.25$ and $|\Delta\beta| = 0.50$ (slow cooling case) or $|\Delta\alpha| = 0.42$ and $|\Delta\beta| = 0.83$ (fast cooling case); see table 2.3. This case can be ruled for either break as both observed $\Delta\alpha$ values are too large and there was no evidence of spectral evolution (see table 2.1 and figure 2.6).

Either of the X-ray light curve breaks might represent the end of the energy injection into the forward shock of the relativistic outflow (Nousek et al., 2006; Zhang et al., 2006), given the lack of spectral variation (and presuming the emission before the break was dominated by the forward shock). However, the first break is the more favourable of the two for this interpretation, as the first break seen in the canonical light curve is typically due to the end of energy injection (see § 1.3.3).

Nousek et al. (2006) consider that a shallow flux decay is caused by continuous energy injection into the external shock either due to a decrease in the Lorentz factor of the outflow towards the end of the

prompt emission or by long lasting central engine activity (see discussions in § 1.3.3 of this work). The decreasing Lorentz factor (Γ) scenario requires that $E(>\Gamma) \propto \Gamma^{1-s}$ with $s > 1$, but Nousek et al. find, on the basis of their observed change in decay slope, when modelling the light curve with a single broken power law, that $s = -16.7 \pm 4.6$ for this burst (see their table 3), thus disallowing this interpretation. However, a more detailed, multi-broken power law analysis shows that this scenario is valid for either of the breaks ($s > 3$ for both breaks, from both version 007 and 008 CALDB files) except when $\nu_{\rm c} < \nu_{\rm x} < \nu_{\rm m}$ for a wind medium ($s \sim -21$ and ~ -63 for the first and second break respectively), where $\nu_{\rm c}$, $\nu_{\rm x}$ and $\nu_{\rm m}$ are the cooling, X-ray and 'typical' synchrotron frequencies respectively.

The long-lasting central engine activity scenario requires that the source luminosity decays slowly with time, $L \propto t^q$ (see § 1.3.3). The total amount of injected energy must increase with time to effect the dynamics of the afterglow shock and cause a shallower decay. This implies $q > -1$; the average value of q found by Nousek et al. was of the order -0.5. The change in decay slope from their single broken power law model leads the authors to find $q = 0.3 \pm 0.1$ for GRB 050505, which is consistent with the lower limit of this mechanism. My analysis shows that the long-lasting central engine activity scenario is valid (i.e. $q > -1$, with q in the range ~ -0.2 to -0.5), again for either of the breaks (and for both versions of the CALDB files), as long as the X-ray frequency, $\nu_{\rm x}$, is above the cooling frequency, $\nu_{\rm c}$. It was not possible, in this case, to distinguish whether a wind or homogeneous circumburst medium is favoured.

Another possible cause of either of the breaks in the light curve of GRB 050505 could be a structured jet outflow. In this case the ejecta energy over solid angle, $dE/d\Omega$, is not constant, but varies with the angle θ measured from the outflow symmetry axis (Mészáros et al., 1998). Panaitescu (2005b) suggests that since afterglow light curves are power laws in time $dE/d\Omega$ can be approximated as a power law in θ, with a power law index of Q given by their equation 13 (repeated here for clarity)[9]:

$$dE/d\Omega \propto \begin{cases} constant & \theta < \theta_c, \\ (\theta/\theta_c)^{-Q} & \theta > \theta_c, \end{cases} \tag{2.3}$$

with a uniform core of half opening angle θ_c to avoid on-axis divergence. Panaitescu (2005b) assumes

[9]The power law index Q used by Panaitescu (2005b) has been capitalised to prevent confusion with the q used in the luminosity relation of Nousek et al. (2006).

that the direction towards the observer lies within this core opening. Therefore, when the ejecta have decelerated sufficiently that the emission from the outflow envelope is beamed relativistically towards the observer (i.e. the bulk Lorentz factor $\Gamma < \theta_c^{-1}$) a break with the following magnitude is seen (equation 14 of Panaitescu 2005b, repeated here for clarity):

$$\Delta\alpha = \begin{cases} \frac{3Q(8-\tilde{Q})}{4\tilde{Q}(8-Q)} & k=0, \\ \frac{Q(4-\tilde{Q})}{2\tilde{Q}(4-Q)} & k=2, \end{cases} \tag{2.4}$$

where k refers to the density profile of the external medium ($\rho_{ext} = Ar^{-k}$)[10] and $\tilde{Q}$ is given by equation 15 of Panaitescu (2005b) provided $Q < \tilde{Q}$ (repeated here for clarity):

$$\tilde{Q} = \begin{cases} \frac{8}{p+4} & (k=0, \nu_{\rm x} < \nu_c) \quad \text{or} \quad (k=2, \nu_c < \nu_{\rm x}), \\ \frac{8}{p+3} & (k=0, \nu_{\rm x} > \nu_c) \quad \text{or} \quad (k=2, \nu_c > \nu_{\rm x}). \end{cases} \tag{2.5}$$

It was possible to calculate p (the electron spectral index) from the observed spectral index ($\Gamma = \beta + 1$; $\beta = 1.01 \pm 0.08$) using the relations given in table 2.3. The measured value of β is not compatible with the fast cooling case. The slow cooling case gives $p = 2.0 \pm 0.2$ and 3.0 ± 0.3, assuming that $\nu_{\rm x}$ is above and below the cooling frequency, $\nu_{\rm c}$, respectively (Zhang & Mészáros, 2004; Sari et al., 1999). Q was then calculated for each break from equations 2.4 and 2.5 using these values of p and the observed values of $\Delta\alpha$. For GRB 050505 the observed values of $\Delta\alpha$ give $Q > \tilde{Q}$, within errors, for both wind and uniform environments and for the observing frequency above or below the cooling frequency.

For $Q > \tilde{Q}$, where $dE/d\Omega$ falls off sufficiently fast that the afterglow emission is dominated by the core of the jet, $\Delta\alpha$ is expected to be equal to 0.75 (homogeneous environment) or 0.5 (wind environment) (Panaitescu, 2005b). Thus a structured jet appears to be just consistent with both breaks. However, α_1 is too shallow to be explained by the fireball model, unless the observer is located off the jet core. In this case the value of α_1 implies that our line of sight should be located exceptionally close to the edge of the core.

The signatures of a jet break, where the relativistic outflow from the GRB slows sufficiently that $\Gamma \sim$

[10] A constant density profile corresponds to $k = 0$ and a 'wind' profile to $k = 2$.

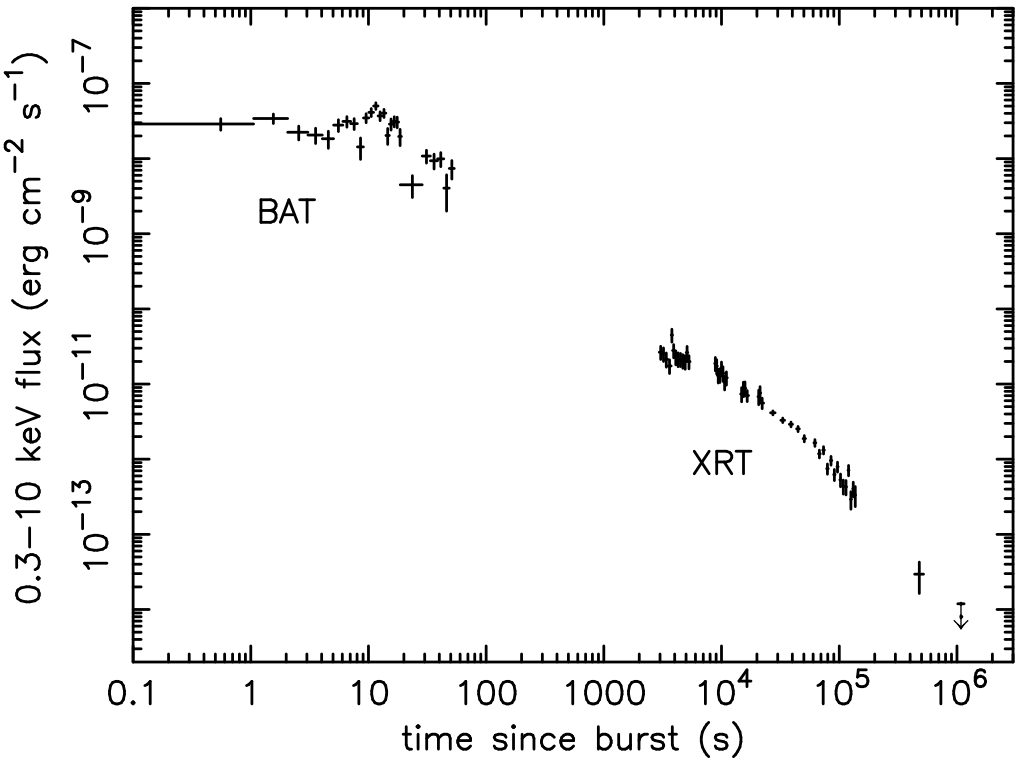

Figure 2.7: The combined BAT-XRT flux light curve, extrapolated into the $0.3 - 10.0$ keV range. For the XRT section of the flux light curve, the count rate was converted into an unabsorbed flux using the best fit power law model. The BAT data were extrapolated into the XRT band using the best fit power law model derived from the BAT data alone.

θ_j^{-1} and the jet spreads laterally, are a temporal break with a typical amplitude of ~ 1 (Rhoads, 1999; Chevalier & Li, 2000; Sari et al., 1999), no spectral variation (Piran, 2005) and a post-break decay index equal to p, the electron spectral index (Rhoads, 1999). The relation of $\alpha = p$ post-break is valid for $p > 2$, otherwise a different $\alpha - p$ relation should be adopted (Dai & Cheng, 2001; Zhang & Mészáros, 2004). There was no evidence for spectral variation during the observations (see Table 2.1). Unfortunately there were insufficent optical detections of this GRB pre- and post-break to confirm the presence of a jet break in other wavelengths at either epoch.

Given that the temporal index of an X-ray light curve post-jet break should be equal to p (Rhoads, 1999), a comparision was made between the calculated p values (2.0 ± 0.2 and 3.0 ± 0.3 for $\nu_{\rm x}$ above and below $\nu_{\rm c}$) and the observed decay slopes. The value of $\alpha_2 = 1.17^{+0.08}_{-0.09}$ is not compatible with either value of p, which rules out the first break being due to a jet break. However, $\alpha_3 = 1.97^{+0.27}_{-0.28}$ which

agrees, within the limits, to the $\nu_{\rm x} > \nu_{\rm c}$ case ($p = 2.0 \pm 0.2$). Since p may be < 2, within the error range, the expected post-break slope was calculated from Dai & Cheng (2001, $\alpha = (p+6)/4$, $\nu_{\rm x} > \nu_{\rm c}$) giving an expected decay index of 2.0 ± 0.2, which is also consistent with α_3. With $p = 2.0 \pm 0.2$ it was possible to constrain the jet break parameters further using equations 49, 50 and 54 from Rhoads (1999) for optically thin and thick cases (summarised for clarity here);

$$\Delta\alpha = \begin{cases} \frac{p+3}{4} & \nu < \nu_{\rm c} \quad \text{optically thin,} \\ \frac{p+2}{4} & \nu > \nu_{\rm c} \quad \text{optically thin,} \\ 1.25 & - \quad \text{optically thick.} \end{cases} \tag{2.6}$$

The second break is consistent with a value of $\Delta\alpha = 1.00 \pm 0.05$, which is the value expected from thin synchrotron emission when $\nu_{\rm x} > \nu_{\rm c}$, thus supporting the case that the second break is a jet break.

Having considered the various potential origins for the breaks in the light curve of GRB 050505 for the doubly broken model I conclude that the first break was due to the end of energy injection into the forward shock, i.e. that GRB 050505 fits with the canonical light curve model proposed by Nousek et al. (2006), and that the second break was due to a jet, either structured or uniform.

The 'smoothly broken' core-dominated power law provided a good fit to the XRT light curve data; however, the large degree of smoothing involved produces a degeneracy between the smoothing parameter, the first decay index and the break time. Taking the example case for $S = 1$ (see figure 2.4), then a break was observed at $T + 18.5^{+4.4}_{-3.2}$ ks in the observer's frame. This translates to $T + 3.5^{+0.8}_{-0.6}$ ks in the rest frame of the burst, with $\Delta\alpha = 1.43^{+0.21}_{-0.22}$.

The magnitude of this break rules out a cooling break or the end of continued energy injection into the forward shock. A structured jet could explain the magnitude of this break if the observer is placed off the jet core (Panaitescu, 2005a). This would then naturally explain the initial shallow decay index and the very smooth break. The magnitude of the break was also compatable with a jet break from optically thick synchrotron emission ($\Delta\alpha = 1.25$). However, a break this early requires an unreasonably large circumburst density ($n \sim 3 \times 10^5$ cm^{-3}) to produce a value of $E_{\gamma,\rm rest}$ (Ghirlanda et al., 2004), the true γ-ray energy released, that is comparable with the typical values of $E_{\gamma,\rm rest}$ seen thus far (Bloom et al., 2003). Thus the parameters of the smoothly broken power law model fit are inconsistent with all of the afterglow models considered here.

2.4.2 Multiwavelength spectral energy distribution

Figure 2.8 shows the optical – X-ray spectrum of GRB 050505. The X-ray fluxes were obtained from a spectral fit between 26 ks and 40 ks after the burst; the optical data (UKIRT K band and the FTN data) were scaled to a common epoch, chosen to be the logarithmic average of the X-ray data (32 ks). The magnitudes have been corrected for the estimated Galactic extinction using the dust maps by Schlegel et al. (1998), and have been converted to fluxes using the calibration provided by Fukugita et al. (1995) for the optical and that by Tokunaga & Vacca (2005) for the infra red magnitudes. Since all optical data were taken between the time of the two breaks the $\alpha_2 = 1.17^{+0.08}_{-0.09}$ XRT light curve decay index was used. However, the decay index in the optical band can be different. Several other values for the decay index were tested, at most 0.5 different from 1.17; it was found that the resulting optical fluxes differ at most by 1σ ($\sim$0.2 mag).

The broad-band spectrum was fit with two basic models, a power law and a broken power law, both accounting for the Lyman break (with the redshift fixed at $z = 4.27$) and intrinsic host-galaxy extinction (also with the redshift fixed at $z = 4.27$). The Lyman break was modelled as described in Madau (1995); the optical/UV absorption was modelled following Pei (1992). A single power law was excluded, even allowing for dramatic extinction in the host galaxy ($\chi^2/\nu = 38.2/4$ with the spectral index fixed at 1.0 as determined from the X-ray data alone). A broken power law, with the high-frequency index β_2 also fixed at 1.0, resulted in a much better fit. Three variants of extinction were applied: none, a Galactic-like extinction curve and an SMC-like extinction curve. The SMC-like extinction curve provided a good fit, resulting in the $B-V$ colour excess being $E(B-V) = 0.10 \pm 0.02$ and the low-frequency index $\beta_1 = 0.41^{+0.05}_{-0.06}$ (1σ confidence limits). The break frequency is largely unrestricted and was kept fixed at a value of 10^{16} Hz, although values of 10^{17} Hz and 10^{15} Hz are acceptable (with varying amounts of host-galaxy extinction). However, the low number of data points result in a relatively low $\chi^2/\nu \sim 0.3$, and shows a certain degeneracy: a Galactic-like extinction curve results in an equally good fit. This is mostly because the observed wavelength of the distinct 2175 Å feature[11] falls between the available photometry at this redshift, and the intrinsic extinction is almost entirely determined from the two K and I band points (the R-band point being located on the edge of the Lyman break). The resulting values for a Galactic extinction curve are $E(B-V) = 0.20 \pm 0.03$ and $\beta_1 = 0.50^{+0.06}_{-0.07}$ (1σ).

[11] A strong increase in absorption is found for both the Milky Way and LMC around this wavelength, but is noticeably absent in the SMC (see e.g. Savage & Mathis, 1979).

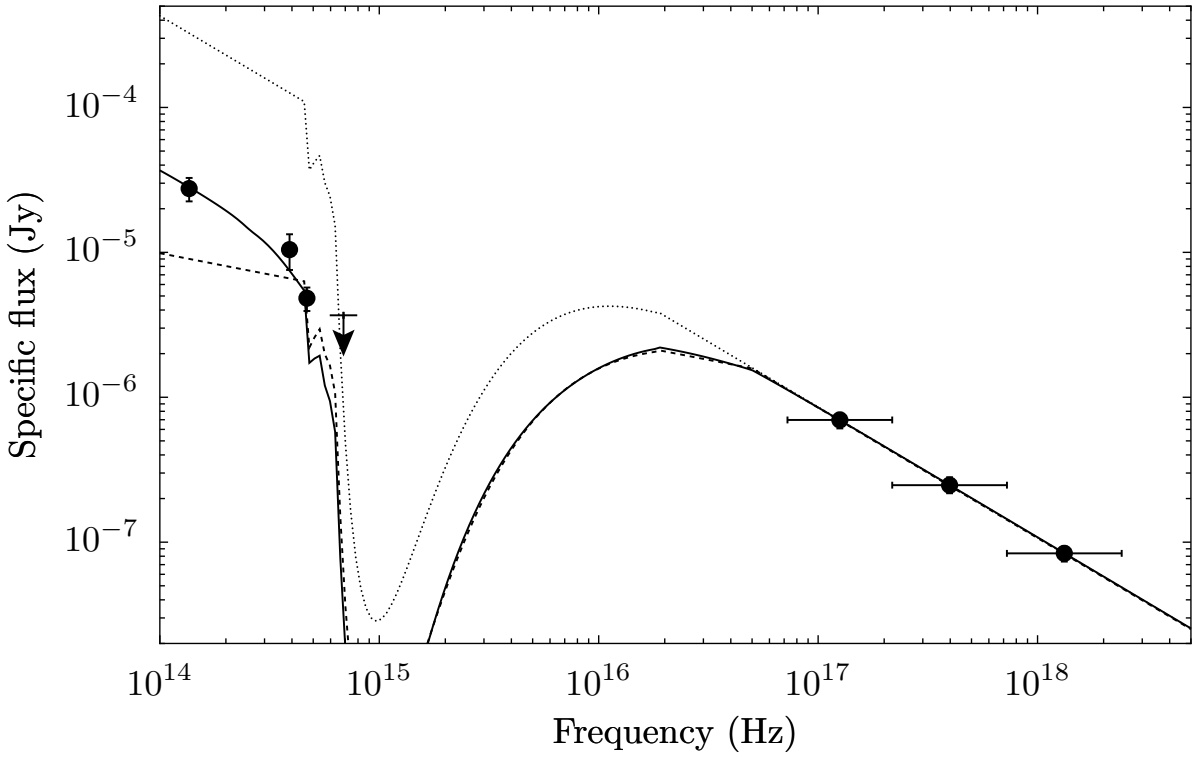

Figure 2.8: The optical-nIR to X-ray spectrum of GRB 050505 at 32 ks after the burst. The X-ray fluxes were corrected for both Galactic and host-galaxy absorption, while the optical-nIR points were corrected for Galactic absorption only. The optical R-band point lies on the edge of the Lyman break, with the Gunn-Peterson trough bluewards of it. The continuous line represents a broken power law, modified by the Lyman break and additional optical/UV host-galaxy extinction (SMC-like, see text). The dashed line uses the same model, but with no additional extinction. The dotted line is the extrapolation from a single power law fitted to the X-rays alone, only accounting for the Lyman break.

The difference between the two power law indices was $\Delta\beta \sim 0.5$. To obtain a better constraint for the break frequency, the indices were fixed at $\beta_1 = 0.4$ and $\beta_2 = 0.9$. This resulted in the cooling frequency being located between 1.8×10^{15} Hz and 1.4×10^{16} Hz (dependent on whether a Galactic or SMC extinction curve was used). The inferred $E(B-V)$ was the same as before.

The best fit results favour a cooling break between the optical and X-ray wavebands; in addition, a modest amount of host-galaxy extinction would be needed to explain the data fully, but no clear distinction between Galactic or SMC-like extinction can be made. A fit with SMC-like extinction, however, agrees marginally better with the expected $\Delta\beta = 0.5$ for a cooling break.

Berger et al. (2006) measured a Hydrogen column density of $\log N_{\rm HI} = 22.05 \pm 0.10$ from the Lyα absorption in their optical spectrum, and a metallicity of $Z \approx 0.06 Z_{\odot}$. This therefore immediately rules out the Galactic-like extinction. Fitting the X-ray spectrum with intrinsic absorption, setting all elements heavier than He to an abundance of 0.06, gives $N_{\rm H} = 7.43^{+3.77}_{-3.41} \times 10^{22}$ cm^{-2}, i.e. $\log N_{\rm H} = 22.87^{+0.18}_{-0.27}$, in addition to the Galactic absorption component. This host absorption was higher than the Hydrogen column directly measured by Berger et al. (2006). It is unlikely that this difference was caused by an evolution of the dust and gas properties, since the timescales of the X-ray and optical observations were similar.

The magnitude of the difference between these two hydrogen column densities is not easily explained. An estimated error in the Galactic $N_{\rm H}$ of the order 10% may be present in this direction. Setting the Galactic column density to 110% of its value did not reduce the excess Hydrogen column density in the rest frame of the burst sufficiently to reconcile the X-ray absorption with the value of Berger et al. (2006). Nor could a difference in column densities of this magnitude be explained by remaining uncertainties in the XRT calibration.

A spectral fit was performed allowing both Galactic and host values of $N_{\rm H}$ to vary, rather than constraining the Galactic value to that given by Dickey & Lockman (1990), using the *XSPEC* `steppar` command to explore the absorption column parameter space. The host absorption column still exceeded the value given by Berger et al. (2006) at greater than 90% confidence. Therefore some curvature of unknown origin may be present in the X-ray spectrum.

From the Hydrogen column density Berger et al. (2006), and using the relation between $N_{\rm HI}$ and $E(B-V)$ for the SMC (Martin et al., 1989), $E(B-V) = 0.24$ was inferred. It should be noted that

this value is likely to be lower (as stated previously), with the metallicity being half of the estimated SMC ISM metallicity ($Z_{\rm SMC} \approx 0.12 Z_{\odot}$, Pei, 1992). The inferred value is moderately in agreement with the $E(B-V) = 0.10$ found from directly fitting the optical – X-ray spectrum with an SMC-like extinction curve (assuming $R_V = 2.39$), although the Galactic extinction curve results in an extinction measurement which is equally well compatible with the inferred $E(B-V)$. This approximately agrees with $A_V = R_V \cdot E(B-V) = 0.3$ as found by Berger et al. (2006). Such a low extinction value is not uncommonly seen in GRB afterglows (e.g. Galama & Wijers, 2001; Stratta et al., 2004).

2.4.3 Burst properties

The redshift of GRB 050505 ($z = 4.27$) and the mean flux over the observed $15 - 350$ keV T_{90} spectrum were used to calculate an isotropic equivalent radiated energy, $E_{\rm iso,rest}$, in the extrapolated $1 - 10^4$ keV rest frame energy range to be $4.44^{+0.80}_{-1.12} \times 10^{53}$ ergs, using the standard cosmology (Spergel et al., 2003): $H_{\rm o} = 71$ km s^{-1} Mpc^{-1}, $(\Omega_M, \Omega_\Lambda) = (0.27, 0.73)$, and a K-correction[12] of $3.09^{+0.48}_{-0.33}$.

If the second break in the light curve is taken to be a jet break then it is possible to calculate the properties of GRB 050505. Using equation 1 of Frail et al. (2001) (repeated here for clarity);

$$\theta_{\rm j} = 0.057 \left(\frac{t_{\rm j}}{1{\rm day}}\right)^{3/8} \left(\frac{1+z}{2}\right)^{-3/8} \left(\frac{E_{\gamma,iso}}{10^{53}{\rm ergs}}\right)^{-1/8} \left(\frac{\eta}{0.2}\right)^{1/8} \left(\frac{n}{0.1{\rm cm}^{-3}}\right)^{1/8}. \qquad (2.7)$$

Assuming that the efficiency of the fireball in converting the energy of the ejecta into γ-rays is ~ 0.2 and that $t_{\rm j}$ is $58.0^{+9.9}_{-15.4}$ ks a range of values for $\theta_{\rm j}$ can be calculated for different values of circumburst density; $2.2^{\rm o}$ ($n = 1$ cm^{-3}) to $3.8^{\rm o}$ ($n = 100$ cm^{-3}) (Panaitescu & Kumar, 2002). Frail et al. (2001) concluded that opening angles of $\leq 3^o$ were required for less than 10% of the *BeppoSAX* GRB sample. However, such a narrow beaming angle would not be unexpected for a high redshift burst as GRBs with wide jets would be too faint to be detected by current γ-ray missions.

From the jet angle the beaming fraction $f_b = (1 - \cos\theta_{\rm j})$ (Sari et al., 1999) was calculated to be between 7.1×10^{-4} ($n = 1$ cm^{-3}) and 2.3×10^{-3} ($n = 100$ cm^{-3}) and $E_{\gamma,{\rm rest}}$, the true γ-ray energy released, to be in the range of $3.17^{+0.86}_{-1.11} \times 10^{50}$ ($n = 1$ cm^{-3}) to $9.99^{+3.00}_{-3.24} \times 10^{50}$ ergs ($n = 100$ cm^{-3})

[12] A K-correction was applied to convert the flux observed in the observer's reference frame into the extrapolated rest frame energy range cited above, taking into account the GRB's redshift.

for a rest frame energy band of $1 - 10^4$ keV. It should be noted that the typical $E_{\gamma,\rm rest}$ of bursts thus far is 9.8×10^{50} ergs (Bloom et al., 2003) with a burst-to-burst variance about this value of ~ 0.35 dex (or a factor of 2.2), thus this burst agrees well with the typical value provided the circumburst density was of the order 100 cm^{-3}.

It was useful to calculate $E_{\rm peak,rest}$ from these values of $E_{\gamma,\rm rest}$ via the Ghirlanda relation (equation 3 of Ghirlanda et al., 2004, repeated in equation 2.8 below) and compare these values to the observed lower limit of $E_{\rm peak,obs} > 52$ keV ($E_{\rm peak,rest} > 274$ keV).

$$E_{\rm peak,rest} = 267.0 \left(\frac{E_{\gamma,\rm rest}}{4.3 \times 10^{50} \rm ergs} \right)^{0.706 \pm 0.047} \quad \rm keV. \tag{2.8}$$

The Ghirlanda relation gave $E_{\rm peak,rest}$ = 215^{+39}_{-51} keV (for $n = 1$ cm^{-3}) and 484^{+130}_{-125} keV (for $n = 100$ cm^{-3}), which agrees with the lower observed limit if the circumburst density was high.

Recently Butler et al. (2007) have applied a Bayesian approach to the spectral fitting of BAT data, using the a priori knowledge of *CGRO* -BATSE burst spectra to constrain the likely range of spectral parameters over the limited BAT energy range. This allowed Butler et al. (2007) to constrain peak energies even if they fell above the measured BAT energy range. GRB 050505 yielded an $E_{\rm peak,obs} = 140^{+343}_{-43}$ keV ($E_{\rm peak,rest} = 738^{+1810}_{-227}$ keV), which is consistent with the observed lower limit and the value given by the Ghirlanda relation, even for relatively low values of the circumburst density.

$E_{\rm peak,rest}$ was calculated via the Amati correlation (Amati et al., 2002; Lloyd-Ronning & Ramirez-Ruiz, 2002), where $E_{\rm peak} \propto E_{\rm iso}^{\sim 0.6}$. Ghirlanda et al. (2005) fitted this relation to a selection of bursts with spectroscopically confirmed redshifts (27 GRBs), as well as a much larger selection (442 GRBs) with pseudo-redshifts calculated from a lag-luminosity correlation (Band et al., 2004), giving the following equations:

$$E_{\rm peak,rest} = (3.2 \pm 0.1) \left(\frac{E_{\rm iso,rest}}{1.1 \times 10^{53} \rm ergs} \right)^{0.56 \pm 0.02} \times 100 \quad \rm keV, \tag{2.9}$$

$$E_{\rm peak,rest} = (4.34 \pm 0.05) \left(\frac{E_{\rm iso,rest}}{7.5 \times 10^{52} \rm ergs} \right)^{0.47 \pm 0.01} \times 100 \quad \rm keV, \tag{2.10}$$

$$E_{\rm peak,rest} = (3.64 \pm 0.04) \left(\frac{E_{\rm iso,rest}}{7.9 \times 10^{52} {\rm ergs}} \right)^{0.51 \pm 0.01} \times 100 \quad {\rm keV}, \tag{2.11}$$

where equations 2.9, 2.10 and 2.11 are equivalent to equations 1 (spectroscopic redshifts only), 6 (pseudo-redshifts only) and 7 (both sets combined) of Ghirlanda et al. (2005). These equations gave $E_{\rm peak,rest} = 699^{+117}_{-136}$, 1000^{+115}_{-151} and 878^{+106}_{-140} keV respectively. All of these values are consistent with the observed limit and the value quoted by Butler et al. (2007).

Butler et al. (2007) calls the Amati and Ghirlanda relations into doubt stating that the quantities $E_{\rm peak}$, $E_{\rm iso}$ and E_γ may only be correlated in the observer's reference frame (or merely narrowly distributed). A correlation in the rest frame of the burst is therefore a result of multiplying these quantities by strong functions of redshift. They assert that the strong correlation of these quantities in the observer's reference frame (and therefore the rest frame) is an artifact of the detector threshold.

Since the publication of my original paper (Hurkett et al., 2006) a very large sample of *Swift* GRBs with well sampled X-ray light curves have been accumulated, but relatively few, $< 10\%$ (Mészáros, 2006), show evidence of a jet break despite their long-term observations (Liang et al., 2008; Burrows & Racusin, 2007; Willingale et al., 2007). Confirmation of corresponding breaks in other wavelengths have been few and are not well constrained. This may be an observational selection effect due to the higher *Swift* average redshift. Breaks therefore occur at later times in the observer's reference frame and thus may not be covered by limited follow-up campaigns at longer wavelengths. Even if late time optical observations are made the higher average redshift means that the optical afterglow is fainter and redder; thus lowering the overall chance of detection.

The lack of confirmed, achromatic jet breaks in the *Swift* era has resulted in an increasing feeling amongst the GRB community that the pre-*Swift* era breaks seen at optical wavelengths may not be jet breaks and that the optical and X-ray afterglows may be generated by different mechanisms. Thus the standard fireball model may need to be reconsidered, possibly by placing more emphasis on structured jets.

2.5 Conclusions

This chapter presents multi-wavelength data for GRB 050505. The earliest X-ray data starts $\sim$47 minutes after the GRB trigger time as the *Swift* satellite was unable to slew to it immediately due to an Earth limb constraint. The X-ray light curve of GRB 050505 (see figures 2.3 and 2.4) was observed between T+0.6 ks and T+ $\sim$ 95 ks in the burst's reference frame; it was adequately fit with either a 'doubly broken' or 'smoothly broken' power law model. The 'smoothly broken' power law model (figure 2.4) favoured a highly smoothed transition between power law segments with a smoothing factor of $0.5-2.0$. Whilst this model provided a good statistical fit ($\chi^2/\nu = 46.9/45$) it was rejected as it was inconsistent with all the afterglow models considered. A 'doubly broken' power law model (figure 2.3) also provided a good fit to the data ($\chi^2/\nu = 38.7/42$) with the following parameters: $\alpha_1 = 0.25^{+0.16}_{-0.17}$, $\alpha_2 = 1.17^{+0.08}_{-0.09}$ and $\alpha_3 = 1.97^{+0.27}_{-0.28}$ with breaks at $t_1 = 1.4^{+0.3}_{-0.3}$ ks and $t_2 = 11.0^{+1.9}_{-2.9}$ ks in the burst's reference frame. There was no observed change in the X-ray spectral properties during *Swift's* observations of GRB 050505. The best fit model parameters for the X-ray spectrum indicates that this burst had a typical photon index of $2.01^{+0.08}_{-0.08}$ and an excess absorption component from the host galaxy of $1.63^{+0.63}_{-0.58} \times 10^{22}$ cm^{-2} ($\chi^2/\nu = 88/96$), using version 008 CALDB files.

The temporal position, amplitude and spectral behaviour of the two breaks in the doubly broken light curve indicate that the first break was due to the end of energy injection into the forward shock (Nousek et al., 2006; Zhang et al., 2006, and references therein) and that the second break was possibly a jet break caused by either a uniform or structured jet. Despite the gap in early time coverage GRB 050505 fits the canonical light curve model proposed by Nousek et al. (2006) despite its high redshift. This indicates that there is no gross change to the canonical light curve over a large range of z.

The identification of the second observed break in GRB 050505's X-ray light curve with a jet break is problematic in the Swift era as $< 10\%$ of well sampled, long-term GRB light curves show evidence for a jet break (Mészáros, 2006). There is no confirmation of the expected achromatic nature of this break due to a lack of observations in additional bands at the time. However, the calculated rest frame burst properties are in good agreement with pre-*Swift* era GRBs with proposed jet breaks, provided that the circumburst density was of the order 100 cm^{-3}; the values were consistent with the Ghirlanda (Ghirlanda et al., 2004, 2005) and Amati (Amati et al., 2002; Lloyd-Ronning & Ramirez-Ruiz, 2002) relations. Furthermore the calculations suggest that GRB 050505 has a narrow beaming angle ($\sim$

$2^o - 4^o$); however, this degree of beaming is expected for GRBs at high redshift since GRBs with wider jets could potentially be too faint to be detected by any of the current γ-ray missions. All of the evidence points to this break originating from the classical jet model. However, the question of whether such late times breaks are truly jet breaks will only be resolved if either late time optical observations confirm (or rule out) their achromatic nature or a satisfactory modification to the standard fireball model can be proposed.

The optical – X-ray spectrum indicated that a cooling break was located between the optical and X-ray bands, as seen in many other GRB afterglows. A modest amount of intrinsic UV/optical extinction was required in addition, which for an SMC-like extinction law would result in $E(B-V) = 0.10$. A Galactic extinction law fits equally well, but the 0.06 Solar metallicity inferred from the optical spectrum (Berger et al., 2006) shows it to be more SMC-like. Interestingly, the $N_{\rm H}$ column density inferred from the X-ray spectrum with the metallicity set to $0.06 Z_{\odot}$ was higher than that directly measured from the HI column by Berger et al. (2006). It is unlikely that this difference was caused by an evolution of the dust and gas properties since the timescales of the two sets of observations were similar. Nor could it be explained by an excess absorption component in our own galaxy above that measured by Dickey & Lockman (1990). The origin of the difference in absorption columns measured in the two spectral energy bands is currently unresolved and could potentially provide an insight into the evolution of GRB environments when compared to other high redshift bursts.

Chapter 3

Line Searches in *Swift* X-ray Spectra: Methods[1]

Prior to the launch of the Swift *mission several X-ray line detections were reported in Gamma Ray Burst afterglow spectra. To date, these pre-*Swift *era results have not been conclusively confirmed. The most contentious issue in this area is the choice of statistical method used to evaluate the significance of these features. In this chapter I compare three different methods already extant in the literature for assessing the significance of possible line features and discuss their relative advantages and disadvantages. For each of the methods the detection limits have been determined for emission line strengths in burst with spectral parameters typical of the Swift era sample.*

3.1 Introduction

It is widely accepted that the spectra of the X-ray afterglow of Gamma-Ray Bursts (GRBs) are dominated by non-thermal emission, the leading candidate for which is synchrotron emission (Piran 2005 and references therein), though alternate emission processes have also been suggested such as self-Compton (Waxman 1997 and Ghisellini & Celotti 1999) or inverse Compton scattering of external light (Brainerd et al. 1994; Shemi 1994; Shaviv & Dar 1995; Lazzati et al. 2004).

[1] Adapted from "Line Searches in *Swift* X-ray Spectra", Hurkett et al. (2008).

Up to the present time the X-ray spectra of *Swift* afterglows are generally well described by an absorbed power law (for counter-examples see Butler 2007), typically absorbed by material with a column density in excess of the well measured Galactic values (Campana et al., 2006c). Table 2 of Campana et al. (2006c) shows that, of the 17 bursts analyzed, 14 have observed $N_{\rm H}$ values greater than the measured Galactic column density, whilst the remaining three have observed $N_{\rm H}$ values that are consistent, within limits, with the measured values.

In the past it has been proposed that there are other spectral features, with varying levels of significance, in addition to the basic absorbed power law spectrum (Piro et al. 1999; Yoshida et al. 1999; Amati et al. 2000 Antonelli et al. 2000; Piro et al. 2000; Reeves et al. 2002; Watson et al. 2002; Watson et al. 2003 and Frontera et al. 2004). Most are attributed to Fe K_α emission lines or the radiative recombination continuum of the same element. Some have been attributed to the K_α lines of Ni, Co or of lighter elements such as Si, S, Ar and Ca. In two cases there were reports of a transient absorption feature also corresponding to Fe K_α (Amati et al. 2000; Frontera et al. 2004).

The models for the production of such emission features are divided into transmission and reflection models, though the large equivalent widths ($\sim$ few keV) inferred from the observed X-ray features favour models in which the line is produced by reflection (Rees & Mészáros 2000; Ballantyne & Ramirez-Ruiz 2001 and Vietri et al. 2001). Proposed models have to overcome two constraints; the *size problem* and the *kinematic problem*. Observing a line at a time t_{obs} after the burst implies that the emitting material must be within a distance of $\sim ct_{obs}/(1+z)$ from the central engine, thus implying that the region must be compact if a line, or lines, are observed at early times (the *size problem*). Additionally the emitting region must contain $\sim 0.1 M_\odot$ of Fe (in the case of Fe K_α features) whilst still being optically thin to electron scattering, in order that Comptonization does not broaden the line beyond the observed widths (Vietri et al., 2001). If the line width is interpreted as being due to the velocity of the supernova remnant, the observed limit on this width implies an age limit on the remnant of $\sim 10-20$ days. However, at this time, Co nuclei outnumber both Ni and Fe nuclei; thus the emission line would be due to Co at an energy of $7.5/(1+z)$ keV, which is the *kinematic problem*.

Various geometries have been suggested for the reflection models, which rely on either a precursor or simultaneous supernova (SN) event. If a SN occurs several tens of days before the GRB this solves both the size and kinematic problems. In these cases the radiation from the GRB jets can either illuminate the inner face of the SN shell remnant (figure 3.1(a)) or the inner faces of wide funnels that they ex-

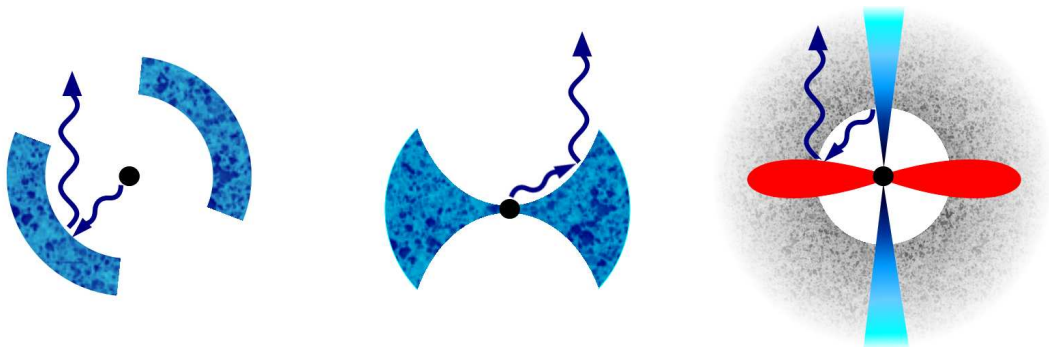

(a) (b) (c)

Figure 3.1: Schematic diagrams of the three models discussed in this chapter, adapted from figure 2 of Vietri et al. (2001). Radiation from the GRB illuminates the inner face of (a) a SN remnant or, (b) funnels excavated through a young remnant. (c) Matter ejected simultaneously with the burst forms an accretion torus; this material is illuminated by phase 0 and afterglow photons scattered by the preburst stellar wind.

---

cavate through young plerionic remnants (figure 3.1(b)). However, these models have been questioned following the simultaneous GRB-SN association indicated by GRB 980425 (Galama et al., 1998) and then confirmed by GRB 030329 (Hjorth et al. 2003; Stanek et al. 2003) and GRB 060218 (Campana et al. 2006b; Pian et al. 2006). In this case the most likely scenario for emission line production occurs if the material ejected during the GRB event collapses to form an equatorial accretion disk. The halo of material surrounding massive stars, ejected by their strong stellar winds towards the end of their main sequence lifetime, scatters a fraction of the photons from the phase 0 emission and afterglow back onto the accretion torus, which then produces X-ray line emission, see figure 3.1(c) (Vietri et al., 2001).

Verifying the presence of such spectral features is of critical importance as they will allow us to probe the circumburst environment of the GRB as well as gaining an indirect indication of the possible structure and behavior of the central engine.

The statistical significance of the 1999-2003 reported features is low (usually $2-3\sigma$), only two detections have a significance $>4\sigma$ (GRB 991216: 4.7σ, Piro et al. 2000; and GRB 030227: 4.4σ, Watson et al. 2003). Though later detections were made with much more sensitive instruments than the early ones, all detections have remained at this low significance level, as a result they remain the subject of

much debate. Arguably the most controversial issue in the discussion of line detections is the choice of statistical method employed to gauge their significance. At least four methods have been proposed and used in the GRB literature:

1. The likelihood ratio test (LRT) and related F-test.
2. Bayes factors.
3. Bayesian posterior predictive probability.
4. Monte Carlo test for peaks in data after 'matched filter' smoothing.

Examples of the application of these methods to GRB X-ray spectra can be found in: Freeman et al. (1999), Yoshida et al. (1999), Piro et al. (1999), Protassov et al. (2002), Rutledge & Sako (2003), Tavecchio et al. (2004), Butler et al. (2005b), Sako et al. (2005), Butler (2007) and references therein.

In all the applications cited above, an underlying continuum was assumed, usually in the form of an absorbed power law (e.g. using the Wisconsin absorption model, see Morrison & McCammon 1983). The detection of a line then amounts to a comparison of two models: M_0, the simple "continuum" model, and M_1, the more complex "continuum + line" model. The strength, location and width of the emission line may be restricted or allowed to be free parameters.

As discussed in depth by Protassov et al. (2002) and Freeman et al. (1999), there are strong theoretical reasons why the LRT is not suitable for assessing the significance of emissions lines, despite its popularity in the literature. When employing the LRT or F-test to choose between two models it is assumed that the simpler, or more parsimonious, model is correct; the tests look for evidence that this assumption is faulty. Such evidence is calibrated via the *reference distribution* (the known distribution of the test statistic under the simple model). If the observed test statistic is extreme according to the reference distribution (e.g. $\chi^2_1 > 10.83$, equivalent to $p < 0.001$), the simple model is rejected in favour of the more complex model (Protassov et al., 2002, and references therein).

However, a test statistic *without* a known reference distribution is problematic as it cannot be used to calculate a false positive rate nor calibrate an observed value. This issue arises when the LRT or F-test is used to ascertain the presence of a spectral emission line; the reference distributions become

unpredictable. This problem is fundamental, i.e. intrinsic to the definition of these tests, and is not due to small sample size, poor signal-to-noise ratio (SNR) or low counts per bin.

Protassov et al. (2002) state that there are two important conditions that must be satisfied for either LRTs or F-tests to be used;

1. The two models being compared must be nested.
2. The null values of additional parameters cannot be on the boundary of the set of possible parameter values.

The second condition is violated when any additional spectral component, such as an emission line, is evaluated since the flux of that component has to be set to zero in the initial case, to ensure that the models are nested, and this is on the boundary of the possible parameter values.

This chapter will present the theory behind the remaining three methods (§ 3.2) and compare their relative merits in terms of their computational efficiency, robustness and sensitivity limits by applying all three methods to X-ray spectra from PKS 0745-19 (§ 3.3) and to simulated libraries of model GRB spectra (§ 3.4). The following chapter will present the results from the application of all of the methods on archival *Swift* data. This is a particularly rich archive because of the combination of the rapid slew response of the *Swift* GRB mission and the powerful X-Ray Telescope (XRT).

3.2 Analysis methods

As noted in § 3.1 several different methods have been used in the past to assess the significance of line detections in the X-ray spectra of GRBs. The F-test / LRT has effectively been ruled out as a reliable method; the remaining three methods are discussed individually in the following subsections and the application of these methods to observed and simulated data is discussed in the following sections (§ 3.3 and 3.4).

3.2.1 Bayes factors

The goal of scientific inference is to draw conclusions about the plausibility of some hypothesis or model, M, based on the available data $\mathbf{D} = \{x_1, x_2, \ldots, x_N\}$, given the background information I (such as the detector calibration, statistical distribution of the data, etc.). However, when presented with data it is usually not possible to compute this directly. What can be calculated directly in many cases is the sampling distribution for data assuming the model to be true, $p(\mathbf{D}|M, I)$. This is usually called the *likelihood* when considered as a function of M for fixed $\mathbf{D}$. Statements about data conditional on the model may be related to statements about the model conditional on the data by Bayes' Theorem[2]. In its usual form Bayes theorem relates the likelihood to the *posterior probability* of the model M conditional on data $\mathbf{D}$ (and any relevant background information I), written $p(M|\mathbf{D}, I)$:

$$p(M|\mathbf{D}, I) = \frac{p(\mathbf{D}|M, I)p(M|I)}{p(\mathbf{D}|I)}. \tag{3.1}$$

The term $p(M|I)$ is the *prior probability* of the model M and describes our knowledge (or ignorance) of the model prior to consideration of the data (often called simply the 'prior'). The term $p(\mathbf{D}|I)$ is effectively a normalization term and is known as the *prior predictive probability* (it describes the probability with which one would predict the data given only prior information about the model). For a more general discussion of Bayes theorem see Lee (1989), Loredo (1990), Loredo (1992), Gelman et al. (1995), Sivia (1996), Gregory (2005) and for discussion in the context of GRB line searches see Freeman et al. (1999, their § 3.1.2) and Protassov et al. (2002). In the rest of this chapter the explicit conditioning on background information I is dropped, but it is taken as accepted that "no probability judgements can be made in a vacuum" (Gelman et al., 1995).

One simple way to represent the posterior probabilities for two alternative models is in terms of their ratio, the *posterior odds* (see Gregory 2005 § 3.5). This eliminates the $p(\mathbf{D})$ term (which has no dependence on M). If we define two competing models, such as one with a line (M_1) and one without (M_0), it is possible to compute the posterior odds:

$$O_{10} = \frac{p(M_1|\mathbf{D})}{p(M_0|\mathbf{D})} = \frac{p(M_1)}{p(M_0)}\frac{p(\mathbf{D}|M_1)}{p(\mathbf{D}|M_0)} = \frac{p(M_1)}{p(M_0)}B_{10}. \tag{3.2}$$

High odds indicate good evidence for the existence of a line in the spectrum. The first term on the right hand side is the ratio of the priors, the second term is the ratio of the likelihoods and is often called the *Bayes factor* (see Kass & Raftery (1995) for a detailed review). In the present context there are no

[2]For general references relating to Bayesian analysis see http://www.astro.cornell.edu/staff/loredo/bayes/

strong theoretical grounds to prefer one or the other model (line or no line) so equal prior probabilities are assigned to each model. Thus the ratio of the priors in equation 3.2 is set to unity and the posterior odds are equal to the Bayes factor. In the following the terms 'posterior odds', 'odds' and 'Bayes factors' are used interchangeably.

The likelihood functions in equation 3.2 are functions of M_i only. If the models contain no free parameters (i.e. are completely specified) then equation 3.2 can be used directly. However, if the model does contain free parameters, the likelihood will be a function of the parameter values. In the present context, where the particular values of the parameters are not the subject of the investigation, the parameters are referred to as *nuisance* parameters. In order to remove the dependence on these nuisance parameters the likelihood function must be written as a function of the N parameters (denoted $\boldsymbol{\theta} = \{\theta_1, \theta_2, \ldots, \theta_N\}$) and integrated, or *marginalized*, over the prior probability density function (PDF) for the parameters:

$$p(\mathbf{D}|M) = \int p(\mathbf{D}, \boldsymbol{\theta}|M) d\boldsymbol{\theta} = \int p(\mathbf{D}|\boldsymbol{\theta}, M) p(\boldsymbol{\theta}|M) d\boldsymbol{\theta}. \tag{3.3}$$

The marginal likelihood is obtained by integrating over all parameter values the joint PDF for the data and the parameters. This joint PDF may be separated into the product of two terms using the rules of probability theory: $p(\mathbf{D}|\boldsymbol{\theta}, M)$ is the likelihood function of the data as a function of the model and its parameters, and $p(\boldsymbol{\theta}|M)$ is the prior for the model parameters. Once these are assigned one can compute the necessary likelihood (a function of M alone) by integration. The Bayes factor for model M_1 (with parameters $\boldsymbol{\theta}_1$) against model M_0 (with parameters $\boldsymbol{\theta}_0$) may now be written:

$$B_{10} = \frac{\int p(\mathbf{D}|\boldsymbol{\theta}_1, M_1) p(\boldsymbol{\theta}_1|M_1) d\boldsymbol{\theta}_1}{\int p(\mathbf{D}|\boldsymbol{\theta}_0, M_0) p(\boldsymbol{\theta}_0|M_0) d\boldsymbol{\theta}_0}. \tag{3.4}$$

The issues of how the relevant likelihoods and priors are assigned, and the integrals computed, are discussed below.

Application to high count X-ray spectra

In the limit of a large number of counts per spectral bin, the Poisson distribution of counts in each bin will converge to the Gaussian distribution, and in this case equation 3.3 can be written in terms of the familiar χ^2 fit statistic (Eadie et al., 1971):

$$L = \ln[p(\mathbf{D}|\boldsymbol{\theta}, M)] = -\frac{1}{2} \sum_{i=1}^{N} \ln[2\pi\sigma_i^2] - \sum_{i=1}^{N} \frac{(x_i - \mu_i(\boldsymbol{\theta}))^2}{2\sigma_i^2} = \text{constant} - \chi^2/2 \tag{3.5}$$

where σ_i is the error on the data (e.g. counts) measured in the ith channel, and $\mu(\boldsymbol{\theta})_i$ is the predicted (e.g. model counts) in the channel based on the model with parameter values $\boldsymbol{\theta}$. The last equality can be made since the term $\sum \ln[2\pi\sigma_i^2]$ is constant given data with errors σ_i. This is why, in the high count limit, finding the parameter values at which χ^2 is minimized is equivalent to finding the Maximum Likelihood Estimates (MLE) of the parameters, $\hat{\boldsymbol{\theta}}$.

Approximating the posterior

In general the integrals of equation 3.3 and 3.4 must be computed numerically, using for example Markov Chain Monte Carlo (MCMC) methods (Gelman et al. 1995 chapter 11; Gregory 2005 chapter 12), which is computationally demanding. However, maximum likelihood theory says that the MLE will become more Gaussian and of smaller variance as the sample size (number of counts) increases, even if the model is non-linear (chapter 11 of Gregory 2005). Therefore, with sufficient counts the likelihood function will approach a multidimensional Gaussian with a peak at the MLE location $\hat{\boldsymbol{\theta}}$, i.e. the location of the best fit (minimum χ^2) in parameter space. Furthermore, if the prior function is relatively flat around the peak of the Gaussian likelihood the prior term in equation 3.3 may be approximated by a constant, namely its value at the best fit location, $p(\hat{\boldsymbol{\theta}}|M)$. Putting this together means that the posterior may be approximated as a Gaussian – often called the *Laplace approximation* – which greatly simplifies the integrations in equations 3.3 and 3.4, since a multidimensional Gaussian may be evaluated analytically, once its peak locations and covariances are known, which avoids the need for computationally expensive numerical integration.

The integral of an unnormalized multidimensional Gaussian is $(2\pi)^{N/2}\sqrt{\det[\boldsymbol{\sigma}^2]}$ times the peak value, where $\boldsymbol{\sigma}^2$ is the covariance matrix[3] evaluated at the peak (best fit location) and N is the number of parameters. Equation 3.3 may now be rewritten as:

$$p(\mathbf{D}|M_i) = \exp(-\chi^2_{(i)}/2)(2\pi)^{N_i/2}\sqrt{\det[\boldsymbol{\sigma}_i^2]}p(\hat{\boldsymbol{\theta}}_i|M_i), \tag{3.6}$$

[3]The covariance matrix is the square, symmetric matrix comprising the covariances of parameters θ_i and θ_j as element σ^2_{ij}. By symmetry $\sigma^2_{ij} = \sigma^2_{ji}$. The diagonal elements are the variances of the parameters. The covariance matrix may be estimated as minus the inverse the Hessian matrix listing all the second derivatives of the log likelihood function $[\nabla\nabla L]_{ij} = \partial^2 L/\partial\theta_i\partial\theta_j$. Given that $L = \log[p(\mathbf{D}|\boldsymbol{\theta}, M)] = \text{constant} - \chi^2/2$ (in the limit of many counts per channel) the covariance matrix may be estimated using $[\sigma^2]_{ij} = 2[(\nabla\nabla\chi^2)^{-1}]_{ij}$. The second derivatives of the $\chi^2(\boldsymbol{\theta})$ function can be evaluated numerically.

which involves the prior density only at the mode of the $p(\hat{\boldsymbol{\theta}}_i|M_i)$ likelihood (i.e. the density at the MLE position) for each model. This can be substituted into equation 3.2 to give the Bayes factor (see Gregory 2005 chapters 10–11):

$$B_{10} = \exp(-\Delta\chi^2/2)(2\pi)^{\Delta N/2} \frac{\sqrt{\det[\boldsymbol{\sigma}_1^2]}}{\sqrt{\det[\boldsymbol{\sigma}_0^2]}} \frac{p(\hat{\boldsymbol{\theta}}_1|M_1)}{p(\hat{\boldsymbol{\theta}}_0|M_0)}, \tag{3.7}$$

where $\Delta N = N_1 - N_0$ and $\Delta\chi^2 = \chi_1^2 - \chi_0^2$. This can be calculated, using the appropriate values of χ^2 and the covariance matrix $\boldsymbol{\sigma}^2$ evaluated at the best fit location for each model, once prior densities are assigned to each parameter. See Gregory (2005), chapters 10–11 for a discussion of essentially the same method.

Validity of the Laplace approximation

There are a number of ways to check the validity of this assumption. One is to inspect the shape of the $\chi^2(\boldsymbol{\theta})$ surface, which is related to the likelihood surface by $L \sim -\chi^2/2$. A Gaussian likelihood is equivalent to a paraboloidal log-likelihood or $\chi^2(\boldsymbol{\theta})$. If the contours of $\Delta\chi^2$ appear paraboloidal around the mimimum, in one and two dimensions, for each parameter or pair of parameters, the likelihood surface must be approximately Gaussian (the conditional and marginal distributions of a Gaussian are also Gaussian, so slices through the χ^2 space should also be paraboloidal). This was generally true for the continuum model for the XRT data.

As a further test of the Gaussian approximation the posterior calculated using the Laplace approximation was compared to the MCMC algorithm discussed in van Dyk et al. (2001). The MCMC method does not use an analytical approximation for the posterior, and therefore is a more general method, but is computationally demanding. Figure 3.2 illustrates the two posterior distributions calculated for the specific case of a spectrum from GRB 060124. The Gaussian data were computed from 10^5 random draws from a multidimensional Gaussian with a covariance matrix evaluated as the minimum χ^2 location using *XSPEC*. The non-Gaussian data were generated from 10^5 draws generated[4] by the MCMC routine of van Dyk et al. (2001). It is clear that the two distributions are not identical but are very similar both in terms of size and shape. In the present context it is important that the "credible regions"

[4]Following van Dyk et al. (2001) five seperate chains were generated, starting from different, 'overdispersed' positions within the parameter space (all outside the 99% confidence region calculated using $\Delta\chi^2$) and the $\hat{R}^{1/2}$ statistic was used to assess their convergence. Data was collected from the chains only after $\hat{R}^{1/2} < 1.01$.

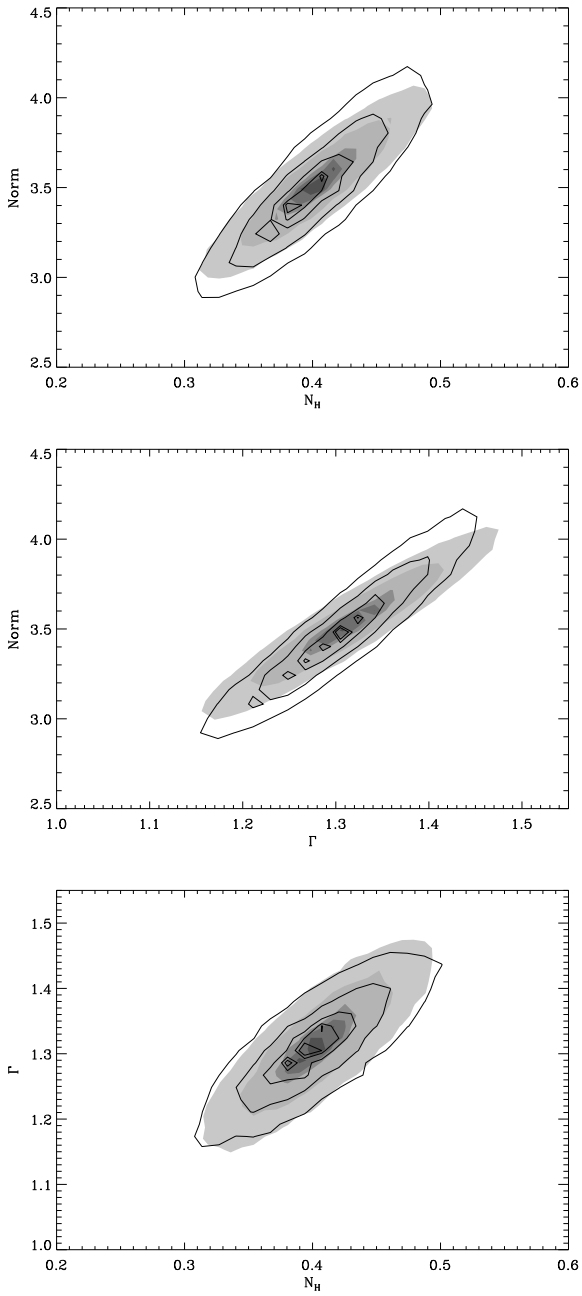

Figure 3.2: Marginal posterior distributions for the continuum parameters of an absorbed power law fit to an XRT spectrum of GRB 060124. The contours enclose 80, 50, 20, 10 and 5% of the distribution (and therefore correspond to 20, 50, 80, 90, 95% credible regions for the parameters). The filled contours were computed assuming the posterior is a Gaussian. The hollow contours were computed using MCMC simulations from the routine of van Dyk et al. (2001). The two distributions are clearly very similar. See § 3.2.1 for details.

occupy similar volumes of parameter space.

The above analyses demonstrate the Gaussian approximation is reasonable for the posterior of the simple "continuum" model M_0, which is the denominator of equation 3.4. The same will be true of the more complex "continuum + line" model M_1 when the line is well detected (see § 11.3 of Gregory 2005). When the line is weakly detected the posterior will be close to the boundary of the parameter space, in which case the Gaussian approximation will not be so accurate. Indeed, when the MLE of the line normalization is close to the boundary the likelihood (and therefore posterior) enclosed in the allowed region of parameter space will be smaller than that given by the Laplace approximation, which assumes the Gaussian function extends to infinity in all directions. This will also happen, for example, when the best-fitting line energy is near the limit of the allowed energy range. In such cases there will be a tendency to overestimate the Bayes factor (i.e. favor M_1). See § 3.4 for further discussion on this point. But when the line is weak there may be multiple peaks in the likelihood (and posterior) which are not accounted for explicitly in the Laplace approximation. Therefore the calculated Bayes factors are only treated as a rough guide to the presence of a spectral line.

Assigning Priors

Bayes factors are sensitive to the choice of prior density. As stated above, using the Laplace approximation the resulting Bayes factors are sensitive to the prior densities only at the MLE parameter values, but care must be exercised in assigning prior density functions in order that these values are reasonable. Fortunately, the prior densities for all parameters that are common to M_0 and M_1 (such as photon index and normalization) are the same for M_0 and M_1, and therefore cancel out in the ratio. There is no cogent information for the other parameters except for their allowed ranges. In such cases the "least informative" prior densities should be used (see e.g. Loredo 1990; Sivia 1996; Gregory 2005 and references therein for further discussion). There are wide ranges of possible line energies and redshifts and so the line energy, $E_{\rm line}$ is only constrained to lie within the useful XRT bandpass, typically $0.3 - 10$ keV. Therefore a uniform prior density $p(E_{\rm line}|M_1) = 1/[E_{\rm max} - E_{\rm min}]$ is assigned over this range. For most spectral fits the line width W was initially held fixed at a value below the instrumental resolution[5], and later allowed as a free parameter. For those models in which the width of the line was a free parameter, the width was assigned a uniform prior over the allowed range (usually $0.0 - 0.7$ keV):

[5] $\sigma = 59$ eV (at 5.895 keV) at launch (A. Beardmore, private communication)

$p(W|M_1) = 1/[W_{\rm max} - W_{\rm min}]$.

In order to test the dependence of the results to the prior densities, two non-informative prior assignments were made for the line strength (normalization), A, following the discussion in Gregory (2005). Firstly, following §4.2 of Sivia (1996) the line strength was assigned a uniform prior between zero and some upper limit $A_{\rm max}$. Previous reports of emission lines have estimated the line flux A to be as little as a few percent (Reeves et al. 2002; Watson et al. 2003) or as much as $\sim 40 - 80\%$ (Yoshida et al. 1999; Piro et al. 2000) of the total flux. $A_{\rm max}$ was conservatively taken to be the total flux of the spectrum over the evaluated bandpass (i.e. the line flux was constrained to be between 0-100% the source flux). However, there are strong arguments (Loredo 1990; Gelman et al. 1995; Gregory 2005) that such as 'scale' parameter should be given a *Jeffreys prior*, $p(A|M_1) \sim 1/A$, which corresponds to a constant density in $\log(A)$. Formally this is an improper prior (cannot be normalized such that its integral is unity), but one can apply reasonable upper and lower bounds in order to form a proper prior density. Following equation 3.38 of Gregory (2005) I used $p(A|M_1) = 1/A \ln[A_{\rm max}/A_{\rm min}]$. In the present context $A_{\rm max}/A_{\rm min} = 800$, since a reasonable lower limit to the X-ray counts from a line is one count, and a reasonable upper limit is 800, the total number of counts in the spectrum. This yields $p(A|M_1) = 1/6.68A$ as a normalised Jeffreys prior. The prior density is therefore higher for weaker lines in the Jeffreys case compared to the uniform case at values (i.e. over $1.25 \times 10^{-3} A_{\rm max} \leq A < 0.15 A_{\rm max}$), and lower for stronger lines.

The ratio of the prior densities at the modes of the two likelihood functions is then simply

$$\begin{aligned} \frac{p(\hat{\boldsymbol{\theta}}_1|M_1)}{p(\hat{\boldsymbol{\theta}}_0|M_0)} &= p(\hat{E}_{\rm line}|M_1) p(\hat{W}|M_1) p(\hat{A}|M_1), \\ &= \frac{1}{([E_{\rm max} - E_{\rm min}][W_{\rm max} - W_{\rm min}] A_P)}, \end{aligned} \tag{3.8}$$

in the ranges $E_{\rm line} \in [E_{\rm min}, E_{\rm max}]$, $W \in [W_{\rm min}, W_{\rm max}]$ and zero elsewhere. Here, $A_P = A_{\rm max}$ in the uniform case or $A_P = 6.68\hat{A}$ in the Jeffreys case. Both uniform and Jeffreys priors were used in the analysis discussed in the next chapter (see § 4.2.11).

3.2.2 Posterior Predictive p-values (ppp)

The use of posterior predictive p-values (*ppp*) was advocated, and demonstrated by application to GRB spectra, by Protassov et al. (2002, see their § 4.1 for a description of their method and §5 for its

application to GRB 970508). Like Bayes factors this method is grounded in Bayesian probability theory.

One uses the posterior density, $p(\boldsymbol{\theta}|\mathbf{D})$, for the model parameters conditional on the data – which defines our state of knowledge about the parameters given the data and the available prior information – to determine the posterior predictive distribution – which is the distribution of possible future data predicted based on the observed data. ('Predictive' because it predicts possible future datasets and 'posterior' because the parameters are drawn from the posterior density of the parameters.) The posterior predictive distribution is:

$$p(\mathbf{D}^{\rm sim}|\mathbf{D}) = \int p(\mathbf{D}^{\rm sim}, \boldsymbol{\theta}|\mathbf{D}) d\boldsymbol{\theta} = \int p(\mathbf{D}^{\rm sim}|\boldsymbol{\theta}) p(\boldsymbol{\theta}|\mathbf{D}) d\boldsymbol{\theta}, \tag{3.9}$$

where $\mathbf{D}^{\rm sim}$ are the possible future datasets (simulations). In practice the posterior density is used to generate a set of random parameter values $\boldsymbol{\theta}_i^{\rm sim}$ ($i = 1, 2, \ldots$) and each of these is used to simulate a random dataset $\mathbf{D}_i^{\rm sim}$. The set of simulated data from all the possible random parameters defines the posterior predictive distribution for simulated data. This in turn can be used to define the posterior predictive distribution for some test statistic $T(\mathbf{D})$ (which is a function of the data):

$$p[T(\mathbf{D}^{\rm sim})|\mathbf{D}] = \int p[T(\mathbf{D}^{\rm sim})|\boldsymbol{\theta}] p[\boldsymbol{\theta}|\mathbf{D}] d\boldsymbol{\theta}, \tag{3.10}$$

(compare with equation 3.9). The posterior predictive p-value (*ppp*) is the fraction of this distribution for which $T(\mathbf{D}^{\rm sim}) > T(\mathbf{D})$, i.e. the area of the tail of the distribution with values of the test statistic more extreme than the value from the observed data.

$$p = \int_{T(\mathbf{D})}^{\infty} p[T(\mathbf{D}^{\rm sim})|\mathbf{D}] d\mathbf{D}^{\rm sim}, \tag{3.11}$$

where the integration is taken over the posterior predictive distribution of $\mathbf{D}^{\rm sim}$. As such the *ppp* value is a Bayesian analogue of the p-value of null hypothesis tests familiar from classical statistics (e.g. the F or χ^2 tests). See chapter 6 of Gelman et al. (1995) or Gelman et al. (1996) for a general discussion of the *ppp* method, and Protassov et al. (2002) for application to GRB data.

Using the posterior predictive distribution from equation 3.9 it is possible to produce a large number of random simulated datasets to be used in a Monte Carlo scheme to calculate the integral of equation 3.11 numerically. The steps for a Monte Carlo method for computing the posterior predictive distribution to calibrate the test statistic T are as follows:

1. Compute the value of the test statistic for the observed data, $T(\mathbf{D})$.

2. Randomly draw N sets of M_0 model parameter values $\boldsymbol{\theta}_i$ for $i = 1, 2, \ldots, N$ according to the appropriate posterior distribution $p(\boldsymbol{\theta}|D)$.

3. For each of $i = 1, 2, \ldots, N$ simulate a dataset $\mathbf{D}_i^{\rm sim}$ using the randomly drawn parameter values $\boldsymbol{\theta}_i$. This accounts for uncertainties in the parameter values.

4. For each of the simulated datasets compute the test statistic $T(\mathbf{D}_i^{\rm sim})$. This is the posterior predictive distribution of the test statistic given the observed data $\mathbf{D}$.

5. Compute the posterior predictive p-value as the fraction of simulated datasets that gave a test statistic more extreme than that for the observed data:

$$p = \frac{1}{N}\sum_{i=1}^{N} \Theta[T(\mathbf{D}_i^{\rm sim}) - T(\mathbf{D})] \tag{3.12}$$

where Θ is the Heaviside step function which simply counts instances where $T(\mathbf{D}_i^{\rm sim}) > T(\mathbf{D})$.

The number of simulations, N, must be large to ensure a good approximation to the integral of equation 3.11 (which is a multiple integral, being itself the integral of the function computed by equation 3.10).

Application to GRB X-ray spectra

As discussed above the posterior density for the parameters may be approximated by using a multidimensional Gaussian centered on the MLE values and with a shape defined by the covariance matrix evaluated at the peak ($\boldsymbol{\sigma}^2$).

For the purposes of this work the change in the χ^2 fit statistic[6] between the two models, M_0 and M_1, was used as the test statistic. This is equivalent to the formulation discussed in Protassov et al. (2002). The observed data were fitted with the model M_0 and the covariance matrix evaluated at the best-fit point used to construct the multivariate Gaussian distribution from which parameter values were

[6] The $\Delta\chi^2$ statistic is familiar to most X-ray astronomers and was used in the Bayes factors method above. It is equivalent to the likelihood ratio test (LRT) statistic, since using equation 3.5 gives $\Delta\chi^2 = \chi^2_{(0)} - \chi^2_{(1)} = -2\ln\lambda$, where $\lambda = p(\mathbf{D}|\hat{\boldsymbol{\theta}}_0, M_0)/p(\mathbf{D}|\hat{\boldsymbol{\theta}}_1, M_1)$ is the ratio of the likelihood maxima of the two models. Under the assumptions for which the LRT is valid this should be distributed as χ^2 with degrees of freedom equal to the number of additional free parameters in model M_1 compared to M_0. The reason for chosing the LRT over related statistics, such as the F-test, is that LRT is more powerful. See Freeman et al. (1999) and Protassov et al. (2002) and references therein for details.

randomly drawn[7]. For each set of model M_0 parameter values a spectrum was simulated with the appropriate response matrix and exposure time, with counts in each channel drawn from a Poisson distribution, and binned in the same manner as the observed data.

In order to calculate the test statistic for each simulation, $T(\mathbf{D}_i^{\rm sim})$ it was necessary to fit each simulated dataset with the two competing models M_0 and M_1, for each one find the best-fitting parameters, and compute $\Delta\chi_i^2$. This necessarily involves a computationally expensive multi-dimensional parameter estimation for each of the N simulations. $N = 10^4$ simulations were used as standard, yielding a p-value accurate to four decimal places at the very highest and lowest p-values (there is an uncertainty on the *ppp* value from the finite number of simulations which is roughly $\sqrt{p(1-p)/N}$ from the binomial distribution). This is acceptable for determining p-values as low as $p \sim 10^{-4}$, i.e. 99.99% 'significance'.

As a further test of the validity of the Gaussian assumption for the posterior (see also § 3.2.1) results were compared with and without this assumption. In particular, the *ppp*-value for a spectrum of GRB 060124 was calculated using Gaussian parameter values and also using values generated by the MCMC method discussed by van Dyk et al. (2001). The two results were reasonably close ($p = 0.050 \pm 0.007$ from the Gaussian simulations and $p = 0.073 \pm 0.008$ from the MCMC, based on 10^3 simulations). This confirms the point made in § 3.2.1, that the Gaussian assumption is reasonable for these data.

Automated fitting of GRB spectra

Given the number of simulated datasets one must resort to an automated model fitting procedure. This has itself been the cause of some debate, with some authors (e.g § 5 of Rutledge & Sako, 2003) claiming that automatic routines do not robustly find the best-fitting parameter values (minimum χ^2). The algorithm used by *XSPEC* for χ^2 minimization is the Levenberg-Marquardt algorithm, which is efficient and very effective when the χ^2 space is well-behaved (e.g. with only one local minimum). However, as this is a 'local' routine there is no guarantee of finding the 'global' minimum in χ^2, and it is possible that the results are biased by the presence of other local minima. For this work several additions were employed to the standard Levenberg-Marquardt minimization algorithm in order to mitigate these problems.

[7] In practice this was performed using the `tclout simpars` command in *XSPEC*

Once a local minimum in χ^2 is found the surrounding region of parameter space is explored for signs of other minima. Each parameter in turn has its value increased and decreased until the χ^2 is increased by at least $\Delta\chi^2 = 2.7$, while simultaneously allowing the other parameters to vary in order to minimize $\Delta\chi^2$. If any non-monotonicity in χ^2 is detected during this search the volume of parameter space explored is increased by increasing the value of $\Delta\chi^2$. If during the course of this search $\Delta\chi^2$ becomes negative (meaning there is a lower minimum nearby) the Levenberg-Marquardt algorithm is re-started from the position of this new minimum. The entire process is repeated by perturbing each parameter in this way until no further improvement can be made by the adjustment of any of them.

The absorbed power law model (M_0) has only three parameters (photon index Γ, normalization and absorption column density), and in all cases finding the χ^2 minimum was straightforward using the above procedure. The alternative model M_1, which includes the emission line, required more care because the presence of a line with unknown energy may cause local χ^2 minima at different energies within the wide bandpass. An initial 'best guess' line energy was computed for each spectrum in the following way. An absorbed power law plus emission line model was constructed using the best-fitting parameters of model M_0 and adding an unresolved emission line fixed at some trial energy E_i and varying the other parameters (including the line normalization) to find the minimum χ^2. One hundred values of the trial energy E_i were used, evenly spread over the entire useful bandpass, and the value that recorded the lowest χ^2 was selected as the 'best guess' for the line energy. The enhanced Levenberg-Marquardt algorithm described above was then used to find the global χ^2 minimum starting from this position.

Simulation tests and comparison with interactive fitting demonstrated the automatic procedure described above was an efficient and very robust procedure for finding the global minimum.

3.2.3 Rutledge and Sako Smoothing (RS)

Rutledge & Sako (2003) proposed an alternative method for line detection using a 'matched filter' to smooth the observed count spectrum with the aim of removing low significance noise and emphasizing any spectral features. The distribution of peak fluxes in the smoothed spectrum is then compared to the result of Monte Carlo simulations to calibrate their significance (p-value).

The counts per PHA channel were extracted from the observed X-ray spectrum and then smoothed

using an energy-dependent kernel (a Gaussian having a FWHM equal to the spectral resolution of the detector; equation 2 of Rutledge & Sako 2003) repeated here for clarity:

$$C(E_i) = \sum_{j[E_i-3\sigma(E_i)]}^{j[E_i+3\sigma(E_i)]} I(j) \frac{1}{\sqrt{2\pi}\sigma(E_i)} \exp\left[-\frac{1}{2}\left(\frac{E_i - E_j}{\sigma(E_i)}\right)^2\right] \delta E_j. \quad (3.13)$$

where $C(E)$ is the smoothed spectrum. $I(j)$ is the observed spectrum, which contains both source and background counts and $j(= 1, 2, ...N)$ is the PHA channel. This equation sums the counts across spectral bins that are within $\pm 3\sigma(E_i)$ of E_i, where $\sigma(E)$ is the $FWHM(E)/2.35$. The distribution of $C(E)$ was then calibrated using Monte Carlo simulations of spectra generated using the method discussed in § 3.2.2 that employs posterior predictive data sets. Each simulation was in turn smoothed using the same energy kernel to produce $C(E)_{sim,i}$. The $C(E)_{sim}$ values were then sorted in descending order for each PHA channel separately. Thus the 99^{th} percentile limit of the $C(E)_{sim,global}$ was then found by extracting the 100^{th} highest value of $C(E)_{sim}$ in each PHA channel.

The smoothed observed spectrum, $C(E)$, was then plotted alongside the n^{th} percentile limits, which were chosen for this analysis to be 90.00, 99.00, 99.90 and 99.99 $\%$. Wherever $C(E)$ exceeds a given limit then a 'feature' has been detected at that confidence limit. Thus a line would show up as a narrow excess whilst other thermal emission components would show up as a broad excess, both of which are easily distinguishable.

It should be noted that Rutledge & Sako 2003 and Sako et al. 2005 did not randomize the parameter values but used fixed MLE values to generate all their simulations. This is equivalent to assuming the posterior to be a delta function located at the best fit point, which is clearly a bad approximation in many cases.

3.2.4 Comparison of the methods

The three methods discussed above have different theoretical motivations, underlying assumptions and require different amounts of computing power. The Bayes factor method is based on a simple application of Bayes theorem combined with the Laplace approximation and assumes uniform priors on the model parameters (or Jeffreys prior for the line normalization). As discussed above, this may not

be the optimal assignment. However, despite its possible drawbacks, the simple priors and Laplace approximation make the calculation extremely simple, requiring only the evaluation of equations 3.7 and 3.8 which require the values of χ^2 and the covariance matrices for the best-fitting line and line-free models, and details of the free parameters and their allowed ranges. As such, it was useful as a 'quick and easy' test. The dependence of choice of priors may be assessed by comparing the results computed using the uniform and Jeffreys prior.

By contrast, the RS and *ppp* methods require a large number of random datasets to be simulated and analyzed, and are therefore considerably more costly in terms of computing time. There is no compelling theoretical reason for applying a matched filter, as in the RS method, although it should be noted that the method, as implemented above, was calibrated using the appropriate posterior predictive distribution. The advantage of the RS method is that no model fitting is required, which is often a time-consuming process and can lead to biased results if not handled properly (§ 3.2.2).

The *ppp* method is grounded in the theory of Bayesian model checking (Gelman et al. 1995; Protassov et al. 2002) but requires time-consuming fits to be performed on each simulated spectrum, and is therefore the most computationally demanding method by a clear margin. However, it is arguably the most rigorous in the sense that it is less sensitive to the choice of priors than are Bayes factors (Gelman et al., 1996; Protassov et al., 2002), and does not apply an ad hoc smoothing, as in the RS method, that may actually act to suppress real spectral features in some cases.

The simulations used for both RS and *ppp* methods were generated assuming a Gaussian posterior for the three parameters of M_0, which, as discussed in § 3.2.1 was a good approximation. Again, this approximation was made to increase computational efficiency, since Gaussian deviates are trivial to generate with standard numerical methods (i.e. the Cholesky method). In situations where the Gaussian approximation is not valid and/or the number of spectra is small enough that considerably more computing time may be spent on each, the *ppp* method or Bayes factors may be computed using results from MCMC simulations (van Dyk et al., 2001; Protassov et al., 2002) which allows for a more accurate evaluation of the posterior density.

Alternative approximate methods

The statistics literature contains many methods developed for the purpose of model selection. In the introduction I listed four methods that have previously been applied to the problem of line detection in X-ray data from GRBs. One method that has not, to my knowledge, been applied specifically to GRB line detection is the Bayesian Information Criterion (BIC; Schwartz (1978)). This aims to approximate the logarithm of the integrated posterior probability for a model with k parameters given data with a sample size N. The BIC takes the form of the logarithm of the likelihood with a penalty term:

$$BIC = -\ln[p(\mathbf{D}|\boldsymbol{\theta}, M)] + (k/2)\ln N \tag{3.14}$$

The model with the smallest BIC is favored. The difference between the BIC values for two competing models (often called the *Schwartz criterion*) is therefore $S = -\ln\lambda + (\Delta k/2)\ln N$ (see footnote 6), and is a rough approximation to the logarithm of the Bayes factor (§ 4.1.3 of Kass & Raftery 1995).

In the high count (large sample size) limit (see equation 3.5) the Schwartz criterion becomes $2S = -\Delta\chi^2 + \Delta k \ln N$. Whether or not the BIC for model M_1 is smaller than that for M_0 is then equivalent to the criterion $\Delta\chi^2 > -\Delta k \ln N$. In the present case the data were selected with fixed N, and $\Delta k = -2$ for the addition of a fixed width line, such that the BIC was equivalent to applying the same $\Delta\chi^2$ criterion to each spectrum, mechanically the same as the LRT, although with a different (generally higher) threshold value. Therefore, in the present context the application of the BIC would be equivalent to a slightly more conservative application of the LRT (see further discussion in § 4.2 and footnote 5). However, as noted in Protassov et al. (2002) and elsewhere, the BIC is often a poor approximation to the integrated posterior probability, and as discussed by Kass & Raftery (1995) is generally a worse approximation than the Laplace approximation employed to calculate Bayes Factors in § 3.2.1.

3.3 Results from an Iron line emitting source

As a first demonstration of the above methods they were applied to a non-GRB *Swift* dataset. Ideally it would be preferrable to examine a source with a GRB-like spectrum, with a similar count rate, but

containing a clearly identified emission line feature. However, it is difficult to find a source that meets all of these criteria. The PC mode calibration dataset (combining all available data from 10/05/2005 to 02/09/2005) of PKS 0745-19 (De Grandi & Molendi (1999) and Chen et al. (2003)) was chosen. This test has some limitations as PKS 0745-19 is fainter than the GRBs analyzed in the following chapter and it is observed in a different mode.

PKS 0745-19 is a galaxy cluster with a thermal spectrum and a known line at 6.07 keV in *Swift's* observations, which is a redshifted 6.7 keV iron line ($z = 0.1$). Even though the underlying spectrum is thermal, with multiple temperature components, it can be modeled by an absorbed power law continuum where the power law index, Γ, is $2.34^{+0.03}_{-0.03}$ ($\chi^2/\nu = 635/511$). An additional `mekal` (Mewe et al., 1985; Arnaud, 1996b) component, with kT = $0.19^{+0.03}_{-0.01}$, slightly improved the fit with $\chi^2/\nu = 610/509$. All spectral parameter errors are quoted at 90% confidence.

Adding a Gaussian component to an absorbed power law fit naturally produced a significantly improved fit to the data ($\chi^2/\nu = 539/508$) with $\Gamma = 2.36^{+0.04}_{-0.03}$ and a line at $6.07^{+0.02}_{-0.02}$ keV (width = $0.06^{+0.02}_{-0.03}$ keV). The spectral fit to this model can be seen in figure 3.3. This was supported by the Bayes factor of 7×10^{14} for a single line being present. RS analysis of the spectrum, figure 3.4, also clearly showed the presence of a Gaussian feature at ~ 6.07 keV with a significance far in excess of the 99.99% confidence limit. The *ppp* analysis placed a significance of $> 99.99\%$ on this feature.

An interesting point to note is that there are shallow 'excesses' at ~ 0.6 keV and ~ 2.3 keV in the RS plot (see the top inset of figure 3.4), which are clearly not line features. Coherent, low level, positive excesses are also seen in the spectral fit at these energies (figure 3.3). Either the power law component was not modeling the data adequately at these points, the energy scale for this spectrum had an offset or the calibration files were less accurate around these two energies. Applying the `gain fit` function in *XSPEC*, to model any discrepancies in the energy scale, improved the fits significantly by adding an offset[8] of -0.07 keV (no change to the slope). The absorbed power law model improved from $\chi^2/\nu = 635/511$ to $606/509$ and the `mekal` component model improved from $\chi^2/\nu = 610/509$ to $585/507$. As a result the two shallow 'excesses' at ~ 0.6 keV and ~ 2.3 keV became far less prominent.

The feature at ~ 0.6 keV could be attributed to the detector oxygen absorption edge at 0.54 keV.

[8] http://swift.gsfc.nasa.gov/docs/heasarc/caldb/swift/docs/xrt/xrt_bias.pdf

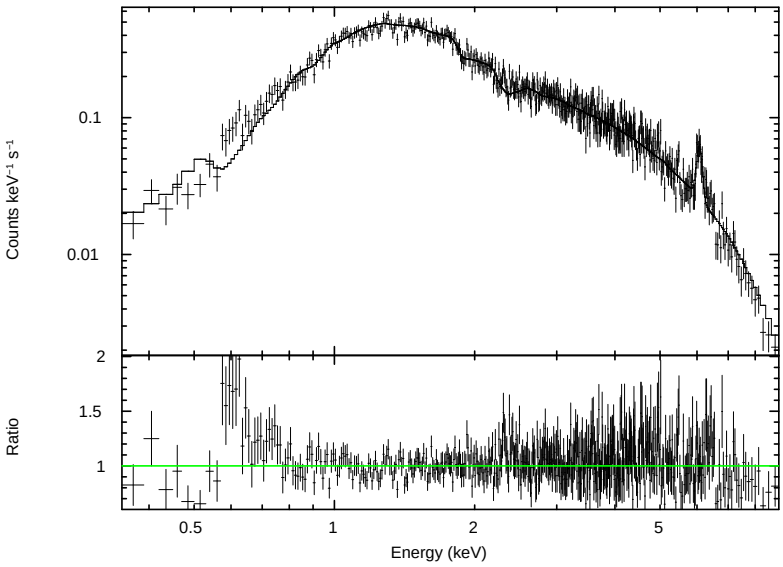

Figure 3.3: Spectral fit to PKS 0745-19 with an absorbed power law plus a narrow Gaussian emission line model. The redshifted Iron line at 6.07 keV is clearly visible. Note also the residuals at 0.6 keV and 2.3 keV, which are thought to be due to the oxygen and gold edges respectively.

Applying the -0.07 keV offset brings the ~ 0.6 keV 'line' in conjunction with this edge, thus reducing its significance below the point at which it would be considered as a real detection. It should be noted that the ~ 2.3 keV feature was coincident in energy with the gold edge due to the XRT mirrors. I have confirmed that this feature was not due to any bad pixel or hot column issues[9].

3.4 Testing the three methods and determining detection limits.

This section discusses the sensitivity limits of the three methods, i.e. the weakest lines that can be reliably detected with each of the three methods, for observations of the type selected for analysis in the next chapter, of a 'typical' *Swift* era burst. This was done by simulating XRT data (using WT mode response files) within *XSPEC* (using version 12.2.1ab or higher) with a continuum spectral model typical of the GRBs observed with *Swift*, but including an emission line, and then applying the three methods described above for line detection. An important value to be considered at this testing stage

[9] http://swift.gsfc.nasa.gov/docs/heasarc/caldb/swift/docs/xrt/SWIFT-XRT-CALDB-01_v5.pdf

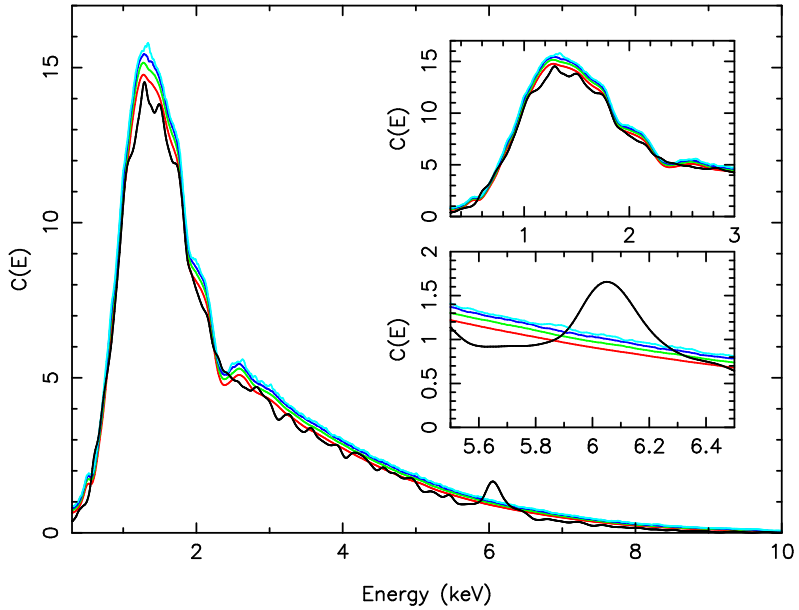

Figure 3.4: PKS 0745-19: RS method. Confidence contours mark the significance of the spectral features. Red $= 90.0\%$, green $= 99.0\%$, dark blue $= 99.90\%$ and light blue $= 99.99\%$. Insets focus on energy ranges of interest.

---

is the range of counts per simulated spectra, which must emulate the selection criteria applied to the observed spectra in the next chapter. Each observed spectrum in the following chapter contains between 800 and 1600 background subtracted counts; this is a compromise between good time resolution and the spectral quality. This range of counts ensures that the binned spectra contain $\sim 40 - 80$ spectral bins, with ~ 20 counts per bin, over the useful bandpass.

In order to generate the simulated data a fiducial spectral model was used comprising a power law with photon index $\Gamma = 2.0$, normalization (at 1 keV) of $N = 0.9$ photons keV^{-1} s^{-1} and an absorption column density of $N_{\rm H} = 1.8 \times 10^{21}$ cm^{-2} (see table 2 of Campana et al. 2006c). These parameters are typical of the X-ray spectra of *Swift* era bursts[10]. In order to measure the sensitivity of the three detection methods to lines in XRT data, spectral data were simulated using the above model plus one

[10]I have assumed a redshift $z = 0$ for the fiducial burst spectrum. The average of the measured redshifts for *Swift* GRBs is higher than this (see http://www.astro.ku.dk/∼pallja/GRBsample.html for the updated values). However, it should be noted that increasing z causes the effects of absorption by the host galaxy absorption (which tends to dominate the total absorption column) to shift out of the observed bandpass, meaning there is relatively more flux at lower energies (< 1 keV). The calculated detection limits should be representative of *Swift* era bursts although perhaps conservative at lower energies.

Gaussian emission line, and subjected to each of the three procedures. A range of values for line energy, normalization and intrinsic width were used in order to calibrate the dependence of the methods to the line parameters:

- Normalisations: $1 \times 10^{-7} \rightarrow 100$ photons cm^{-2} s^{-1} taken in logarithmically increasing steps.
- Line energies: 0.4, 0.6, 0.8, 1.0, 2.0, 3.0, 4.0, 5.0, 7.0 and 9.0 keV.
- Line intrinsic widths: 0.0 keV (i.e. unresolved), 0.2 keV (broad line) and 0.7 keV (broad continuum excess).

The *ppp* and RS method result in p-values with the conventional frequentist interpretation. If the detection threshold is set at α, and a detection is identified as $p \leq \alpha$ then the rate of type I errors (i.e. false positive detections) will be α. For the purpose of sensitivity analysis $\alpha = 0.01$ was used, equivalent to a "99% significance" criterion. In contrast to these, the Bayes factor is the ratio of the marginal likelihoods of models M_1 and M_0; in the case of uniform priors for the two models this is the ratio of posterior probabilities $B_{10} = p(M_1|\mathbf{D})/p(M_0|\mathbf{D})$ where the probabilities are interpreted directly as probabilities for models M_0 and M_1, respectively.

For the purpose of numerical comparison with the p-values, the Bayes factors were converted into probabilities (assuming $p(M_1|\mathbf{D}) + p(M_0|\mathbf{D}) = 1$; see equation 3.19 of Gregory (2005)), and $p(M_0|\mathbf{D}) < 0.01$ was taken as the criterion for detection. This is equivalent to $p(M_1|\mathbf{D}) > 0.99$, and approximately equivalent to a Bayes factor $B_{10} > 100$, which is conventionally taken as strong evidence in favor of M_1 over M_0 (Kass & Raftery, 1995). However, I stress that the interpretation of p-values and Bayes factors are fundamentally different. A p-value is the tail area of the probability density function of the test statistic, assuming a null hypothesis (M_0) is true, and is used to decide whether or not to reject the hypothesis. As such, a p-value is not the probability for the model M_0, instead it corresponds to the frequency of more extreme test statistics (e.g. $\Delta\chi^2$) given a large number of repeat experiments (assuming the null hypothesis). By contrast, $p(M_0|\mathbf{D})$ is the posterior probability for model M_0 based on data $\mathbf{D}$ and the priors (in the present case an approximation thereof was used), as $p(M_1|\mathbf{D})$ is for M_1, and Bayes factors are used to select between two models based on the ratio of these two. This fundamental difference in the interpretation of Bayes factors means there is no expectation that α is the frequency of type I errors from a large number of repeat observations when using a $p(M_0|\mathbf{D}) < \alpha$ criterion.

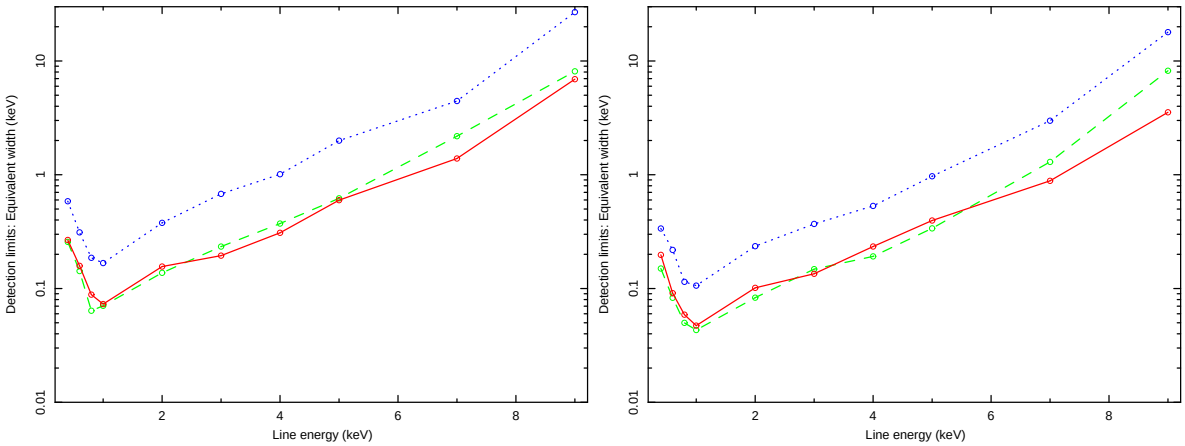

Figure 3.5: *Narrow Gaussian line (width $<$ instrumental resolution) for a spectrum containing 800 counts (left) and 1600 counts (right).* Comparison of the detection limits, in equivalent width (keV), of the three methods over the energy band pass of *Swift*. The data are as follows; dotted blue - Bayes factor analysis, solid red - RS method, and dashed green - posterior predictive p-value analysis.

In § 3.2.1 it was confirmed that using the Laplace approximation assumption in the calculation of the Bayes factor was valid for the fiducial absorbed power law spectral model. The same was also found to be true of the spectra with simulated Gaussian lines at, and above, the detection limit detailed above.

For each value of the line normalization the Bayes factors and $p(M_0|\mathbf{D})$ values were calculated for 50 independent simulations. The $p(M_0|\mathbf{D})$ values at each normalization were averaged and a linear interpolation between points at adjacent normalizations was conducted to map $p(M_0|\mathbf{D})$ as a function of normalization. The limiting sensitivity was taken to be the normalization at which the mean $p(M_0|\mathbf{D})$ value falls below 0.01.

Figure 3.5 shows the detection limits for an intrinsically narrow line ($W = 0$) at different energies for spectra with ~ 800 and ~ 1600 counts (left and right panels, respectively). The limiting sensitivities are shown in units of equivalent width (keV), which is easier to interpret physically, than the absolute normalization, by comparing the normalization to the underlying continuum model. Figures 3.6 and 3.7 show the detection limits for different line widths ($W = 0.2$ and 0.7 keV, respectively). The Bayes factor points in these figures have been calculated using the uniform prior, rather than the Jeffreys prior. See § 4.2.11 for further discussion on the effect of using the two different priors in the calcualtion of the Bayes factors for the observed data sets.

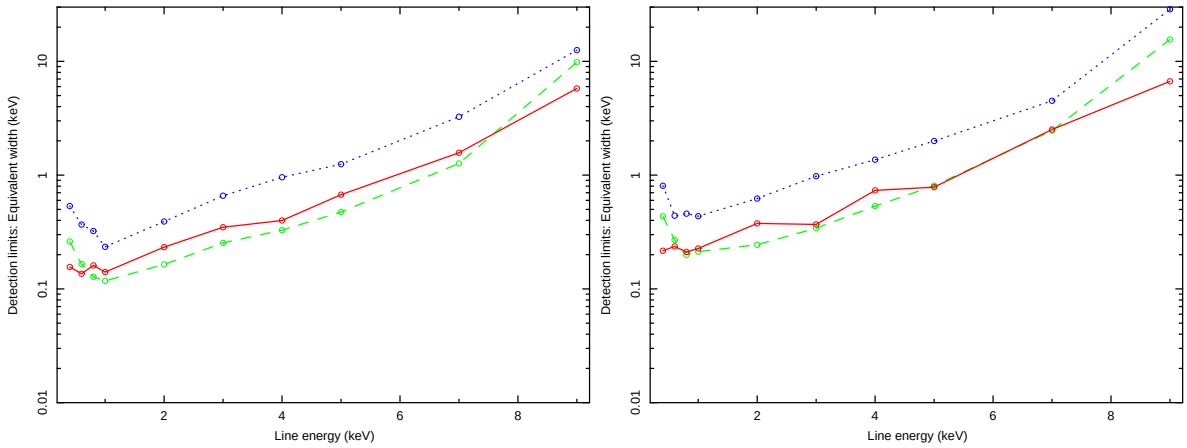

Figure 3.6: *Broad Gaussian line (width = 0.2 keV) for a spectrum containing 800 counts (left) and 1600 counts (right).* Comparison of the detection limits, in equivalent width (keV), of the three methods over the energy band pass of *Swift*. The data are as follows; dotted blue - Bayesian analysis, solid red - RS method, and dashed green - *ppp* .

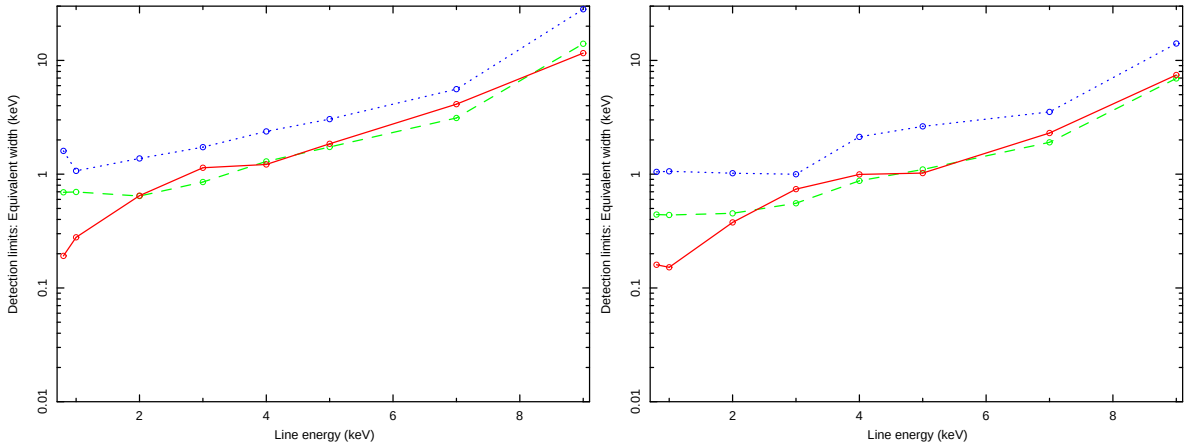

Figure 3.7: *Broad excess (width = 0.7 keV) for a spectrum containing 800 counts (left) and 1600 counts (right).* Comparison of the detection limits, in equivalent width (keV), of the three methods over the energy band pass of *Swift*. The data are as follows; dotted blue - Bayes factor analysis, solid red - RS method, and dashed green - *ppp* . Values below 0.7 keV have been excluded due to the width of the features being analyzed.

The *ppp* and RS methods require a large number of spectral simulations in order to calibrate their distribution and estimate the p-value. The computational demands of this[11] are such that it was not feasible to produce a sufficiently large set of simulations to carry out the methods on each and every line spectrum (e.g. which includes several spectra at each trial value of line energy, width and normalization, for both ~ 800 and ~ 1600 count spectra). Two libraries of 10^4 simulations were therefore constructed, one for ~ 800 and one for ~ 1600 count spectra, that could be used for each test. They were constructed by simulating an appropriate spectrum based on the fiducial model, and using this to generate the posterior predictive distribution from which to draw 10^4 simulations following the recipe discussed in § 3.2.1. These libraries were then used to calibrate the distribution of the $\Delta\chi^2$ statistic for the *ppp* method and thus to calculate the value of $\Delta\chi^2$ that corresponds to a p-value of 0.01. Similarly these libraries were used to compute the 99.00% significance contour from the fiducial model for the RS method. These simulation libraries were used only for the purposes of comparing the different algorithms. For the analysis of real observations (discussed in the next chapter), each observation was assessed using independently generated simulations matching the particular observational parameters.

For the *ppp* method each of the spectra containing a line was fitted with an absorbed power law with and without an additional Gaussian component, and the change in χ^2 noted. The $\Delta\chi^2$ values were averaged at each normalization, and these points linearly interpolated, to map the $\Delta\chi^2$ as a function of normalization. As with the Bayes factor, the limiting sensitivity was taken to be the normalization at which the mean p-value falls below 0.01, calculated using the appropriated value of $\Delta\chi^2$ value from each simulation library. The limiting sensitivity, as a function of energy, is shown as green dotted curves in Figures 3.5, 3.6 and 3.7 for different configurations of line parameters.

For the RS method each line spectrum was smoothed individually. The $C(E)_{sim}$ values over an energy channel range equal to the central energy, E_{line}, $\pm$ line width were extracted. These values were compared to the 99.0% confidence limit over the same energy channel range found from the appropriate simulation library (see figure 3.8). The number of channels within this range where $C(E)_{sim} > C(E)_{99.0}$ was recorded for each simulation. The detection limit was taken to be the lowest line normalization where $N(C(E)_{sim} > C(E)_{99.0}) = 0$.

Analysis of the (line free) library simulations showed the Bayes factors produced $< 1\%$ false positives

[11] To give a specific example, for the simulation and fitting methods described in section 3.2.2 a set of $N = 10^4$ simulations takes ~ 1 day on a top-range PC.

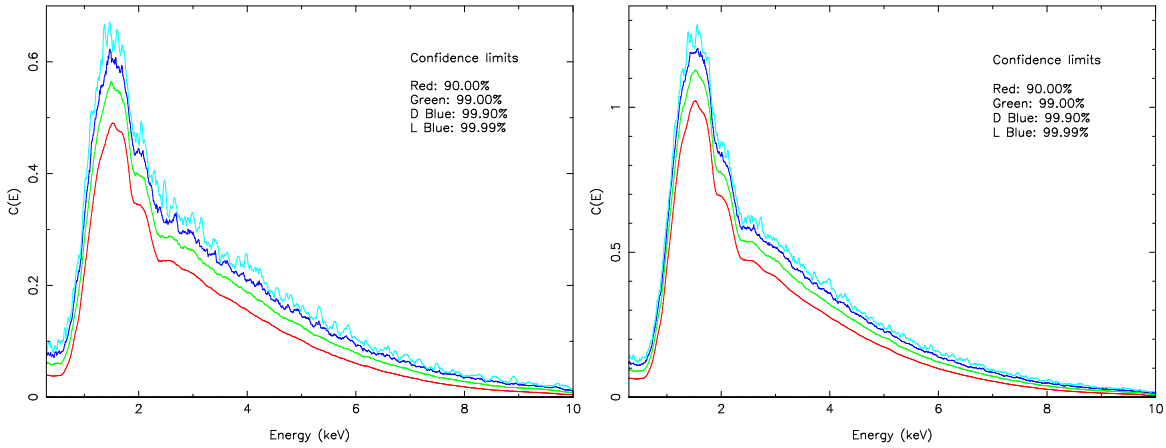

Figure 3.8: Confidence limits across the XRT bandpass for RS simulations libraries of simulations containing 800 counts (left) and 1600 counts (right).

---

when $B_{10} \geq 100$ was used as a detection criterion. This shows the method is, if anything, slightly conservative as expected given the conservative $A_{\max}$ assumption. Conversely, the false negative detection rate is negligible above the detection limit.

The origin of the false positives for the Bayes method is two-fold. Equation 3.7 indicates that the odds can be skewed to erroneously favour the presence of a feature by affecting either the value of $\Delta\chi^2$ or $\sqrt{det[\sigma_1^2]}$. The least significant of the two causes, affecting $\Delta\chi^2$, is due to *XSPEC* producing a model fit with all of the parameters within the *allowed* ranges but outside of the *physical* range of the data. For example a simulated spectrum once binned may only extend from $0.3 - 7.0$ keV, however, *XSPEC* may fit a line at 9.0 keV to compensate for one or two 'noisy' bins at the end of the spectrum. This is still within the allowed range but would normally be rejected due to lack of evidence. Normally such a spurious fit would not improve the χ^2 value of the fit substantially.

The second cause, affecting $\sqrt{det[\sigma_1^2]}$, is more common. If the errors on the line parameters are large then they cover the whole of the allowed parameter space, $P(\theta)$. Thus $P(\theta)$ is predicting the model well, resulting in large odds, even though the parameters themselves are not well constrained (see figures 3.9 and 3.10). The only way to reduce this effect would be to increase the allowed parameter ranges further, so that even poorly constrained parameters covered a relatively smaller fraction of the overall parameter space. However, the parameter values chosen are extremely generous and there is no physical nor theoretical motivation to increase them further. More importantly one, or more, of

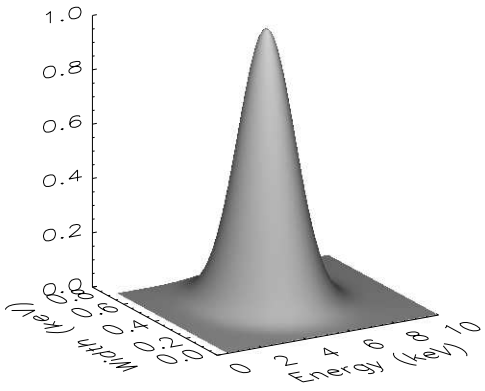

Figure 3.9: A Gaussian function indicating a spread of the emission line errors over parameter space (in this case over emission line energy and width). Even though the parameters are not well constrained in this example they cover a significant fraction of $P(\theta)$, resulting in large odds.

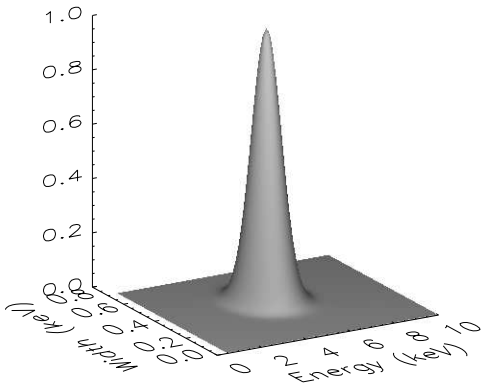

Figure 3.10: A Gaussian function indicating a spread of the emission line errors over parameter space (in this case over emission line energy and width). In this figure the parameters are better constrained than those in figure 3.9, however, as they cover a smaller fraction of $P(\theta)$, they result in smaller odds.

---

the best-fitting parameters may be close to the allowed limits (given by the boundaries of their prior distributions, see figure 3.11). If this is the case the likelihood enclosed in the allowed region of parameter space will be smaller than that given by the Laplace approximation, which assumes that the likelihood is a multivariate Gaussian that extends to infinity in all directions. This means that when no line is present (giving a best fitting normalisation close to zero), or the best-fitting line energy is near the limit of the allowed energy range, there will be a slight tendency to overestimate the odds in favour of a line.

As expected the detection limits are higher for the spectrum with a lower number of counts, by a factor of $\sim$1.5. For the fiducial spectral model used here the optimum energy range for detecting lines is $0.4 - 6$ keV, where the line only requires a contribution of a few $\%$ of the total spectral flux. In the best cases (1600 counts and narrow line) a line with an equivalent width as small as $\sim$ 50 eV may be detected around 1 keV (observed frame) at 99% significance (in a single trial), whereas only very

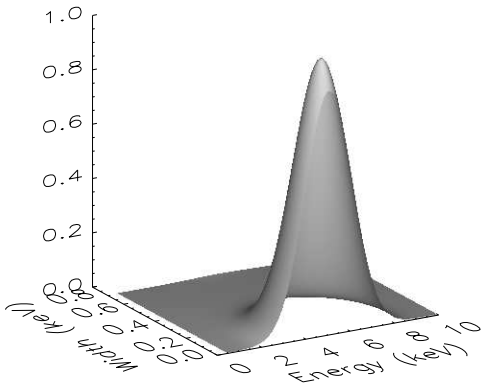

Figure 3.11: A Gaussian function indicating a spread of the emission line errors over parameter space (in this case over emission line energy and width). If one or more of the best-fitting parameters is close to the boundary conditions then the likelihood enclosed in the allowed region of parameter space will be smaller than that given by the Laplace approximation, thus leading to an overestimate of the odds in favour of a line.

---

strong lines may be detected between $6 - 10$ keV. Additional simulations were carried out with a higher absorption column density (1.0×10^{22} cm^{-2}; the mean values stated in Reichart & Price (2002) assuming that long bursts occur in molecular clouds). The dependence of line detection with respect to energy for all three methods were the same at energies >1 keV. However it should be noted that simulating the spectra with much larger absorption columns significantly degraded the ability to detect lines features below 1 keV.

3.5 Conclusions

Analysis of the galaxy cluster PKS 0745-19, which has a known 6.07 keV emission line, produced a convincing detection by all three methods and also uncovered two further features at 0.6 keV and 2.3 keV. Both features are likely to be due to an energy scale offset that causes the instrumental oxygen and gold absorption edges respectively to be poorly fitted (§ 3.3).

A series of simulations over a range of emission line parameters allowed an estimation of the sensitivity to Gaussian-like features, both broad and narrow. For all three methods, using GRB parameters typical for *Swift* bursts, the optimum range for emission line detection was found to be $0.4 - 6$ keV, with line equivalent widths as low as ~ 50 eV detectable in principle from data with only ~ 1600 counts.

Whilst the Bayes factor method for line detection is the fastest and computationally the least expensive of the three methods it is clear from figures 3.5, 3.6 and 3.7 that it is the least sensitive when using the $p > 0.01$ (equivalent to $B_{10} > 100$) detection criterion. Changing the assumed prior ranges (line width, energy and strength) could, in principle, lower the detection limit down to that of the RS and *ppp* methods, however, there is no physical reason to do this. In practice this method could not be used on its own to determine the presence of a Gaussian line but should be used in conjunction with other methods such as *ppp*.

Both the RS and ppp methods yield very similar detection limits in figures 3.5, 3.6 and 3.7. The level of agreement between the two methods is most likely due to the simple Gaussian nature of the additional spectral component. If the additional spectral feature were more complex, i.e. a `mekal` component, the two methods would be less likely to produce such similar detection limits.

The RS method is extremely good at indicating that an additional component is present in the spectrum, however, the interpretation of the additional component can be debatable, especially if the feature is on the limit of detection. For example a series of 'excesses' rising just above a significance line could be evidence for a series of Gaussian features or a `mekal` (etc) component. Like the Bayes factor this method should not be used on its own to determine the presence of additional spectral features for this reason.

Of the three methods tested in this chapter the *ppp* method is by far the most rigorous as it is able to place an accurate detection significance on a known type of spectral component. As such it could be used on its own to determine the presence of an emission line in a spectrum. If a definitive statement is to be made regarding the presence of an emission line feature, or features, in a GRB spectrum this method must be utilised. However, it is computationally prohibitive to use this method to test for additional spectral features for every reasonably sampled GRB spectrum obtained. Therefore, in practice, the total number of spectra selected for use with this method must be reduced by other methods; either by basic spectral fitting, the Bayes factor method, the RS method or a combination of these methods.

Chapter 4

Line Searches in *Swift* X-ray Spectra: Results and Conclusions[1]

The methods described in the previous chapter were applied to the early time (< few ks post trigger in the rest frame of the burst) spectra of 40 bright bursts from the Swift *archive. Based on this thorough analysis no evidence was found for emission lines in WT mode spectra, if the effects of the current calibration status of* Swift *and host galaxy absorption columns were taken into account. The recent line detections reported by* Butler (2007) *are also discussed in the context of the methods and results of the work presented in this chapter; no compelling evidence was found to support these claims. If emission line features are present in the early temporal regime then they must be completely dominated by the underlying afterglow power law component.*

4.1 Data reduction

This chapter reports on the analysis of Windowed Timing (WT) mode data from GRB 050128 to GRB 060510B, covering a total of 153 bursts, 40 of which contained sufficient WT mode data for the analysis methods discussed in the previous chapter. WT mode data was chosen primarily because the time interval covered by these observations, typically T+0 s to T+$\sim$500 s (though for bright bursts this

[1] Adapted from "Line Searches in *Swift* X-ray Spectra", Hurkett et al. (2008).

may extend up to T+few ks) in the rest frame of the burst, is rarely explored. Prior observations of the 1999-2003 bursts typically start at 20+ hours after the trigger in the observer's reference frame, though Antonelli et al. (2000) report on an emission line detection at T+$\sim$ 12 hours; Amati et al. (2000) and Frontera et al. (2004) report absorption line features in very early time data (T+$<$20 s and T+$<$300 s respectively) from the WFC of *BeppoSAX* . There is a greater chance of detecting additional spectral features when the signal-to-noise ratio (SNR) of the spectrum is high i.e. whilst the GRB afterglow is bright; therefore in this analysis only WT mode data is considered. All of the methods discussed can easily be extended to Photon Counting (PC) mode data. I acknowledge that the current theoretical models for line emission indicate that lines could occur at times not covered by WT mode data, however, the same models do not rule out this time period either.

All data have been obtained from the UK *Swift* archive[2] (Tyler et al., 2006) and processed through *xrtpipeline* v0.10.3[3] using version 008 calibration files and correcting for the WT mode gain offset (if present). Version 008 of the CALDB is a marked improvement over the previous release (Campana et al., 2006a)[4], however, it may be the case that low energy calibration features have still not been optimally corrected. No systematic correction factors were applied to the errors of the spectra covered in this work because the recommended factor was very much smaller than the statistical errors in these spectra. Grade $0-2$ data, using extraction regions of 20$\times$3 pixels, for both source and background regions were used. At count rates below 100 counts s^{-1} WT mode data does not suffer from pile-up (Romano et al., 2006a), however, some of the time intervals considered contained sufficient flux to cause pile-up effects (see § 2.2.1). Following Romano et al. (2006a) central regions were excluded when necessary as detailed in their Appendix A (see also table 4.1), splitting the 20$\times$3 pixel region into two 10$\times$3 pixel regions placed either side of the central exclusion region.

All spectral fitting and simulations were carried out using *XSPEC* version 12.2.1ab or higher with background subtracted spectra binned to $\geq$20 counts bin^{-1}. This binning permits the use of χ^2 minimization as a Maximum Likelihood method. Data for each GRB being considered were time-sliced with the following criteria in mind:

1. Each spectrum must contain $800-1600$ background subtracted counts. This was a compromise between good time resolution and spectral quality.

[2]http://www.swift.ac.uk/swift_live/obscatpage.php

[3]Release date 2006-03-16

[4]http://heasarc.gsfc.nasa.gov/docs/heasarc/caldb/swift/docs/xrt/SWIFT-XRT-CALDB-09.pdf

Flux (counts s^{-1})	Pixels to be excluded
$0-100$	0
$100-300$	1
$300-400$	2
$400+$	4

Table 4.1: Incident flux and the corresponding number of pixels to exclude to avoid pile-up in XRT WT mode data (adapted from Romano et al. 2006a).

2. If one or more flares were present in the data, wherever possible (not violating condition 1), separate spectra were extracted for the rising and falling sections of the flare, since spectral evolution is likely to occur at this time (Burrows et al. 2005b, Zhang 2007 and references therein).

3. If data are affected by pile-up then these time periods were extracted separately from the non piled-up data.

The range of $800-1600$ counts was chosen to ensure good time resolution while maintaining sufficient counts to obtain a reasonable spectrum, with $\sim 40-80$ spectral bins (each with ~ 20 counts) over the useful bandpass. The data considered here were taken during the early, bright phases of the afterglow evolution (typically T+0 s to T+500 s), during which the X-ray flux and (possibly) spectrum are often highly variable. Time resolution was therefore important to reduce the effects of flux/spectral variation on the modelling of individual spectra. Furthermore, previous claims of emissions lines have often reported the features as transient phenomena and so time resolution may be important for detecting lines.

4.2 Results from *Swift* archival GRB afterglow data

The sample covered a subset of 40 GRBs, out of the total of 153 from GRB 050128 up to GRB 060510B, which were selected for the quality of their WT mode data. Some bursts only contained sufficient data for a single WT mode spectrum to be analyzed, whilst the majority contained sufficient data to be time-sliced into multiple spectra (see the criteria in § 4.1). In total 332 spectra were analyzed.

A range of energies and time spans were sampled even though the complete redshift distribution of this data set is unknown. The subset of this sample with known z indicates that regions between T+0 s to T+$\sim$500 s (or up to T+few ks if the burst is very bright) post trigger and between ~ 1.0 and ~ 50 keV in the rest frame of the burst are being explored. Throughout this chapter error bars indicate nominal 90% confidence limits on one interesting parameter.

All the data were fitted using automated procedure described in § 3.2.2 and the solutions checked by hand. In practice four models were fitted to each spectrum:

1. absorbed power law,
2. absorbed power law plus an unresolved Gaussian emission line,
3. absorbed power law plus a variable-width Gaussian emission line,
4. absorbed power law plus a blackbody component.

The results presented in this chapter (and in my paper Hurkett et al. 2008) focus on the line models, as the blackbody parameters were found in general to be very poorly constrained. Ideally, all three methods should be applied to all 332 WT spectra to assess the significance of lines (or other) features in the data. But, as discussed in the previous chapter (§ 3.2.4 and 3.4), the RS and especially *ppp* methods are computationally demanding and so it was not practical to apply these methods to every spectrum.

The (approximate) Bayes factor method, being computationally economical, was applied to every spectrum, while the more computationally expensive RS and *ppp* methods were applied only to subsets of the data. In particular, any spectrum that showed a Bayes factor $B_{10} \geq 1$ (in favor of a line), or a $\Delta\chi^2 \geq 4.61$ upon inclusion of a line[5], was considered for more detailed analysis. These were deliberately chosen to be extremely relaxed selection criteria (especially so given the large number of

[5] $\Delta\chi^2 = 4.60517$ is the 90th percentile for the χ^2 distribution with 2 degrees of freedom (Press et al., 1992). As such, it corresponds to a 90% detection 'significance' ($p < 0.10$) in a classical likelihood ratio test (LRT) when including two additional parameters (see footnote 6 in the previous chapter). The LRT should not be used directly for the purposes of detecting an emission line (for reasons discussed in Protassov et al. 2002), but in practice the p-value calculated from the analytical test is usually within an order of magnitude of the value calibrated using the *ppp* method. It is therefore extremely unlikely that a dataset producing $\Delta\chi^2 < 4.61$ would yield a solid detection (e.g. $p < 10^{-3}$) after *ppp* analysis.

independent tests, see below), so as to avoid removing any plausible line candidates and only remove those spectra without any hint of a line, and to counteract the conservative nature of the Bayes factors (§ 3.4). This screening effectively reduced the sample of spectra worth considering in more detail by a factor of ~ 4. I re-iterate that no judgement about the presence/absence of a line in a spectrum was made purely on the basis of the Bayes factor method, which, as discussed in the previous chapter, is an approximation and is sensitive to the choice of priors. Only spectra with a low Bayes factor ($B_{10} < 1$) *and* little improvement in the fit statistic upon including a line ($\Delta\chi^2 < 4.61$) were not considered for further analysis. This subsample was then subjected to the RS method with a low detection threshold ($p < 0.1$, i.e. a 90% single trial significance, again very weak given the multiple trial effect). This further reduced the sample size to a level where the rigorous but computationally expensive *ppp* method could be applied.

As stated above, this screening was only necessary to reduce the sample to a manageable size for *ppp* analysis. Numerical tests showed that the *ppp* method invariably gave a higher p-value (i.e. lower significance) than the RS method, and so no data that might have shown a detection with the rigorous *ppp* method would have been lost by the selection process.

The large number of spectra examined means the effects of multiple trials must be included in the analysis. For example, to reach a global detection significance of only 90.0% given a sample of 332 spectra, would require a single trial significance[6] in excess of 99.97%. Of the 332 spectra from 40 GRBs, 12 spectra from 10 GRBs gave a single trial detection of $\geq 99.9\%$ significance in at least one of the methods. As the best line candidates in the sample, each of these is now considered in turn. (All significances are single trial values, unless otherwise stated and all times are stated as post BAT trigger in the observer's rest frame.)

4.2.1 GRB 050730

The data from this burst were split into 9 spectra, covering several flaring events. A single Gaussian feature was detected in the spectrum extracted from T+692s to T+792s, which was concurrent with a flare in the WT mode data (Starling et al., 2005; Pandey et al., 2006). An absorbed power law plus

[6]Calculated using the standard Bonferroni-type correction factor: $p_1 = 1 - (1 - p_N)^{1/N}$, where p_1 is the single trial p-value that gives p_N as the rate of type I errors in a set of N independent trials. This is sometimes known as the Šidàk equation. In this limit of small p_N and large N this tends to $p_1 = p_N/N$.

a broad Gaussian (width $= 0.34^{+0.08}_{-0.16}$ keV) at $1.14^{+0.48}_{-0.44}$ keV provided the best fit to the data with $\chi^2/\nu = 47/52$ (table 4.2). When the line width was restricted to below the detector resolution a Gaussian feature at $0.73^{+0.02}_{-0.03}$ keV was detected ($\chi^2/\nu = 57/53$).

The Bayes factor was $B_{10} = 300$, favouring a line. The RS method (Appendix 4A, figure 4.6) indicated that a line was present in the spectrum at ~ 0.7 keV with a confidence of 99.90%. This compared favourably to the parameters found in the spectral fit when the Gaussian width was restricted to a value below the instrumental resolution. There was no evidence for the broader feature found when the width of the Gaussian was a free parameter (see inset to figure 4.6, Appendix 4A).

A *ppp* analysis was carried out in both cases. The significance of the unresolved-width and free-width Gaussian features were found to be 88.50% and 99.92% respectively. It is surprising that the *ppp* analysis appears to favour the wider line at $E_{\rm line} = 1.14^{+0.48}_{-0.44}$ keV, as there was no evidence of a feature with this energy in the RS plot. However, it should be noted that the large errors on this line energy are consistent with a feature at $0.73^{+0.02}_{-0.03}$ keV at the limit of their range.

Applying the `gain fit` function to this spectrum, to counter any potential discrepancies in the spectral energy scale (see § 3.3), resulted in an improved fit ($\Delta\chi^2 = 6$) for an unresolved-width line feature at $0.68^{+0.07}_{-0.04}$ keV, with an offset of -55 eV (all other spectral parameters were unchanged within previous limits). Combining this energy offset with the error on the line energy was not sufficient to prove an association with the oxygen absorption edge at 0.54 keV, as discussed for PKS0745-19 (§ 3.3). Applying the `gain fit` function to the free-width Gaussian model was inconclusive, with regards to an association to the oxygen absorption feature, owing to the poorly constrained line energy of < 1.00 keV. (For further discussion on the application of the `gain fit` function to this and other GRBs see § 4.3.)

The redshift for this burst was reported as $z = 3.967$ (Chen et al., 2005; Holman et al., 2005; Prochaska et al., 2005b; Starling et al., 2005). Further fits were conducted with two $N_{\rm H}$ columns originating from the Galactic column (`wabs`[7], fixed at the value given by Dickey & Lockman (1990)) and the host galaxy (`zwabs`[8]). This had the effect of marginally improving the fit for the absorbed power law model ($\chi^2/\nu = 61/55$, $\Delta\chi^2 = 3$) with a Galactic column density fixed at 3.21×10^{20} cm^{-2} and a host galaxy component of $9.80^{+6.80}_{-6.20} \times 10^{21}$ cm^{-2}. All of the other spectral parameters were the same

[7]Wisconsin absorption model, Morrison & McCammon (1983).

[8]Redshifted Wisconsin absorption model, Morrison & McCammon (1983).

as the previous fit within the error limits. The fit to the other models, containing Gaussian components, did not change significantly and the parameter values were the same within the error limits. Bayes factor analysis including the `zwabs` component indicated marginal evidence for the presence of a line ($B_{10} = 5$). Applying the additional `zwabs` component to the RS method (see Appendix 4A, figure 4.7) also decreased the significance of the 0.73 keV feature from 99.90% confidence (dotted line) to 99.0% (solid line). A *ppp* analysis, taking the `zwabs` component into account, found that the significance of the free-width feature had decreased to 99.49% (i.e. $\sim 2.8\sigma$ detection) in this single trial. It was concluded that the line detection (unresolved or free-width) in GRB 050730 was not significant at 3σ and that the redshift-corrected line energy does not correspond to a K-shell transition of a common element.

4.2.2 GRB 060109

This burst had insufficient flux to produce multiple spectra therefore the dataset as a whole was considered. The spectrum covers data from T+109s to T+199s. An absorbed power law plus a narrow Gaussian at $0.74^{+0.03}_{-0.03}$ keV (width restricted to below the detector resolution, $\chi^2/\nu = 40/40$) and a free-width Gaussian at < 0.72 keV (width = $0.23^{+0.12}_{-0.06}$ keV, $\chi^2/\nu = 35/39$) were equally good fits to the data (table 4.2).

The Bayes factor for the unresolved-width Gaussian model indicated the presence of a line ($B_{10} = 200$), however, the same analysis on the free-width Gaussian was much less convincing ($B_{10} = 3$). The RS method indicated that there may be a feature at ~ 0.7 keV with a significance of 99.90% (see Appendix 4A, figure 4.8). However, the *ppp* method gave only 88.99% and 99.28% significance for unresolved (fixed) and free-width Gaussian lines respectively. In § 4.2.1, it was shown that the significance of a similar feature decreased below 3σ when the spectral fit was changed to include an absorption component at the redshift of the host galaxy. This was generally true for those GRBs for which a redshift is known (see § 4.3). Unfortunately, in this case, the redshift is not known and it is not possible to determine whether or not the same is true for this burst.

4.2.3 GRB 060111A

The data from this burst were split into 11 spectra, covering several flaring events that showed significant spectral variation during the observation. The Bayes factor ($B_{10} = 0.05$) gave no evidence for a free-width line (at $0.65^{+0.09}_{-0.06}$ keV, width < 0.13 keV) in the spectrum covering T+174s to T+234s, despite producing a modest improvement in the fit ($\Delta\chi^2 = 8$; table 4.2). The RS results (Appendix 4A, figure 4.9) indicated a feature at ~ 0.65 keV with $\geq 99.90\%$ confidence.

A further feature at $0.79^{+0.02}_{-0.01}$ keV (width < 0.15 keV) was detected in the spectrum covering T+319s to T+339s. The Bayes factor indicated that the presence of a line in this spectrum was unlikely ($B_{10} = 0.1$) but the RS method (Appendix 4A, figure 4.10) strongly suggested an additional spectral feature.

Whilst the ~ 0.65 keV feature for the T+174s to T+234s spectrum and the ~ 0.79 keV feature in the T+319s to T+339s spectrum both look promising from the RS method, the *ppp* analysis showed that they were only 85.13% and 99.56% significant, respectively; not strong detections given the number of trials (see above).

4.2.4 GRB 060115

This burst had insufficient flux to produce multiple spectra; therefore the dataset as a whole was considered. The spectrum covered data from T+121s to T+253s. An absorbed power law plus a Gaussian at $0.81^{+0.07}_{-0.07}$ keV with a width of $0.10^{+0.06}_{-0.05}$ keV provided the best fit to the data with $\chi^2/\nu = 82/77$ (table 4.2). The Bayes factor gave no evidence for a line ($B_{10} = 0.03$), but the RS results (Appendix 4A, figure 4.11) indicated that there was a feature at ~ 0.75 keV at the 99.90% significance level. However, *ppp* analysis gave only 96.16% significance for the same feature.

A redshift of $z = 3.53$ was reported for this GRB by Piranomonte et al. (2006). Further fits were conducted with two $N_{\rm H}$ columns originating from the Galactic column (`wabs`, fixed at the value given by Dickey & Lockman 1990) and the host galaxy (`zwabs`). This led to no change in the statistical fit nor parameter values for an absorbed power law model or models containing Gaussian components. It was concluded that the line detection in GRB 060115 was only moderately significance in a single trial, and not significant (to 3σ) in multiple trials; note that the redshift-corrected line energy does not correspond to a K-shell transition of a common element.

4.2.5 GRB 060124

A precursor ~ 570 s before the main burst peak allowed *Swift's* narrow-field instruments to be positioned on the GRB location ~ 350 s before the burst occurred (Romano et al., 2006a). Therefore the WT mode data covered the phase 0 emission from the burst. The flux detected over the observation was sufficient to produce a time series containing 46 spectra. Bayes factor analysis indicated that 8 of these showed evidence for additional spectral features and a further 9 showed evidence from the raw $\Delta\chi^2$ improvements. However, RS and *ppp* analyses carried out on all of these potential line spectra revealed only one with an acceptable detection (with both methods giving a significance of $> 99.90\%$). This spectrum spanned T+537s to T+542s (i.e. occurring just prior to the main burst peak). The best fit model to this spectrum was an absorbed power law plus a broad (width $= 0.48^{+0.17}_{-0.11}$ keV) Gaussian component at $2.30^{+0.21}_{-0.23}$ keV (table 4.2).

The Bayes factor was $B_{10} = 20$ for a free-width Gaussian feature in this spectrum. RS results (Appendix 4A, figure 4.12) showed a 99.99% significance feature at ~ 2.55 keV. A *ppp* analysis indicated that the feature was significant to 99.97%.

Whilst this appears to be a significant detection it seems to be very broad for a single line feature, requiring a velocity dispersion of the order $0.5c$. Using an absorption redshift of 2.30 (Mirabal & Halpern, 2006a; Cenko et al., 2006; Prochaska et al., 2006b) it was possible to identify this feature with K_α emission of Cobalt (7.5 keV). It could in principle be a series of unresolved line features, a thermal component or indicating a break in the spectrum. Fitting the spectrum with a blackbody component (kT = $0.76^{+0.14}_{-0.11}$ keV) did not provide a good fit ($\chi^2/\nu = 61/45$) nor did an absorbed broken power law model ($\chi^2/\nu = 56/45$).

A further possibility is that it could be due to a poor fit to the gold M-edge as seen in § 3.3. However, applying an energy offset to the data does not significantly improve the absorbed power law model ($\Delta\chi^2/\nu = 73/45$, offset = -0.08 keV, no change to the slope).

4.2.6 GRB 060202

This burst contained sufficient flux to extract 18 spectra. Of these spectra only one, spanning T+429 s to T+529 s, appeared to contain an additional spectral feature. The Bayes factor was $B_{10} = 300$ in

favour of a single free-width line. An absorbed power law plus a broad (width < 0.34 keV) Gaussian feature at $0.94^{+0.05}_{-0.08}$ keV ($\chi^2/\nu = 96/100$) was a slightly better fit than an absorbed power law alone ($\chi^2/\nu = 109/103$; see table 4.2). RS results for the T+429 s to T+529 s data (Appendix 4A, figure 4.13) indicated a broad feature at ~ 0.95 keV, which exceeded the 99.99% confidence interval. A *ppp* analysis of the same data placed a significance of 99.74% on this broad feature.

No redshift value was reported via the GCN for this burst so a well constrained two component absorption fit was not performed during the initial analysis. Since that time a host galaxy redshift of $z = 0.783$ has been published (Butler, 2007). The quality of fit for the absorbed power law alone decreased to $\chi^2/\nu = 113/103$ when setting the Galactic contribution to 5.14×10^{20} cm^{-2} (Dickey & Lockman, 1990) and adding a host $N_{\rm H}$ column contribution ($= 4.71^{+0.42}_{-0.39} \times 10^{21}$ cm^{-2}). All other spectral parameters were consistent with the original values within the error limits. Adding a redshifted absorption component to the free-width Gaussian model produced a slight improvement to the fit ($\Delta\chi^2 = 2$). However, the spectral parameters were less well constrained; photon index $= 1.93^{+0.11}_{-0.11}$, line energy < 1.35 keV, line width > 0.32 keV and a host $N_{\rm H}$ column $= 1.36^{+0.29}_{-0.15} \times 10^{22}$ cm^{-2}.

The Bayes factor in favour of a single free-width line subsequently improved to $B_{10} = 624$, however, this large increase was almost certainly due to the larger limits on the spectral parameters causing the area under the multi-variate Gaussian to be artificially inflated (see § 3.4). RS smoothing of simulations containing the additional absorption column indicated that the potential feature became far less significant, decreasing to 99.00% (see Appendix 4A, figure 4.14). A *ppp* analysis, taking the `zwabs` component into account, found that the significance of the free-width feature had decreased to 94.00%. It was concluded that the line detection in GRB 060202 was not significant to 3σ and was therefore a spurious detection.

4.2.7 GRB 060210

This burst contained sufficient flux to extract a time series containing 8 spectra. Of these spectra only one, spanning T+233s to T+353s, appeared to contain an additional spectral feature. A model containing a Gaussian feature at $0.67^{+0.03}_{-0.04}$ keV (width = $0.06^{+0.05}_{-0.03}$ keV) was a much better fit than an absorbed power law alone ($\Delta\chi^2 = 13$; table 4.2). The Bayes factor was $B_{10} = 1$. The RS results (Appendix 4A, figure 4.15) indicated the presence of a feature at ~ 0.65 keV with a significance of

99.99%. A *ppp* analysis of the spectrum indicated that the same feature was significant to 99.83%.

A redshift of 3.91 was reported by Cucchiara et al. (2006) for this burst. A two component absorption fit was carried out on the data. This produced a significantly improved fit to the absorbed power law (photon index $= 2.50^{+0.12}_{-0.11}$) model with a host $N_{\rm H}$ column contribution of $5.65^{+0.85}_{-0.77} \times 10^{22}$ cm^{-2} and $\chi^2/\nu = 80/72$ ($\Delta\chi^2 = 18$ compared to the fit with free Galactic absorption only). Adding a Gaussian component to this gave a photon index $= 2.46^{+0.12}_{-0.12}$, a host absorption column of $5.71^{+0.94}_{-0.83} \times 10^{22}$ cm^{-2} and $\chi^2/\nu = 76/69$ ($\Delta\chi^2 = 5$ compared to the fit with free Galactic absorption only). The addition of the `zwabs` component did not change the energy of the feature but was only able to place an upper limit of < 0.10 keV on its width. Bayes factor analysis after allowing for a `zwabs` component indicated no evidence for an additional spectral feature ($B_{10} = 5 \times 10^{-4}$). It was concluded that this feature was most likely a false positive detection.

4.2.8 GRB 060218

Campana et al. (2006b) have reported on this GRB in great detail; the following is a summary of their findings. The BAT burst profile for GRB 060218 was unusually long with $T_{90} = 2100 \pm 100$ s and consisted of a single smooth pulse, peaking at 431 ± 60 s. The NFI instruments began observations at T+159 s. The XRT recorded a smooth rise in count rate with a peak at 985 ± 15 s and ~ 100 counts s^{-1}. After the peak the X-ray flux decayed exponentially until ~ 10 ks, when it flattened to a shallow decay with $\alpha \approx 1.2$. The emission detected by the UVOT steadily brightened and peaked in a broad plateau in the UV (188 nm) and optical (439 nm) wavelengths at 31.3 ± 1.8 ks and 39.6 ± 2.5 ks respectively. After decaying to an initial minimum at ~ 200 ks a rebrightening was seen in all bands, which peaked again at $700 - 800$ ks. The spectroscopic signature of a Type Ic SN (SN 2006 aj) was detected (Masetti et al., 2006; Pian et al., 2006) at a redshift of $z = 0.033$ (Mirabal & Halpern, 2006b). Ferrero et al. (2006) modelled the optical light curve of this burst using a template derived from SN 19998 bw; SN 2006 aj was found to evolve much faster than the original template and was $\sim$30% less luminous across all bands.

Spectral analysis of the *Swift* data found that the X-ray spectra were well fit by a cutoff power law[9], which softened over time, plus a blackbody component (kT ≈ 0.17 keV), which was observed up

[9]The E_{peak} of the cutoff power law component was recorded at $= 4.9^{+0.4}_{-0.3}$ keV, placing this burst in the XRF category.

to $\sim$ 10 ks and showed a marginally decreasing temperature profile over this time. Campana et al. (2006b) equate this thermal component with a direct measurement of the shock break out from the stellar envelope. The luminosity of the thermal component increased over time; Campana et al. (2006b) state that this behaviour corresponds to an increase in the apparent emission radius and, furthermore, it implies an expansion speed of the emitting material of $(2.7 \pm 0.8) \times 10^9$ cm s^{-1}. This estimate is consistent with that expected from a Type Ic SN.

The WT mode data considered for this study were split into 53 time intervals, from which the Bayes factor analysis indicated an additional component in the spectrum in all data from $\sim$T+750 s (with $B_{10} > 50$). This was confirmed by RS and *ppp* analysis. The RS results (Appendix 4A, figure 4.16, T+159 s to T+2770 s) indicated that this feature was unlikely to be a Gaussian emission line as its profile was too broad. It was possible that it could be a series of unresolved lines, however, a power law plus blackbody component gave the best fit to all of the spectra suggesting an additional spectral feature. Similarly, individual time-slices (see Appendix 4A, figure 4.17, T+2359 s to T+2409 s for one such example) show the presence of this broad feature.

Analysis of the spectra selected for this work concurs with the spectral properties and trends seen by Campana et al. (2006b). The spectral models containing a blackbody component were fit with absorption from both our Galaxy (`wabs`, $N_{\rm H} = 1.14 \times 10^{21}$ cm^{-2}, Dickey & Lockman 1990) and from the host galaxy (`zwabs`, $N_{\rm H} = 5.00 \times 10^{21}$ cm^{-2}, Campana et al. 2006b). Figures 4.1 and 4.2 illustrate the evolution of the photon index and blackbody kT over time.

4.2.9 GRB 060418

A time series of 12 spectra were extracted from this GRB, two of which appear to contain additional spectral components. These were the spectra spanning T+119 s to T+129 s and T+169 s to T+194 s.

A Gaussian component at $2.42^{+0.02}_{-0.03}$ keV improved the fit to the T+119 s to T+169 s data by $\Delta\chi^2 = 16$ (see table 4.2), even though the Bayes factor was unconvincing ($B_{10} = 0.05$). The RS analysis (Appendix 4A, figure 4.18) showed a feature at this energy that clearly exceeded the 99.99% confidence limit. A *ppp* analysis found 99.85% significance for the same feature. However, as noted previously in the analysis for GRB 060124 and PKS0745-19 (§3.3), a feature at this energy is coincident with the gold M-edge.

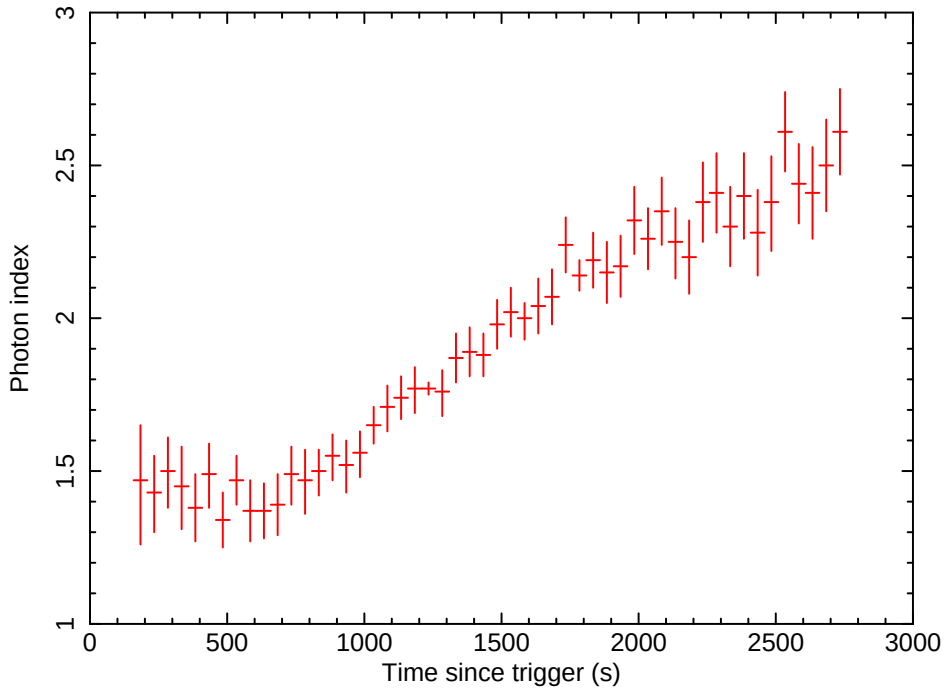

Figure 4.1: GRB 060218: evolution of the photon index with respect to time. The spectrum softens with time, as reported by Campana et al. (2006b).

A similar improvement in the fit was found for the second spectrum (T+169 s to T+194 s), with $\Delta\chi^2 = 10$; the Bayes factor was more promising ($B_{10} = 30$) in this case. An unresolved-width Gaussian at < 0.75 keV provided the best fit to this spectrum with $\chi^2/\nu = 43/49$ (table 4.2). RS (Appendix 4A, figure 4.19) and *ppp* analysis supported the presence of this feature at the 99.99% and 99.98% confidence limit respectively.

The 2.42 keV feature of the T+119 s to T+129 s spectrum can be explained by the gold M-edge but the 0.69 keV feature of the T+169 s to T+194 s spectrum cannot be matched to another elemental absorption edge in the same manner. Two component absorption fits were carried out with a $N_{\rm H}$ column density of 9.17×10^{20} cm^{-2} from our Galaxy and a contribution from the host galaxy at $z = 1.49$ (Dupree et al., 2006; Vreeswijk & Jaunsen, 2006). This produced a significant improvement in the absorbed power law model fit, which gave a photon index $= 2.48^{+0.18}_{-0.13}$ and a host $N_{\rm H} = 0.73^{+0.23}_{-0.20} \times 10^{22}$ cm^{-2} ($\chi^2/\nu = 53/52$, $\Delta\chi^2 = 9$ compared to the fit with free Galactic absorption only). The addition of a `zwabs` component to the Gaussian model gave a photon index $= 2.22^{+0.22}_{-0.15}$, a line with an energy of < 0.65 keV and width of $0.47^{+0.06}_{-0.08}$ keV and a host absorption $< 0.21 \times 10^{22}$ cm^{-2} ($\chi^2/\nu = 46/49$). The

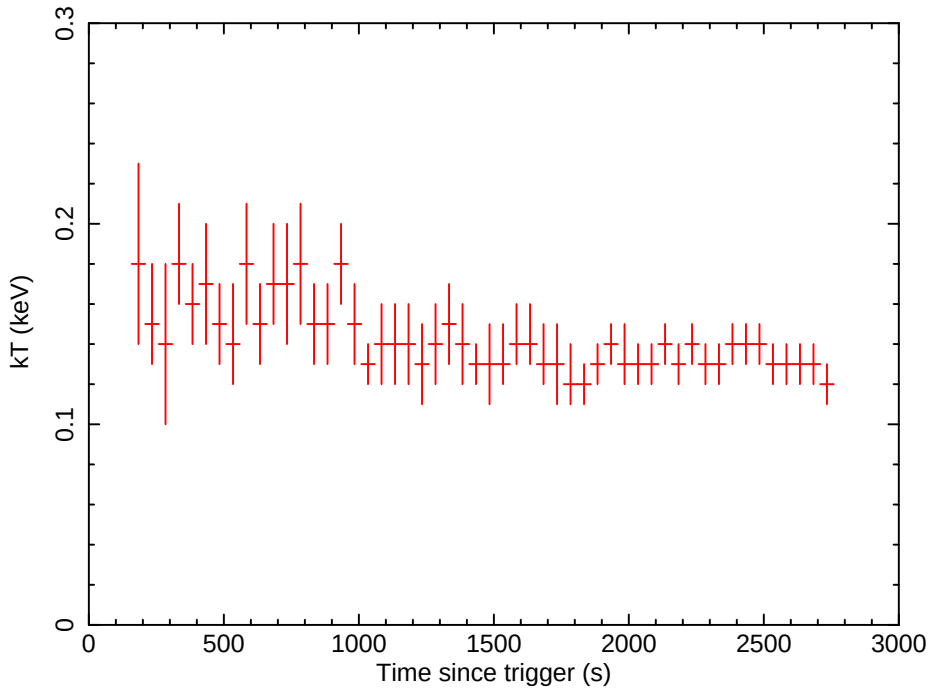

Figure 4.2: GRB 060218: evolution of the blackbody temperature with respect to time. The thermal component shows a slight decrease with time, as reported by Campana et al. (2006b).

Bayes factor for the spectra containing the `zwabs` component indicates that the odds of an additional spectral component have been significantly reduced to $B_{10} = 1$. It was concluded that this feature was most likely not real, but a spurious detection due to the baseline assumption of no host galaxy absorption.

4.2.10 GRB 060428B

Data from this burst were split into two sets, T+212 s to T+252 s and T+252 s to T+418 s. An absorbed power law model was a poor fit to the first spectrum with $\chi^2/\nu = 78/63$ whilst an absorbed power law plus a Gaussian feature at $0.76^{+0.05}_{-0.06}$ keV (width = $0.09^{+0.05}_{-0.03}$ keV) was a much better fit with $\chi^2/\nu = 63/60$. However, the Bayes factor was less encouraging with $B_{10} = 0.1$ against a line feature. The RS analysis (Appendix 4A, figure 4.20) indicated the presence of two possible features; one at ~ 0.75 keV at a significance of 99.99% and another at ~ 0.90 keV at 99.90%. However, no stable spectral fit could be found using an emission line at ~ 0.9 keV, hence it was not possible to calculate a Bayes factor, nor calculate the $\Delta\chi^2$ needed for a *ppp* calculation. A *ppp* analysis of the feature at

$0.76^{+0.05}_{-0.06}$ keV yielded a significance of 99.85%.

The second spectrum, T+252 s to T+418 s, was best fit by an absorbed power law model ($\chi^2/\nu = 58/64$, table 4.2) and the Bayes factor gave only very weak evidence to indicate a line ($B_{10} = 3$). RS analysis (Appendix 4A, figure 4.21) indicated a possible feature at ~ 0.7 keV with a significance of 99.90%, however a *ppp* analysis placed a much lower significance of 95.87% on this.

No redshift value has been reported for this burst, preventing a well constrained two component absorption fit being preformed. This could potentially determine if the features at ~ 0.7 keV are due to poor modeling of the absorption continuum due to a missing absorption component from the host galaxy.

Model[a]	Photon index	Line energy (keV)	Line width (keV)	Line norm. ($\times 10^{-2}$ photons cm^{-2} s^{-1})	Equiv. width (eV)	$N_{\rm H}$ ($\times 10^{20}$ cm^{-2})	χ^2/ν
GRB 050730 (T+692s to T+792s)							
1	$2.03^{+0.14}_{-0.13}$	...	...	...	...	$5.84^{+2.32}_{-2.14}$	64/55
2	$1.98^{+0.15}_{-0.13}$	$0.73^{+0.02}_{-0.03}$	$<$ Inst. res.	$0.95^{+0.58}_{-0.57}$	50	$8.88^{+6.57}_{-4.72}$	57/53
3	$1.78^{+0.18}_{-0.19}$	$1.14^{+0.48}_{-0.44}$	$0.34^{+0.08}_{-0.16}$	$22.5^{+7.5}_{-18.5}$	3400	$7.08^{+3.95}_{-4.03}$	47/52
GRB 060109 (T+109s to T+199s)							
1	$2.29^{+0.18}_{-0.17}$	...	...	...	...	$31.9^{+5.5}_{-5.0}$	48/42
2	$2.29^{+0.20}_{-0.17}$	$0.74^{+0.03}_{-0.03}$	$<$ Inst. res.	$3.11^{+3.08}_{-1.95}$	94	$34.4^{+6.4}_{-5.6}$	40/40
3	$2.20^{+0.18}_{-0.18}$	< 0.72	$0.23^{+0.12}_{-0.06}$	$17.5^{+13.8}_{-7.7}$	560	$39.6^{+9.8}_{-7.6}$	35/39
GRB 060111A (T+174s to T+234s)							
1	$3.05^{+0.22}_{-0.20}$	...	...	...	...	$29.9^{+4.8}_{-4.5}$	52/50
2	$3.09^{+0.23}_{-0.21}$	$0.64^{+0.03}_{-0.03}$	$<$ Inst. res.	$11.6^{+15.2}_{-4.9}$	73	$32.6^{+5.7}_{-5.1}$	44/48
3	$3.07^{+0.09}_{-0.21}$	$0.65^{+0.09}_{-0.06}$	< 0.13	$14.0^{+16.0}_{-10.1}$	94	$33.0^{+7.9}_{-5.8}$	44/47

Continued on Next Page...

Table 4.2 – Continued

Model[a]	Photon index	Line energy (keV)	Line width (keV)	Line norm. ($\times 10^{-2}$ photons cm^{-2} s^{-1})	Equiv. width (eV)	$N_{\rm H}$ ($\times 10^{20}$ cm^{-2})	χ^2/ν
GRB 060111A (T+319s to T+339s)							
1	$1.97^{+0.14}_{-0.14}$	...	...	...	...	$18.8^{+3.9}_{-3.6}$	69/61
2	$1.94^{+0.14}_{-0.14}$	$0.79^{+0.02}_{-0.01}$	$<$ Inst. res.	$9.42^{+4.86}_{-4.18}$	80	$19.5^{+4.1}_{-3.9}$	54/59
3	$1.94^{+0.07}_{-0.09}$	$0.79^{+0.02}_{-0.01}$	< 0.15	$9.42^{+11.9}_{-4.18}$	80	$19.5^{+2.7}_{-2.2}$	54/58
GRB 060115 (T+121s to T+253s)							
1	$1.88^{+0.12}_{-0.11}$	...	...	...	...	$16.6^{+3.3}_{-3.1}$	93/80
2	$1.85^{+0.12}_{-0.12}$	$0.89^{+0.03}_{-0.03}$	$<$ Inst. res.	$0.67^{+0.44}_{-0.42}$	39	$16.3^{+3.1}_{-3.2}$	86/78
3	$1.82^{+0.13}_{-0.11}$	$0.81^{+0.07}_{-0.07}$	$0.10^{+0.06}_{-0.05}$	$2.09^{+2.21}_{-1.22}$	100	$17.0^{+4.3}_{-2.7}$	82/77
GRB 060124 (T+537s to T+542s)							
1	$1.30^{+0.16}_{-0.14}$	...	...	...	...	$29.5^{+6.7}_{-8.0}$	72/47
2	$1.29^{+0.15}_{-0.15}$	$2.49^{+0.06}_{-0.01}$	$<$ Inst. res.	$11.8^{+6.3}_{-6.5}$	800	$27.8^{+9.3}_{-7.8}$	62/45
3	$1.13^{+0.19}_{-0.24}$	$2.30^{+0.21}_{-0.23}$	$0.48^{+0.17}_{-0.11}$	$57.7^{+42.0}_{-25.2}$	150	$18.3^{+9.7}_{-9.9}$	51/44

Continued on Next Page...

Table 4.2 – Continued

Model[a]	Photon index	Line energy (keV)	Line width (keV)	Line norm. ($\times 10^{-2}$ photons cm^{-2} s^{-1})	Equiv. width (eV)	$N_{\rm H}$ ($\times 10^{20}$ cm^{-2})	χ^2/ν
GRB 060202 (T+429s to T+529s)							
1	$2.16^{+0.11}_{-0.10}$	...	...	...	...	$47.1^{+4.3}_{-4.0}$	109/103
2	$2.15^{+0.11}_{-0.11}$	$0.94^{+0.03}_{-0.02}$	$<$ Inst. res.	$2.69^{+1.51}_{-1.30}$	54	$48.1^{+4.8}_{-4.2}$	97/101
3	$2.12^{+0.10}_{-0.12}$	$0.94^{+0.05}_{-0.08}$	< 0.34	$4.94^{+5.01}_{-2.80}$	99	$50.0^{+1.1}_{-5.0}$	96/100
GRB 060210 (T+233s to T+353s)							
1	$2.72^{+0.16}_{-0.15}$	...	...	...	...	$20.6^{+3.1}_{-2.9}$	98/72
2	$2.71^{+0.16}_{-0.15}$	$0.66^{+0.04}_{-0.02}$	$<$ Inst. res.	$4.63^{+3.06}_{-2.40}$	63	$21.5^{+3.5}_{-3.1}$	85/70
3	$2.68^{+0.18}_{-0.16}$	$0.67^{+0.03}_{-0.04}$	$0.06^{+0.05}_{-0.03}$	$7.06^{+5.94}_{-4.54}$	100	$21.6^{+4.0}_{-3.2}$	81/69
GRB 060418 (T+119s to T+129s)							
1	$1.82^{+0.13}_{-0.12}$	...	...	...	...	$24.3^{+5.1}_{-4.6}$	72/59
2	$1.82^{+0.13}_{-0.12}$	$2.42^{+0.02}_{-0.03}$	$<$ Inst. res.	$7.21^{+3.00}_{-2.97}$	190	$23.7^{+5.0}_{-4.6}$	56/57

Continued on Next Page...

Table 4.2 – Continued

Model[a]	Photon index	Line energy (keV)	Line width (keV)	Line norm. ($\times 10^{-2}$ photons cm^{-2} s^{-1})	Equiv. width (eV)	$N_{\rm H}$ ($\times 10^{20}$ cm^{-2})	χ^2/ν
3	$1.82^{+0.13}_{-0.12}$	$2.42^{+0.02}_{-0.04}$	< 0.14	$7.21^{+4.74}_{-2.98}$	190	$23.7^{+4.6}_{-4.5}$	56/56
GRB 060418 (T+169s to T+194s)							
1	$2.70^{+0.22}_{-0.19}$	...	...	...	...	$22.3^{+4.3}_{-3.9}$	62/52
2	$2.67^{+0.07}_{-0.12}$	$0.69^{+0.02}_{-0.02}$	$<$ Inst. res.	$10.8^{+5.6}_{-5.5}$	58	$22.2^{+2.1}_{-2.0}$	52/50
3	$1.82^{+0.22}_{-0.66}$	< 0.75	$0.57^{+0.09}_{-0.20}$	110^{+31}_{-75}	2300	$11.0^{+0.1}_{-0.1}$	43/49
GRB 060428B (T+212s to T+252s)							
1	$3.02^{+0.18}_{-0.16}$	...	...	...	...	$11.6^{+2.6}_{-2.3}$	78/63
2	$2.94^{+0.18}_{-0.16}$	$0.77^{+0.03}_{-0.02}$	$<$ Inst. res.	$3.56^{+1.84}_{-1.87}$	39	$10.6^{+2.6}_{-2.2}$	69/61
3	$2.83^{+0.16}_{-0.16}$	$0.76^{+0.05}_{-0.06}$	$0.09^{+0.05}_{-0.03}$	$8.38^{+4.92}_{-3.69}$	100	$9.21^{+2.37}_{-2.27}$	63/60
GRB 060428B (T+252s to T+418s)							
1	$2.64^{+0.14}_{-0.14}$	...	...	...	...	$2.28^{+1.63}_{-1.50}$	58/64

Continued on Next Page...

Table 4.2 – Continued

Model[a]	Photon index	Line energy (keV)	Line width (keV)	Line norm. ($\times 10^{-2}$ photons cm^{-2} s^{-1})	Equiv. width (eV)	$N_{\rm H}$ ($\times 10^{20}$ cm^{-2})	χ^2/ν
2	$2.58^{+0.15}_{-0.14}$	$0.69^{+0.02}_{-0.03}$	$<$ Inst. res.	$0.62^{+0.37}_{-0.37}$	34	$1.73^{+1.64}_{-1.51}$	50/62
3	$2.33^{+0.14}_{-0.22}$	< 1.07	$0.33^{+0.06}_{-0.17}$	$9.71^{+5.48}_{-8.19}$	2100	$0.39^{+1.93}_{-0.17}$	48/61

Table 4.2: Summary of spectral fits for all candidate spectra. Models[a]: [1] Absorbed power law, [2] absorbed power law plus a narrow Gaussian (width restricted to less than the instrumental resolution) and [3] absorbed power law plus a free-width Gaussian. Models containing blackbody components are not reported in this table as the fits were poorly constrained. All errors are quoted at 90.0% confidence.

4.2.11 Use of alternative prior

In § 3.2.1 two different choices for assigning an uninformative prior to the line normalization were discussed. The approximate Bayes factors given above were calculated assuming a uniform prior for the line normalization, but using the Jeffreys prior did not change the results significantly. For example, GRB 060115 changed from $B_{10} = 0.03$ with the uniform prior to $B_{10} = 0.05$ with the Jeffreys prior. At the other extreme, the favorable Bayes factor of $B_{10} = 300$ for GRB 060202 (T+429 s to T+529 s) using the uniform prior was virtually unchanged. Spectra that were not included for further analysis, due to a low Bayes factor ($B_{10} < 1.0$) and a small χ^2 improvement ($\Delta\chi^2 < 4.61$) were similarly affected by a change in priors. In general the Bayes factors changed very little between uniform and Jeffreys priors, reflecting the fact that typical best-fitting line normalizations were usually $\sim 10\%$ of the total flux (see § 3.2.1).

4.3 Discussion of *Swift* XRT results

The previous section shows that of 332 WT mode spectra analyzed by our methods only 12 produced possible detections at $\geq$ 99.90% (single trial). These detections were tightly clustered around two energies in the observer frame: 0.64-0.94 kev (10/12, figures 4.3 and 4.4) and 2.30-2.49 keV (2/12, figure 4.5), with equivalent widths of $\sim$0.9 keV and $\sim$0.5 keV respectively.

The coincidence of many spectral feature detections close to 0.7 keV is suspicious as intrinsic GRB emission line features would be expected to be located at different *observed* energies, as the GRBs span a large range of redshifts. This clustering strongly hints at an instrumental origin. Modeling the WT mode spectra with an energy offset, in case of imperfect bias subtraction at the processing stage, improved the fit statistics for an absorbed power law model (average $\Delta\chi^2 \sim 5$). However, even if the combined error on the line energy and the offset corrections (1 to 70 eV) are taken, this would still not be enough to provide a plausible association with the oxygen K-edge as seen in the PKS 0745-19 example (§ 3.3).

An additional absorption component, at the host galaxy redshift, was applied to those candidates with a known redshift measurement. In every case the feature at 0.7 keV became insignificant and it is expected that the same reduction in significance would occur if well constrained two absorption com-

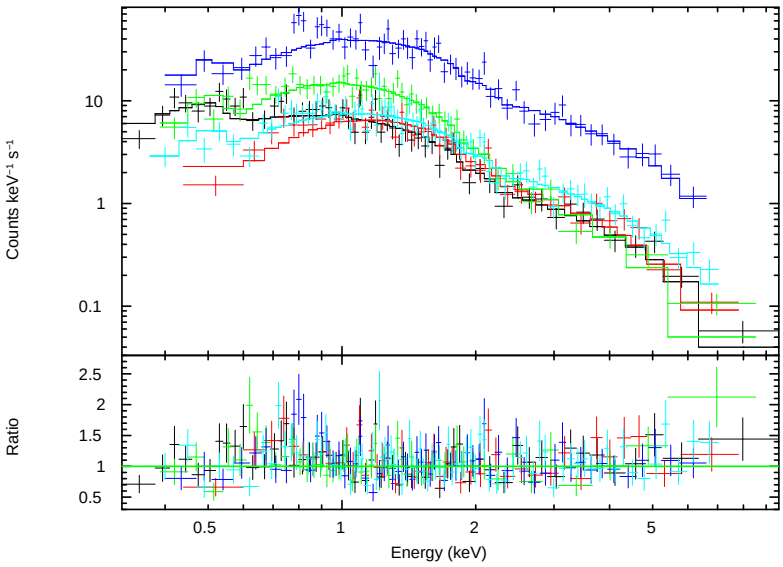

Figure 4.3: Spectra modeled with an absorbed power law model: GRB 050730 (black), GRB 060109 (red), GRB 060111A (T+174 s to T+234 s, green), 060111A (T+319 s to T+339 s, dark blue) and 060105 (light blue). Note the residuals around 0.7 keV.

---

ponent fits were conducted on the GRBs with unknown redshifts. It could be argued that this decrease in line significance stems only from the increased complexity in the model. If this were the case then an overall increase in the level of the RS contours should be seen over the whole energy range. In figure 4.7 it can be seen that the effect of the adding a `zwabs` component is not uniform across the energy range. It has negligible effect at energies >1.2 keV. Below this energy the `zwabs` component acts to increase the total absorption at very low energies (<0.55 keV) and decrease it in the 0.55 keV to 1.2 keV range. Thus the addition of the second absorption component is imposing a real, energy dependant effect on the confidence contours, rather than increasing them uniformly across the whole energy range. I conclude that the absorption was not being modeled accurately at low energies by assuming that all of the $N_{\rm H}$ column was at a redshift of zero.

I have confirmed that the features at 2.3 keV are not due to bad pixel or hot column issues. The two detections have the following single-trial significances: 99.97% (GRB 060124) and 99.85% (GRB 060418). Taken in the context of all the trials performed these significances become 90.09% ($< 1.7\sigma$) and 50.20% ($< 0.7\sigma$) respectively. There was no significant improvement to the model fits if the `gain`

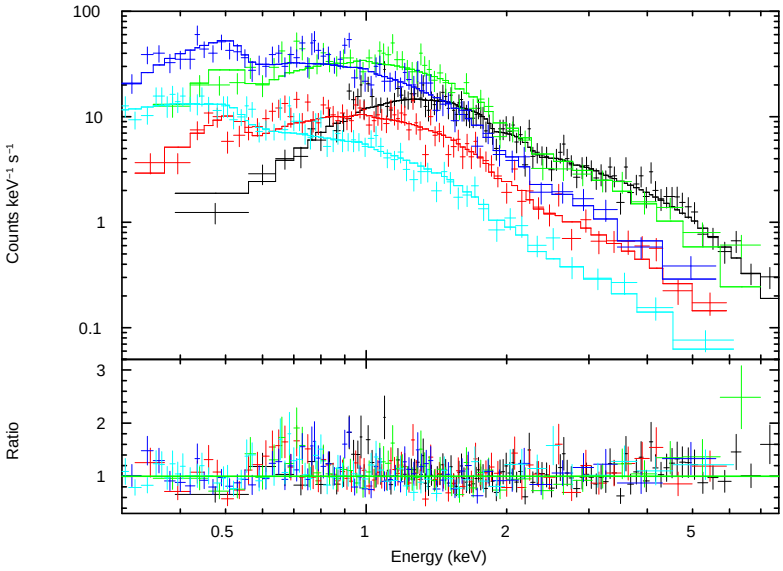

Figure 4.4: Spectra modeled with an absorbed power law model: GRB 060202 (black), GRB 060210 (red), GRB 060418 (T+169 s to T+194 s, green), 060428B (T+212 s to T+252 s, dark blue) and 060428B (T+252 s to T+418 s, light blue). Note the residuals around 0.7 keV.

`fit` function was applied. Adding a blackbody component to the underlying absorbed power law or using an absorbed broken power law does not yield a significantly improved fit either. However, both of these features are coincident with the gold M-edge complex.

Since all of the features are found to be narrowly clustered around two energies in the observer frame, one of which was also found in the PKS 0745-19 example, it is my conclusion that none are real detections of emission lines in GRB spectra, but are instead either due to residual calibration issues, imperfect bias subtraction at the processing stage or incorrect modeling of the host galaxy absorption column (most likely for the 0.7 keV features).

In addition of the order of 3 false positive detections would be expected at 99.00% for 332 spectral analyses.

It is also interesting that the majority of GRBs with potential features occur in the first few months of 2006. There are no physical, instrumental or calibration issues associated with that period of operations that could explain such temporal clustering. However, it should be noted that the actual response of the

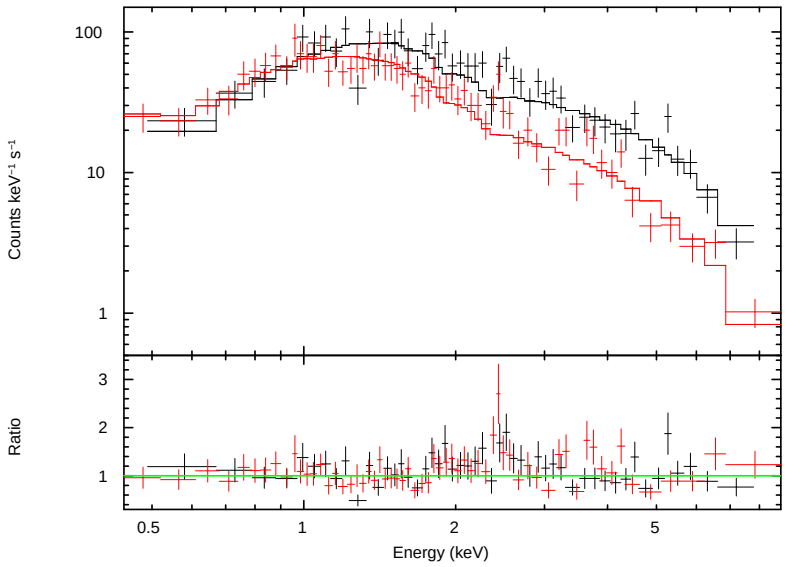

Figure 4.5: Spectra modeled with an absorbed power law model: GRB 060124 (black) and GRB 060210 (T+119 s to T+129 s, red). Note the residuals around 2.3 keV.

XRT CCD is possibly evolving while the response is modeled by the calibration files as being constant.

Butler (2007) has recently published analysis citing the detection of line complexes in GRBs 050714B, 050822, 060202 and 060218. However, the same paper and Butler & Kocevski (2007a) also provided alternate reasons for these apparent lines detections (thermal components or broken power laws). GRB 050714B was not included in our selection of bursts as the WT mode spectrum did not contain sufficient counts to meet our minimum criteria.

No compelling evidence was found from GRB 050822 using any of the analysis methods to suggest that there were any line features in these data, hence it does not feature in §4.2. Butler (2007) quotes a significance of 4.4σ for a complex of 5 lines (0.81, 0.91, 1.04, 1.23 and 1.49 keV) for one spectrum spanning T+489.5 s to T+509.4 s, with equivalent widths of 82, 142, 194, 221 and 265 eV respectively. Note that the features are spaced 100 eV apart, though no obvious physical explanation for this presents itself. It should be noted that Butler's spectra ($\sim$ 500 counts) was contained within our analysis from T+471 s to T+661 s ($\sim$ 860 counts); the spectrum used in my analysis cannot be sub-divided further whilst still being directly comparable to the rest of the data analysis presented in this chapter. None of

Model[a]	Photon index	High energy cutoff (keV)	Line energy (keV)	Line width (keV)	Line norm. ($\times 10^{-2}$ photons cm^{-2} s^{-1})	Equiv. width (eV)	$N_{\rm H}$ ($\times 10^{20}$ cm^{-2})	χ^2/ν
1	$5.20^{+0.52}_{-0.44}$	...	...	...	...	...	$34.0^{+7.7}_{-6.4}$	90/40
2	$2.84^{+0.57}_{-0.18}$	...	< 0.47	$0.40^{+0.04}_{-0.07}$	49^{+10}_{-20}	240	< 12.2	49/37
3	$2.27^{+0.57}_{-0.18}$	$0.51^{+0.01}_{-0.01}$	...	...	...	...	$18.0^{+7.1}_{-4.0}$	70/39
4	$2.25^{+0.12}_{-0.12}$	$0.82^{+0.03}_{-0.03}$	$0.68^{+0.04}_{-0.04}$	$0.20^{+0.05}_{-0.04}$	$8.50^{+1.64}_{-1.64}$	300	$9.51^{+0.86}_{-0.79}$	55/36

Table 4.3: Summary of spectral fits for GRB 0500822 (T+471 s to T+661 s). Models[a]: [1] Absorbed power law, [2] absorbed power law plus a free-width Gaussian, [3] absorbed cutoff power law, [4] absorbed cutoff power law plus a free-width Gaussian.

---

the power law (or cutoff power law) models tested provided a good fit to the data (table 4.3), though cutoff power laws appear to give a much better fit to the data. Adding a blackbody component to an absorbed power law gave poorly constrained parameters: photon index < 1.98; kT $= 0.17^{+0.02}_{-0.02}$; and $N_{\rm H} = 4.58^{+5.16}_{-3.08} \times 10^{20}$ cm^{-2} ($\chi^2/\nu = 46/38$).

RS analysis of my spectra compared to a base model of an absorbed cutoff power law shows a feature at ~ 0.7 keV at $> 99.99\%$ significance. However, *ppp* analysis only placed a significance of 99.74% on the same feature. In addition the appearance of a feature at 0.7 keV indicates that the absorption column may not have been modeled accurately, as seen in other bursts in the previous section. As there is no report of a redshift for this burst this cannot be confirmed by carrying out a well constrained two component absorption fit.

GRBs 060202 and 060218 have both been discussed in the previous section. I agree with the presence of a blackbody component in 060218 (Campana et al., 2006b). The single feature found in 060202 only occurred in 1 of the 18 time sliced spectra with a significance of 99.74% (single trial). If the multiple trials carried out are considered this drops to a significance of 95.4%. My analysis indicates that it is a broad feature ($\sigma < 0.34$ keV) at 0.9 keV rather than a series of resolved or overlapping lines, however it does occur at the same energy over which Butler (2007) reports 4 individual narrow lines. No evidence was found for the reported feature at 4.70 ± 0.07 keV.

4.4 Conclusions

The search for emission lines in GRB spectra was motivated by low significance (usually 2-3 σ) Gaussian features reported in the literature in the pre-*Swift* era; often at late times with respect to the GRB trigger. If such features were to be detected they could provide a significant insight into the environment surrounding the GRB and the emission geometry of the burst. The advent of *Swift's* rapid follow up capabilities has produced a new archive of spectra in the sparsely explored early temporal regime. Afterglows at such times are bright and therefore provide spectra with a high SNR, making additional spectral features easier to detect than late-time, low-SNR spectra. With such motivations in mind an extensive search of WT mode spectra was conducted using a suite of different methods as described and tested in the previous chapter.

Of the 332 WT mode spectra assessed, only 12 produced possible detections at $\geq$99.90% significance (single trial). These were all located around two energies in the observer frame: 0.7 keV (10/12) and 2.3 keV (2/12). The coincidence of many spectral features close to 0.7 keV is suspicious as intrinsic GRB emission line features would be expected to be located at different observed energies, as the GRBs span a large range of redshifts. For those candidates with a redshift measurement the feature at 0.7 keV became insignificant once an absorption component at the redshift of the host galaxy was applied. It is expected that the same reduction in significance would occur if well constrained two absorption component fits were conducted on the GRBs with unknown redshifts. The 2.3 keV features are thought to be associated with the gold M-edge, which was also detected in the PKS 0745-19 spectrm (chapter 3). It is my conclusion that all of these features are either due to calibration issues, imperfect bias subtraction at the processing stage or incorrect modelling of the host absorption column (most likely case for the 0.7 keV features), rather than intrinsic GRB emission line detections. The only non-power law emission component I accept as intrinsic is the blackbody component detected in GRB 060218.

This study primarily shows that the verification of such features cannot be carried out using popular detection techniques such as LRT or the F-test but must instead be subjected to statistically rigorous tests, or a combination of mutually supporting tests, as discussed in chapter 3 of this work. Furthermore it has become apparent that two component absorption models (with Galactic and host galaxy contributions) must be applied to such spectra to avoid spurious detections of low energy features.

This work has provided stringent limits on the normalisation of any emission line features present in

early time WT observations, as illustrated in figures 3.5, 3.6 and 3.7 of the previous chapter. Whilst it is still possible that such features could be present, if a theoretical framework can be provided to alleviate the size and kinematic problem (§3.1), then they must be completely dominated by the underlying afterglow power law component.

4.A Appendix: Rutledge and Sako smoothing plots.

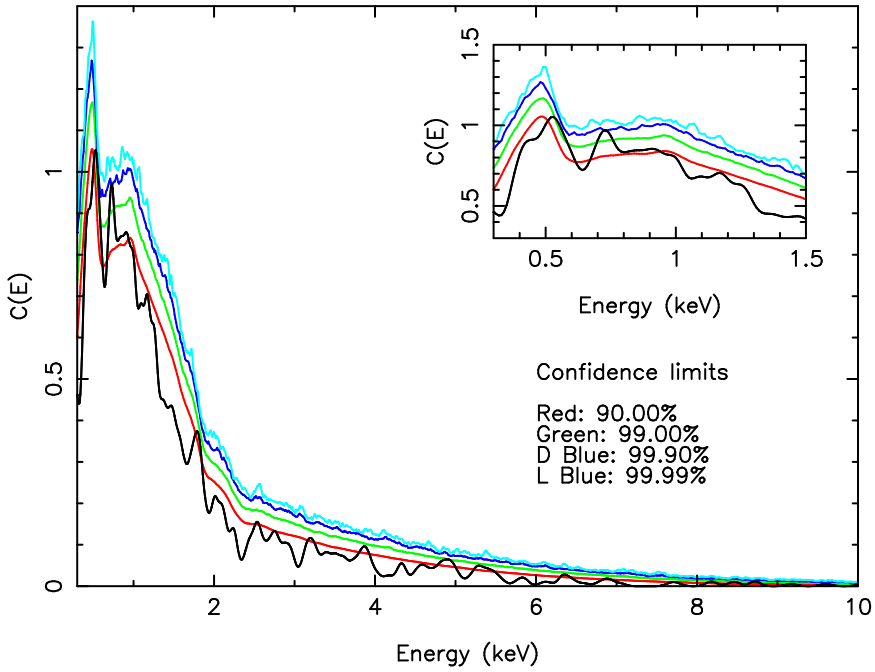

Figure 4.6: GRB 050730 (T+692s to T+792s): RS method. Inset focuses on energy range of interest.

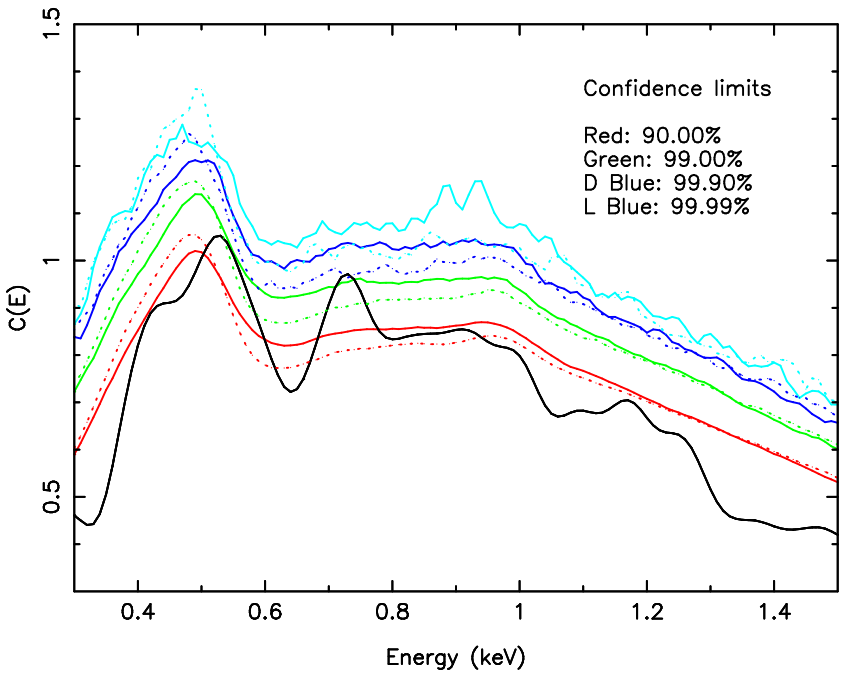

Figure 4.7: GRB 050730 (T+692s to T+792s): RS comparison between the absorbed power law models containing a single $N_{\rm H}$ component (wabs, dotted lines) and two components (wabs and zwabs, solid lines). Note that the feature becomes far less significant with the addition of the $N_{\rm H}$ column at the appropriate redshift.

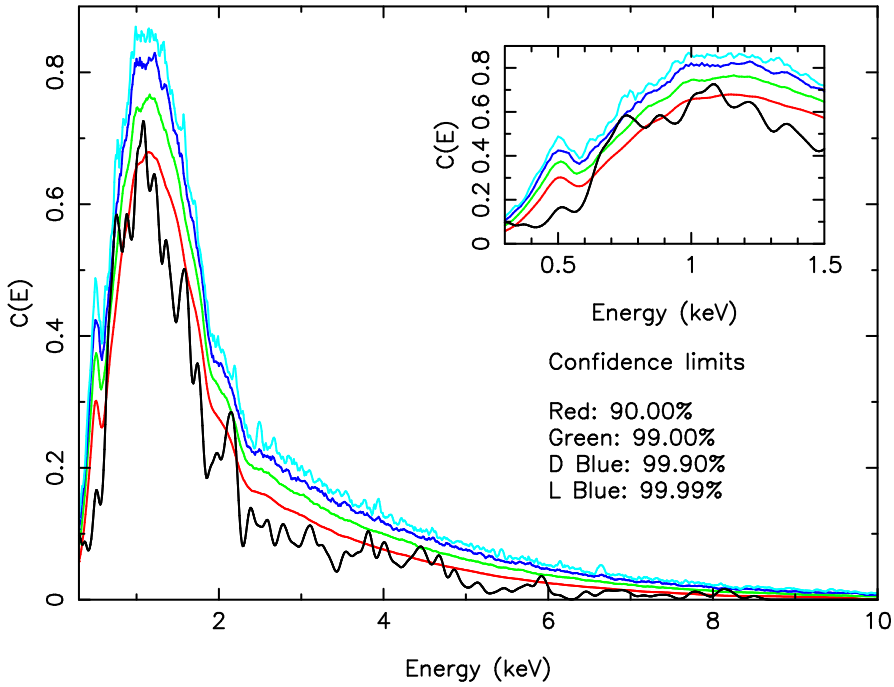

Figure 4.8: GRB 060109: RS results.

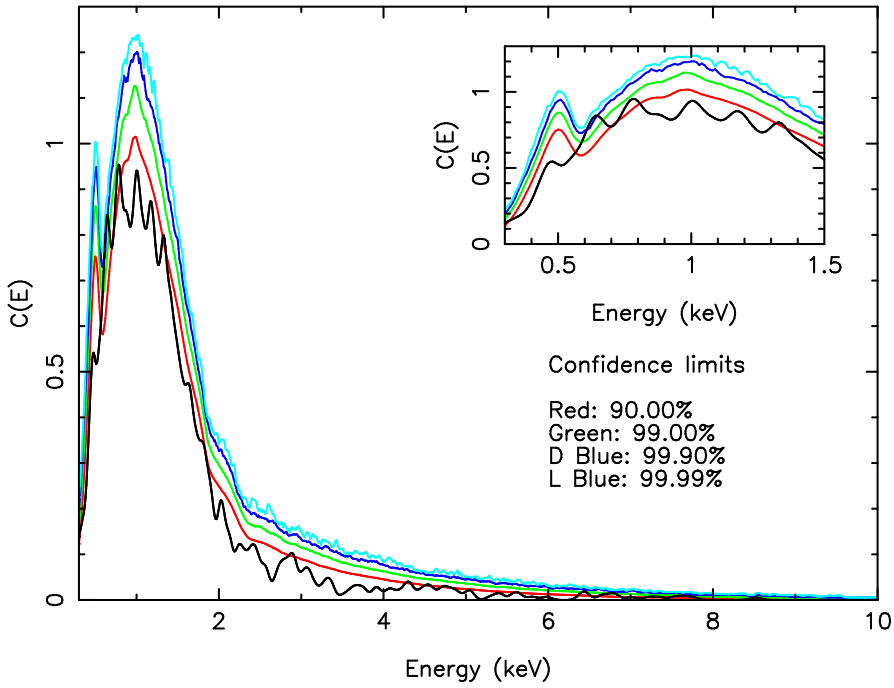

Figure 4.9: GRB 060111A (T+164s to T+234s): RS results.

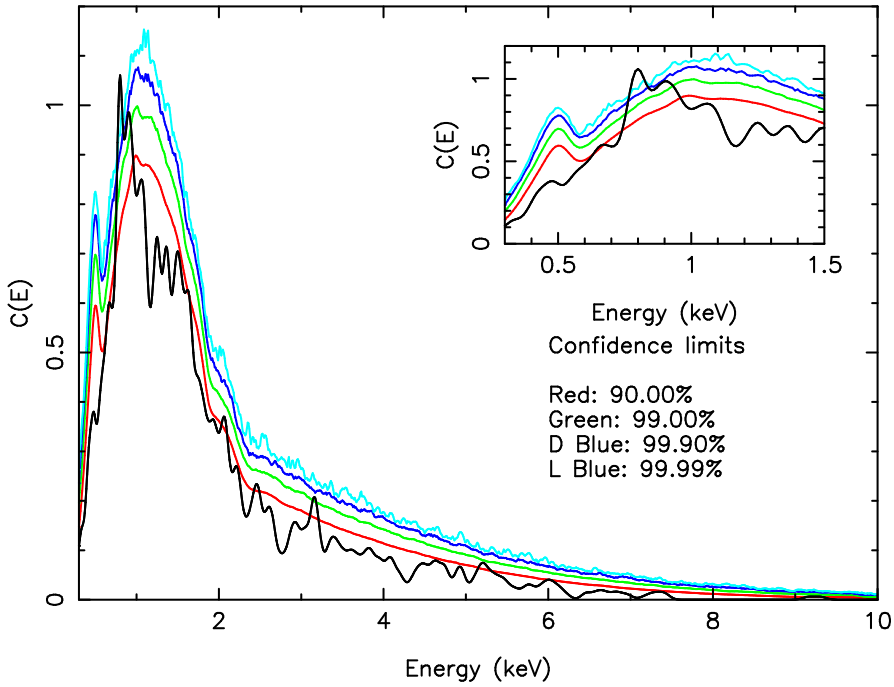

Figure 4.10: GRB 060111A (T+319s to T+339s): RS results.

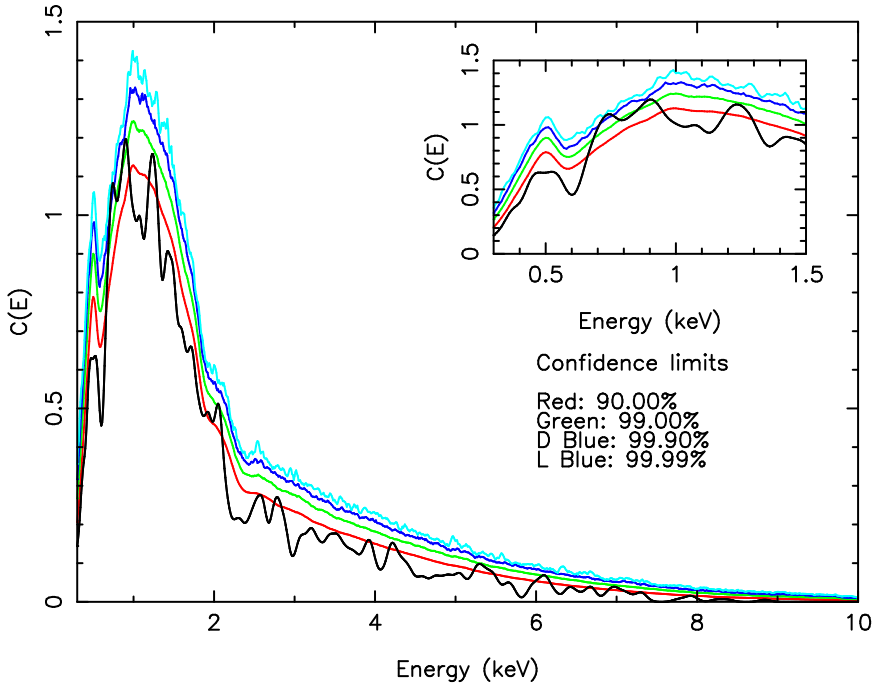

Figure 4.11: GRB 0601115 (T+121s to T+253s): RS results.

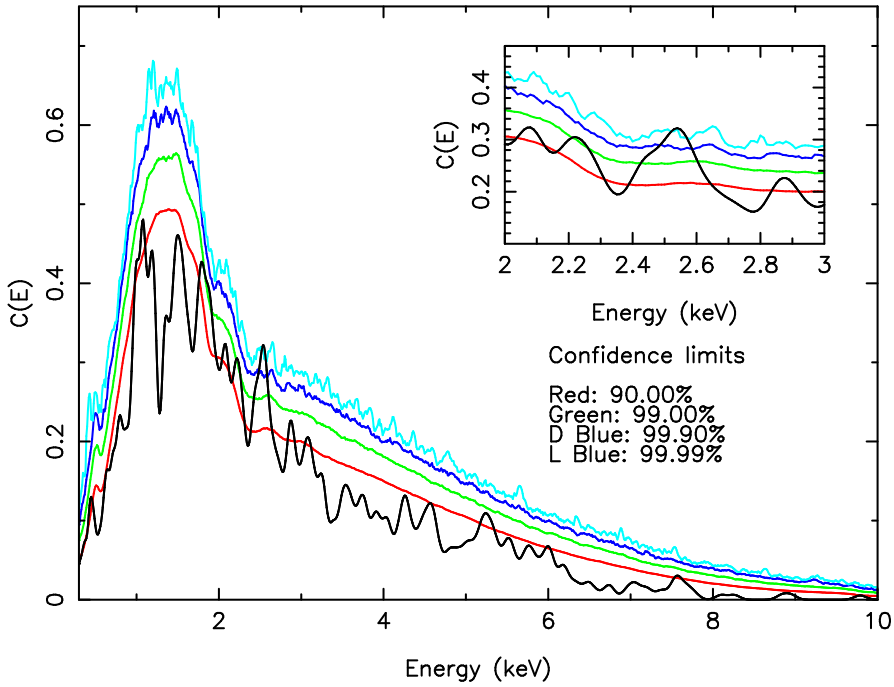

Figure 4.12: GRB 060124 (T+537s to T+542s): RS results.

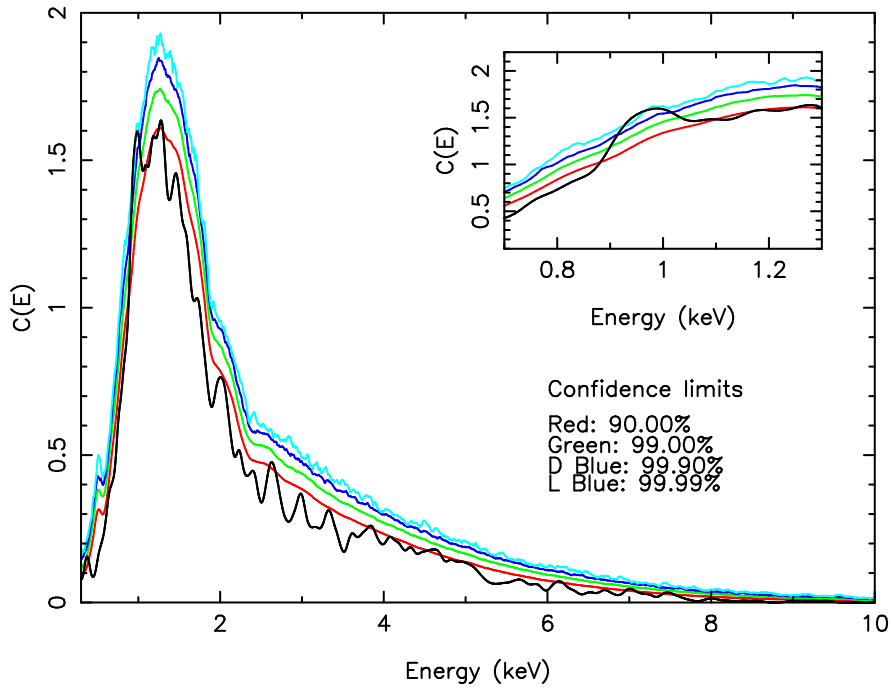

Figure 4.13: GRB 060202 (T+429s to T+529s): RS results.

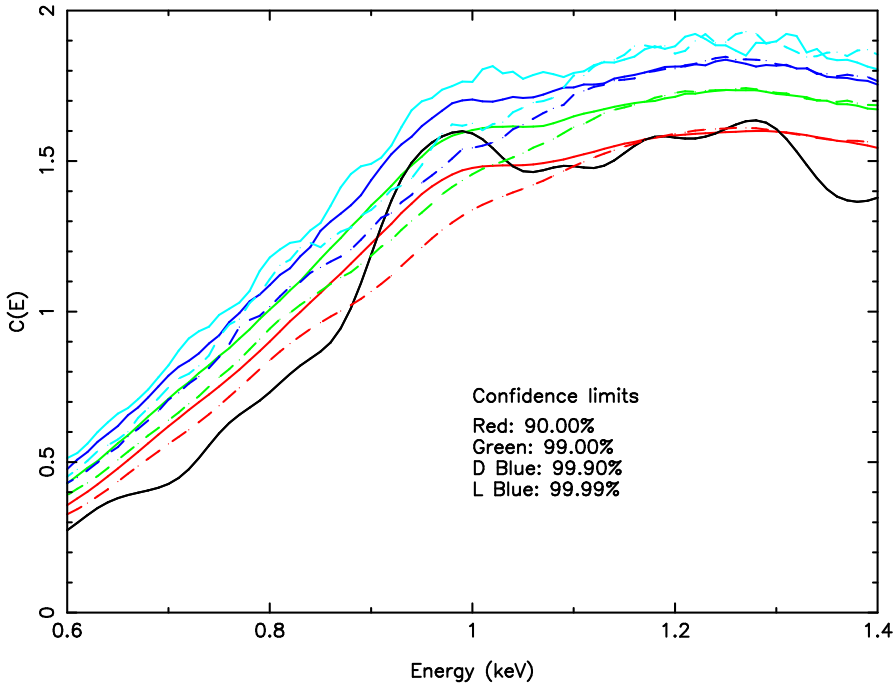

Figure 4.14: GRB 060202 (T+429s to T+529s): RS comparison between the absorbed power law models containing a single $N_{\rm H}$ component (`wabs`, dashed lines) and two components (`wabs` and `zwabs`, solid lines). Note that the feature becomes far less significant with the addition of the $N_{\rm H}$ column at the appropriate redshift.

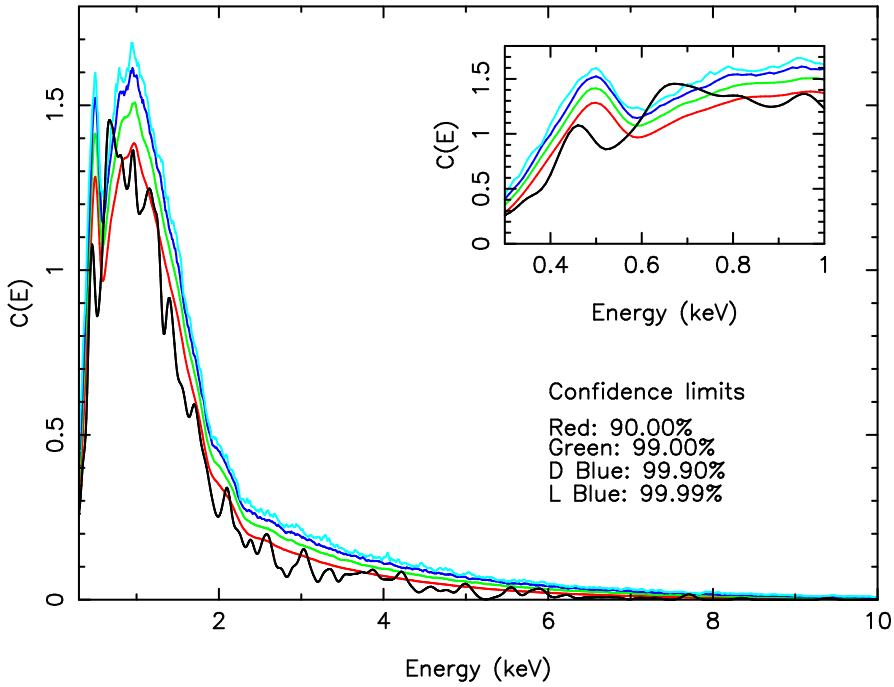

Figure 4.15: GRB 060210 (T+233s to T+353s): RS results.

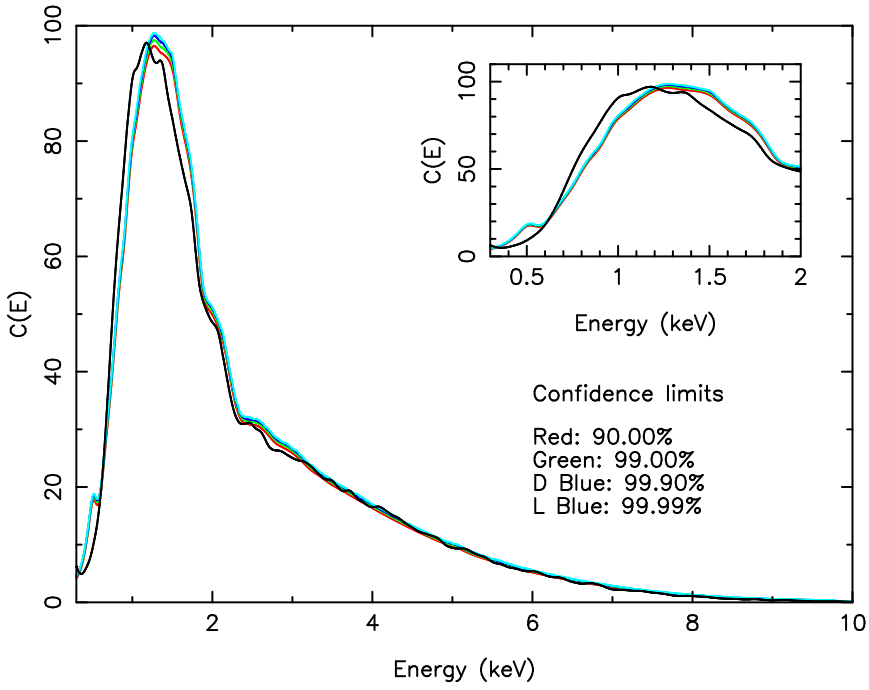

Figure 4.16: GRB 060218 (T+159s to T+2770s): RS results.

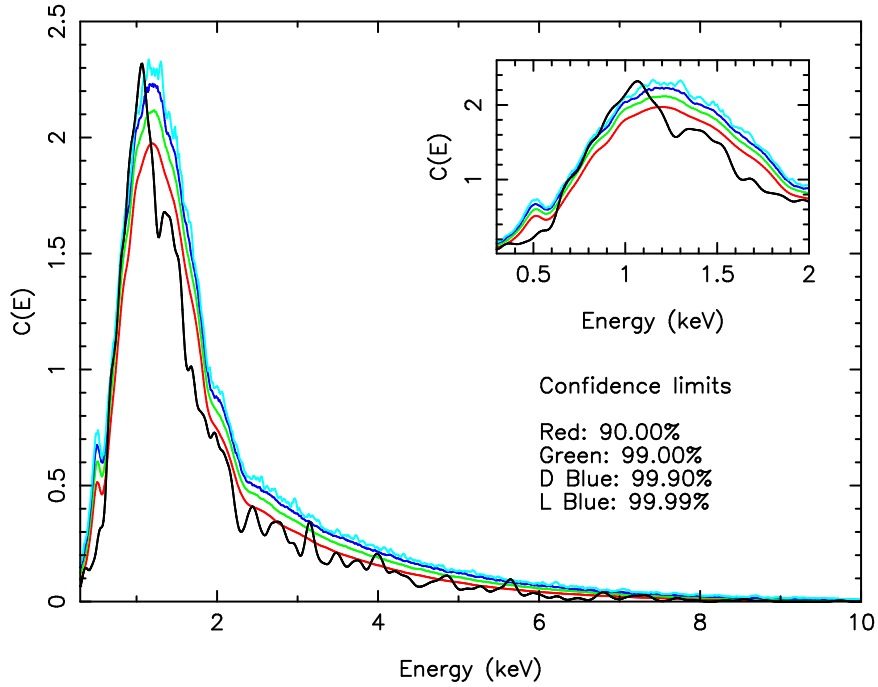

Figure 4.17: GRB 060218 (T+2359s to T+2409s): RS results.

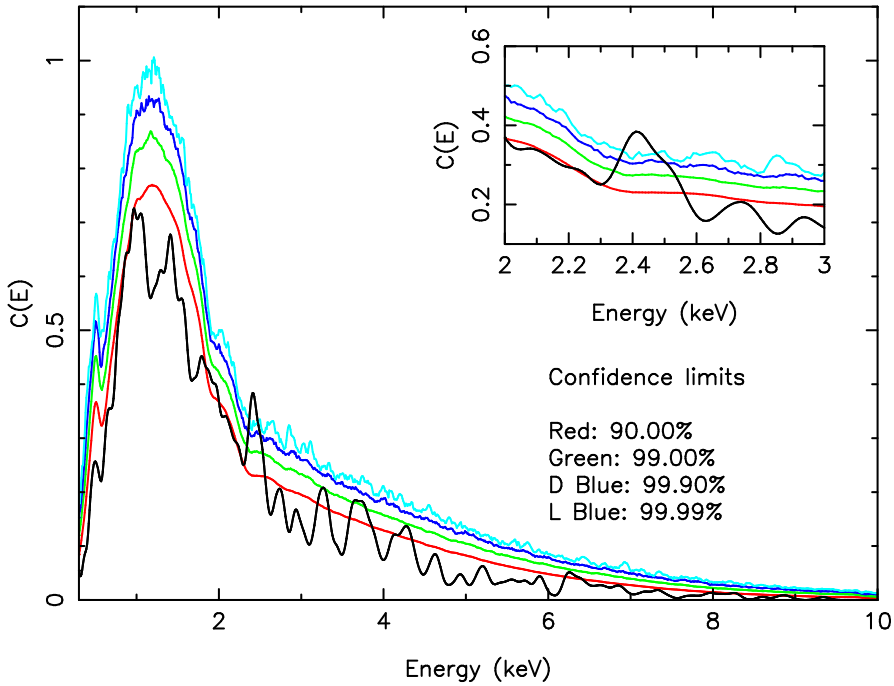

Figure 4.18: GRB 060418 (T+119s to T+129s): RS results.

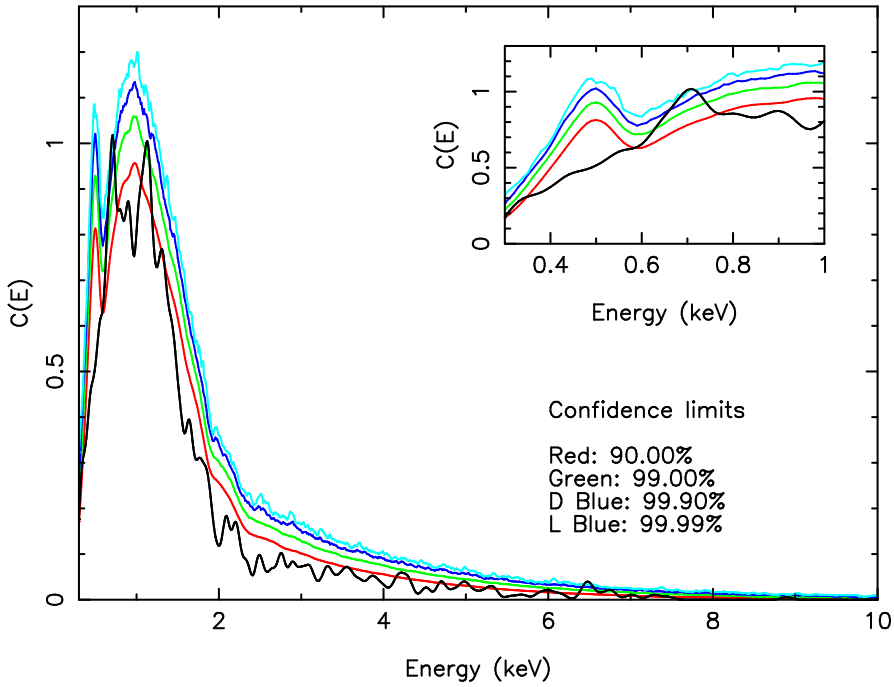

Figure 4.19: GRB 060418 (T+169s to T+194s): RS results.

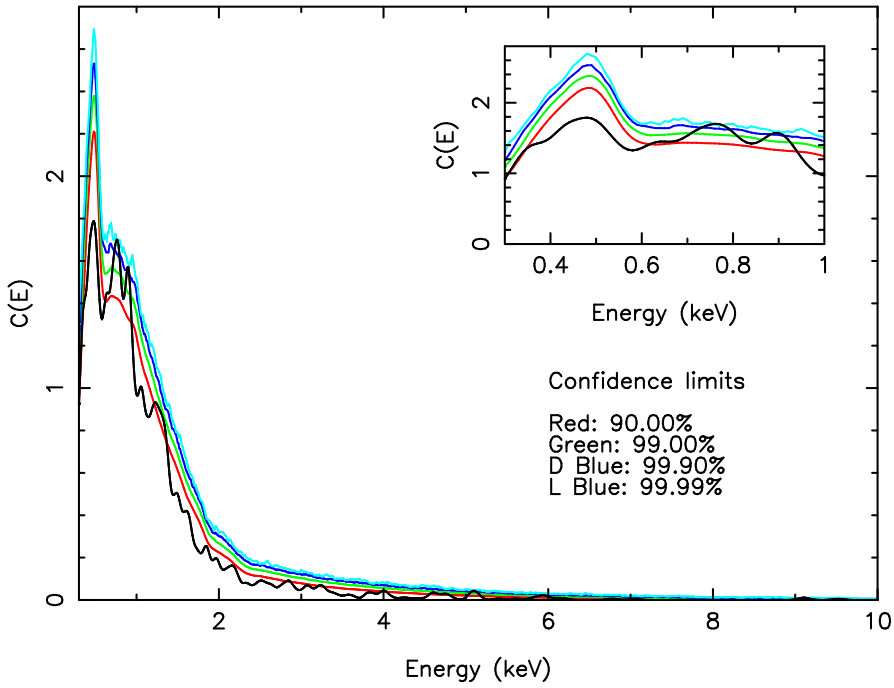

Figure 4.20: GRB 060428B (T+212s to T+252s): RS results.

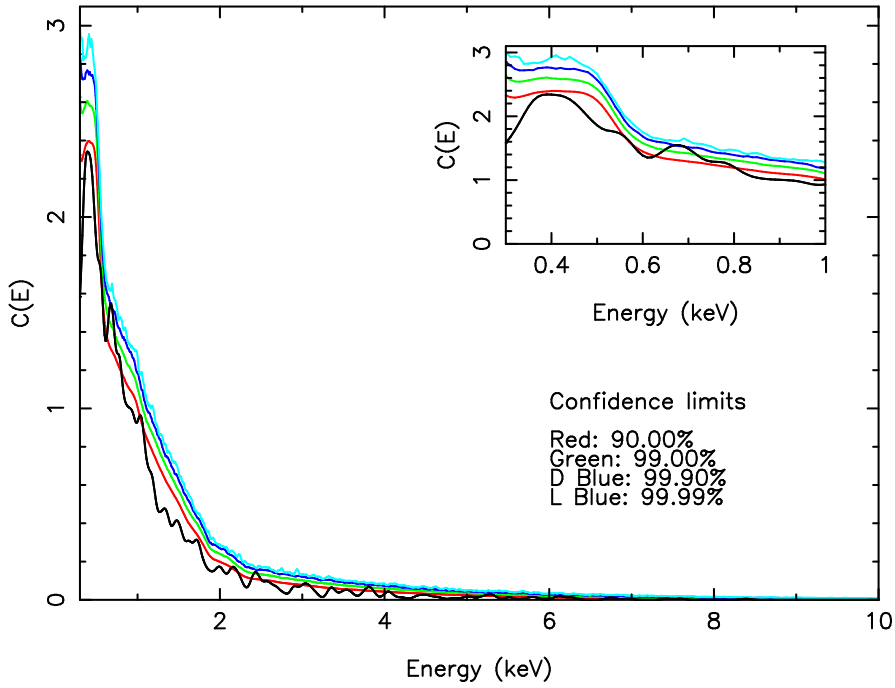

Figure 4.21: GRB 060428B (T+252s to T+418s): RS results.

Chapter 5

Precursors and long quiescent times in *Swift* GRBs

The current observational status of GRBs appears to show that their emission follows a canonical behaviour, as seen in previous chapters of this work. However, one debated feature briefly mentioned in §1.2.1 but not described in §1.3.3 is 'precursor' emission. The earliest theoretical models (Colgate, 1973, 1974) predicted that there may be some signature emission that occurs before the main phase 0 emission, which may have a separate physical origin and therefore spectral signature. This chapter explores the definition of a 'precursor', describes the historical, theoretical and observational status of such events and characterises quiescent periods within phase 0 emission. I then proceed to define my own selection criteria for further investigation into precursors/long quiescent periods. The GRBs thus selected all showed behaviour typical of other Swift *GRBs; both spectrally and temporally. No strong evidence was found to suggest that the 'precursors'/early time emission pulses in this sample were spectrally different to the rest of the phase 0 emission period over the energy ranges observed by BAT. This study indicates a common origin for events normally ascribed to 'prompt emission' and 'flares', in line with previous investigations (e.g. Chincarini et al., 2007), and extends it to cover 'precursor' emission.*

5.1 Introduction

The earliest theoretical GRB models predicted that the 'main'[1] burst of γ-rays should be preceded by a transient thermal signal. Originally Colgate (1973; 1974) predicted that the strong shock developed in the low density stellar envelope of a SN should lead to a high temperature precursor to the shock wave, which produces bremsstrahlung and inverse Compton radiation. Since then theoretical models of GRB progenitors have evolved to the point where the predicted precursors can be subdivided into two classes: *fireball precursors*, which are associated with the transition of the fireball from an optically thick to optically thin regime, and *progenitor precursors*, which are associated with the interaction of the fireball/jet with the progenitor itself. Most of these scenarios are only applicable to GRBs with massive stellar progenitors (LGRBs), though the model proposed by Lyutikov & Usov (2000) could potentially result in precursors from SGRBs.

Fireball precursors have been predicted in pure radiation fireballs (Paczynski, 1986), baryon loaded fireballs (Mészáros & Rees, 2000; Daigne & Mochkovitch, 2002) and magnetic outflows (Lyutikov & Usov, 2000). They are expected to have a thermal spectrum and an observed temperature ranging from several tens of keV, for baryon-dominated fireballs, to several MeV for clean fireballs (either magnetic or radiation dominated). The models described by Paczynski (1986), Mészáros & Rees (2000) and Daigne & Mochkovitch (2002) state that the thermal precursor emission originates from the progenitor's photosphere, naturally producing spectra with thermal signatures in the X-ray energy range. Daigne & Mochkovitch (2002) point out that the precursor emission is likely to be too weak to be detected if it occurs simultaneously with the non-thermal emission originating from internal shocks in the jet. Conversely the precursor can be seen if the relativistic wind is produced with a smooth distribution so that the internal shock activity is delayed.

Lyutikov & Usov (2000) considered an alternative scenario whereby a GRB is produced from a relativistic, strongly magnetized wind flowing out from a rapidly rotating compact progenitor. They stated that there are three possible regions where energetic photons could be emitted: the thermal photosphere of the relativistic wind, the region where the wind magnetic field developes instabilities and the region where the outflowing wind interacts with the surrounding medium. Lyutikov & Usov (2000) state that

[1]The definition of the 'main' emission is some what contentious, as I shall elaborate on later in this chapter. For the purposes of this work the 'main' emission will be defined as the prominent emission period in the γ-ray band that typically triggers the GRB detector and is normally referred to as phase 0 emission throughout the rest of this thesis.

emission from the first site, the photosphere, may produce a weak precursor (its intensity being tens to hundreds of times smaller than the main emission). It is expected to have a blackbody spectrum with a mean photon energy of $\sim$ 1 MeV and a duration of 0.1-10 s. If the central engine is a millisecond pulsar, with a nonstationary outflow, it is also possible that the precursor may be strongly variable, with a timescale of the order 10^{-3} s. Lyutikov & Usov (2000) point out that the precursor emission component will not be detectable if it occurs simultaneously with the non-thermal emission from the instabilities in the magnetic wind (c.f. the point raised by Daigne & Mochkovitch 2002).

Measuring properties such as the delay between the precursor and main emission, the duration, luminosity and typical energy of the precursor for this class of models would allow the derivation of the Lorentz factor of the ejecta, their temperature at the transparency radius, and the internal shock radius. All these parameters are extremely hard to measure otherwise.

Progenitor precursors are due to thermal radiation emitted by shocked stellar material that is exposed as the jet breaks through the surface of the massive stellar progenitor. The spectrum is again expected to be thermal, though it can be modified by interaction with the jet itself. If the jet is optically thin at the star's surface and non-thermal particles are present, inverse Compton scattering can produce non-thermal spectra (Ramirez-Ruiz et al., 2002b). Waxman & Mészáros (2003) expand upon this model by considering the jet emergence process, as well as the shock heating and expansion of the stellar material that builds up in front of the jet (which the authors refer to as a 'cork'), in greater detail. They show that a series of increasingly shorter and harder thermal X-ray pulses are produced as successive cycles of shock (and rarefaction) waves pass through the stellar 'cork' material as the jet ejects it beyond the boundary of the stellar envelope.

However, a model invoking the one-time breakout of the jet from the stellar envelope can only explain delays between the precursor and main emission of $\sim$ 10 s (Wang & Mészáros, 2007, and references therein). Longer delays can be accommodated if more than one jet is launched by the central engine. Wang & Mészáros (2007) propose that a precursor could be produced by a weak relativistic jet, containing $\sim$ 10^{50} ergs, launched prior to the main jet. The expected precursor spectrum from the jet itself is non-thermal, however, a transient thermal pulse (duration of the order 10 s) with kT $\sim$ 10 keV may be observed from the channel opened by the jet through the stellar envelope. Wang & Mészáros (2007) calculate that the channel created by the precursor jet closes on a timescale comparable to the jet breakout time ($\sim$ 10 s). A closed channel is an important condition for the collimation of the main

jet, which is launched $\sim$ 100 s later. Should a precursor be recognised as a progenitor precursor, its properties would place important constraints on the dynamics of the jet propagation in the progenitor and on the size of the progenitor star.

5.1.1 Notable cases of observed precursor emission

The soft and faint nature of precursor emission means that they rarely trigger GRB monitors, though a few have either been sufficiently bright to produce a trigger or they were detected serendipitously in data preceding the main burst emission.

The first reported detection of a precursor occurred with GRB 900126. Murakami et al. (1991) stated that the *GINGA* satellite (Makino, 1987; Murakami et al., 1989) had observed an X-ray event $\sim$ 10 s before the onset of the main burst emission. The spectra of the main emission, consisting of two distinct peaks separated by $\sim$ 6 s, were fit with a thermal bremsstrahlung model with kT $\sim$ 120 keV and 85 keV respectively. The precursor emission was poorly fit by the same model ($\chi^2/\nu = 25/12$); it was found to be better fit by a blackbody model with kT $= 1.58^{+0.26}_{-0.23}$ keV ($\chi^2/\nu = 19/12$). Further work by the same group (Murakami et al., 1992) indicated that *GINGA* detected at least three more events in subsequent GRBs, which showed clear separation from the main emission. In all cases the precursor emission was spectrally much softer than the emission that followed it. Six GRBs with precursor activity were reported by Sazonov et al. (1998) from a catalogue of GRBs detected by *GRANAT-WATCH* (Lund, 1986). However, their classification of a precursor is not well defined, other than an excess in the 8-20 keV energy range before the main burst. They report that the precursors are softer than the main emission but do not quote any spectral models.

Piro et al. (2005) reported on two precursors observed in the light curve of GRB 011121 by *BeppoSAX* . They occurred at $\sim$ 22 s and $\sim$ 10 s prior to the main emission of this GRB and contained $\sim$2% of the fluence observed in the main event. Unlike the precursors reported by Murakami et al. (1991, 1992) neither precursor was well fit by a blackbody model over the 2-700 keV energy range. They were well fit by a power law model with a photon index of 1.00 ± 0.11 ($\chi^2/\nu = 26/26$) and 1.25 ± 0.10 ($\chi^2/\nu = 19/26$) respectively. Vanderspek et al. (2004) also reported the detection of two precursor events ($\sim$ 20 s and $\sim$ 5 s prior to the main emission) in the light curve of GRB 030329 by *HETE-2* .

Again the spectra of these events were non-thermal, being well fit[2] by a power law model with a photon index of $2.16^{+0.38}_{-0.44}$ and $2.01^{+0.31}_{-0.30}$ respectively.

An event with a delay of $\sim$250 s between the precursor and the main emission was observed in GRB 041219A by a variety of GRB missions (McBreen et al., 2006). The *INTEGRAL* (Winkler et al., 2003) light curve shows no emission in the 20 keV to 8 MeV energy band between the precursor and the main emission. However, BAT detected emission, particularly in the 15-50 keV energy band, during this interval; *ROSSI X-ray Timing Explorer* (*RXTE*; Bradt et al., 1993) also detected a spectrally soft pulse during this time. The precursor spectrum, as measured by BAT, was fit with a Band function giving the following model parameters: low energy power law index $= 0.45^{+0.37}_{-0.30}$, high energy power law index $= 2.62^{+0.73}_{-7.40}$ and break energy $= 145.4^{+79.7}_{-48.1}$ keV ($\chi^2/\nu = 12/11$). However, McBreen et al. (2006) state that a model consisting of a power law plus a blackbody component was a better fit: kT $= 45.7^{+9.1}_{-8.7}$ keV, photon index $= 1.58^{+0.53}_{-0.28}$ ($\chi^2/\nu = 9/11$). The blackbody component contributed $\sim$49% of the observed flux in this fit.

5.1.2 Archival searches for precursors

As stated in § 5.1.1 precursors rarely trigger GRB detectors. Consequently Koshut et al. (1995) and Lazzati (2005), hereafter K95 and L05 respectively, conducted searches for precursor emission in the data recorded prior to GRB triggers in the archival *BATSE* records over the 30-300 keV energy range.

The search conducted by K95 focussed on data spanning T-1000 s to T+1000 s around each GRB trigger time. They defined a precursor to be emission that preceded the main burst and that had a lower peak intensity than the main burst. The precursor and main emission had to be separated by background[3] level emission for a time interval at least as long as the duration of the main burst. No requirements were placed on the energy range in which the precursor was detected, i.e. no bias was introduced favouring spectrally hard or soft precursors. The temporal resolution of the data used was 1.024 s, thus no events with a duration less than this could be detected. $\sim$3% of *BATSE* bursts were found to exhibit precursor events as defined by their criteria. In two cases the peak rates of the precursors were comparable to the main emission epidsode; in all other cases the precursor peak rates were $< 60\%$

[2]No χ^2/ν values for these fits are given in Vanderspek et al. (2004) beyond the qualitative statement of the goodness of fit.

[3]They defined the background level to be less than 5% of the precursor counts.

of the main episode. Hardness ratio analysis found that there was a weak tendency for the precursor emission to be softer, on average, than the main emission. However, there were several instances where the precursor was spectrally harder than the main emission. K95 stated that they found no significant correlations between the various characteristics (i.e. duration, fluence etc) of the precursor and main emission. They concluded that there was no evidence to suggest that the characteristics of the main episode of emission were dependent upon the existence of the precursor, nor was there any evidence to suggest that the two periods of emission were the result of different burst environments or production mechanisms.

A later study by L05 applied a different definition for a precursor. Whilst the precursor still had to be observed before the main emission no limits were imposed on the separation of the two emission periods. The main emission period in this definition was deemed to start at the GRB trigger time; L05 acknowledges that this was somewhat of an instrumental definition. However, they justify this selection criterion by stating that they were searching for weak precursor emission, as predicted by theory, therefore pre-trigger time activity turned out to be an effective definition for their study. Nor was there a requirement that the emission between the two events had to return to the background level; there merely had to be a reduction in the detected flux. This restriction was primarily used to exclude slowly rising GRB emission from the sample. The time period searched around the trigger times was limited to T-262 s to T+T_{90} s for GRBs with T_{90} durations > 5 s (therefore excluding SGRBs). L05 found that $\sim$20% of *BATSE* bursts exhibited precursors as defined by their criteria; typical intervals were of the order of tens of seconds but intervals of up to 200 s were observed. Most of the precursors were weak, containing a fraction of a percent of the total counts of the whole event. All of the precursors were softer than the time-integrated main emission, which is in opposition to the results of K95. The sample contained 19 precursors with sufficient data to allow spectral analysis; of these only 2 were well fit with thermal models. Lazzati (2005) reported a mild correlation of the precursor duration (but not its delay) with the burst T_{90} and its variability time-scale. Like K95 they found no evidence for correlations between other temporal characteristics of the two emission periods.

5.1.3 Quiescent intervals

It can be seen from the previous discussion that the definition of a precursor varies from study to study, as does the energy range in which the detection is made. This raises the question: can the precursor

events be separated from the main emission in all cases, or should they be treated as part of the same phase of emission?

Nakar & Piran (2002, hereafter NP02) analysed the distribution of the time intervals between pulses and the pulse widths of 68 bright[4] (*BATSE* peak flux > 10.19 photons s^{-1} cm^{-2}) LGRBs within phase 0 emission. They found that the distribution of the width, δt, of the pulses was consistent with a log-normal distribution. The distribution of the intervals between pulses[5], Δt, deviated from a log-normal distribution unless intervals containing long duration *quiescent times*[6] were eliminated. They noted that in nature such deviations from log-normal behaviour occur when different mechanisms govern the high end tail of the distribution. They felt that the simularity between the δt and Δt (without quiescent intervals) distributions suggested that both distributions were influenced by the same (source) physical parameters. This assertation was backed up with evidence of correlations between pulse widths and the intervals adjacent to them[7]; a significant correlation with δt was found with *preceding* intervals for all GRBs in the sample. A significant correlation between δt and the *following* intervals was also found for 60% of the GRBs. In all bursts considered by NP02 the significance of the correlation between δt and the preceding interval was higher, or equal to, the correlation with the following interval.

Quiescent times were seen in 35/68 GRBs in the NP02 sample. Most bursts contained one or two quiescent times; some contained three. These intervals typically lasted for several tens of seconds; the full range spanned 1 s (the arbitary lower limit considered in NP02's work) to hundreds of seconds. In some bursts the quiescent periods were a significant fraction of the total burst duration. NP02 hypothesised that the quiescent intervals corresponded to periods in which the activity of the central engine differs from its normal behaviour; it may not be active at all, or the inner engine may emit a sequence of shells that do not collide (e.g. shells with decreasing Lorentz factors) during this time.

NP02 stress that the quiescent periods found in their work are not the same as the delays between precursor and main emission reported by K95, mainly because of the spectral differences seen by K95

[4]NP02 also selected 24 dimmer LGRBs from the *BATSE* sample and conducted the same analysis as the bright bursts; the results were consistent with those of the bright sample, indicating that the 68 bursts in the primary study were representative of GRBs as a whole.

[5]The interval Δt was defined as the interval between successive pulse peaks.

[6]A quiescent time was defined to be an interval over which no emission was detected above the background level over the whole *BATSE* bandpass. The minimum duration of a quiescent interval in this study was defined to be ~ 1 s.

[7]Comparisons were carried out burst by burst in order to eliminate redshift or intrinsic effects that would have produced spurious correlations if the dataset had been considered as a whole.

in the two emission periods. Despite this fact it is interesting to note that the timescales discussed in both works (and L05) bear a striking resemblance. Given that there is increasing evidence that phase 0 and phase V emission originate from the same emission (internal shocks) could it be possible that all three emission events (precursors, main emission and flares) have the same origin and properties?

Chincarini et al. (2007, hereafter C07) conducted a survey of X-ray flares from GRBs observed by *Swift* up to 31$^{\rm st}$ January 2006 and compared their properties to those of the 'prompt' emission. The 'full' sample contained 33 GRBs, however, several were excluded from the full analysis due to data quality issues; the 'restricted' sample contained 30 GRBs, 9 of which had redshift measurements. Their work concluded that the properties of the flares studied ruled out reverse and external[8] shocks as possible emission sites. Furthermore C07 stated that the flare spectral properties (harder than the underlying afterglow, showing an evolution from spectrally hard to soft over time; see also Burrows et al. (2005b); Falcone et al. (2006); Romano et al. (2006b)) indicated a different physical mechanism from that which produces the afterglow; instead the flares are likely to be produced by the same mechanism as the 'prompt' emission. No correlation was found between the number of γ-ray pulses and X-ray flares seen for individual GRBs within the sample. Nor was there a correlation between the interval between preceding pulses and the peak brightness of either γ-ray pulses or X-ray flares; C07 concluded that this was further evidence for a common mechanism for both. An anti-correlation was found between the flare $\rm t_{peak}$ and peak intensity ($r_s = 0.54$, P $= 5.24 \times 10^{-6}$)[9], though the authors also argue that this correlation could be biased by flares at late times as there is a large scatter in the relationship for $t > 10^3$ s. From this, and measurements of flare duration, C07 infer that late flares have a lower peak intensity but last much longer, thus the fluence of late-time flares can be very large. Further correlations were seen between flare equivalent width and $\rm t_{peak}$ and the decay index of the flare (assuming a power law decay model[10]) and $\rm t_{peak}$.

In this chapter I select a sample of *Swift* GRBs with long quiescent intervals, as seen in the BAT (15-350 keV) light curves, and analyse their temporal and spectral properties to investigate whether there is a

[8]Kobayashi et al. (2007) state that the external shock may produce a flare-like signature but only if very carefully balanced conditions are met.

[9]Where r_s is the Spearman Rank Correlation coefficient (Press et al., 1992), a non-parametric measure of the correlation between two sets of variables. It varies between $-1 \rightarrow 1$; a value of $r_s = 0$ indicates no correlation, 1 a positive correlation and -1 an anti-correlation between the variable sets.

[10]Using this model C07 found that the $\alpha_{\rm decay}$ indices were consistent with the 'curvature effect' provided appropriate values of $\rm T_0$ were used.

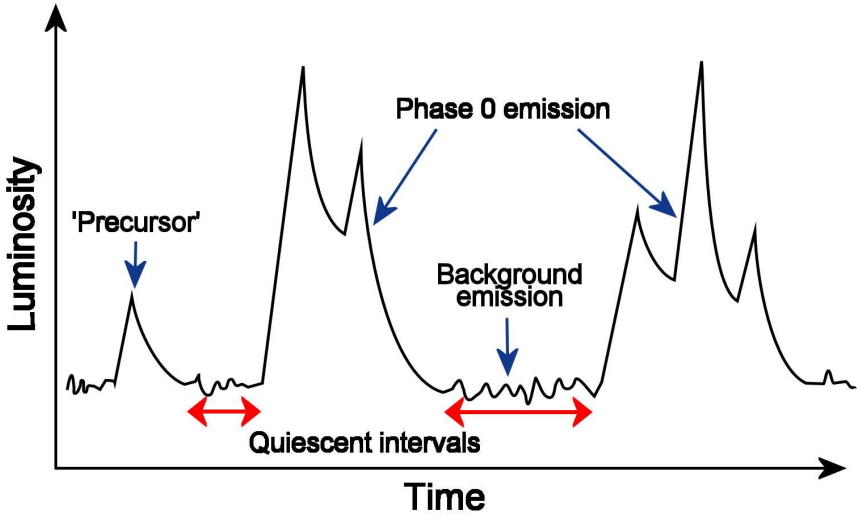

Figure 5.1: A diagram illustrating an idealised BAT light curve. A Q-time is defined here as the time between successive emission pulses where there appears to be no pulse activity above the background instrumental level. Such intervals may be found between 'precursors' and Phase 0 emission or between two prominent periods of Phase 0 emission.

---

link between precursors, main emission and flares within these bursts, and also to provide a comparison with previous studies (K95; L05 and C07).

5.2 Selection criteria

This chapter reports on the analysis of BAT and XRT data for bursts with large quiescent intervals (hereafter 'Q-times') between successive periods of emission, wherein no distinction is made between periods that have previously been labelled as due to 'precursor', 'phase 0' or 'flare' (phase V) emission. A Q-time is defined here as the time between successive emission pulses where there appears to be no pulse activity above the background instrumental level (see figure 5.1). A total of 276 bursts were considered, ranging from GRB 050128 to GRB 070729. Earlier bursts were excluded due to the partially commissioned status of *Swift* at that time.

An initial selection of GRBs with at least one significant Q-time in the observer's reference frame

was made using the archival results from the Malindi automated burst analysis tools[11]; these results were autonomously generated by running the `batgrbproduct`[12] software on BAT data to produce a series of standard light curve and spectral products. The selection criteria detailed below were applied to the 'full time interval[13]' 1 s binned mask weighted light curves (measured in units of counts s^{-1} $detector^{-1}$). The mask weighting technique, as applied to the coded aperature mask of the BAT, produces light curves that are background subtracted. Due to the nature of the instrumental γ-ray background rate it was sometimes difficult to distinguish between low-level emission events and residual background events at the 1 s binning level. In such cases the 64 ms and 16 ms binned light curves, over reduced temporal ranges, were also considered to disambiguate between low level GRB emission and background events. The following criteria were used to produce the candidate bursts:

- As in K95 a long interval criteion was used, but unlike that study the interval was not chosen in reference to the main emission period of each GRB, which itself is problematic to define. Instead a Q-time with reference to the entire *Swift* sample was used; > 50 s in the observer's reference frame. This interval is comparable to the time during which a typical BAT burst emits 50% of its energy (see figure 9 of Sakamoto et al., 2008). This selection parameter varies somewhat from the previous studies conducted by K95 and L05; both of which applied different a priori assumptions from precursor theory (such as lower peak intensities for precursor pulses) and criteria which may be strongly affected by instrumental biases. However, since the very nature of precursors are uncertain I chose to avoid overly restrictive selection criteria; no constraints were placed on the relative peak intensities of emission before or after this interval. Such a temporal criterion may have excluded many of the precursors discussed in the previous sections, if they had been observed in a comparable energy band to that of the BAT. Smaller delays between precursor and main emission may exist but if they are short then it is difficult to disambiguate between these delays and those from the intervals between individual pulses in a period of emission that would normally be considered to reflect continuous central engine activity.

- GRBs must have both BAT and XRT data, to allow spectral analysis to be carried out in both energy bands. Furthermore the XRT data allowed a comparison of the late-time light curve

[11]Originally only available to *Swift* team members, these products are now made available when a BAT refined analysis message is submitted to the GCN.

[12]http://swift.gsfc.nasa.gov/docs/swift/analysis/threads/batgrbproductthread.html

[13]The 'full time interval' Malindi automated light curves cover the entire timespan of the GRB observation mode dataset, typically covering from T-200 s before the BAT trigger to T+800 s, barring data loss due to entry into the SAA.

properties to be carried out for all bursts in the sample.

- Any bursts with known late time BAT emission that occurred whilst the BAT was in 'survey mode' (Barthelmy et al., 2005a) were also included in the initial selection (i.e. data that would not have been present in the Malindi automated analysis); e.g. GRB 060124.

This produced 21 potential candidates, reported in table 5.1. The Q-times measured are approximate values only as the exact start and finish of the intervals could not be measured accurately due to the highly variable nature of the BAT background. A final selection criterion was imposed on the candidate bursts such that only bursts with known redshifts (11/276 or $\sim$4 % of the total sample) were considered for further analysis.

5.3 Data reduction

All data were obtained from the UK *Swift* archive[14] (Tyler et al., 2006). BAT data were processed using the standard BAT pipeline, `batgrbproduct`, as described in the *Swift* BAT Software Guide[15]. A systematic error vector was applied to the BAT spectra before fitting in *XSPEC* using the task `batphasyserr`, as detailed in the Software Guide and the online BAT digest materials[16]. The systematic error vector was constructed by the BAT calibration team by assuming that the correction vector has a minimum value of 4% for the entire energy range, with larger values above 80 keV and below 35 keV, as determined by modelling Crab calibration data. XRT data were processed using *xrtpipeline* v0.11.5[17] using version 008 calibration files[18]. No systematic correction factors were applied to the errors of the X-ray spectra because the recommended factor[19] is very much smaller than the statistical errors in the XRT spectra. All spectral fitting was carried out using *XSPEC* version 12.3.1x or higher.

[14] http://www.swift.ac.uk/swift_live/obscatpage.php

[15] http://heasarc.gsfc.nasa.gov/docs/swift/analysis/bat_swguide_v6_3.pdf

[16] http://swift.gsfc.nasa.gov/docs/swift/analysis/bat_digest_old#phasyserr.html.

[17] Release date 2007-08-23

[18] http://heasarc.gsfc.nasa.gov/docs/heasarc/caldb/swift/docs/xrt/SWIFT-XRT-CALDB-09.pdf

[19] http://swift.gsfc.nasa.gov/docs/swift/analysis/xrt_digest.html

GRB	Redshift	Approximate Q-times from Malindi burst analysis data		Largest *interval** (s, rest frame)	References for redshift measurement
		observed (s)	rest frame (s)		
050319	3.240	100	24	$23.2^{+0.7}_{-0.6}$	[1, 2]
050820A	2.612	200	55	$61.9^{+0.3}_{-0.2}$	[3]
060115	3.530	60	13	$65.2^{+4.9}_{-3.1}$	[4]
060124	2.297	100	30	$90.4^{+1.2}_{-1.4}$	[5, 6]
060210	3.910	120	24	$36.0^{+0.5}_{-0.6}$	[7]
060418	1.489	60	40	$18.5^{+0.5}_{-0.5}$	[8]
060526	3.221	220	52	$58.1^{+0.2}_{-0.3}$	[2, 9]
060607A	3.082	50	12	$21.2^{+1.5}_{-1.2}$	[10]
060714A	2.711	50	13	$17.9^{+1.1}_{-1.2}$	[2, 11]
060904B	0.703	120	70	$93.4^{+0.9}_{-1.5}$	[12]
061121	1.314	50	22	$25.6^{+0.1}_{-0.1}$	[13]
060204B	-	90	-	-	-
060322	-	120	-	-	-
060929	-	450	-	-	-
061019	-	160	-	-	-
061202	-	60	-	-	-
070107	-	280	-	-	-
070129	-	100	-	-	-
070306	-	100	-	-	-
070704	-	200	-	-	-
070721B	-	360	-	-	-

Table 5.1: Summary of redshifts and Q-times for GRBs that meet the selection criteria. * Interval measured between successive 'pulse' start times as obtained from emission pulse fits to luminosity light curves; see § 5.7 and Appendix 5.B. References: [1] Fynbo et al. (2005), [2] Jakobsson et al. (2006a), [3] Prochaska et al. (2005a), [4] Piranomonte et al. (2006), [5] Cenko et al. (2006), [6] Cenko et al. (2006), [7] Cucchiara et al. (2006), [8] Vreeswijk & Jaunsen (2006), [9] Berger & Gladders (2006), [10] Ledoux et al. (2006), [11] Jakobsson et al. (2006b), [12] Fugazza et al. (2006), [13] Bloom et al. (2006).

5.3.1 Spectral quality

Extracting BAT data over designated Good Time Intervals (GTIs) using standard data processing tools resulted in spectra that were binned such that they always contained 58 PHA bins over the 15-150 keV energy range[20]. At low energies (i.e. 15-50 keV) the relative error on the spectral intensities was modest, even for relatively short GTIs. However, data $\geq$ 50 keV were usually poorly constrained; the overall quality of the spectrum was highly dependent on the incident flux and the GTI used.

To conduct well resolved time analysis of the BAT data for each candidate GRB the maximum number of spectra needed to be extracted in each case. Ideally such spectra should cover separate 'rising' and 'falling' sections of individual pulses, since noticeable spectral evolution is expected to occur at such times (Burrows et al., 2005b; Falcone et al., 2007, and references therein). However, the incident flux over these time periods was normally insufficient to produce good spectral quality above > 50 keV, making it extremely difficult to extract well constrained parameter values from the spectral models being applied. Thus it was often necessary to increase the GTIs to cover the whole pulse duration or, in severe cases, over several pulses to obtain good model fits. Each series of extracted spectra were assessed on a case-by-case basis to manually find the optimum balance between spectral quality (and therefore well constrained model parameter values) and temporal resolution.

Similarly time resolved analysis was important for the X-ray data. GTIs were selected to produce background corrected spectra with $\sim$30 PHA bins[21] over the 0.3-10 keV energy range, with $\geq$20 counts bin^{-1}. This binning permits the use of χ^2 minimization as a Maximum Likelihood method. If an overlap was present between BAT and XRT GTIs then these spectra were extracted separately over the relevant time periods. Both spectra were then fitted simultaneously within *XSPEC*, allowing for a normalisation offset between the two data sets to compensate for any residual inter-instrumental calibrational uncertainties.

[20]The recommended energy range for spectral fitting, see http://swift.gsfc.nasa.gov/docs/swift/analysis/xrt_digest.html and § 5.7.8 of the *Swift* BAT Software Guide.

[21]Note that this is fewer counts than the spectra selected in chapter 4. The results from that investigation indicated that it is highly unlikely that there will be any additional spectral components in the X-ray data, thus fewer bins were needed to constrain the absorbed power law model parameters.

5.3.2 Correcting for pile-up

BAT spectra do not suffer from pile-up, however, XRT spectra are prone to such effects in both Windowed Timing (WT) and Photon Counting (PC) modes if the incident flux is high enough (see previous discussion and methods for countering pile-up effects in § 2.2.1 and § 4.1 of this work). Grade 0-2 data were extracted for WT mode data using a 20×3 pixel rectangular extraction region for both source and background spectra if no pile-up was present. In the piled-up case the source region was modified to two 10×3 pixel regions placed either side of a central exclusion region, following the methodology of Romano et al. (2006a) (see also § 4.1). PC mode, grade 0-12, spectra were extracted from a 30 pixel radius circular extraction region for the source and a 60 pixel radius circular extraction region for the background. Pile-up effects in PC mode data were countered by extracting source spectra from an annular region (see previous details in § 2.2.1).

Ancillary response functions (ARFs) generated by the `xrtmkarf` function correct the spectral flux for the loss of counts, in both modes, caused by the use of separated (WT) or annular (PC) extraction regions. ARFs do not correct count rates values when pile-up is present. True count rate values are required for X-ray light curve generation thus a correction factor must be calculated manually for each spectrum as detailed in § 5.4.

5.4 Light curve generation

BAT count rate light curves were created by extracting the event light curve, summed over all energy channels, generated by the standard processing pipeline and rebinning it so that each data point contains a signal-to-noise ratio (SNR)[22] = 3. XRT count rate light curves were taken from the *Swift* XRT GRB light curve repository[23] (Evans et al., 2007). Count rate light curves in the observer's reference frame were of limited use, other than to compare gross phenomenological properties and trends. They were converted into flux light curves (extrapolated over the 1-20 keV energy range[24]) in the GRB's rest frame to allow for direct comparisons between bursts. All of the light curves were shifted in the time domain

[22] SNR = 3 was taken to give statistically significant data points whilst still retaining low flux/'weak' features.

[23] http://www.swift.ac.uk/xrt_curves/

[24] This energy range was chosen to provide the maximum overlap of rest frame energy ranges when the observed range of 0.3-10.0 keV was corrected for redshift for each burst.

so that the zero point, T_0, was the *peak* of the first emission pulse (as evaluated at SNR = 3), rather than the BAT trigger time, to avoid the problem of the on-board triggering software missing early 'weak' pulses.

The conversion from a count rate light curve to a flux light curve requires two correction factors to be applied; an energy correction factor (ECF) and a geometrical correction factor (GCF). The ECF takes into account the time dependent spectral properties of the burst by relating the ratio of the (extrapolated) unabsorbed spectral flux over the 1-20 keV energy range in the rest frame of the burst to the count rate of the corresponding spectra. This value is dependent on the spectral parameters measured, therefore a new ECF must be computed for each GTI investigated and applied to the appropriate light curve time interval. A GCF is required to counter the loss of counts due to: the effects of pile-up (see §5.3.2 for details); the exclusion of "hot pixels" during standard pipeline processing; or the damage caused by the micro-meteoroid hit (see Abbey et al. 2006)[25]. The calculation and application of both types of correction factor are described below for BAT and XRT data individually.

5.4.1 Application of correction factors to BAT data

There was no need to apply a GCF to the BAT data since pile-up is not an issue for this detector and micro-meteoroid damage and 'hot' pixel effects are accounted for during standard pipeline processing. Thus only an ECF was required to produce a flux light curve.

The BAT spectra were fit over the 15-150 keV (observer's reference frame) and individual spectra were often well fit by a single power law model[26]. However, extrapolating this power law to lower energy values (1-20 keV in the rest frame of the GRB) was problematic as there may have been a spectral break below the BAT energy band, which may vary with time. A much more accurate ECF can be found by jointly fitting BAT and XRT spectra over contemporaneous GTIs (where applicable), allowing the low energy spectral parameters to be well constrained. For BAT GTIs immediately prior to joint BAT-XRT

[25]The damage caused by the micro-meteoroid resulted in the formation of several new 'hot'/bad columns within the XRT CCD, which are permanently screened out during the processing stages. Unfortunately, these lie near the centre of the CCD, thus the Point Spread Function (PSF) of the GRB often extends over these bad columns.

[26]High energy GRB spectra are more appropriately modelled by a cutoff power law model or Band function but the cutoff (or peak) energy typically lies above the BAT band and cannot be well constrained, thus a single power law model often produced a good fit to the data

GTIs it is possible to fix the low energy power law index and break energy to that found from the joint fit *as long as* the subsequent joint BAT-XRT or XRT-alone spectra do not show strong spectral evolution.

If there were no closely associated (in the time domain) joint BAT-XRT fits, or there was evidence for strong spectral evolution, then there was no real way to constrain the low energy power law index. Other studies such as O'Brien et al. (2006) and O'Brien & Willingale (2007) suggest extrapolating the BAT data to lower energies using a power law index that is a mean of the best fit BAT and best fit XRT spectra. Again, this approach was problematic since the 'best fit' XRT power law index at late times may not be a good indication of the low energy index at earlier times, especially if the BAT GTI occurs prior to a Q-time and the XRT GTI occurs after. In that case there was no firm theoretical ground on which to assume that the emission processes for the two GTIs were related. In such a situation I was limited to modelling and extrapolating the BAT spectra with an unbroken power law alone.

It could be argued that an alternative spectral model could be used to extrapolate the flux to low energies, however, this is only appropriate if the model is a good statistical fit to the data and the resultant model parameters are well constrained. In every case, in this study, the best fit spectral model was either a single power law or broken power law. Even for jointly fit BAT-XRT spectra thermal models, such as blackbody components, were a poor fit to the data. Band models (Band et al., 1993) were also applied to the spectra, however, the limited spectral energy range available meant that no firm limits could be placed on the characteristic, or break, energy value.

5.4.2 Application of correction factors to XRT data

Both a GCF and ECF must be applied to XRT data. Even if the XRT data are not piled-up there is likely to be measurable count rate loss from the overlap of the GRB's PSF and the 'hot' columns created by the micro-meteoroid impact (Abbey et al., 2006) and by additional 'hot' pixels. A separate exposure map for each GTI was created (using the task `xrtexpomap`) and used to generate two ARF files for each spectrum using the `xrtmkarf` function; one with a PSF correction and exposure map applied and another without either applied. The GCF was then calculated by simultaneously fitting the data with the two ARF files with the same spectral model plus a `constant` function,

i.e. `zpo*zwabs*wabs*constant`[27], with the parameter values for the power law and host galaxy absorption (`zwabs`) components tied. The `constant` parameter value was then frozen at a value of 1.00 for the spectrum with the ARF created with no PSF correction and no exposure map. The resulting (untied) value for the `constant` parameter from the other spectrum yields the GCF (which is always ≥ 1). The raw count rate value of the spectrum was then multiplied by this value to create a corrected count rate value.

The same spectral fit was used to ascertain the flux value over the relevant observer reference frame energy range which equated to 1-20 keV (see footnote 24) in the rest frame of the GRB, as calculated by using the appropriate redshift value for each burst. The ECF was then calculated by taking the ratio of the flux to the corrected count rate value. At later times, during the latter stages of the afterglow decay, there was insufficient incident flux to accumulate a statistically reliable spectrum. For these time intervals the last measurable GCF and ECF values were used instead. This was a valid approach as by this stage of the afterglow evolution the spectral properties, and therefore ECF values, had settled to a constant value. This was verifed by checking that the hardness ratio (HR) plots were constant over these time intervals, indicating that there was no spectral change.

5.4.3 Converting to luminosity light curves

To create luminosity light curves the luminosity distances, D_L, to each burst were calculated given their known redshift and using the standard cosmological parameters (Spergel et al., 2003, see also § 2.4.3 of this work): $H_0 = 71$ km s^{-1}, $\Omega_M = 0.27$ and $\Omega_\Lambda = 0.73$. These values of D_L were then used to compute a conversion factor from units of flux (ergs cm^{-2} s^{-1}) to luminosity (ergs s^{-1}) which are reported in table 5.2. No further K-corrections (see § 2.4.3) were required since the flux light curves had already been corrected to the rest frame values of each burst individually using the data processing methods described in § 5.4.1 and 5.4.2.

[27]The values for redshift were frozen at the known value and the `wabs` component was frozen at the appropriate galactic absorption column value given by Dickey & Lockman (1990).

GRB	Redshift	D_L ($\times 10^4$ Mpc)	Conversion factor ($\times 10^{58}$ cm^2)
050319	3.240	2.84	9.65
050820A	2.612	2.18	5.69
060115	3.530	3.14	11.80
060124	2.297	1.87	4.18
060210	3.910	3.55	15.10
060418	1.489	1.09	1.42
060526	3.221	2.82	9.52
060607A	3.082	2.67	8.53
060714A	2.711	2.28	6.22
060904B	0.703	0.43	0.22
061121	1.314	0.93	1.03

Table 5.2: Table containing luminosity distance, D_L, for each burst in our redshift sample and their respective light curve flux-to-luminosity conversion factors.

5.5 Creating hardness ratio (HR) plots

The values for the XRT hardness ratio (HR) plots, with an energy band ratio of (1.5-10 keV)/(0.3-1.5 keV), for the GRBs in the sample have been collated from the *Swift* /XRT GRB light curve repository website[28] (Evans et al., 2007).

BAT HR plots, with an energy band ratio of (50-350 keV)/(15-50 keV)[29], were calculated directly from the four channel light curve files generated by the standard data processing pipeline, which contain the count rate data for the following energy ranges: 15-25, 25-50, 50-100 and 100-350 keV. A HR series, with a constant SNR value per data point, was created in a similar manner to the full energy range light curve in §5.4. The counts in the 'low' energy band (15-25 and 25-50 keV) and 'high' energy band

[28] http://www.swift.ac.uk/xrt_curves/

[29] As measured in the observer's reference frame.

(50-100 and 100-350 keV) were summed separately; a HR point was only generated when the SNR in *both* bands was ≥ 1. Using a value of SNR $\gg$1 results in poorly time resolved HR series.

5.6 Modelling the light curves

Individual luminosity light curves, HR plots (BAT and XRT) and power law photon indices plotted with respect to the rest frame time for all of the GRBs included in this sample can be found in Appendix 5.A. The 1-20 keV luminosity light curves generated, as described in § 5.4, were modelled within the *QDP* program as a series of sharply broken power law segments superimposed upon which were multiple Fast Rise Exponential Decay (FRED) components, one for each distinguishable emission pulse (see Apeendix 5.B). The FRED model, called *BURS* within *QDP*, is defined as a linear rise followed by an exponential decay given by the following equations;

$$FRED = \begin{cases} 0 & \text{for X<ST;} \\ BN * (X - ST)/(PT - ST) & \text{for ST<X<PT;} \\ BN * \exp(-(X - PT)/DT) & \text{for PT<X,} \end{cases} \quad (5.1)$$

where *BN* is the burst normalisation or 'peak' flux, *ST* is the start time of the FRED component, *PT* is the time of the pulse peak and *DT* is the decay coefficient of the exponential decay.

The whole light curve was not modelled with a series of smoothly broken power laws. From experience (see chapter 2 of this work) it is normally very difficult to constrain the parameters of a smoothly broken power law fit unless the light curve is very well sampled, even without the added complication of additional light curve components such as FRED pulses. The smoothing factors are often problematic and show a high degree of degeneracy unless severe restrictions are placed on the allowed parameter ranges of the power law indices and break times. Since there was no a priori reason to enforce such restrictions afterglow models with multiple smooth breaks would not produce any meaningful fits over the full light curve temporal range. Therefore modelling the light curves with a smoothly broken power law was limited to the data points after phase I emission, or the end of the last decay portion of a late time flare, i.e. the start of the 'uncontaminated' phase II emission and beyond. A power law model with a single smooth break was used instead of a smooth doubly broken power law model since the

degeneracy of a single smoothing factor was challenging enough to constrain; it would be impossible to constrain the parameters of two such breaks with the temporal resolution of the light curves in this study.

5.7 Analysis

The spectral properties of the bursts analysed in this study were consistent with those reported for other *Swift* GRBs and are illustrated in Appendix 5.A. Where sufficient temporal resolution was available at early times the individual pulses showed the standard flare spectral properties (spectra were harder than the underlying afterglow and an evolution from spectrally hard to soft was seen over time) as described in previous work by Burrows et al. (2005b); Falcone et al. (2006); Romano et al. (2006b). Late-time photon indices for my sample showed no significant spectral variation and had an average value of $1.97^{+0.03}_{-0.02}$. This value is consistent with the average photon index of the sample presented in Nousek et al. (2006) (2.02 ± 0.05; 27 GRBs) and the median value obtained from the sample of automated spectral fits[30] to PC mode spectra[31] (2.16; 306 GRBs).

5.7.1 Are precursors spectrally different to main emission?

There was an indication in 8/11 of the cases analysed in this study that the photon index of the first GTI was slightly lower (i.e. harder) than the subsequent individual and averaged GTI spectra covering pulse activity, though the values were sometimes consistent at the limits of their 90% confidence error ranges (see table 5.3). Of the other three cases, two had spectra that were consistent within the error limits with the subsequent spectra, whilst the first GTI spectrum of GRB 061121 showed evidence of being softer than later spectra. This is counter to the trends noted in previous studies in which the majority (K95, McBreen et al. 2006), or all (Murakami et al. 1991, 1992, L05), of the precursors were found

[30] In virtually all cases the spectral parameters of the absorbed power law model fits conducted by the automated process were well constrained, with photon index values of $\sim$2. However, in rare cases ($\sim$ 5 spectra), the automated routine selected an incorrect source region. The resultant fits to non-GRB spectra produced poorly constrained parameter values with spuriously large photon index values. Thus the average photon index value found from the whole sample was skewed by these values; I therefore took the median value as a more accurate representation of the spectral properties of the true GRB spectra in the sample.

[31] P. Evans, private communication 2008.

to be softer than the subsequent emission. However, given that some of the GTIs covered more than one pulse (see § 5.3.1) it was difficult to quantify whether this was a real effect or was the result of averaging several individual pulse spectra.

The quality of data and the method used to produce the HR time series (Appendix 5.A) produced data points at early epochs with such large error bars that it was not possible to distinguish with any degree of certainty whether spectral variation was occurring. Separate HR values were calculated using intervals that spanned (a) the first pulse (as defined in Appendix 5.B), (b) the remaining period of pulse activity[32] and (c) the total emission period. A Spearman Rank Correlation test (Press et al., 1992, see also footnote 9) was calculated between the HR value of the first pulse and the average HR of the total emission period with null results ($r_s = 0.14$, P $= 0.69$); a similar result was found between the HR of the first pulse versus the average HR of the remainder of the emission period ($r_s = -0.17$, P $= 0.61$). The Kendall Tau[33] results for the same parameter sets were $\tau = 0.05$ (P$= 0.88$) and $\tau = -0.09$ (P$= 0.76$) respectively. See table 5.4. From these results, and the spectral fits noted above, I find no strong evidence to suggest that the spectral properties of the first pulse was different to that of the later period of emission.

5.7.2 Is there spectral evolution during long Q-times?

Q-times, by their definition, are periods of low flux therefore it was not possible to extract any statistically meaningful spectra over such intervals. Any spectra extracted were poorly constrained; the error ranges made it extremely difficult to ascertain whether the spectral parameters were consistent with the instrumental background emission or whether there was a contribution from any underlying afterglow emission. Again the error bars present on the HR time series (Appendix 5.A) were so large that it was not possible to conclusively state whether there was any evidence for spectral evolution over these periods.

[32]The HR of the remainder of the emission period was calculated over a period that began at the start of the second pulse and ended when the final pulse had decayed to 5% of its peak luminosity.

[33]The Kendall Tau coefficient (Kendall, 1938) is another non-parametric statistic used to measure the correlation between two sets of variables. Like the Spearman Rank coefficient it varies between values of $-1 \rightarrow 1$; a value of $\tau = 0$ indicates no correlation, 1 a positive correlation and -1 an anti-correlation between the variable sets. Calculations carried out using online software at http://www.wessa.net/rwasp_kendall.wasp/ (Wessa, 2008). The numerical values of r_s and τ are not expected to agree precisely, since they originate from different tests.

GRB	Photon index of first GTI†	Photon index (indices) subsequent GTIs	Average photon index of the remainder of the emission period‡.
050319	$1.86^{+0.17}_{-0.16}$	$2.06^{+0.22}_{-0.23}$	$2.06^{+0.22}_{-0.23}$
050820A	$1.64^{+0.64}_{-0.58}$	$1.68^{+0.15}_{-0.15}$, $1.75^{+0.17}_{-0.17}$, $1.64^{+0.22}_{-0.21}$	$1.37^{+0.08}_{-0.08}$
		$0.92^{+0.14}_{-0.15}$, $1.23^{+0.08}_{-0.07}$, $1.10^{+0.32}_{-0.31}$	
060115	$1.78^{+0.19}_{-0.19}$	$1.70^{+0.15}_{-0.15}$	$1.70^{+0.15}_{-0.15}$
060124	$1.82^{+0.23}_{-0.22}$	$2.47^{+0.67}_{-0.53}$	$2.47^{+0.67}_{-0.53}$
060210	$1.24^{+0.28}_{-0.29}$	$0.93^{+0.13}_{-0.13}$, $1.37^{+0.09}_{-0.09}$, $1.69^{+0.35}_{-0.33}$	$1.61^{+0.17}_{-0.15}$
		$1.75^{+0.37}_{-0.34}$, $2.30^{+0.67}_{-0.53}$	
060418	$1.46^{+0.09}_{-0.09}$	$1.38^{+0.07}_{-0.07}$, $1.65^{+0.12}_{-0.12}$, $1.75^{+0.18}_{-0.17}$	$1.75^{+0.08}_{-0.07}$
		$1.69^{+0.08}_{-0.08}$, $2.15^{+0.20}_{-0.19}$, $1.89^{+0.33}_{-0.30}$	
060526	$1.48^{+0.21}_{-0.21}$	$1.96^{+0.37}_{-0.34}$, $2.10^{+0.20}_{-0.19}$, $1.96^{+0.72}_{-0.59}$	$2.01^{+0.28}_{-0.24}$
060607A	$1.34^{+0.17}_{-0.17}$	$1.37^{+0.07}_{-0.07}$, $1.56^{+0.12}_{-0.12}$, $1.62^{+0.26}_{-0.25}$	$1.52^{+0.10}_{-0.10}$
060714	$1.72^{+0.20}_{-0.19}$	$2.01^{+0.17}_{-0.16}$, $2.16^{+0.13}_{-0.12}$	$2.09^{+0.11}_{-0.10}$
060904	$1.39^{+0.11}_{-0.11}$	$2.54^{+0.35}_{-0.31}$	$2.54^{+0.35}_{-0.31}$
061121	$1.70^{+0.13}_{-0.13}$	$1.56^{+0.05}_{-0.05}$, $1.32^{+0.04}_{-0.04}$, $1.33^{+0.03}_{-0.03}$	$1.50^{+0.04}_{-0.04}$
		$1.30^{+0.04}_{-0.04}$, $1.73^{+0.12}_{-0.12}$, $1.72^{+0.13}_{-0.13}$	
		$1.89^{+0.20}_{-0.19}$, $1.14^{+0.19}_{-0.10}$	

Table 5.3: Table summarising the photon indices obtained from spectral fits to the BAT data during pulse emission. See § 5.3.1 for a description of how the GTIs were chosen; note that this means that some GTIs covered more than one pulse in order to accumulate a statistically relevant spectrum and therefore represent the average spectral form over these times. These photon indices are presented in graphical form in the fourth panel of each figure in Appendix 5.A. † The first GTI begins at the start time of the first pulse. ‡ The photon index reported here is an unweighted average of the photon indices in the preceding column.

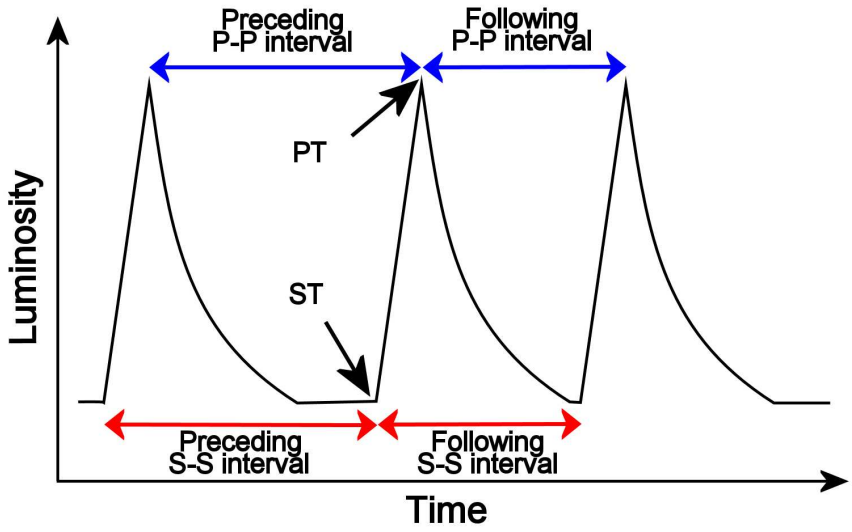

Figure 5.2: A diagram illustrating the various intervals used for the Spearman Rank correlations. Individual pulses were modelled with a Fast Rise Exponential (FRED) model (see § 5.6). ST is the pulse start time, PT is the pulse peak time and DT is the decay coefficient of the exponential decay. The pulse duration is deemed to cover a time span beginning at the start time of the burst and ending when the pulse decays to 5% of its peak intensity; therefore duration $= ((PT - ST) + (3DT))$.

5.7.3 Emission pulses: r_s and τ correlations.

Following the work of previous studies, Spearman Rank Correlations (Press et al., 1992) were conducted for various temporal and energetic parameters of these bursts using model fits to GRB rest frame corrected flux and luminosity light curves. Parameter sets with weak or no correlation ($-0.4 < r_s < 0.4$) are reported in table 5.4, whilst those with stronger correlations ($r_s > 0.4$ or $r_s < -0.4$) are shown in table 5.5. Figure 5.2 illustrates the various temporal intervals used for the Spearman Rank correlations. In addition Kendall Tau (Kendall, 1938) correlations were also carried out for the same parameter sets and are reported in table 5.4 and 5.6.

As expected, a positive correlation was found between T_{90} and, to a lesser extent, T_{50} with the largest interval within a burst ($r_s = 0.47$ and 0.38, $\tau = 0.39$ and 0.28 respectively; see tables 5.4, 5.5 and 5.6), i.e. the longer duration bursts were able to accommodate long Q-time intervals. Following the work of L05 Spearman Rank correlations were also calculated for T_{90}, and T_{50}, versus the duration of the first

pulse (c.f. the 'precursor'). L05 reported a 'mild' but 'not statistically compelling' correlation ($r_s = 0.11$) between T_{90} and precursor duration, whereas this study found a weak anti-correlation; $r_s(T_{90}) = -0.27$, $\tau(T_{90}) = -0.17$, $r_s(T_{50}) = -0.38$ and $\tau(T_{50}) = -0.28$ (see table 5.4). The duration of emission before and after the largest interval versus the largest interval of each GRB was also calculated (see tables 5.5 and 5.6 and figure 5.3(a)). The duration of the prior emission appeared to be anti-correlated with the duration of the largest interval ($r_s = -0.45$, $\tau = -0.31$), conversely the duration of the post emission appeared to be correlated with the duration of the largest interval ($r_s = 0.53$, $\tau = 0.38$). However, given the limited sample number in my study, further cases need to be evaluated before a conclusive statement can be made about the certainty of these correlations.

Similarly to NP02, a strong correlation was found between pulse duration and the preceding interval when using both pulse start and peak times as reference points; $r_s = 0.62$ ($P < 1.0 \times 10^{-6}$) and $r_s = 0.73$ ($P < 1.0 \times 10^{-6}$) respectively, see table 5.5 and figure 5.3(b). The equivalent τ values for pulse duration versus the preceding interval using the pulse start and peak times were $\tau = 0.44$ ($P = 5.4 \times 10^{-7}$) and $\tau = 0.54$ ($P = 8.8 \times 10^{-10}$) respectively, see table 5.6. A weaker correlation was also found between the following start-to-start interval and pulse duration with $r_s = 0.45$ ($P = 3.2 \times 10^{-4}$) and $\tau = 0.33$ ($P = 1.9 \times 10^{-4}$). This may reflect the result that 60% of the sample analysed by NP02 also showed a correlation between pulse duration and the following interval. However, in the NP02 study the individual bursts contained a sufficient number of pulses to conduct correlations for each burst separately, whereas my results are based on a consideration of my entire sample. This amalgamation may be acting to reduce the significance of the correlation. Interestingly a far less convincing correlation was seen between the following peak-to-peak interval and pulse duration ($r_s = 0.26$, P(r_s)$= 0.05$ and $\tau = 0.25$, P(τ)$= 0.01$).

C07 noted an anti-correlation ($r_s = -0.54$, $P = 5.24 \times 10^{-6}$) between the pulse peak time and peak intensity using values in the observer's reference frame, though C07 warn that this correlation could be biased by flares observed at late times. Correcting to the rest frame of the GRB I found a similar anti-correlation between start/peak times versus peak luminosity and peak flux. The peak luminosity correlations were: start time versus peak luminosity, $r_s = -0.45$ ($P= 8.4 \times 10^{-5}$) and $\tau = -0.30$ ($P = 2.7 \times 10^{-4}$); and peak time versus peak luminosity $r_s = -0.48$ ($P = 2.6 \times 10^{-5}$) and $\tau = -0.32$ ($P = 5.5 \times 10^{-5}$). The peak flux correlations were: start time versus peak flux, $r_s = -0.44$ ($P = 1.0 \times 10^{-4}$) and $\tau = -0.28$ ($P = 5.1 \times 10^{-4}$); and peak time versus peak flux, $r_s = -0.46$ ($P = 6.6 \times 10^{-5}$) and $\tau = -0.29$ ($P = 3.5 \times 10^{-4}$). See tables 5.5 and 5.6 and figures 5.3 c, d, e) for the

bursts considered in this work. A true anti-correlation between these respective parameters sets would be expected to produce a scatter of points around a central trend line, however, the figures appear to indicate that there is a threshold, with respect to time, above which pulses can be detected in the data. Above this threshold the data points are widely scattered. It is possible that the underlying afterglow may be swamping out weak pulses at early times or that the mechanism controlling the production of the pulses may have a higher threshold for rapid energy release at early times. It is not likely to be a detector resolution effect as C07 proved that the instrumental resolution of the BAT is sufficient to detect early narrow pulses, see their § 4.4.1 and figure 8. C07 also conducted a series of simulations to ascertain the impact of the underlying afterglow on flare detection, see their § 4.4.2 and figure 10. They found that a flare with a ∼90% detection probability at 10 ks only had a ∼30% detection probability if it occurred at 300 s. C07 were not able to produce an absolute quantitative value on the flare detection threshold at early times but note that it would have a significant impact on the ability to detect weak pulses at such times. However, if the anti-correlations noted in my study (i.e. start time versus peak flux etc) had been purely instrumental in origin than an anti-correlation between pulse total fluence with respect to start, or peak, time would also have been expected; neither of which was noted (see table 5.4).

Correlation calculations were also carried out separately for pulses that occurred before, and after, the Q-times of the respective bursts. The r_s values for pulse start time versus peak flux did not noticeably change when they were split in this manner; r_s(before Q-time) = -0.44, r_s(after Q-time) = -0.40 compared to r_s(total) = -0.44. See table 5.6 for the equivalent changes in τ values. This partition caused the anti-correlation between pulse peak time and peak flux to become marginally more significant for pre-Q-time pulses (r_s(before Q-time) = -0.52) but did not affect the post-Q-time pulses (r_s(after Q-time) = -0.41 compared to r_s(total) = -0.46). Again see table 5.6 for the equivalent changes in τ values. There was a noticeable decrease in the P values, compared to their original values, of all of the r_s and τ values calculated in this manner, see tables 5.5 and 5.6. This is most likely a result of the reduced sample sizes available before and after the Q-time. Separating the pulses into the two temporal subsets did cause a noticeable loss of significance for the anti-correlation found between pulse start time and peak luminosity (r_s(before Q-time) = -0.20 and r_s(after Q-time) = -0.35 compared to r_s(total) = -0.45) and pulse peak time and peak luminosity (r_s(before Q-time) = -0.33 and r_s(after Q-time) = -0.31 compared to r_s(total) = -0.48). A loss of correlation with a similar magnitude was seen for the τ values (see table 5.6).

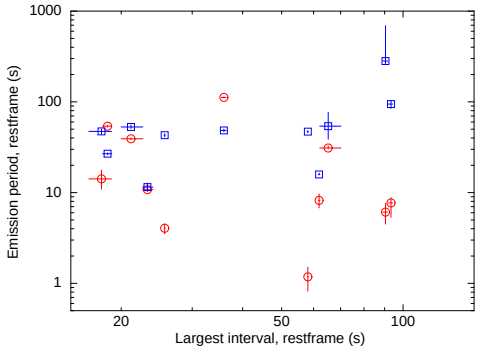

(a) Correlation plot between the largest interval† versus the emission period before (red circles; $r_s = -0.45$, $\tau = -0.31$) and after (blue squares; $r_s = 0.53$, $\tau = 0.38$) the largest interval.

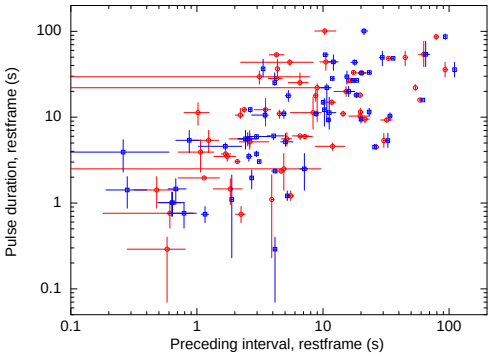

(b) Correlation plot between the preceding start-to-start (red circles; $r_s = 0.62$, $\tau = 0.44$) or peak-to-peak (blue squares; $r_s = 0.73$, $\tau = 0.54$) versus pulse duration.

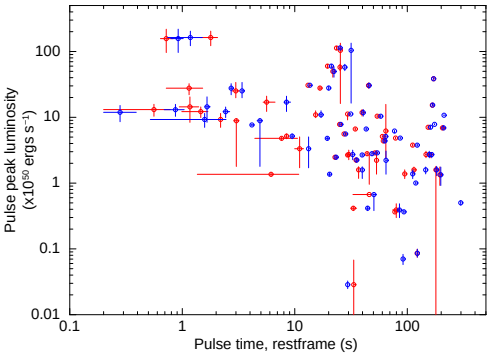

(c) Correlation plot between the start time (red circles; $r_s = -0.45$, $\tau = -0.30$) and peak time (blue squares; $r_s = -0.48$, $\tau = -0.32$) of the pulse versus the peak luminosity.

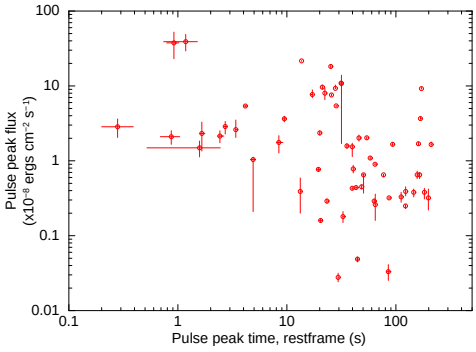

(d) Correlation plot between the peak time of the pulse versus the peak flux ($r_s = -0.46$, $\tau = -0.29$).

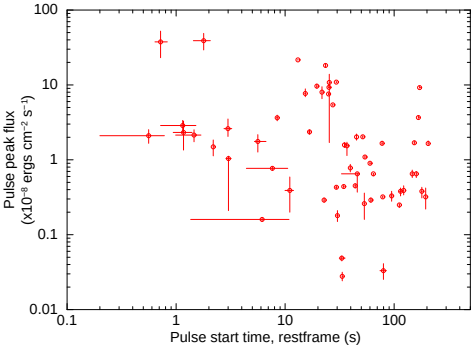

(e) Correlation plot between the start time of the pulse versus the peak flux ($r_s = -0.44$, $\tau = -0.28$).

Figure 5.3: Spearman Rank correlation plots between sets of pulse properties (see also tables 5.5 and 5.6). Quantities are as measured in the rest frame of the burst. (b) - (d) Show data from the total emission period. †As measured between successive pulse start times.

Counter to the statement of C07 that there was no evidence for a correlation between the preceding pulse interval and the peak brightness of the pulses, I found evidence for an anti-correlation between both start-to-start and peak-to-peak preceding intervals with both peak flux and peak luminosity. The peak flux correlations were: preceding start-to-start interval versus peak flux, $r_s = -0.50$ (P $= 5.0 \times 10^{-5}$) and $\tau = -0.36$ (P $= 6.0 \times 10^{-5}$); and preceding peak-to-peak interval versus peak flux, $r_s = -0.56$ (P $= 4.0 \times 10^{-6}$) and $\tau = -0.40$ (P $= 9.5 \times 10^{-6}$). The peak luminosity correlations were: preceding start-to-start interval versus peak luminosity, $r_s = -0.51$ (P $= 3.8 \times 10^{-5}$) and $\tau = -0.36$ (P $= 6.0 \times 10^{-5}$); and preceding peak-to-peak interval versus peak luminosity, $r_s = -0.62$ (P $< 1.0 \times 10^{-6}$) and $\tau = -0.47$ (P $= 9.3 \times 10^{-6}$). See tables 5.5 and 5.6 and figures 5.4 a, b, c and d for the bursts considered in this work.

Again correlation calculations were carried out separately for pulses that occurred before, and after, the Q-times of the respective bursts. The r_s values for preceding start-to-start (and peak-to-peak) intervals versus peak flux did not noticeably change when they were split in this manner, see table 5.5 and 5.6. However, there was a noticeable decrease in the P values compared to their original values, again most likely a result of the reduced sample sizes available. Separating the pulses in the same manner decreased the overall anti-correlations seen the preceding start-to-start (and peak-to-peak) intervals versus peak luminosity. The start-to-start correlations were: r_s(before Q-time) $= -0.40$ and r_s(after Q-time) $= -0.47$ compared to r_s(total) $= -0.51$. The peak-to-peak correlations were: r_s(before Q-time) $= -0.48$ and r_s(after Q-time) $= -0.63$ compared to r_s(total) $= -0.62$. Note that the exception for the peak-to-peak case where there was no notable change in the correlation for pulses after the Q-time compared to the original value. A loss of correlation with a similar magnitude was seen for the τ values (see table 5.6). Furthermore the correlations seen between the following pulse intervals and pulse flux, or luminosity, were much weaker, see table 5.4.

There appeared to be no (anti-)correlation between any combination of pulse start (peak) time or preceding (following) intervals with respect to pulse total fluence or total energy. This seems to indicate that the mechanism producing the pulses has no memory of when the GRB started nor is there an evolution of energy release over time (bar the point at which the central engine ceases activity completely). However, a positive correlation was seen between pulse start, and peak, times and the pulse decay constant 'DT' ($r_s = 0.52$ and 0.50, $\tau = 0.37$ and 0.41 respectively, see figure 5.4(e)). Perna et al. (2006) proposed that X-ray flares are due to accretion from a fragmented disk. Accretion masses, or 'blobs', initially far from the central black hole take longer to be accreted, due to the viscous evolution

of the disk, and are therefore more spread out when accretion occurs. Consequently the accretion rate is lower for later events. This naturally gives rise to the anti-correlations seen between: start (peak) times and peak luminosity; start (peak) times with 'DT'; and pulse duration and peak luminosity (see figure 5.4(f)). An equivalent behaviour could also potentially be seen if a magnetic barrier is responsible for moderating a continuous accretion flow near the black hole (Proga & Zhang, 2006).

5.7.4 Pulse distribution

C07 studied the relationship between the BAT flares and XRT pulses using the ratio of peak intensities between two successive pulses/flares. They found that the distribution of the log of this ratio ($\log(\mathrm{peak}_{i+1}/\mathrm{peak}_i)$) was distributed normally for both samples. Furthermore the BAT and XRT samples appeared to be closely related, see figure 5.5(a). Combining the two samples produced a distribution with $<\log(\mathrm{peak}_{i+1}/\mathrm{peak}_i) >= -0.258$ and $\sigma_{\log} = 0.68$. However, C07 argued that two outlying pulses should be excluded from this distribution giving best fit values of $<\log(\mathrm{peak}_{i+1}/\mathrm{peak}_i) >= -0.157$ and $\sigma_{\log} = 0.41$. C07 concluded that this was evidence for a common origin of γ-ray pulses and X-ray flares. On average, the next event had a peak $10^{-0.157} \sim 0.7$ times that of the preceding event with a scatter between 0.3 and 1.8 (quoted at the 90% confidence level for one interesting parameter).

A similar study was conducted using the pulse data obtained in this study, see figure 5.5(b). Fitting a Gaussian to this distribution gave $<\log(\mathrm{peak}_{i+1}/\mathrm{peak}_i) > = 5 \times 10^{-4}(+8.61 \times 10^{-2}, -8.13 \times 10^{-2})$ and $\sigma_{\log} = 0.45(+0.12, -0.09)$; $\chi^2/\nu = 45/19$. This indicated that, on average, the following pulse had the same peak as the preceding one, with a scatter between 0.82 and 1.21 (quoted at the 90% confidence level for one interesting parameter). Even given the large error range associated with the value of $<\log(\mathrm{peak}_{i+1}/\mathrm{peak}_i) >$ for this study it does not appear to be fully consistent with the average behaviour noted by C07. The scatter range, whilst narrower than that reported by C07, is consistent.

5.7.5 Average pulse luminosity light curve

Lazzati et al. (2008) compute the average luminosity of X-ray flares as a function of time, for a sample of 10 *Swift* LGRBs. They concluded that the mean luminosity, averaged over a timescale longer than the duration of the individual flares, declines as a power law in time with an index of $\sim -1.5 \pm 0.16$.

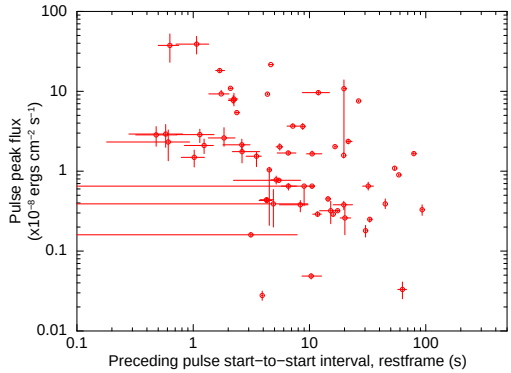

(a) Correlation plot between preceding start-to-start interval versus pulse peak flux ($r_s = -0.50$, $\tau = -0.36$).

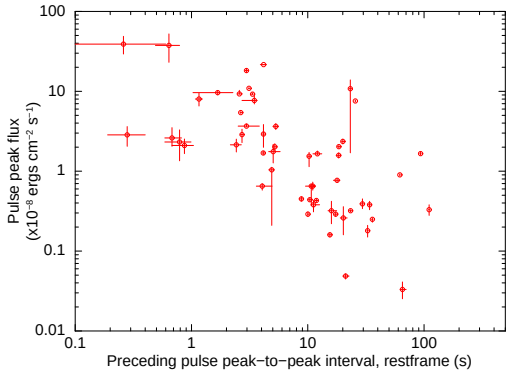

(b) Correlation plot between preceding peak-to-peak interval versus pulse peak flux ($r_s = -0.56$, $\tau = -0.40$).

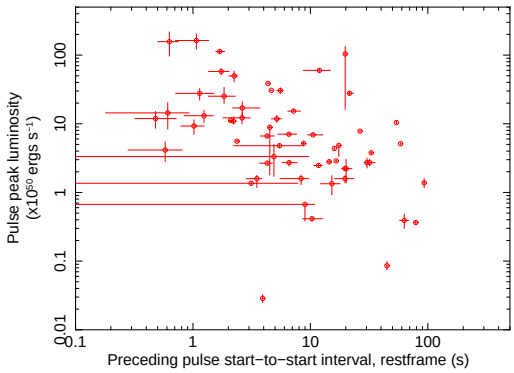

(c) Correlation plot between preceding start-to-start interval versus pulse peak luminosity ($r_s = -0.51$, $\tau = -0.36$).

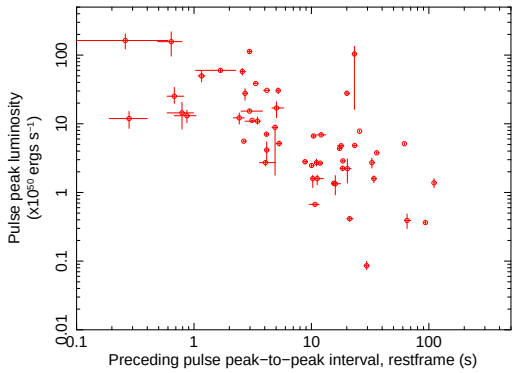

(d) Correlation plot between preceding peak-to-peak interval versus pulse peak luminosity ($r_s = -0.62$, $\tau = -0.47$).

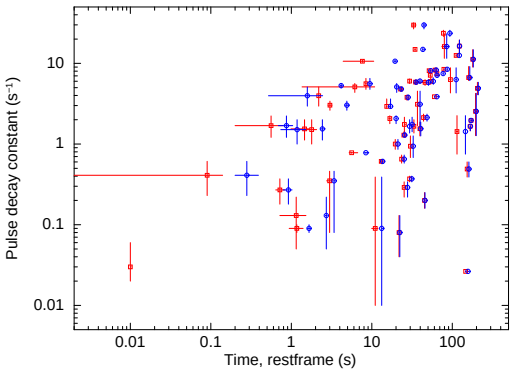

(e) Correlation plot between flare start (red squares; $r_s = 0.52$, $\tau = 0.37$), and peak (blue circles; $r_s = 0.50$, $\tau = 0.41$), time versus flare decay constant, 'DT'.

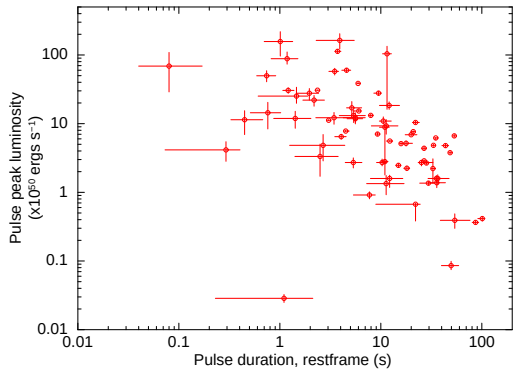

(f) Correlation plot between pulse duration and pulse peak luminosity ($r_s = -0.64$, $\tau = -0.47$).

Figure 5.4: Spearman Rank correlation plots between sets of pulse properties (see also tables 5.5 and 5.6) showing data from the total emission period. Quantities are as measured in the rest frame of the burst.

Correlation properties	r_s	P*	τ	P*
HR of 1st pulse vs average HR of total emission	0.14	0.69	0.05	0.88
HR of 1st pulse vs HR of the remainder of the emission	-0.17	0.61	-0.09	0.76
T_{50} vs largest interval	0.38	$> 5.0 \times 10^{-2}*$	0.28	0.35
T_{90} vs 1st pulse duration	-0.27	$> 5.0 \times 10^{-2}*$	-0.17	0.60
T_{50} vs 1st pulse duration	-0.38	$> 5.0 \times 10^{-2}*$	-0.28	0.35
P-P‡ interval (following) vs pulse duration	0.26	0.05	0.25	0.01
S-S† interval (following) vs peak flux	-0.33	0.01	-0.22	0.02
P-P interval (following) vs peak flux	-0.28	0.03	-0.20	0.03
S-S interval (following) vs peak luminosity	-0.35	0.01	-0.26	0.01
P-P interval (following) vs peak luminosity	-0.36	0.01	-0.27	0.01
Start time vs total fluence	0.11	0.35	0.07	0.36
Peak time vs total fluence	0.15	0.21	0.10	0.24
Start time vs total energy	0.08	0.51	0.06	0.47
Peak time vs total energy	0.11	0.34	0.08	0.31
S-S interval (following) vs total fluence	0.12	0.37	0.07	0.42
S-S interval (preceding) vs total fluence	0.05	0.71	0.04	0.69
P-P interval (following) vs total fluence	0.11	0.40	0.08	0.38
P-P interval (preceding) vs total fluence	0.02	0.86	0.01	0.89
S-S interval (following) vs total energy	0.11	0.39	0.07	0.43
S-S interval (preceding) vs total energy	-0.03	0.80	-0.03	0.76
P-P interval (following) vs total energy	0.07	0.56	0.06	0.50
P-P interval (preceding) vs total energy	0.01	0.98	0.01	0.94

Table 5.4: Summary of Spearman (r_s) and Kendall Tau (τ) Rank Order Correlation data. Various property sets, over the whole period of activity, are reported in the first column. Probabilities marked with '$*$' were calculated using tabulated confidence values for correlations with fewer than 10 degrees of freedom (www.sussex.ac.uk/users/grahamh/RM1web/Rhotable.htm). * Probabilities are quoted as two-tailed values. † 'S-S' interval was measured between start times of the respective flares. ‡ 'P-P' interval was measured between peak times of the respective flares.

Correlation properties	Total emission period		Emission before Q-time		Emission after Q-time	
	r_s	P*	r_s	P*	r_s	P*
T_{90} vs largest interval	0.47	$> 5.0 \times 10^{-2}*$	-	-	-	-
Emission duration before largest interval vs largest interval†	-0.45	1.7×10^{-1}	-	-	-	-
Emission duration after largest interval vs largest interval‡	0.53	$> 5.0 \times 10^{-2}*$	-	-	-	-
S-S†† interval (preceding) vs pulse duration	0.62	$<1.0\times10^{-6}$	0.57	2.2×10^{-3}	0.55	7.6×10^{-4}
P-P‡‡ interval (preceding) vs pulse duration	0.73	$<1.0\times10^{-6}$	0.57	2.5×16^{-3}	0.75	$<1.0\times10^{-6}$
S-S interval (following) vs pulse duration	0.45	3.2×10^{-4}	0.32	5.6×10^{-2}	0.86	$<1.0\times10^{-6}$
Start time vs peak flux	-0.44	1.0×10^{-4}	-0.44	7.0×10^{-3}	-0.40	2.0×10^{-2}
Peak time vs peak flux	-0.46	6.6×10^{-5}	-0.52	9.0×10^{-4}	-0.41	1.3×10^{-2}
Start time vs peak luminosity	-0.45	8.4×10^{-5}	-0.20	2.4×10^{-1}	-0.35	3.6×10^{-2}
Peak time vs peak luminosity	-0.48	2.6×10^{-5}	-0.33	8.2×10^{-2}	-0.31	1.5×10^{-1}
S-S interval (preceding) vs peak flux	-0.50	5.0×10^{-5}	-0.55	3.8×10^{-3}	-0.60	2.2×10^{-3}
P-P interval (preceding) vs peak flux	-0.56	4.0×10^{-6}	-0.62	6.4×10^{-4}	-0.66	9.2×10^{-4}
S-S interval (preceding) vs peak luminosity	-0.51	3.8×10^{-5}	-0.40	4.2×10^{-2}	-0.47	2.4×10^{-2}
P-P interval (preceding) vs peak luminosity	-0.62	$<1.0\times10^{-6}$	-0.48	2.4×10^{-2}	-0.63	1.8×10^{-3}
Start time vs decay constant	0.52	2.0×10^{-6}	0.36	2.2×10^{-2}	0.30	8.0×10^{-2}
Peak time vs decay constant	0.50	2.6×10^{-5}	0.49	2.2×10^{-3}	0.30	8.0×10^{-2}
Pulse duration vs peak flux	-0.59	$<1.0\times10^{-6}$	-0.50	1.5×10^{-3}	-0.62	1.1×10^{-4}
Pulse duration vs peak luminosity	-0.64	$<1.0\times10^{-6}$	-0.54	6.4×10^{-4}	-0.61	1.2×10^{-4}

Table 5.5: Summary of Spearman Rank Order Correlation data. Various property sets are reported in the first column. * Probabilities are quoted as two-tailed values. † Interval measured between successive pulse start times. ‡ Several GRBs had emission that appeared to extend into a data gap thus the post-Q-time durations could not be calculated. †† 'S-S' interval was measured between start times of the respective flares. ‡‡ 'P-P' interval was measured between peak times of the respective flares. Probabilities marked with '$*$' were calculated using tabulated confidence values for correlations with fewer than 10 degrees of freedom (www.sussex.ac.uk/users/grahamh/RM1web/Rhotable.htm).

Correlation properties	Total emission period		Emission before Q-time		Emission after Q-time	
	τ	P*	τ	P*	τ	P*
T_{90} vs largest interval	0.39	1.8×10^{-1}	-	-	-	-
Emission duration before largest interval vs largest interval†	-0.31	2.1×10^{-1}	-	-	-	-
Emission duration after largest interval vs largest interval‡	0.38	1.2×10^{-1}	-	-	-	-
S-S†† interval (preceding) vs pulse duration	0.44	5.4×10^{-7}	0.42	3.1×10^{-3}	0.39	1.4×10^{-3}
P-P‡‡ interval (preceding) vs pulse duration	0.54	8.8×10^{-10}	0.40	4.2×10^{-3}	0.59	1.6×10^{-6}
S-S interval (following) vs pulse duration	0.33	1.9×10^{-4}	0.22	5.5×10^{-2}	0.68	5.6×10^{-6}
Start time vs peak flux	-0.28	5.1×10^{-4}	-0.30	9.6×10^{-3}	-0.25	4.2×10^{-2}
Peak time vs peak flux	-0.29	3.5×10^{-4}	-0.36	1.9×10^{-3}	-0.27	2.1×10^{-2}
Start time vs peak luminosity	-0.30	2.7×10^{-4}	-0.13	2.7×10^{-1}	-0.23	5.5×10^{-2}
Peak time vs peak luminosity	-0.32	5.5×10^{-5}	-0.23	4.8×10^{-2}	-0.20	1.0×10^{-1}
S-S interval (preceding) vs peak flux	-0.36	6.0×10^{-5}	-0.30	3.4×10^{-2}	-0.35	2.0×10^{-2}
P-P interval (preceding) vs peak flux	-0.40	9.5×10^{-6}	-0.43	1.6×10^{-3}	-0.54	5.1×10^{-4}
S-S interval (preceding) vs peak luminosity	-0.36	6.0×10^{-5}	-0.30	3.4×10^{-2}	-0.35	2.0×10^{-2}
P-P interval (preceding) vs peak luminosity	-0.47	9.3×10^{-6}	-0.37	1.8×10^{-2}	-0.51	1.2×10^{-3}
Start time vs decay constant	0.37	2.2×10^{-6}	0.24	3.9×10^{-2}	0.23	4.7×10^{-2}
Peak time vs decay constant	0.41	2.4×10^{-7}	0.36	2.4×10^{-3}	0.24	4.4×10^{-2}
Pulse duration vs peak flux	-0.43	1.3×10^{-7}	-0.34	2.9×10^{-3}	-0.50	3.2×10^{-5}
Pulse duration vs peak luminosity	-0.47	9.3×10^{-9}	-0.39	7.0×10^{-4}	-0.48	6.6×10^{-5}

Table 5.6: Summary of Kendall Tau Rank Order Correlation data. Various property sets are reported in the first column. * Probabilities are quoted as two-tailed values. † Interval measured between successive pulse start times. ‡ Several GRBs had emission that appeared to extend into a data gap thus the post-Q-time durations could not be calculated. †† 'S-S' interval was measured between start times of the respective flares. ‡‡ 'P-P' interval was measured between peak times of the respective flares. Probabilities marked with '$*$' were calculated using tabulated confidence values for correlations with fewer than 10 degrees of freedom (www.sussex.ac.uk/users/grahamh/RM1web/Rhotable.htm).

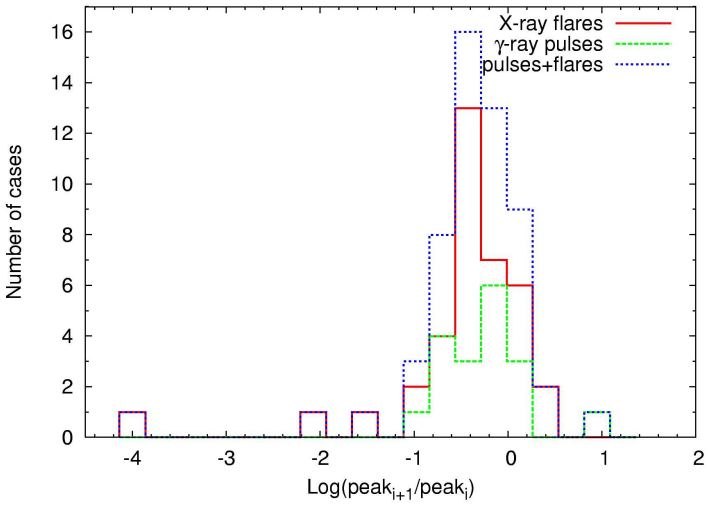

(a) Reproduction of Chincarini et al. (2007) figure 12 showing the distribution of the ratio of peak intensities between two successive events: X-ray flares (solid red line, 68 flares), γ-ray pulses (dashed green line, 46 pulses) and the combined sample (dotted blue line, 104 pulses). This distribution was fit with a Gaussian function giving $<\log(\mathrm{peak}_{i+1}/\mathrm{peak}_i) >= -0.157$ and $\sigma_{\log} = 0.41$, provided two outlying points are ignored (see § 5 C07).

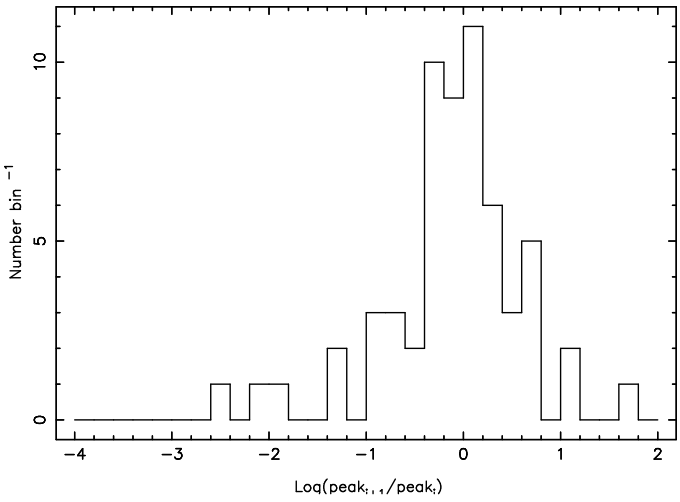

(b) Cumulative frequency plot using pulse values from this study (73 pulses). Applying a Gaussian function to this distribution gives $<\log(\mathrm{peak}_{i+1}/\mathrm{peak}_i) >= 5 \times 10^{-4}$ and $\sigma_{\log} = 0.45$.

Figure 5.5: Comparison plots displaying the distribution of the ratio between the peaks of two successive pulses from C07 and this study.

Three of the ten GRBs used in Lazzati et al. (2008) are included in the sample used in this work (GRB 050820A, 060115 and 060124).

The average flare luminosity in Lazzati's work was calculated using the following formula (their equation 1):

$$< L >_{t_1,t_2} = \frac{1}{n_{\rm GRB}} \sum_{i=1}^{n_f} L_i \delta t_{i,1,2}, \tag{5.2}$$

where L_i is the average luminosity of the $i^{\rm th}$ flare during its active time, $n_{\rm GRB} = 11$ is the total number of GRBs considered in this work, $n_f = 73$ is the total number of flares and $0 \leq \delta t_{\rm i,1,2} \leq 1$ is the fraction of the time in the interval (t_1, t_2) during which the $i^{\rm th}$ is active. Following the method of Lazzati et al. (2008) this prescription is equivalent to the assumption that the flares have a square shape. The authors argued that when both a Gaussian and triangular profile were used the resultant values for the average luminosity were consistent with the simplified approximation, within the error limits. Whilst not being a realistic approximation to the temporal characteristics of typical GRB flares/pulses this prescription has been retained in this analysis so that the results obtained are directly comparable to those obtained by Lazzati et al. (2008).

Figure 1 of Lazzati et al. (2008) is reproduced in figure 5.6(a), whilst the results from the pulses in this study are shown in figure 5.6(b). Attempting a power law fit to the data in figure 5.6(b) produced an index of $-0.37^{+0.10}_{-0.09}$, which gave an extremely poor χ^2 fit; nor was it consistent with the value found by Lazzati et al. (2008). Fixing the decay index at -1.5 worsened the fit further. However, it should be noted that the results of this work cover a much shorter time span than that covered by Lazzati et al. (2008). If the first three points of figure 5.6(a) are considered on their own (time $<$ 200 s) then the power law index would be somewhat shallower than -1.5, perhaps indicating that there is a slightly different average pulse luminosity behaviour at early times. However, given the small sample numbers in both works it is difficult to ascertain whether this is a real trend or not.

Lazzati et al. (2008) also convert their average flare luminosity values into equivalent accretion rates (in solar masses $\rm s^{-1}$, their figure 3), assuming that: the GRB jet is beamed into 1% of the sky; and there was an efficiency of 0.1% when the accretion rate was converted to jet luminosity. All of their data points lie below the level at which the material surrounding the central BH switches from a neutrino-cooled to

an advective disk. This occurs at $\sim 10^{-3} - 10^{-2} M_{\odot} s^{-1}$ depending on the viscosity prescription used (Chen & Beloborodov, 2007). On the same figure they also show the average accretion rate during the prompt phase to be above this switch threshold. However, as can be seen from a comparison of figure 5.6(a) and 5.6(b), the early time, average flare luminosities calculated from my study (i.e. a measurement of this prompt phase) are at a comparable absolute value to Lazzati's earliest data points. Conducting a similar conversion to accretion rate using the same assumptions would not place my data points above the switching threshold.

5.7.6 Underlying afterglow behaviour

Whilst collating the flux light curves it was noted that there appeared to be strong similarities between the late-time afterglow behaviour and absolute flux values for several GRBs in the sample. Given the limited number of GRBs considered by this study such similarities could be entirely spurious. However, with that caveat in mind, the light curves were separated into four groups:

- Group 1: 050319, 060714A, 060904B, see figure 5.7(a).
  - $\text{Flux}_{\text{ave.}}(1\text{ ks}) \sim 1 \times 10^{-11}$ ergs cm^{-2} s^{-1}. At that time the afterglow exhibits phase II decay with $\alpha_{\text{ave}} \sim 0.39$.
  - $\text{Flux}_{\text{ave.}}(40\text{ ks}) \sim 2 \times 10^{-13}$ ergs cm^{-2} s^{-1}. At that time the afterglow exhibits phase III decay with $\alpha_{\text{ave}} \sim 1.37$.
- Group 2: 050820A, 060124, 061121, see figure 5.7(c).
  - $\text{Flux}_{\text{ave.}}(1\text{ ks}) \sim 2 \times 10^{-10}$ ergs cm^{-2} s^{-1}. At that time the afterglow appears to be at the end of phase II decay with $\alpha \sim_{\text{ave}} 0.26$.
  - $\text{Flux}_{\text{ave.}}(40\text{ ks}) \sim 2 \times 10^{-12}$ ergs cm^{-2} s^{-1}. At that time the afterglow exhibits phase III decay with $\alpha_{\text{ave}} \sim 1.29$.
- Group 3: 060115, 060526, see figure 5.7(e).
  - $\text{Flux}_{\text{ave.}}(1\text{ ks}) \sim 4 \times 10^{-12}$ ergs cm^{-2} s^{-1}. At that time the afterglow exhibits phase II decay with $\alpha_{\text{ave}} \sim 0.49$.

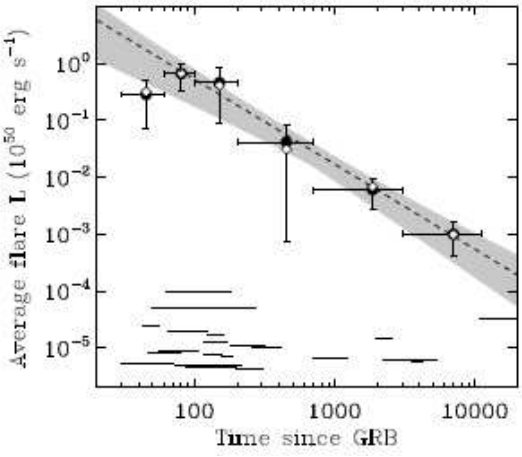

(a) A reproduction of Lazzati et al. (2008) figure 1.

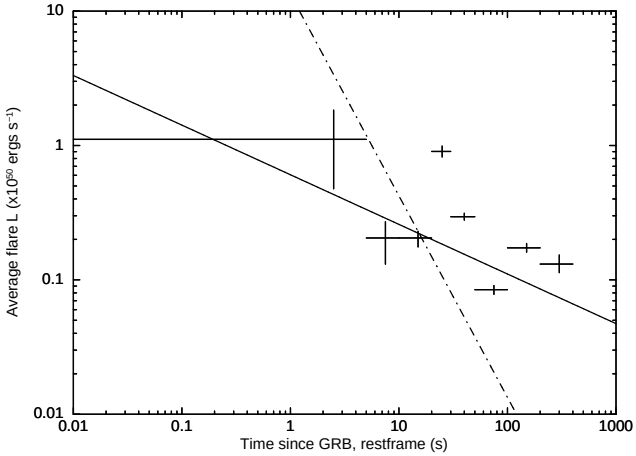

(b) Average flare luminosity plot using pulse data from the long Q-time GRBs selected for this study.

Figure 5.6: Average flare luminosity light curves. (a) This figure shows the average flare luminosity, as calculated by equation 5.2, with respect to time since the GRB onset. The dashed line shows the best power law fit; the shaded area indicates the 1σ confidence region of the power law index and normalisation. The data with solid black circles assume a Band model spectrum for the flares (Band et al., 1993; Falcone et al., 2007); the white diamonds assume a power law spectral model. The horizontal lines at the bottom of the plot show the times at which flares have been observed. Their ordinate is arbitary. (b) Note the reduced temporal range of this study compared to the Lazzati et al. (2008) sample. Spectral models are as described in § 5.4. The solid black lines indicates the 'best' fit power law index of $-0.37^{+0.10}_{-0.09}$. For comparison to figure (a) a power law index of -1.5 (dash-dot line) has been plotted; this produced an extremely poor fit to the data.

  - Flux$_{\rm ave.}$(40 ks) $\sim 1 \times 10^{-13}$ ergs cm^{-2} s^{-1}. At that time the afterglow exhibits phase III decay with $\alpha_{\rm ave} \sim 1.50$.

- Group 4: 060210, 060418, 060607A, see figure 5.7(g).

  - Flux$_{\rm ave.}$(1 ks) $\sim 5 \times 10^{-11}$ ergs cm^{-2} s^{-1}. At that time the afterglow exhibits phase II decay with $\alpha_{\rm ave} \sim 1.11$.
  - Flux$_{\rm ave.}$(40 ks) has a wide dispersion from $\sim 4 \times 10^{-14}$ to $\sim 1 \times 10^{-12}$ ergs cm^{-2} s^{-1}. At that time the afterglow also exhibits a wide dispersion with a decay index between 1.50 and 3.24.

It is interesting to note that despite the differences in the late-time afterglow behaviour all groups appear to have a break between phase II and III at ~ 5 ks.

Previously Boër & Gendre (2000), Gendre & Boër (2005) and Gendre et al. (2008) proposed that there are several subclasses of GRB afterglow behaviour, dependant in their X-ray and optical behaviour. Focussing only on the X-ray behaviour Gendre et al. (2008) separates these into group I and II bursts, which have average fluxes of $\sim 7.0 \times 10^{-12}$ ergs cm^{-2} s^{-1} and 3.1×10^{-13} ergs cm^{-2} s^{-1} respectively at 1 day in the observer's reference frame assuming an average redshift of 1 (equivalent to 40 ks in the burst's rest frame). The classes proposed above broadly fit in with Gendre & Boër's (2008) classification: the flux of group 2 bursts have the same order of magnitude flux as group I at 40 ks, whilst the flux of group 1 and 3 is approximately the same as Gendre & Boër's (2008) group II. The fluxes of group 4 bursts at 40 ks are widely distributed so it is not possible to constrain, with this sample number, which subclass they belong to.

The same groupings were retained for the composite plots of the GRB luminosity light curves (figures 5.7 b, d, f and h) to see if the afterglow behaviour remained closely related. Whilst the absolute shape of the late-time afterglows remained the same, the luminosities were markedly different. In the future the analysis of more long Q-time bursts with known redshifts would confirm whether these are distinct afterglow subclasses, but for the time being no firm conclusions can be drawn.

Decay indices and break times of the underlying afterglow behaviours for this sample are reported in table 5.7 (assuming sharply broken power law segments); GRBs are collated into the groups stated above to illustrate the similarity of their late-time afterglow behaviour and to make it easier to compare

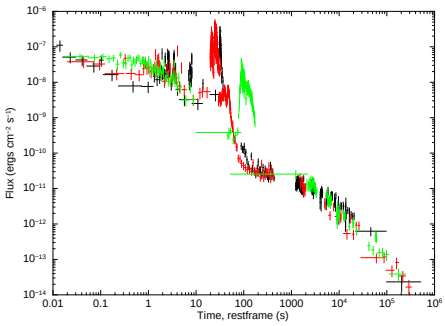

(a) Group 1: GRB 050319 (black), GRB 060714A (red) and GRB 060904B (green)

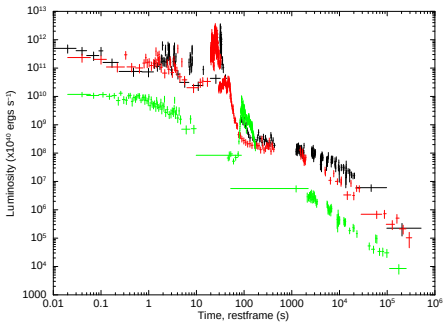

(b) Group 1: GRB 050319 (black), GRB 060714A (red) and GRB 060904B (green)

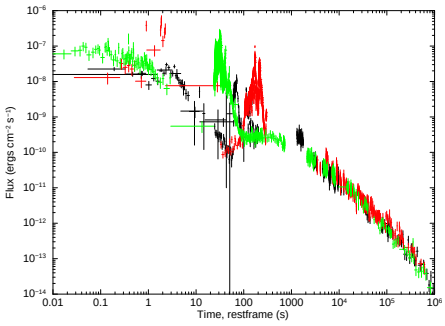

(c) Group 2: GRB 050820A (black), GRB 060124 (red) and GRB 061121 (green)

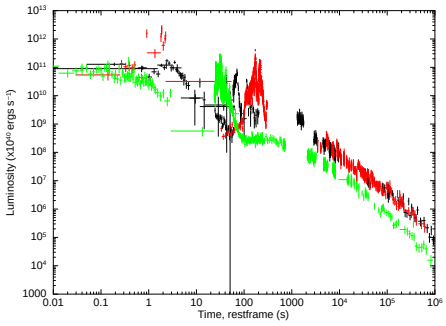

(d) Group 2: GRB 050820A (black), GRB 060124 (red) and GRB 061121 (green)

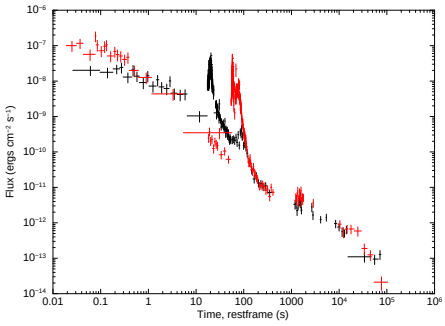

(e) Group 3: GRB 060115 (black), GRB 060526 (red)

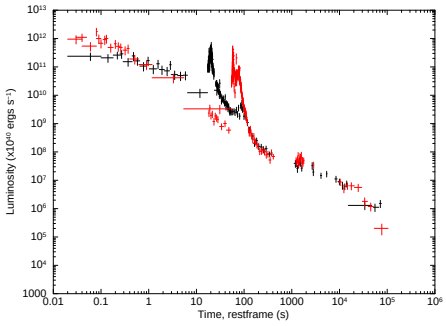

(f) Group 3: GRB 060115 (black), GRB 060526 (red)

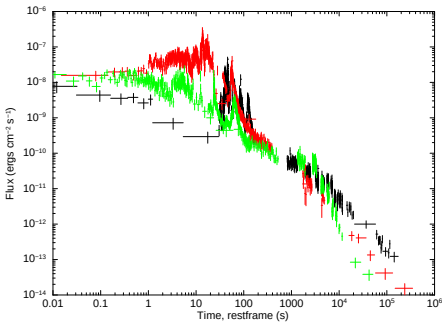

(g) Group 4: GRB 060210 (black), GRB 060418 (red) and GRB 060607A (green)

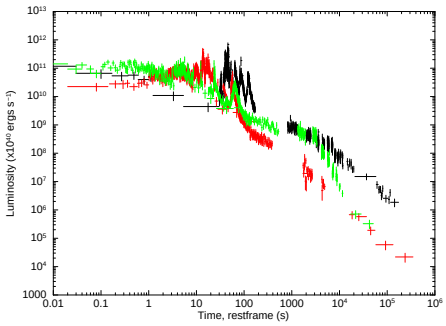

(h) Group 4: GRB 060210 (black), GRB 060418 (red) and GRB 060607A (green)

Figure 5.7: Flux light curve (1-20 keV) in the rest frame of the burst, compared to luminosity light curves (over the same energy range).

their early time behaviour. As stated in § 5.6 smoothly broken power law models were also applied to selected portions of the late-time afterglows, the results of which are reported in table 5.8.

The general behaviour of the majority of the light curves modelled in this sample is that of the canonical light curve described in § 1.3.3, plus a power law afterglow contribution to the phase 0 emission (in addition to the typical pulse behaviour). It should be noted that there are gaps in the model parameters reported in table 5.7; these were either due to periods when the GRB light curves were poorly/not sampled or as result of multiple, overlapping pulses obscuring the underlying behaviour and preventing well constrained, 'stable'[34] fits with multiple breaks from being carried out. In such cases a model containing the maximum number of expected breaks did not produce well constrained values, therefore a model with fewer breaks had to be utilised. As a result the phase I decay portion of the canonical light curve may have been present but could not be modelled as it appeared to have been obscured by a contemporaneous pulse; for example GRB 060714A and GRB 060904B.

GRBs included in the fourth 'group' (060210, 060418 and 060607A) appeared to be markedly different from the other bursts included in this sample; nor do they appear to reflect canonical afterglow behaviour. They potentially belong to a subset of bursts that do not show a 'normal' plateau phase but instead decay rapidly.

5.7.7 Phase 0 emission: Prompt power laws

Phase 0 emission appears to be typified by an underlying power law with a decay index of ~ 0.5, which is strikingly similar to that seen during canonical phase II decay. The decay indices of the two phases in question are plotted in figure 5.7; this plot seems to indicate that there may be an anti-correlation between the two values. A Spearman Rank test gave $r_s = -0.71$ for a total of 7 degrees of freedom. Tabulated confidence values[35] for correlations with fewer than 10 degrees of freedom indicated that the apparent negative correlation was not significant at the 95% confidence level. The same relationship was analysed using the Kendall tau coefficient giving $\tau = -0.62$ (P$= 0.07$) also indicating that the apparent anti-correlation was not significant given the available data.

[34] A 'stable' model fit is, as expected, defined as one where the parameter values do not change if a `fit` or `error` command was issued once best efforts had been made to find the global minimum fit.

[35] www.sussex.ac.uk/users/grahamh/RM1web/Rhotable.htm

Group	GRB	Phase 0 decay index	Break_1 (s)	Phase I decay index	Break_2 (s)	PhaseII decay index	Break_3 (ks)	Phase III decay index	Break_4 (ks)	Phase IV† decay index
	050319	$0.65^{+0.09}_{-0.09}$	66^{+10}_{-11}	$3.76^{+0.84}_{-0.87}$	133^{+13}_{-9}	$0.49^{+0.04}_{-0.03}$	$7.38^{+1.64}_{-0.84}$	$1.47^{+0.04}_{-0.10}$	-	-
1	060714A	$0.87^{+0.26}_{-0.07}$	-	-	111^{+84}_{-104}	$0.29^{+0.17}_{-0.21}$	$1.25^{+0.54}_{-0.42}$	$1.23^{+0.06}_{-0.06}$	-	-
	060904B	$0.86^{+0.03}_{-0.03}$	-	-	-	-	$3.98^{+1.43}_{-1.60}$	$1.41^{+0.11}_{-0.12}$	-	-
	050820A	$0.11^{+0.31}_{-0.22}$	4^{+4}_{-2}	$2.07^{+0.22}_{-0.25}$	‡	‡	‡	$1.24^{+0.04}_{-0.03}$	188^{+106}_{-73}	$1.74^{+0.23}_{-0.19}$
2	060124	-	-	$1.30^{+0.09}_{-0.18}$	36^{+5}_{-14}	$0.24^{+0.02}_{-0.06}$	$5.43^{+0.30}_{-0.34}$	$1.31^{+0.03}_{-0.03}$	345^{+35}_{-205}	$2.09^{+1.16}_{-0.78}$
	061121	$0.41^{+0.04}_{-0.05}$	1^{+1}_{-1}	$1.68^{+0.03}_{-0.02}$	11^{+1}_{-1}	$0.28^{+0.04}_{-0.05}$	$1.64^{+0.18}_{-0.15}$	$1.33^{+0.01}_{-0.02}$	-	-
3	060115	$0.22^{+0.06}_{-0.09}$	28^{+3}_{-6}	$2.48^{+0.59}_{-0.18}$	210^{+35}_{-66}	$0.71^{+0.10}_{-0.12}$	$9.07^{+10.44}_{-4.47}$	$1.24^{+0.51}_{-0.24}$	-	-
	060526	$0.91^{+0.04}_{-0.06}$	139^{+42}_{-17}	$2.32^{+1.42}_{-0.50}$	276^{+66}_{-59}	$0.26^{+0.18}_{-0.16}$	$4.87^{+1.84}_{-1.45}$	$1.73^{+0.26}_{-0.23}$	-	-
	060210	$0.50^{+0.03}_{-0.04}$	-	-	1210^{+230}_{-270}	$0.98^{+0.07}_{-0.07}$	$5.85^{+0.69}_{-0.60}$	$1.42^{+0.06}_{-0.06}$	-	-
4	060418	$0.10^{+0.11}_{-0.15}$	-	-	16^{+5}_{-3}	$1.23^{+0.03}_{-0.03}$	$3.75^{+5.21}_{-1.99}$	$1.58^{+0.22}_{-0.12}$	-	-
	060607A	$0.39^{+0.02}_{-0.02}$	-	-	-	-	$3.06^{+0.09}_{-0.09}$	-	-	$3.24^{+0.13}_{-0.13}$

Table 5.7: Summary of GRB rest frame light curve properties assuming sharply broken power law segments. All values are reported in the rest frame of the burst. T_0 is taken to be the peak of first emission pulse (SNR = 3). † The temporal placement of this decay segment is consistent with phase IV but it may not reflect the physical properties expected from canonical phase IV decay. ‡ Due to the break in observations of GRB 050820A it was not possible to constrain any decay slopes or breaks between $\sim$ 80 - 1280 s.

GRB	Best fit parameters for a smoothly broken power law				
	α_1	α_2	break time (s)	χ^2/ν	smoothing
050319	$0.40^{+0.08}_{-0.15}$	$2.24^{+0.36}_{-0.21}$	21300^{+7890}_{-5860}	106/131	$-0.63^{+0.12}_{-0.20}$
060714A	$0.33^{+0.14}_{-0.20}$	$1.22^{+0.07}_{-0.06}$	1320^{+370}_{-380}	56/51	$-12.6^{+0.08}_{-0.11}$
060904B	< 0.35	$1.41^{+0.35}_{-0.04}$	1040^{+12000}_{-630}	32/50	-1 (f)
050820A	$1.12^{+0.03}_{-0.03}$	$1.74^{+0.12}_{-0.09}$	129000^{+6660}_{-6620}	137/140	-1 (f)
060124	$0.71^{+0.07}_{-0.10}$	$1.43^{+0.04}_{-0.02}$	4900^{+200}_{-200}	350/285	-1 (f)
061121	$0.25^{+0.06}_{-0.06}$	$1.49^{+0.04}_{-0.04}$	2600^{+750}_{-550}	292/321	-1 (f)
060115†					
060526	$0.29^{+0.14}_{-0.16}$	$1.95^{+0.36}_{-0.30}$	6710^{+4690}_{-3030}	24/28	-1 (f)
060210	$0.26^{+0.32}_{-0.44}$	$1.45^{+0.14}_{-0.09}$	1820^{+2350}_{-710}	261/246	-1 (f)
060418	$1.04^{+0.04}_{-0.03}$	$1.75^{+0.11}_{-0.10}$	3730^{+1380}_{-850}	154/136	-1 (f)
060607A	$0.40^{+0.04}_{-0.04}$	$3.90^{+0.24}_{-0.21}$	3650^{+210}_{-210}	294/203	-1 (f)

Table 5.8: Summary of 'afterglow' light curve fits using a smoothly broken power law model, where T_0 is taken to be the peak of first emission pulse (SNR = 3). These fits only include data after phase I emission or the end of the last decay portion of a late time flare. All break time values are in the rest frame of the burst. Smoothing values followed by (f) indicate that the smoothing parameter has been frozen at the standard value of -1 (see discussion in § 2.2.1 of this thesis). †GRB 060115: a smoothly broken power law model gives very poorly constrained parameters.

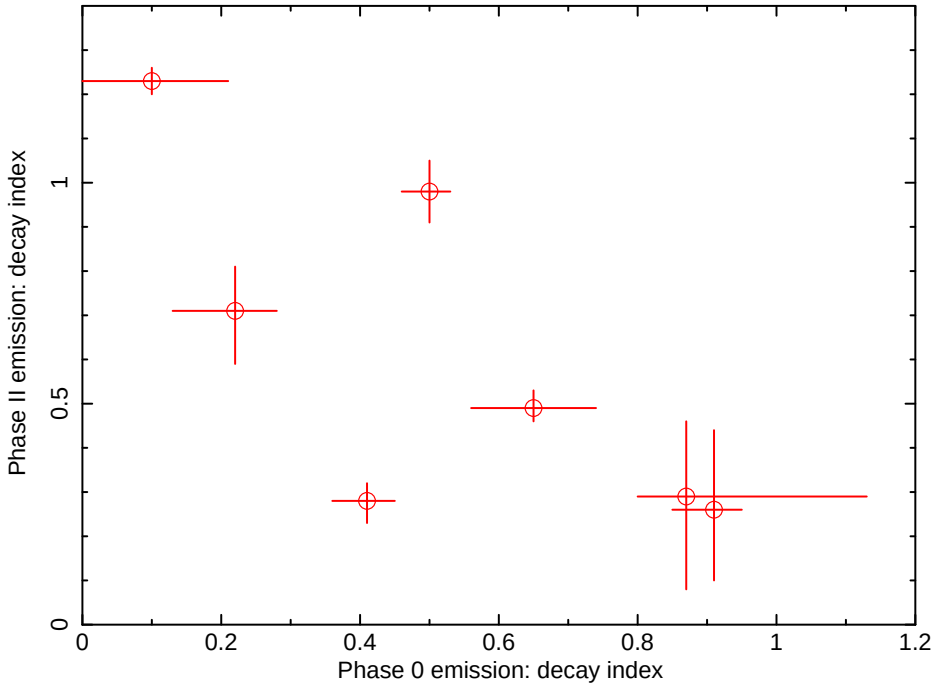

Figure 5.8: Phase 0 decay index plotted versus phase II decay index, plotted from data in table 5.7.

It is possible that the phase 0 power law values measured here may be indicative of a period of energy injection akin to the standard explanation for phase II emission. Thus phase 0 emission potentially originates from the first series of pulses/ the 'precursor' whilst phase II potentially originates from the pulses that occur after the Q-time. See further discussion in § 5.7.9.

GRB 060124 was the only GRB in the sample without a measured phase 0 decay index. I attempted a further fit with a model comprising of five power law segments (sharply broken) and sixteen pulses, however, this model proved to be more complex than *QDP* could handle. Instead a different four power law/ sixteen pulse model was applied, this time attempting to find a phase 0 decay index at the expense of the phase 'IV' index. This produced a statistically comparable fit with intermediate (phase I to III) decay indices and break times that were consistent with those reported in table 5.7. However, the phase 0 decay index of this fit was not well constrained, $\alpha_{\mathrm{phase\,0}} < 0.50$, with a break seen at 5^{+1}_{-1} s. This would be consistent with the trend noted above, given the measured phase II decay index of $0.24^{+0.02}_{-0.06}$, if the decay index was near the upper limit given.

5.7.8 Phase I emission: High latitude emission

A decay index of ~ 3 is typically observed during phase I of the canonical light curve and is attributed to high latitude emission (also known as the 'curvature effect') as explained in § 1.3.3. Therefore phase I emission should have the following relation between temporal and spectral properties: $\alpha = 2 + \beta$. GRBs 050319, 060115 and 060526 were consistent with this relationship, whilst GRBs 050820A, 060124 and 061121 were not. The latter group of GRBs appeared to have decay slopes that were too shallow to be described by the 'curvature effect'. This may be a result of a slowly declining energy influx to the afterglow at such times. The measured phase II decay indices of GRB 060124 and 061121 were much flatter than other bursts in this study ($0.24^{+0.02}_{-0.06}$ and $0.28^{+0.04}_{-0.05}$ respectively); this may also be indicative of a higher rate of energy injection for these bursts.

5.7.9 Origin of the light curve breaks

The 'late-time' afterglow decay indices (phase II onwards) appear to show the expected canonical behaviour (with the exception of the 'group 4' bursts). In the following I shall compare the temporal indices and break magnitudes to the various standard physical processes that can cause such breaks.

Cooling breaks

The signature of a cooling break passing through the X-ray band would in $|\Delta\alpha| = 0.25$ and $|\Delta\beta| = 0.50$ (slow cooling case) or $|\Delta\alpha| = 0.42$ and $|\Delta\beta| = 0.83$ (fast cooling case) assuming $p \sim 2$; see table 2.3. Table 5.7 indicates that there are several candidate breaks that fit these criteria:

- 050820A, $\Delta\alpha = 0.50^{+0.23}_{-0.19}$,
- 060115, $\Delta\alpha = 0.53^{+0.52}_{-0.27}$,
- 060124, $\Delta\alpha = 0.78^{+1.16}_{-0.78}$,
- 060210, $\Delta\alpha = 0.48^{+0.08}_{-0.08}$,
- 060210, $\Delta\alpha = 0.44^{+0.09}_{-0.09}$,

- 060418, $\Delta\alpha = 0.35^{+0.22}_{-0.12}$.

However, none of these breaks show any *definite* signs of spectral change either from the spectra at the break time or hardness ratio (HR) plots at the same time (if spectra are not available due to low counts; see Appendix 5.A). GRB 050820A potentially shows a change in spectral properties from the HR plot but the spectra at this time are consistent with an unchanging photon index of ~ 2. Thus I rule out cooling breaks as an origin for any of the breaks measured in this analysis.

Jet breaks

The signatures of a jet break are: $\Delta\alpha = 1.0$, no spectral variation across the break and the post-break decay index should be equal to the electron spectral index, p (as long as $p > 2$, otherwise a different $\alpha - p$ relation should be adopted; Zhang & Mészáros 2004; Dai & Cheng 2001). There were several candidate bursts with temporal breaks consistent with the expected value (see table 5.9). Only one break, the second (downwards) sharp break in the afterglow of GRB 060124, was consistent with $\Delta\alpha = 1.0$ and $\alpha_{\rm post\ break} = p$. In this case it was not possible to distinguish between the two emission scenarios, i.e. $\nu > \nu_c$ or $\nu < \nu_c$.

End of energy injection

A break is expected to be present between canonical phase II and III decay as a result of the end of energy injection from the central engine, see § 1.3.3; such breaks should show little or no spectral evolution. Using the equations detailed in § 1.3.3 I have calculated the expected post-break decay indices from the measured spectral parameters for a variety of ν relations and circumburst densities for the scenario whereby energy injection is moderated by ejecta with a wide Lorentz factor distribution. The corresponding power law indices s ($E(>\Gamma) \propto \Gamma^{1-s}$, $s > 1$ for significant energy injection) and a ($E(t > t_i) \propto t^a$) were also calculated.

Given the similarity of the measured values for phase 0 and phase II decay indices (§ 5.7.7) it is possible that the underlying phase 0 emission was a result of the same energy injection process. Therefore calculations were carried out to assess whether any of the breaks between phase 0 and phase I would fit

GRB	$\Delta\alpha$	β	$\alpha_{\rm post\ break}$	p†		$\alpha_{\rm post\ break}$
				$(\nu > \nu_c)$	$(\nu < \nu_c)$	consistent with p?
050319	$0.98^{+0.06}_{-0.10}$	$1.07^{+0.17}_{-0.17}$	$1.47^{+0.04}_{-0.10}$	$2.14^{+0.34}_{-0.34}$	$3.14^{+0.34}_{-0.34}$	Not consistent
060714	$0.94^{+0.18}_{-0.22}$	$0.98^{+0.19}_{-0.19}$	$1.23^{+0.06}_{-0.06}$	$1.96^{+0.38}_{-0.38}$	$2.96^{+0.38}_{-0.38}$	Not consistent
060124	$1.07^{+0.04}_{-0.07}$	$0.88^{+0.20}_{-0.13}$	$1.31^{+0.03}_{-0.03}$	$1.76^{+0.40}_{-0.26}$	$2.76^{+0.40}_{-0.26}$	Not consistent
060124	$0.78^{+1.16}_{-0.78}$	$0.98^{+0.11}_{-0.11}$	$2.09^{+1.16}_{-0.78}$	$1.96^{+0.40}_{-0.26}$	$2.96^{+0.40}_{-0.26}$	Both consistent
061121	$1.05^{+0.04}_{-0.05}$	$1.01^{+0.12}_{-0.12}$	$1.33^{+0.01}_{-0.03}$	$2.02^{+0.24}_{-0.24}$	$3.01^{+0.24}_{-0.24}$	Not consistent

Table 5.9: Summary of jet break candidates. Only the second (downwards) sharp break in GRB 060124 is consistent with a jet break. † These values were calculated using the observed value of β ($3^{\rm rd}$ column) and the relationship between p and β for afterglow models during the jet phase, for the case where $\nu > \nu_c$ and $\nu < \nu_c$, as given by table 1 of Zhang & Mészáros (2004) (and references therein) assuming $p > 2$.

with this hypothesis for the model where energy injection is moderated by ejecta with a wide Lorentz factor distribution; the results are reported in table 5.10. No combination of parameters produced an acceptable fit to the phase 0 to phase I decay for GRB 060115 or GRB 060526. The remaining GRBs (050319, 050820A and 061121) indicated that scenarios where $\nu > \nu_m$ were favoured, however, there was no clear trend to indicate a favoured circumburst environment. These results, combined with the measured magnitude of the decay indices, indicates that the underlying behaviour of phase 0 may be related to energy injection.

Table 5.11 reports the allowed conditions for the breaks seen between phase II and phase III for the same model. Similarly to the phase 0 to phase I transition examples discussed above the scenario where $\nu > \nu_m$ was favoured in the majority of cases for the measured phase II to phase III break. There appeared to be no consistent trend for the circumburst environment, though two cases (GRB 050319 and 061121) could only be fit by a model with $\nu_m < \nu < \nu_c$ and k $= 0$. Interestingly no combination of parameters were able to fit the breaks in GRB 060526, indicating that neither break can be explained by energy injection from ejecta with a wide Lorentz factor distribution.

The scenario wherein long term central engine activity provides the source of energy injection was

GRB	Case	k†	Expected post-break decay index	Observed post-break decay index	s‡	a⋆
050319	$\nu_m < \nu < \nu_c$	2	$2.09^{+0.33}_{-0.35}$	$3.76^{+0.84}_{-0.87}$	$17.81^{+11.86}_{-12.30}$	$2.03^{+2.71}_{-2.81}$
050820A	$\nu_m < \nu < \nu_c$	0	$1.19^{+2.28}_{-1.73}$	$2.07^{+0.22}_{-0.25}$	$8.05^{+15.86}_{-12.03}$	$1.41^{+5.54}_{-4.20}$
	$\nu_m < \nu < \nu_c$	2	$1.69^{+2.28}_{-1.73}$	$2.07^{+0.22}_{-0.25}$	$-6.36^{+10.13}_{-13.31}$	$2.19^{+4.93}_{-6.48}$
	$\nu > \max(\nu_m, \nu_c)$	0	$0.69^{+2.28}_{-1.73}$	$2.07^{+0.22}_{-0.25}$	$22.63^{+51.17}_{-39.08}$	$2.19^{+9.90}_{-7.56}$
	$\nu > \max(\nu_m, \nu_c)$	2	$0.69^{+2.28}_{-1.73}$	$2.07^{+0.22}_{-0.25}$	$-6.36^{+10.13}_{-13.31}$	$2.19^{+4.93}_{-6.48}$
061121	$\nu_m < \nu < \nu_c$	0	$1.52^{+0.18}_{-0.18}$	$1.68^{+0.03}_{-0.02}$	$4.12^{+0.22}_{-0.22}$	$0.84^{+0.03}_{-0.03}$
060115	None applicable	-	-	-	-	-
060526	None applicable	-	-	-	-	-

Table 5.10: Decay index break between phase 0 and phase I: summary of calculated parameters for a scenario whereby ejecta with varying Lorentz factors could result in energy injection. † Circumburst density profile, where $k = 0$ corresponds to a constant density profile and $k = 2$ coresonds to a 'wind' profile. ‡ Power law index of the Lorentz factor distribution of the ejected material, such that $E(> \Gamma) \propto \Gamma^{1-s}$. $s > 1$ for significant energy injection. ⋆ Power law index of the energy injection profile, $E(t > t_i) \propto t^a$.

also considered for the above breaks. In all cases the breaks were consistent with this type of energy injection and no constraints could be placed on the relation of the observed ν with respect to ν_c or ν_m or on the circumburst environment.

GRB	Case	k†	Expected post-break decay index	Observed post-break decay index	s‡	a⋆
050319	$\nu_m < \nu < \nu_c$	0	$1.61^{+0.26}_{-0.26}$	$1.47^{+0.04}_{-0.10}$	$3.16^{+0.55}_{-0.61}$	$0.64^{+0.22}_{-0.25}$
060714A	$\nu_m < \nu < \nu_c$	0	$1.47^{+0.29}_{-0.29}$	$1.23^{+0.06}_{-0.06}$	$3.13^{+0.87}_{0.97}$	$0.63^{+0.35}_{-0.39}$
	$\nu > \max(\nu_m, \nu_c)$	0	$0.97^{+0.29}_{-0.29}$	$1.23^{+0.06}_{-0.06}$	$4.70^{+1.37}_{-1.53}$	$0.95^{+0.55}_{-0.62}$
	$\nu > \max(\nu_m, \nu_c)$	2	$0.97^{+0.29}_{-0.29}$	$1.23^{+0.06}_{-0.06}$	$76.20^{+310.88}_{-365.94}$	$0.95^{+5.48}_{-6.45}$
060124	$\nu_m < \nu < \nu_c$	0	$1.55^{+0.33}_{-0.29}$	$1.31^{+0.03}_{-0.03}$	$3.46^{+0.78}_{-0.69}$	$0.71^{+0.31}_{-0.28}$
	$\nu > \max(\nu_m, \nu_c)$	0	$1.05^{+0.33}_{-0.20}$	$1.31^{+0.03}_{-0.03}$	$5.33^{+1.20}_{-1.09}$	$1.05^{+0.47}_{-0.43}$
	$\nu > \max(\nu_m, \nu_c)$	2	$1.05^{+0.33}_{-0.20}$	$1.31^{+0.03}_{-0.03}$	$-76.82^{+165.50}_{-164.33}$	$1.05^{+3.21}_{-3.19}$
061121	$\nu_m < \nu < \nu_c$	0	$1.52^{+0.18}_{-0.18}$	$1.33^{+0.01}_{-0.02}$	$3.41^{+0.17}_{-0.17}$	$0.69^{+0.02}_{-0.02}$
060115	$\nu > \max(\nu_m, \nu_c)$	0	$1.18^{+0.15}_{-0.14}$	$1.24^{+0.51}_{-0.24}$	$2.60^{+2.61}_{-1.37}$	$0.50^{+1.00}_{-0.53}$
	$\nu > \max(\nu_m, \nu_c)$	2	$1.18^{+0.15}_{-0.14}$	$1.24^{+0.51}_{-0.24}$	$5.00^{+6.97}_{-3.65}$	$0.50^{+0.99}_{-0.52}$
060526	None applicable	-	-	-	-	-
060210	$\nu > \max(\nu_m, \nu_c)$	0	$1.45^{+0.36}_{-0.33}$	$1.42^{+0.06}_{-0.06}$	$2.17^{+0.61}_{-0.58}$	$0.38^{+0.22}_{-0.20}$
	$\nu > \max(\nu_m, \nu_c)$	2	$1.45^{+0.36}_{-0.33}$	$1.42^{+0.06}_{-0.06}$	$3.48^{+1.21}_{-1.16}$	$0.38^{+0.19}_{-0.18}$
060418	$\nu_m < \nu < \nu_c$	0	$1.53^{+0.41}_{-0.38}$	$1.58^{+0.22}_{-0.12}$	$1.67^{+1.14}_{-0.38}$	$0.23^{+0.32}_{-0.20}$
	$\nu_m < \nu < \nu_c$	2	$2.03^{+0.41}_{-0.38}$	$1.58^{+0.22}_{-0.12}$	$3.12^{+2.45}_{-1.55}$	$0.35^{+0.38}_{-0.24}$

Table 5.11: Decay index break between phase II and phase III: summary of calculated parameters for a scenario whereby ejecta with varying Lorentz factors could result in energy injection. † Circumburst density profile, where k $= 0$ corresponds to a constant density profile and k $= 2$ corresonds to a 'wind' profile. ‡ Power law index of the Lorentz factor distribution of the ejected material, such that $E(> \Gamma) \propto \Gamma^{1-s}$. $s > 1$ for significant energy injection. ⋆ Power law index of the energy injection profile, $E(t > t_i) \propto t^a$.

5.8 Conclusions

It has long been hypothesised (Colgate, 1973, 1974) that phase 0 GRB emission is preceded by a transient signal with a different physical origin, and therefore spectral properties, to the rest of the burst. Current theoretical models propose that 'precursors' are subdivided into two classes: *fireball* and *progenitor* precursors (§5.1). Both are thought to generate thermal signals, however, these may be up-scattered to produce non-thermal spectra or be obscured by non-thermal radiation emitted at the same time. Definitions of such precursor emission vary greatly between different studies in the literature and often depend on the observed energy range and instrument used. One particular ambiguity in the models proposed so far is the delay between the precursor and phase 0 emission; times range between little as 10 s (Wang & Mészáros, 2007) up to several 100 s (Koshut et al., 1995; Lazzati, 2005).

A separate study conducted by Nakar & Piran (2002) indicated that there are unusually long intervals of little or no emission during phase 0 that they call *quiescent times* (Q-times, §5.1.3). They stress that such periods are not the same as the delays between precursor and phase 0 emission reported by Koshut et al. (1995), however, it is interesting to note that the timescales discussed in both works bear a striking resemblance. Such quiescent periods indicate that there is a change in central engine activity during these times. Given the increasing evidence that phase 0 and phase V emission share a common origin (internal shocks) there is a possibility that precursors are merely another aspect of this emission.

Rather than adopt fully instrumentally based criteria (i.e. emission occurring before a burst 'trigger' etc) in this study I chose to select GRBs with long quiescent, since quiescent periods indicate a change in central engine activity, which is the essence of the definition of a precursor. Studying bursts with long Q-times may help to distinguish whether their early time emission (i.e. whether they show evidence for precursor emission as discussed in the literature), pulse properties as a whole or their long term afterglows are different to those of other GRBs. In this work I have taken a subsection of *Swift* GRBs with long Q-times (> 50 s in the observer's reference frame) and known redshifts (with a range between 0.703 and 3.910) to produce a series of joint BAT-XRT flux and luminosity light curves covering a rest frame energy range of $1 - 20$ keV. Pulse spectral, temporal and energetic properties were extracted from these light curves. No strong evidence was found to suggest that the precursors/early time emission pulses in this sample were spectrally different to the rest of the main emission period over the energy ranges observed by BAT. Pulse properties were used to calculate a series of Spearman Rank

and Kendall Tau correlations. Several correlations and anti-correlations were found in the pulse temporal and energetic properties that indicated a common origin for all pulses (as suggested by previous studies), irrespective of which instrument or energy range they are typically observed in.

This study has reaffirmed that, at the current stage of theoretical understanding, constructing a definition for precursor events is as important as studying them. Furthermore it has provided evidence for extending the link between phase 0 emission and flares to events that were previously designated as precursors. Potentially all of these seemingly separate events may share a common origin. The correlations between pulse properties noted were all consistent with the accretion models proposed by Perna et al. (2006, delayed accretion from a fragmented disk) and Proga & Zhang (2006, accretion moderated by a magnetic barrier). I was not able to confirm the average pulse luminosity light curve as proposed by Lazzati et al. (2008).

Additionally the underlying afterglows of this subset of bursts were modelled; all of which were consistent with the canonical GRB light curve model. A similarity was noted between the underlying phase 0 and phase II decay indices hinting at a common origin for both. My analysis showed that both decay indices were consistent with existing energy injection models.

5.A Appendix: GRB properties wrt time.

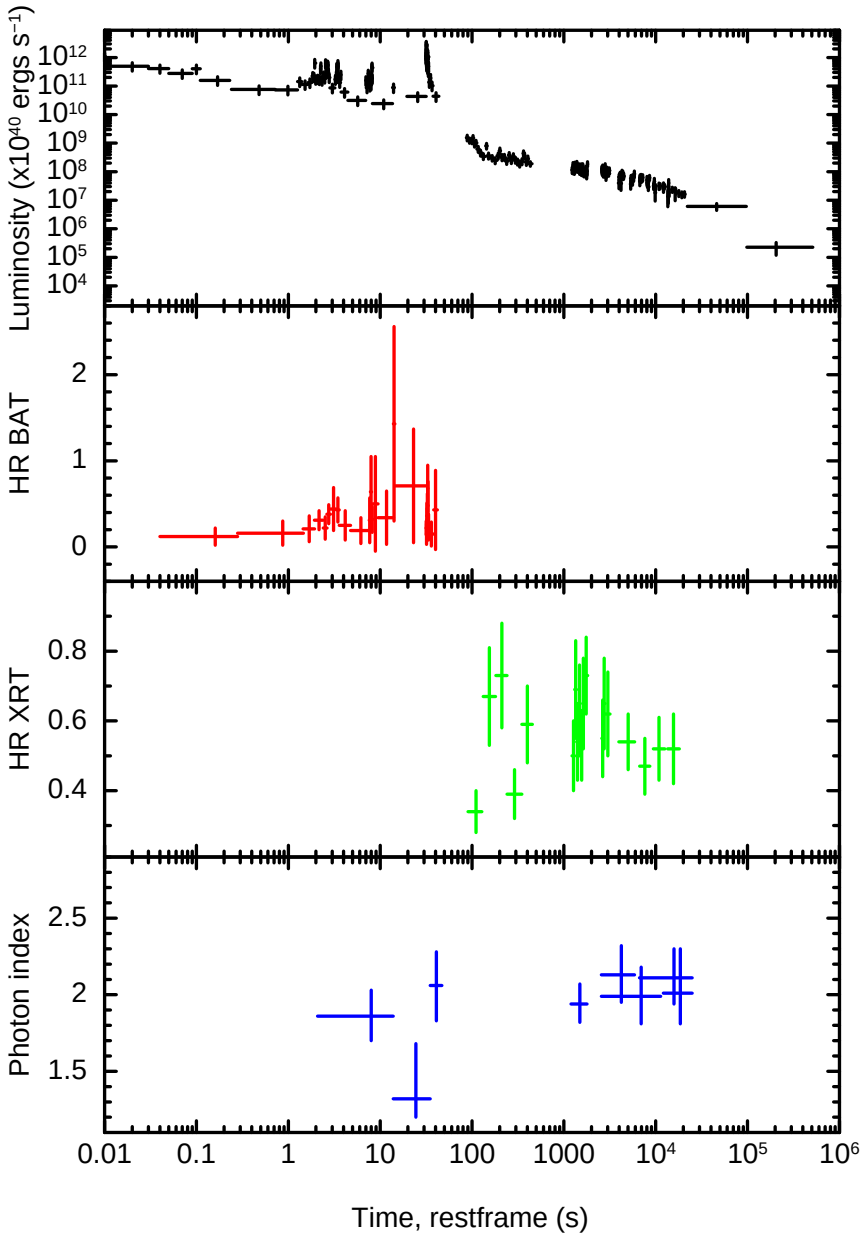

Figure 5.9: GRB 050319: Combined BAT and XRT luminosity light curve (1-20 keV) in the rest frame of the burst [top]. BAT hardness ratio plot [second plot], XRT hardness ratio plot [third plot] and photon index value from absorbed power law spectral fits [bottom]. Mode switching in the XRT occasionally causes WT mode and PC mode data to be accumulated over concurrent time intervals. Photon index data points [bottom panel] with overlapping temporal intervals are the result of this effect. T_0 has been set to the peak of the first flare emission.

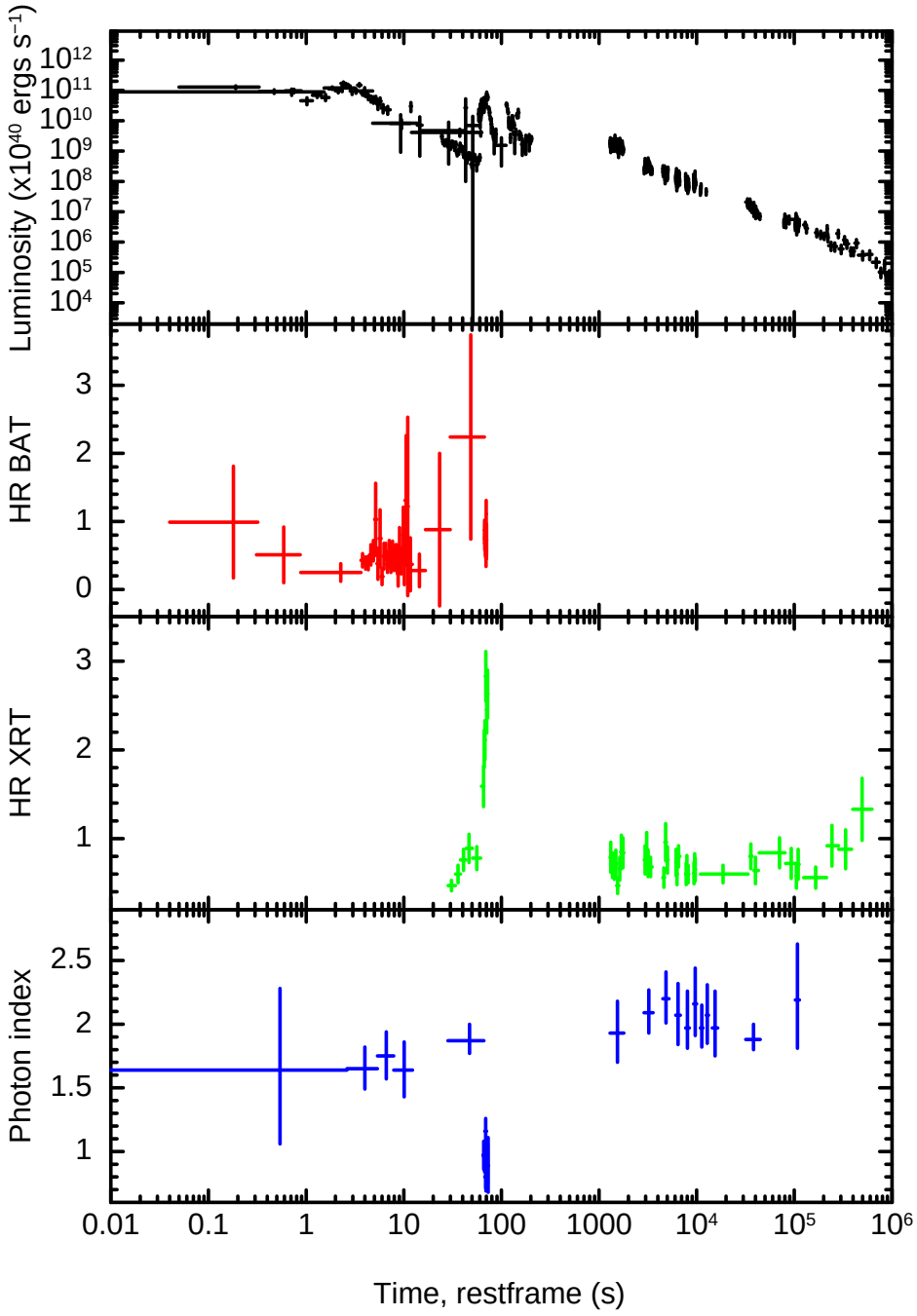

Figure 5.10: GRB 050820A: Combined BAT and XRT luminosity light curve (1-20 keV) in the rest frame of the burst [top]. BAT hardness ratio plot [second plot], XRT hardness ratio plot [third plot] and photon index value from absorbed power law spectral fits [bottom]. T_0 has been set to the peak of the first flare emission.

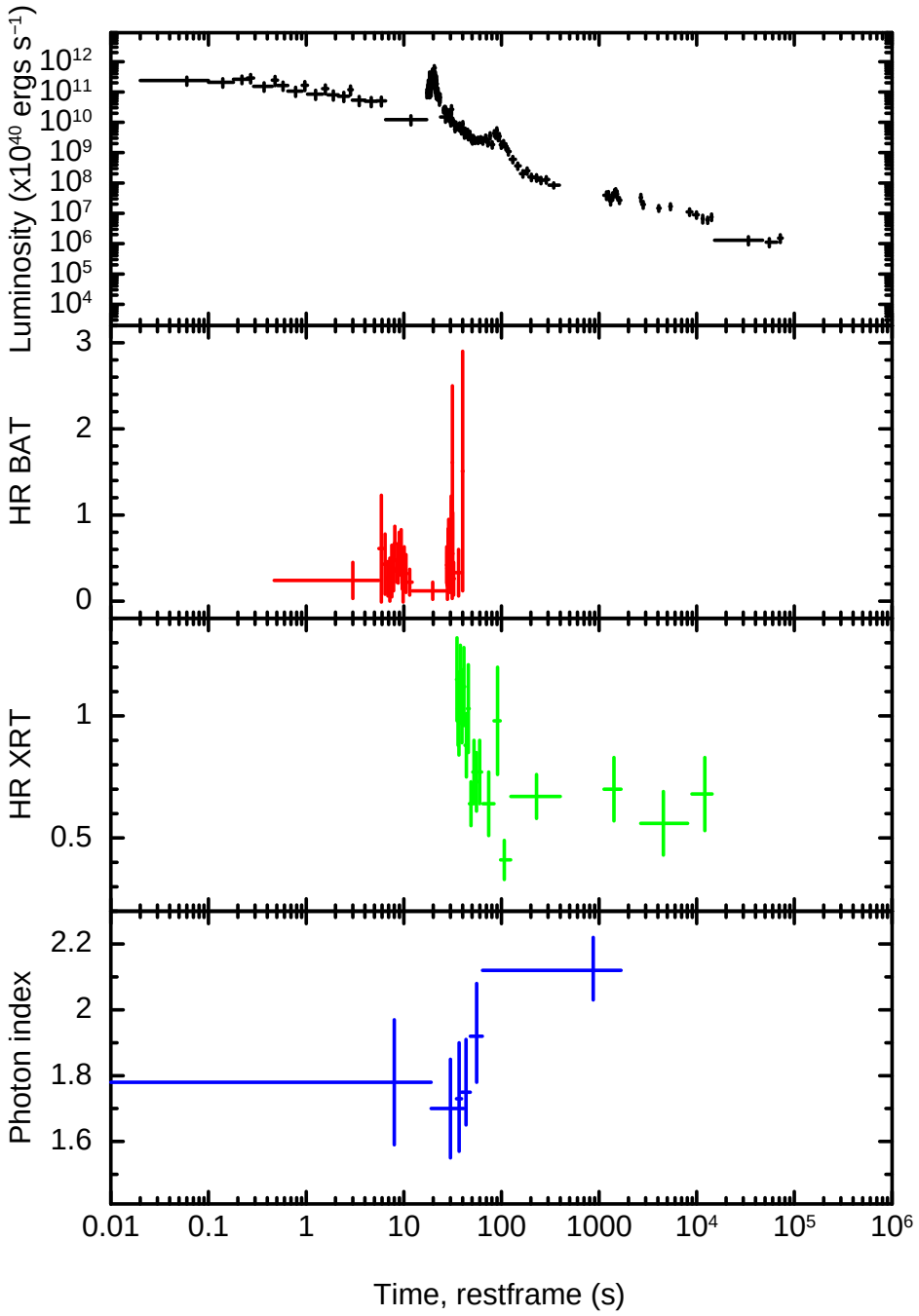

Figure 5.11: GRB 060115: Combined BAT and XRT luminosity light curve (1-20 keV) in the rest frame of the burst [top]. BAT hardness ratio plot [second plot], XRT hardness ratio plot [third plot] and photon index value from absorbed power law spectral fits [bottom]. Mode switching in the XRT occasionally causes WT mode and PC mode data to be accumulated over concurrent time intervals. Photon index data points [bottom panel] with overlapping temporal intervals are the result of this effect. T_0 has been set to the peak of the first flare emission.

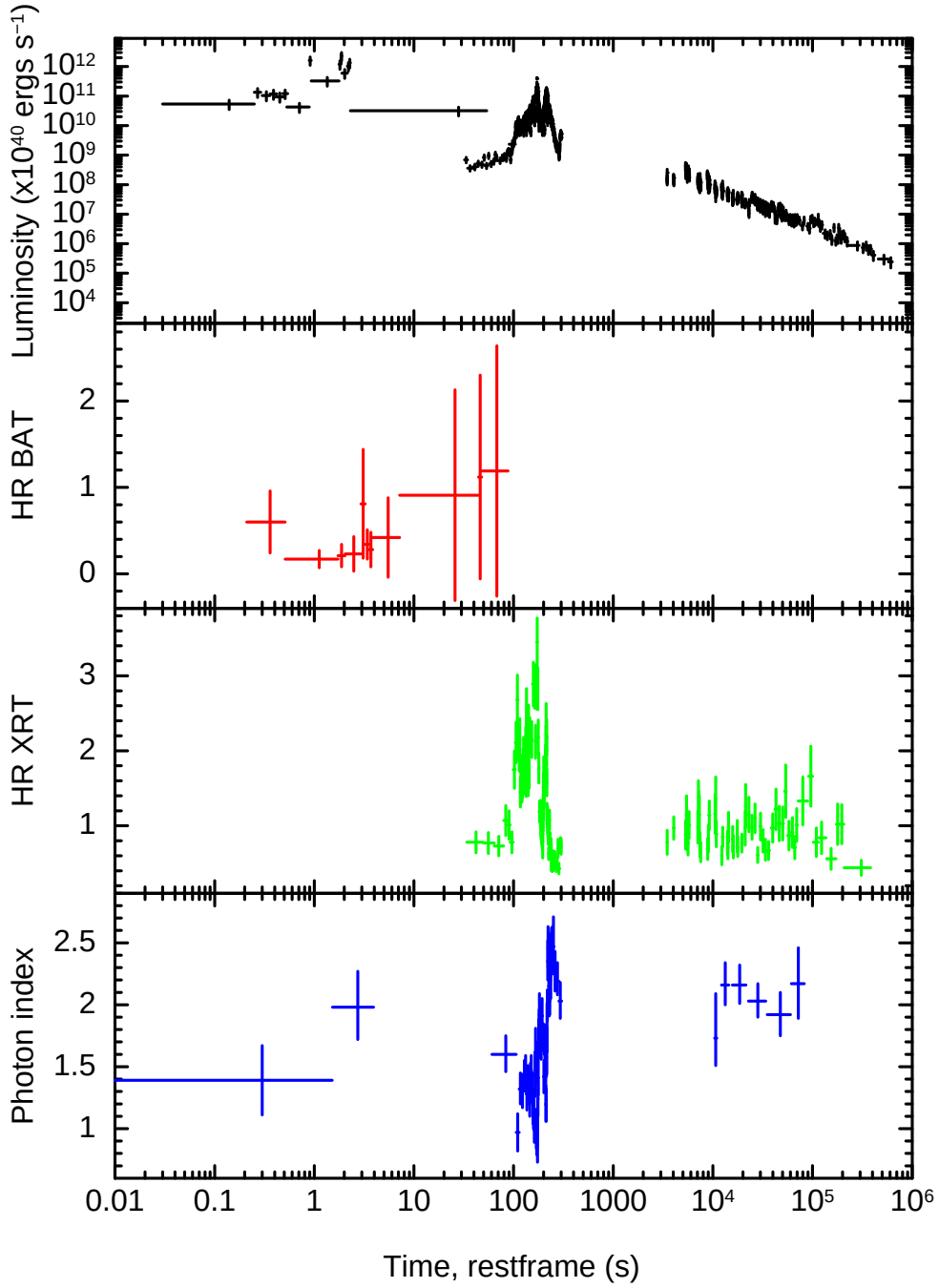

Figure 5.12: GRB 060124: Combined BAT and XRT luminosity light curve (1-20 keV) in the rest frame of the burst [top]. BAT hardness ratio plot [second plot], XRT hardness ratio plot [third plot] and photon index value from absorbed power law spectral fits [bottom]. T_0 has been set to the peak of the first flare emission.

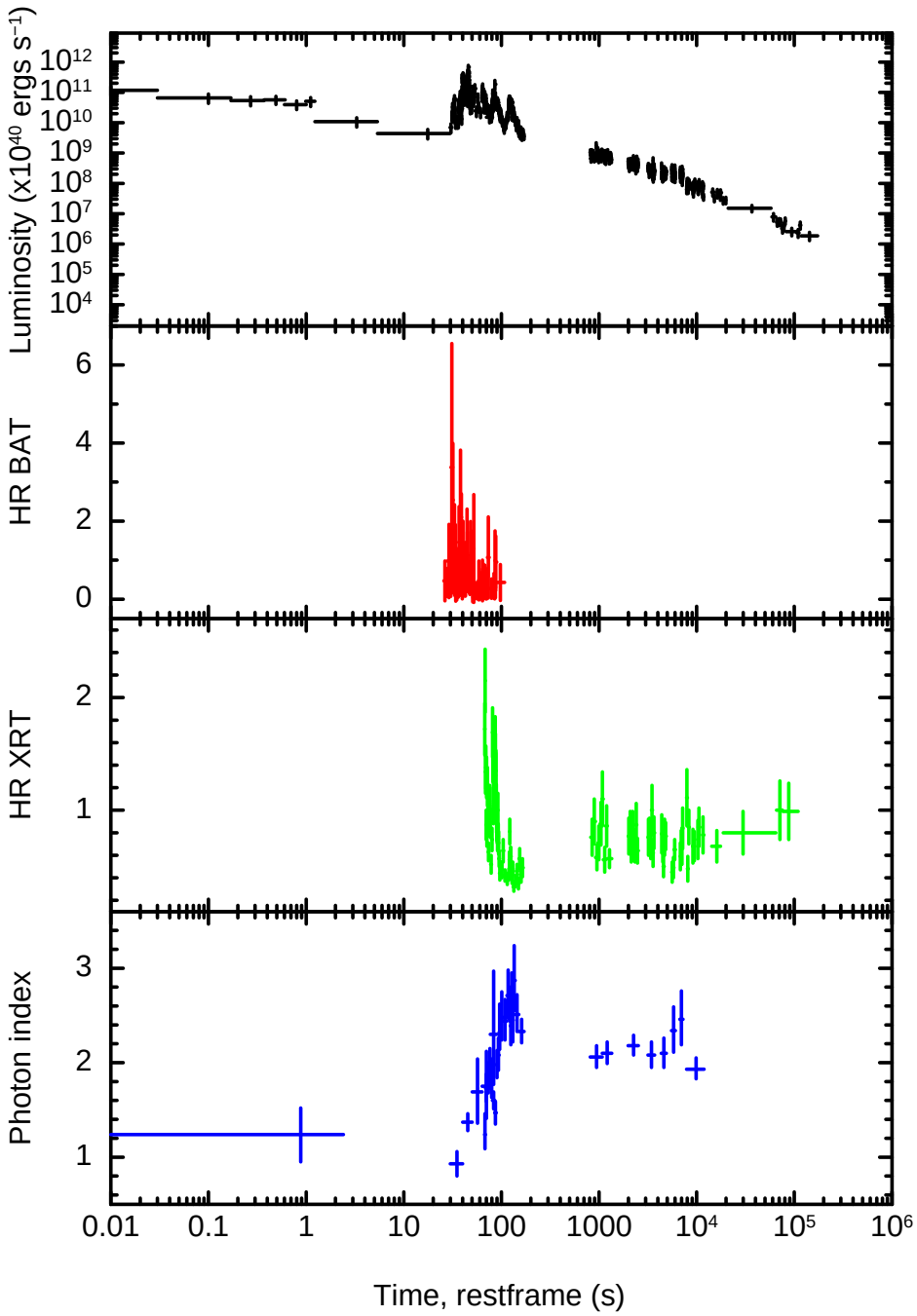

Figure 5.13: GRB 060210: Combined BAT and XRT luminosity light curve (1-20 keV) in the rest frame of the burst [top]. BAT hardness ratio plot [second plot], XRT hardness ratio plot [third plot] and photon index value from absorbed power law spectral fits [bottom]. T_0 has been set to the peak of the first flare emission.

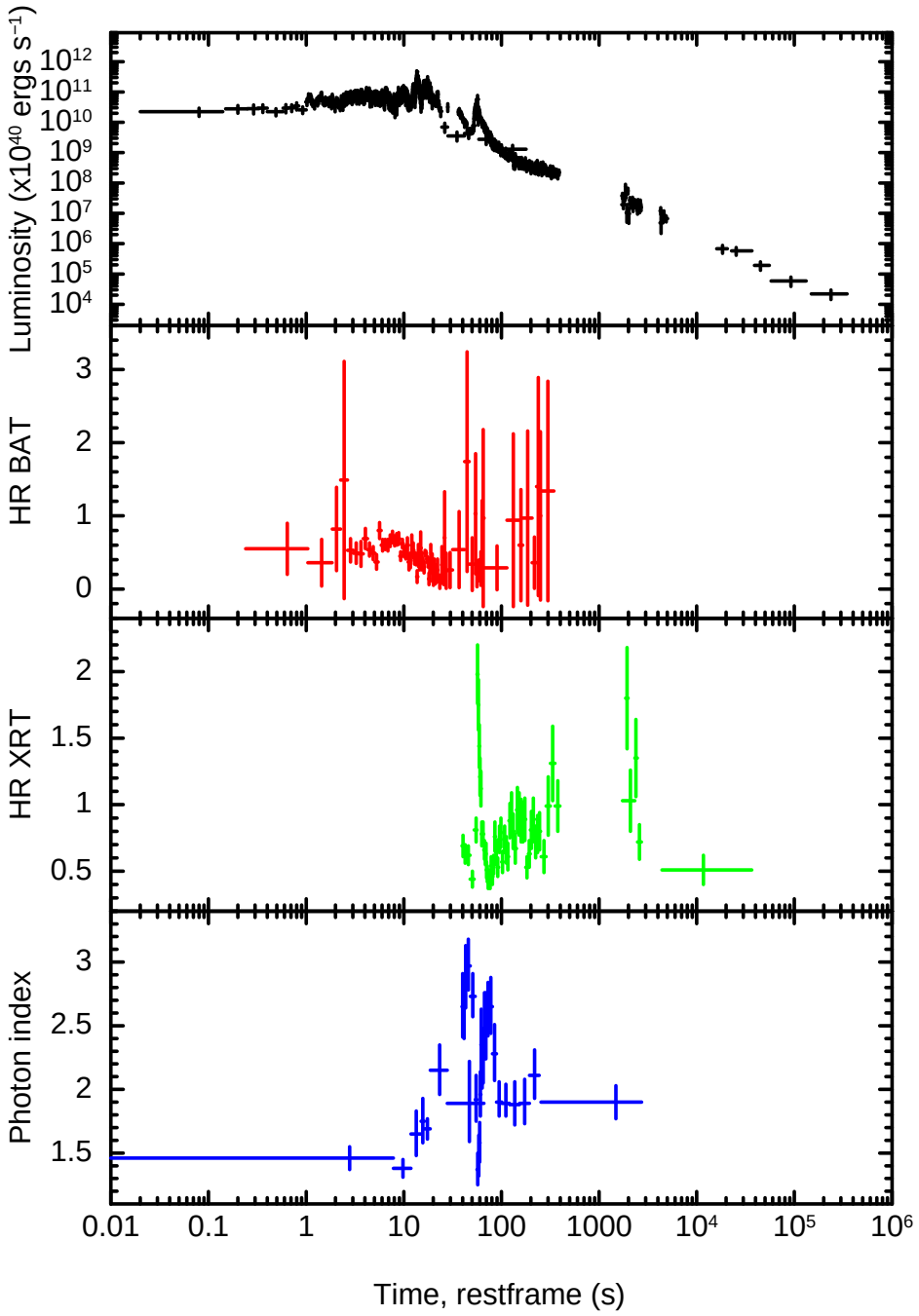

Figure 5.14: GRB 060418: Combined BAT and XRT luminosity light curve (1-20 keV) in the rest frame of the burst [top]. BAT hardness ratio plot [second plot], XRT hardness ratio plot [third plot] and photon index value from absorbed power law spectral fits [bottom]. Mode switching in the XRT occasionally causes WT mode and PC mode data to be accumulated over concurrent time intervals. Photon index data points [bottom panel] with overlapping temporal intervals are the result of this effect. T_0 has been set to the peak of the first flare emission.

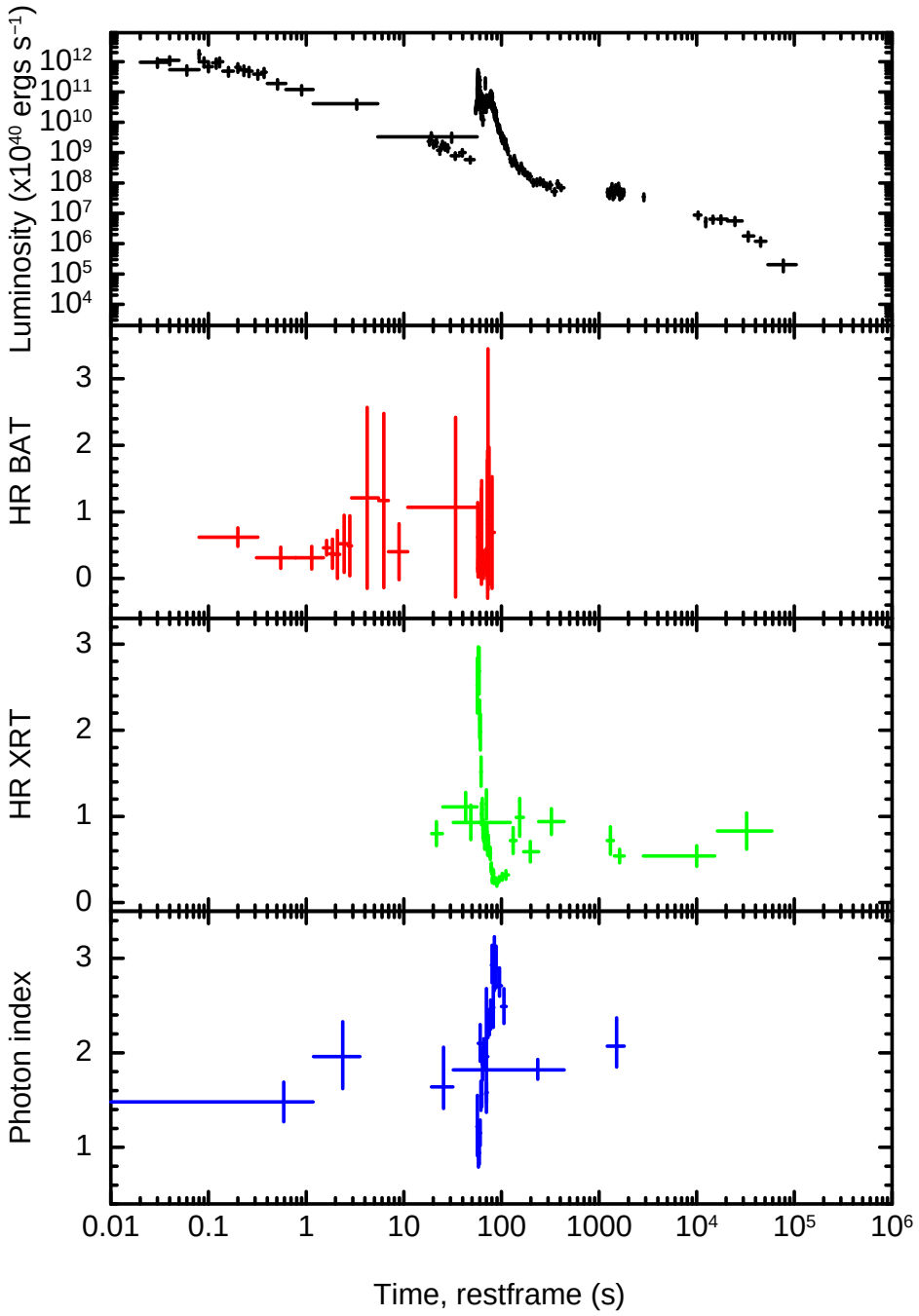

Figure 5.15: GRB 060526: Combined BAT and XRT luminosity light curve (1-20 keV) in the rest frame of the burst [top]. BAT hardness ratio plot [second plot], XRT hardness ratio plot [third plot] and photon index value from absorbed power law spectral fits [bottom]. Mode switching in the XRT occasionally causes WT mode and PC mode data to be accumulated over concurrent time intervals. Photon index data points [bottom panel] with overlapping temporal intervals are the result of this effect. T_0 has been set to the peak of the first flare emission.

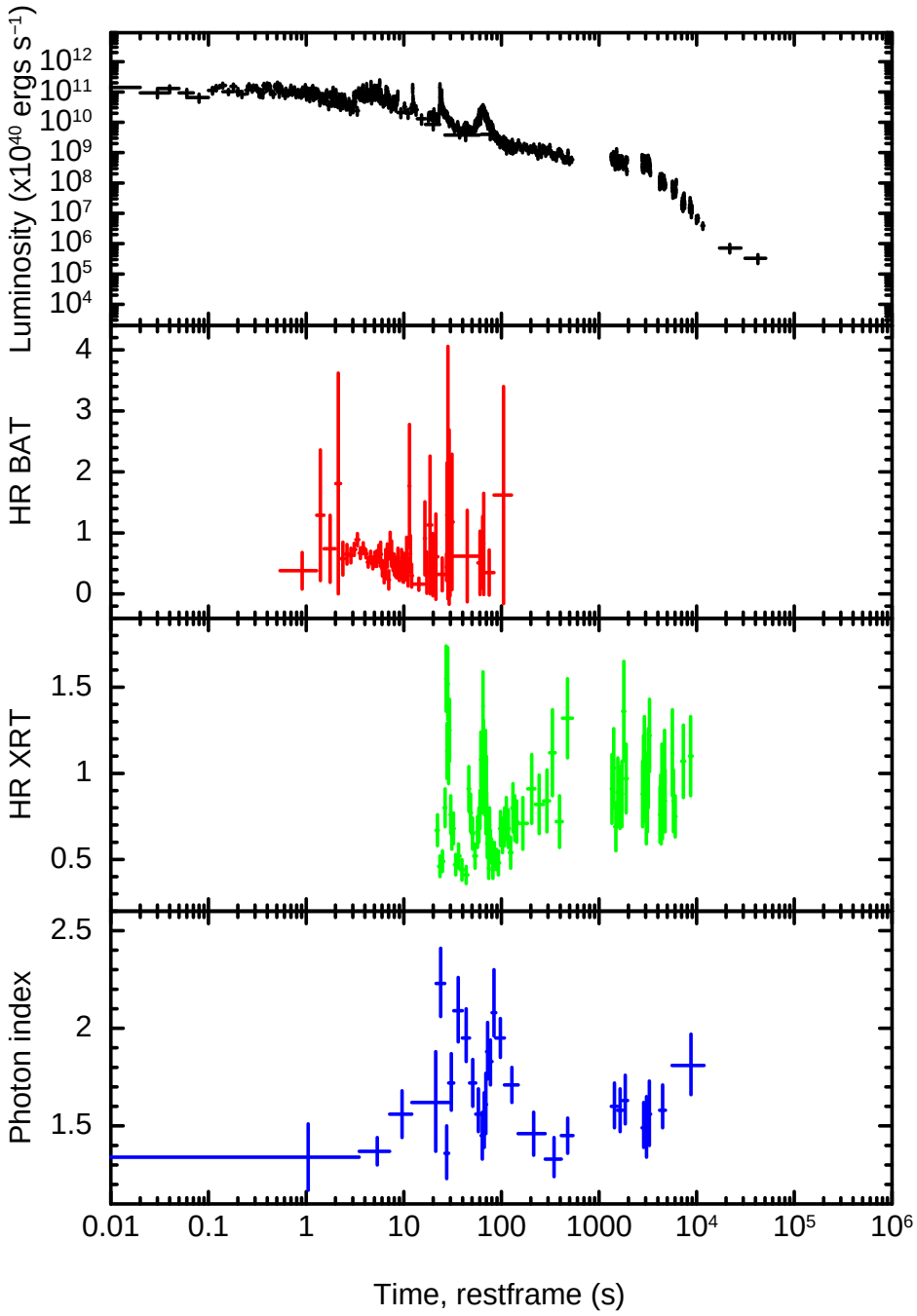

Figure 5.16: GRB 060607A: Combined BAT and XRT luminosity light curve (1-20 keV) in the rest frame of the burst [top]. BAT hardness ratio plot [second plot], XRT hardness ratio plot [third plot] and photon index value from absorbed power law spectral fits [bottom]. Mode switching in the XRT occasionally causes WT mode and PC mode data to be accumulated over concurrent time intervals. Photon index data points [bottom panel] with overlapping temporal intervals are the result of this effect. T_0 has been set to the peak of the first flare emission.

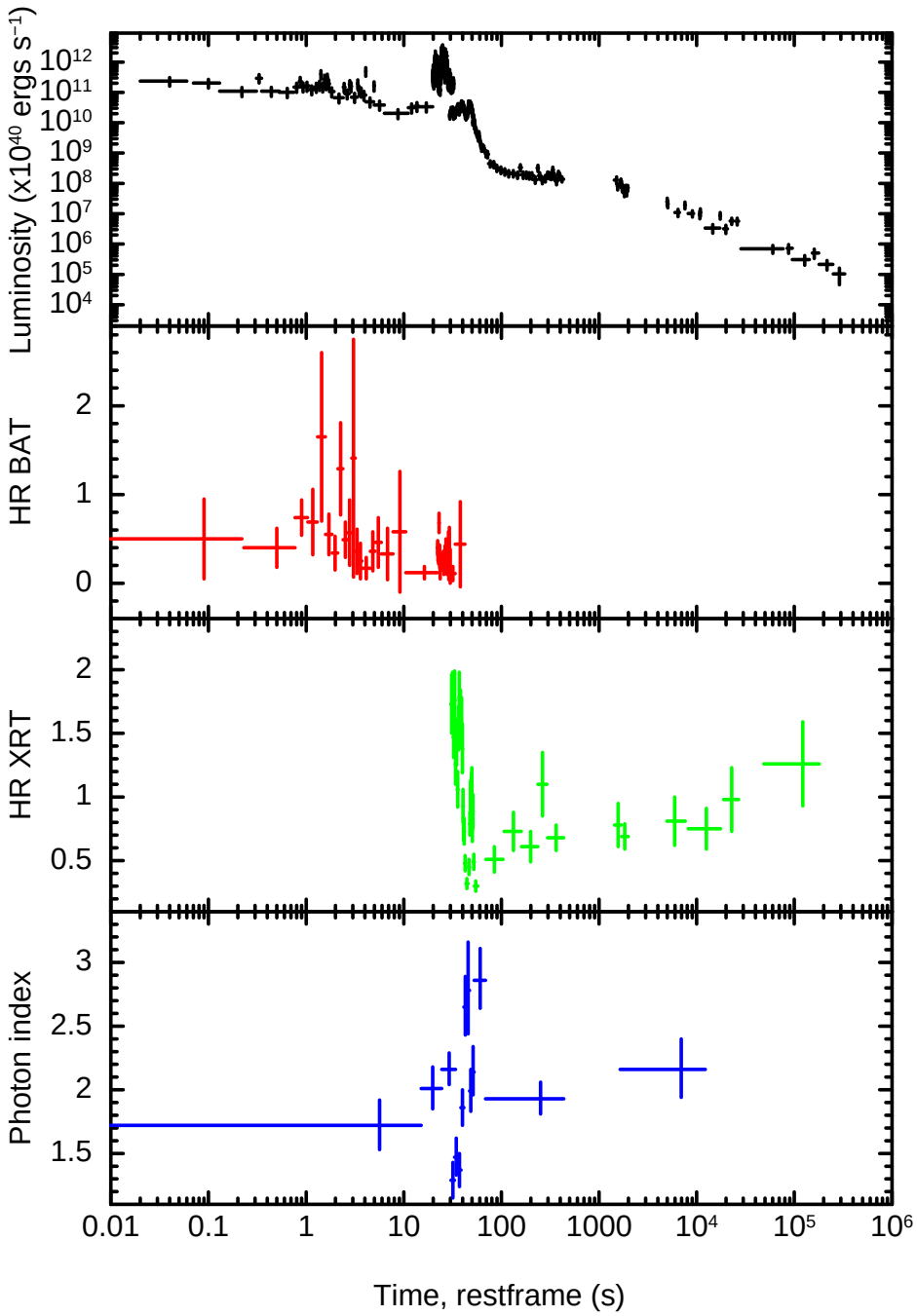

Figure 5.17: GRB 060714A: Combined BAT and XRT luminosity light curve (1-20 keV) in the rest frame of the burst [top]. BAT hardness ratio plot [second plot], XRT hardness ratio plot [third plot] and photon index value from absorbed power law spectral fits [bottom]. T_0 has been set to the peak of the first flare emission.

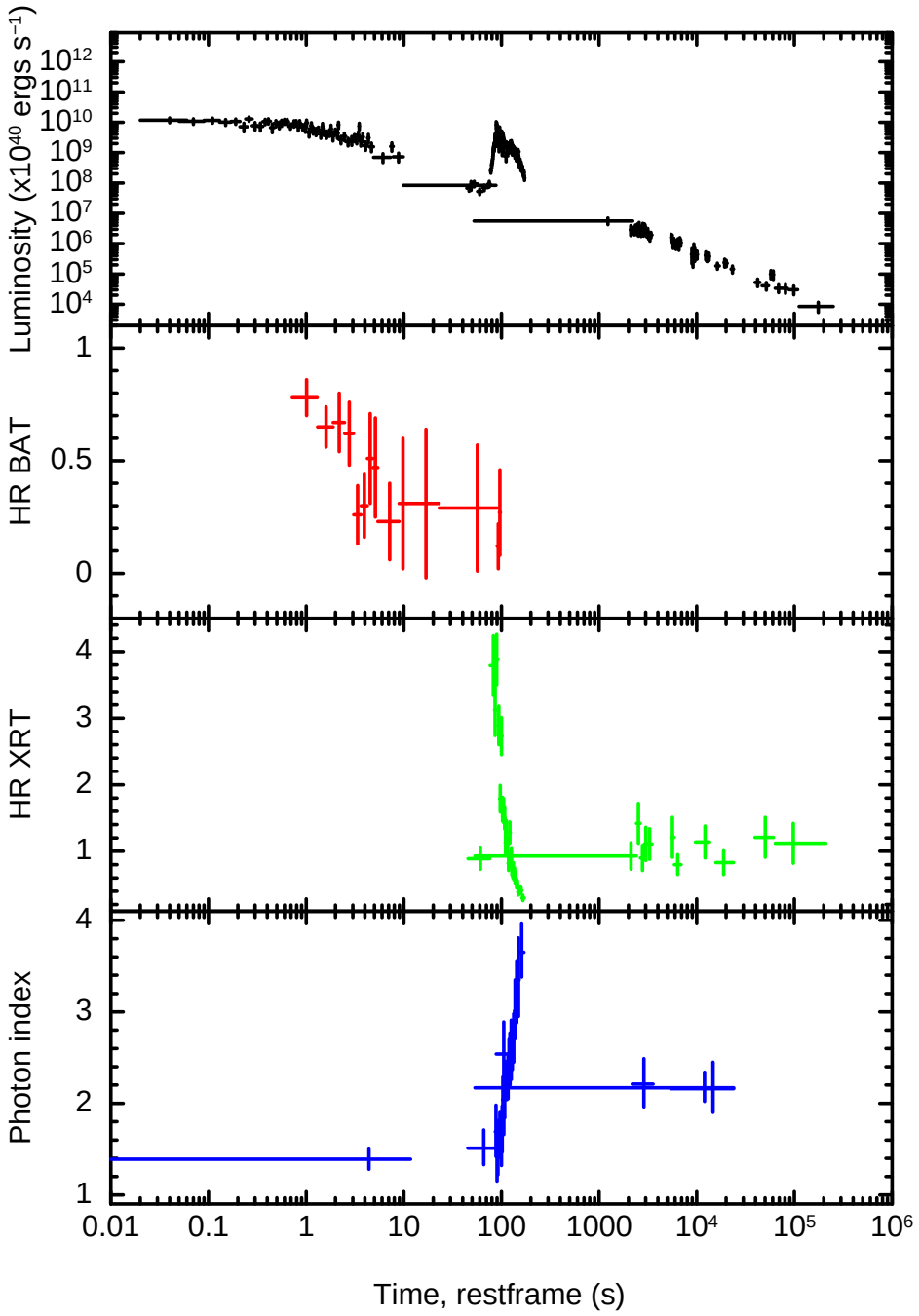

Figure 5.18: GRB 060904B: Combined BAT and XRT luminosity light curve (1-20 keV) in the rest frame of the burst [top]. BAT hardness ratio plot [second plot], XRT hardness ratio plot [third plot] and photon index value from absorbed power law spectral fits [bottom]. Mode switching in the XRT occasionally causes WT mode and PC mode data to be accumulated over concurrent time intervals. Photon index data points [bottom panel] with overlapping temporal intervals are the result of this effect. T_0 has been set to the peak of the first flare emission.

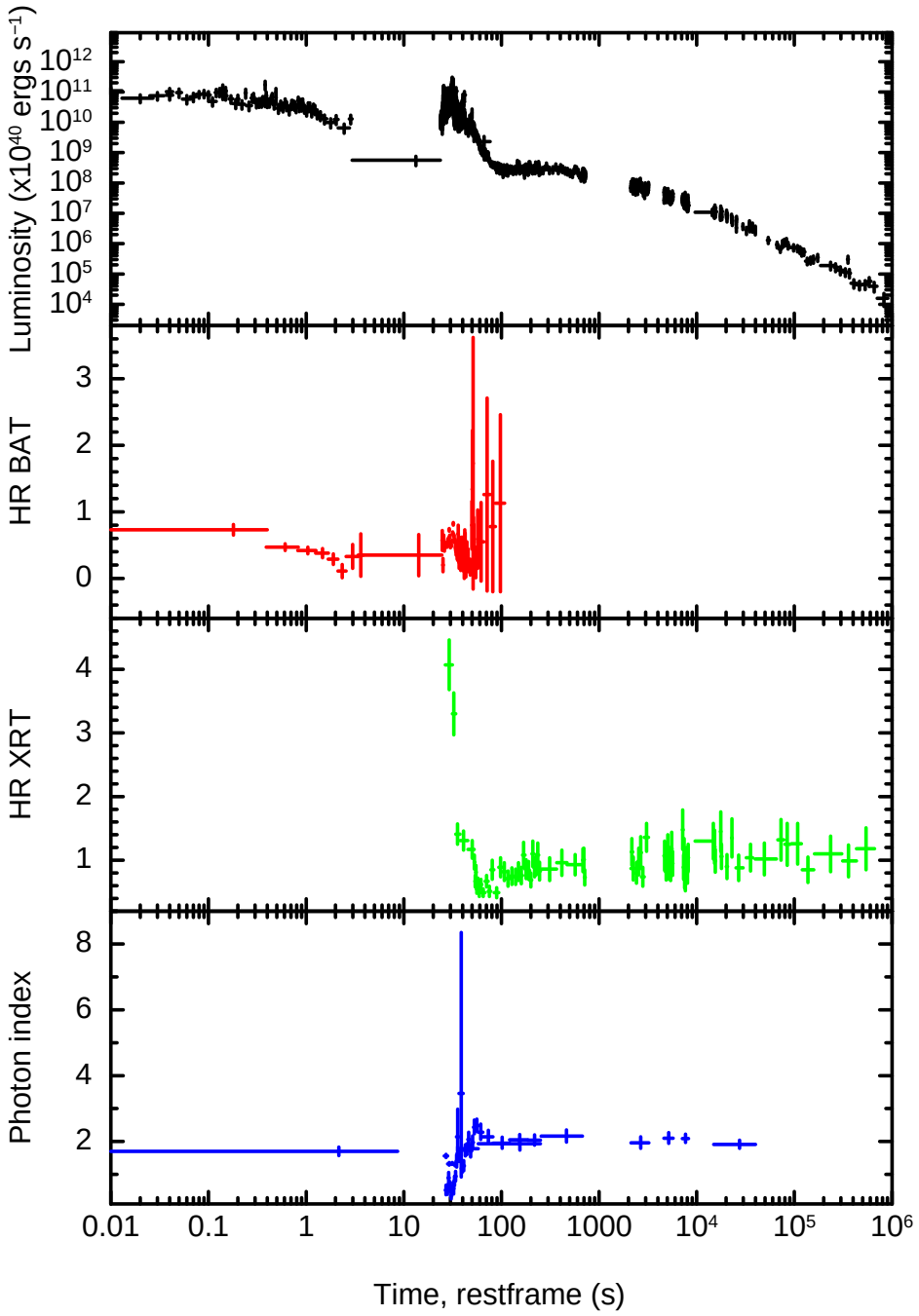

Figure 5.19: GRB 061121: Combined BAT and XRT luminosity light curve (1-20 keV) in the rest frame of the burst [top]. BAT hardness ratio plot [second plot], XRT hardness ratio plot [third plot] and photon index value from absorbed power law spectral fits [bottom]. Mode switching in the XRT occasionally causes WT mode and PC mode data to be accumulated over concurrent time intervals. Photon index data points [bottom panel] with overlapping temporal intervals are the result of this effect. T_0 has been set to the peak of the first flare emission.

5.B Appendix: Emission pulse fits.

BN ($\times 10^{-8}$ ergs cm^{-2} s^{-1})	ST (s)	PT (s)	DT (s)
GRB 050319			
$7.14^{+4.13}_{-4.13}$	$0.01(-)$	$0^{+0.01}_{-0.03}$	$0.03^{+0.03}_{-0.01}$
$2.87^{+0.49}_{-0.59}$	$1.15^{+0.37}_{-0.43}$	$2.72^{+0.08}_{-0.08}$	$0.13^{+0.09}_{-0.08}$
$2.61^{+0.90}_{-0.56}$	$2.99^{+0.25}_{-0.24}$	$3.40^{+0.12}_{-0.04}$	$0.35^{+0.11}_{-0.27}$
$1.76^{+0.41}_{-0.49}$	$5.62^{+1.06}_{-0.39}$	$8.44^{+0.73}_{-0.43}$	$0.78^{+0.01}_{-0.01}$
$10.80^{+3.10}_{-9.10}$	$25.41(-)$	$31.67^{+0.09}_{-0.47}$	$1.75^{+0.40}_{-0.33}$
GRB 050820A			
$2.14^{+0.41}_{-0.42}$	$-1.16^{+0.40}_{-0.67}$	$0^{+0.14}_{-0.24}$	$0.76^{+0.68}_{-0.31}$
$2.14^{+0.38}_{-0.40}$	$1.46^{+0.23}_{-0.47}$	$2.43^{+0.21}_{-0.13}$	$1.54^{+0.46}_{-0.42}$
$0.90^{+0.03}_{-0.03}$	$60.07^{+0.51}_{-0.16}$	$64.34^{+0.24}_{-0.12}$	$3.86(-)$
GRB 060115			
$1.56^{+0.20}_{-0.19}$	$-4.77^{+1.71}_{-0.58}$	$0^{+0.33}_{-0.48}$	$2.44^{+0.90}_{-0.76}$
$2.36^{+0.16}_{-0.17}$	$16.74^{+0.31}_{-0.47}$	$20.02^{+0.20}_{-0.12}$	$2.07^{+0.17}_{-0.28}$
$(3.31^{+0.80}_{-0.78}) \times 10^{-2}$	$79.73^{+5.32}_{-5.56}$	$85.24^{+4.92}_{-3.08}$	$16.15^{+7.09}_{-4.60}$
GRB 060124			
$2.72^{+0.96}_{-1.07}$	$-0.39^{+0.23}_{-0.12}$	$0.0^{+0.04}_{-0.03}$	$1.92 \times 10^{-2}(-)$
$2.85^{+0.77}_{-0.80}$	$0.09^{+0.05}_{-0.10}$	$0.28^{+0.11}_{-0.08}$	$0.41^{+0.20}_{-0.18}$
$37.60^{+14.70}_{-14.50}$	$0.72^{+0.11}_{-0.08}$	$0.92^{+0.10}_{-0.13}$	$0.27^{+0.10}_{-0.09}$
$39.00^{+9.80}_{-9.70}$	$1.79^{+0.27}_{-0.35}$	$1.18^{+0.33}_{-0.44}$	$1.51^{+0.49}_{-0.51}$
$(1.68^{+0.30}_{-0.30}) \times 10^{-2}$	$53.58^{+6.67}_{-7.88}$	$91.62^{+1.13}_{-1.29}$	$2.00^{+2.12}_{-1.31}$
$0.33^{+0.05}_{-0.05}$	$94.82^{+1.61}_{-2.00}$	$111.73^{+1.28}_{-1.32}$	$6.29^{+2.52}_{-1.99}$
$0.38^{+0.04}_{-0.05}$	$114.54^{+3.37}_{-3.13}$	$145.71^{+0.50}_{-0.40}$	$1.43^{+0.82}_{-0.68}$

Continued on Next Page...

Table 5.12 – Continued

BN ($\times 10^{-8}$ ergs cm^{-2} s^{-1})	ST (s)	PT (s)	DT (s)
$0.65^{+0.08}_{-0.07}$	$146.53^{+1.00}_{-1.22}$	$156.75^{+0.06}_{-0.04}$	$(2.64^{+0.05}_{-0.07}) \times 10^{-2}$
$1.69^{+0.09}_{-0.08}$	$153.09^{+0.42}_{-0.38}$	$160.89^{+0.12}_{-0.08}$	$0.49^{+0.11}_{-0.10}$
$0.65^{+0.05}_{-0.07}$	$159.67^{+1.06}_{-0.76}$	$164.95^{+0.86}_{-0.44}$	$6.66^{+2.47}_{-0.54}$
$3.67^{+0.24}_{-0.09}$	$166.85^{+0.06}_{-0.04}$	$167.92^{+0.05}_{-0.07}$	$1.66^{+0.03}_{-0.20}$
$9.21^{+0.34}_{-0.14}$	$171.20^{+0.04}_{-0.03}$	$171.27^{+0.02}_{-0.05}$	$1.96^{+0.06}_{-0.06}$
$0.38^{+0.05}_{-0.07}$	$179.54^{+1.37}_{-2.83}$	$182.47^{+1.44}_{-0.56}$	$11.23^{+3.53}_{-2.23}$
$0.32^{+0.10}_{-0.10}$	$194.77^{+2.24}_{-1.06}$	$198.44^{+1.00}_{-0.87}$	$2.54^{+1.71}_{-1.27}$
$1.65^{+0.14}_{-0.05}$	$205.30^{+0.01}_{-0.29}$	$210.54^{+0.47}_{-0.53}$	$4.90^{+0.93}_{-0.82}$
$0.12^{+0.01}_{-0.01}$	$288.01^{+0.79}_{-0.61}$	$298.54^{+0.86}_{-1.84}$	$12.26^{+136.44}_{-6.21}$
GRB 060210			
$0.32^{+0.14}_{-0.13}$	$-0.16(-)$	$0^{+0.22}_{-0.47}$	$0.84^{+0.57}_{-0.45}$
$0.18^{+0.03}_{-0.03}$	$30.19^{+0.50}_{-0.41}$	$32.71^{+0.40}_{-0.19}$	$0.94^{+0.32}_{-0.26}$
$0.44^{+0.02}_{-0.02}$	$34.47^{+0.38}_{-0.33}$	$43.12^{+0.43}_{-0.39}$	$14.90^{+0.69}_{-0.70}$
$0.78^{+0.09}_{-0.09}$	$39.64^{+0.29}_{-0.39}$	$40.59^{+0.13}_{-0.16}$	$1.55^{+0.32}_{-0.29}$
$2.02^{+0.19}_{-0.19}$	$45.19^{+0.07}_{-0.05}$	$45.80^{+0.03}_{-0.05}$	$0.20^{+0.05}_{-0.04}$
$0.29^{+0.02}_{-0.02}$	$61.18(-)$	$63.17^{+0.50}_{-0.57}$	$8.26^{+0.51}_{-0.49}$
$0.32^{+0.01}_{-0.01}$	$78.63^{+0.30}_{-0.35}$	$86.51^{+0.26}_{-0.28}$	$8.44^{+0.41}_{-0.41}$
$0.25^{+0.01}_{-0.01}$	$111.62^{+0.76}_{-0.54}$	$122.46^{+0.42}_{-0.48}$	$12.54^{+0.49}_{-0.48}$
GRB 060418			
$5.39^{+0.15}_{-0.15}$	$-0.87^{+0.20}_{-0.21}$	$4.16^{+0.13}_{-0.14}$	$5.30^{+0.33}_{-0.36}$
$2.92^{+0.92}_{-0.93}$	$-0.29^{+0.11}_{-0.22}$	$0^{+0.01}_{-0.01}$	$0.001(-)$
$3.64^{+0.31}_{-0.32}$	$8.46^{+0.11}_{-0.17}$	$9.47^{+0.23}_{-0.26}$	$5.59^{+0.92}_{-0.83}$
$21.60^{+0.09}_{-0.09}$	$13.11^{+0.03}_{-0.04}$	$13.64^{+0.03}_{-0.04}$	$0.61^{+0.03}_{-0.04}$

Continued on Next Page...

Table 5.12 – Continued

BN ($\times 10^{-8}$ ergs cm^{-2} s^{-1})	ST (s)	PT (s)	DT (s)
$7.69^{+1.16}_{-0.74}$	$15.32^{+0.15}_{-0.20}$	$17.11^{+0.21}_{-0.75}$	$2.93^{+0.69}_{-0.16}$
$1.58^{+0.12}_{-0.12}$	$35.00(-)$	$35.55^{+0.41}_{-0.49}$	$5.85^{+0.38}_{-0.38}$
$2.03^{+0.07}_{-0.08}$	$51.56^{+0.14}_{-0.16}$	$54.05^{+0.21}_{-0.18}$	$8.11^{+0.20}_{-0.22}$
GRB 060526			
$9.28^{+2.34}_{-1.54}$	$-0.01^{+0.01}_{-0.01}$	$0^{+0.02}_{-0.01}$	$0.39^{+0.11}_{-0.12}$
$1.09^{+0.05}_{-0.05}$	$53.96^{+0.20}_{-0.20}$	$58.06^{+0.15}_{-0.25}$	$5.98^{+0.66}_{-0.49}$
$0.65^{+0.01}_{-0.04}$	$64.47^{+0.51}_{-0.41}$	$76.98^{+0.16}_{-0.42}$	$7.48^{+0.37}_{-0.33}$
GRB 060607A			
$1.55^{+0.05}_{-0.06}$	$-1.49^{+0.08}_{-0.06}$	$0^{+0.07}_{-0.08}$	$2.15^{+0.14}_{-0.14}$
$1.04^{+0.08}_{-0.83}$	$3.02^{+0.18}_{-0.16}$	$4.90^{+0.21}_{-0.28}$	$3.03^{+0.37}_{-0.41}$
$0.16^{+0.01}_{-0.01}$	$6.15^{+4.70}_{-4.79}$	$20.39^{+0.44}_{-0.57}$	$5.11^{+0.52}_{-0.75}$
$0.39^{+0.20}_{-0.19}$	$11.04^{+0.91}_{-1.06}$	$13.27(-)$	$0.09^{+0.30}_{-0.08}$
$0.29^{+0.02}_{-0.02}$	$22.77^{+0.11}_{-0.15}$	$23.30^{+0.15}_{-0.13}$	$4.80^{+0.30}_{-0.30}$
$(4.87^{+0.34}_{-0.40}) \times 10^{-2}$	$33.10^{+2.37}_{-1.71}$	$44.45^{+1.47}_{-1.15}$	$29.88^{+1.95}_{-3.16}$
$0.26^{+0.10}_{-0.10}$	$53.25^{+0.57}_{-0.45}$	$64.68^{+0.58}_{-0.33}$	$7.11^{+0.37}_{-0.35}$
GRB 060714A			
$3.54^{+0.60}_{-0.65}$	$-0.68^{+0.11}_{-0.17}$	$0^{+0.01}_{-0.07}$	$0.50^{+0.19}_{-0.15}$
$2.10^{+0.43}_{-0.44}$	$0.56^{+0.22}_{-0.36}$	$0.87^{+0.17}_{-0.18}$	$1.69^{+0.54}_{-0.48}$
$2.32^{+0.97}_{-0.97}$	$1.17^{+0.23}_{-0.23}$	$1.66^{+0.11}_{-0.08}$	$0.09^{+0.01}_{-0.01}$
$1.49^{+0.35}_{-0.36}$	$2.19(-)$	$1.58^{+0.87}_{-1.06}$	$3.97^{+1.12}_{-1.02}$
$0.77^{+0.04}_{-0.05}$	$7.64^{+2.93}_{-3.23}$	$19.45^{+0.59}_{-0.65}$	$10.62^{+0.38}_{-0.35}$
$9.64^{+0.63}_{-0.62}$	$19.55^{+0.16}_{-0.21}$	$21.13^{+0.07}_{-0.07}$	$1.00^{+0.14}_{-0.14}$
$8.01^{+1.46}_{-1.46}$	$21.79^{+0.07}_{-0.08}$	$22.29^{+0.03}_{-0.04}$	$0.08^{+0.05}_{-0.04}$

Continued on Next Page...

Table 5.12 – Continued

BN ($\times 10^{-8}$ ergs cm^{-2} s^{-1})	ST (s)	PT (s)	DT (s)
$18.20^{+1.20}_{-1.10}$	$23.48^{+0.15}_{-0.10}$	$25.26^{+0.07}_{-0.07}$	$0.65^{+0.08}_{-0.07}$
$9.28^{+1.01}_{-1.06}$	$25.22^{+0.25}_{-0.37}$	$27.84^{+0.14}_{-0.07}$	$0.29^{+0.05}_{-0.07}$
$0.43^{+0.02}_{-0.02}$	$29.51^{+0.39}_{-0.47}$	$39.69^{+0.36}_{-0.31}$	$6.03^{+0.37}_{-0.41}$
$0.45^{+0.03}_{-0.03}$	$43.94^{+0.44}_{-0.44}$	$48.51^{+0.18}_{-0.23}$	$2.13^{+0.22}_{-0.21}$
GRB 060904B			
$4.16^{+0.46}_{-0.50}$	$-1.44^{+0.53}_{-2.20}$	$0^{+0.18}_{-0.13}$	$2.09^{+0.31}_{-0.28}$
$1.66^{+0.11}_{-0.07}$	$77.54^{+0.30}_{-0.31}$	$93.36^{+0.88}_{-1.47}$	$23.61^{+2.10}_{-2.05}$
$0.39^{+0.06}_{-0.05}$	$122.39^{+0.31}_{-0.39}$	$122.90^{+0.50}_{-0.40}$	$16.38^{+3.09}_{-3.28}$
GRB 061121			
$6.28^{+0.53}_{-0.52}$	$-1.41^{+0.21}_{-0.41}$	$0^{+0.08}_{-0.10}$	$0.88^{+0.14}_{-0.12}$
$7.57^{+0.22}_{-0.20}$	$25.02^{+0.04}_{-0.04}$	$25.64^{+0.02}_{-0.02}$	$1.29^{+0.12}_{-0.07}$
$5.42^{+0.14}_{-0.12}$	$27.39^{+0.09}_{-0.06}$	$28.29^{+0.05}_{-0.03}$	$3.79^{+0.27}_{-0.30}$
$10.90^{+0.20}_{-0.20}$	$29.48^{+0.07}_{-0.05}$	$31.41^{+0.01}_{-0.02}$	$0.37^{+0.03}_{-0.03}$
$(2.78^{+0.38}_{-0.36}) \times 10^{-2}$	$33.40(-)$	$29.52^{+0.03}_{-0.01}$	$1.66^{+0.34}_{-0.29}$
$1.54^{+0.18}_{-0.40}$	$36.90^{+0.35}_{-0.65}$	$39.78^{+0.40}_{-0.34}$	$3.11^{+1.42}_{-1.42}$
$0.65^{+0.02}_{-0.28}$	$45.89^{+1.84}_{-13.00}$	$50.50^{+0.83}_{-1.11}$	$5.81^{+0.48}_{-0.48}$

Continued on Next Page...

Table 5.12 – Continued

BN ($\times 10^{-8}$ ergs cm^{-2} s^{-1})	ST (s)	PT (s)	DT (s)

Table 5.12: Summary of emission pulse properties as modelled by the FRED/*BURS* component in *QDP*, where T_0 is taken to be the peak of first emission pulse (SNR = 3). All fits are from BAT data unless otherwise stated. BN is the normalisation of the *BURS* component (or 'peak' flux), ST is the start time, PT the peak time and DT is the decay constant of the exponential decay (see equation 5.1 for a further definition of the FRED/*BURS* component). All times are quoted in the rest frame of the burst.

Chapter 6

Summary and Future Work

The launch of the *Swift* mission has provided new insights into the GRB phenomenon and has helped to advance our understanding of these violent events. This body of work investigates several aspects of the broad field of GRB research as new avenues of enquiry have opened up. Chapter 2 reports on the study of the multi-wavelength afterglow behaviour of the high redshift GRB 050505, including evidence for a proposed jet-break. Chapters 3 and 4 investigate the presence of X-ray emission lines in GRB spectra, as suggested by pre-*Swift* observations; chapter 3 provides a discussion of these prior observations and a comparison of three methods already extant in the literature for assessing the significance of such spectral features whilst chapter 4 applies these methods to a sample of 40 *Swift* bursts. The final chapter investigates the phenomena of 'precursors' and 'quiescent intervals'. The following subsections outline the important results from each chapter and explore the potential for further work in each field.

6.1 GRB 050505: A high redshift burst detected by Swift.

This chapter presents multi-wavelength data for GRB 050505 ($z = 4.27$), the third most distant burst, measured by spectroscopic redshift, discovered so far. Studying high redshift bursts are important as they enable us to investigate the evolution of the GRB population spectral and temporal properties, as well as their host galaxy environments.

There was no evidence for variation of the X-ray spectra over the duration of the observations. The pho-

ton index observed, $2.01^{+0.08}_{-0.08}$, is typical of the photon indices seen in other GRB afterglows (Nousek et al., 2006), even though a higher range of spectral energies ($1.6 - 53$ keV) are being sampled due to the high redshift of this burst. The optical – X-ray spectrum indicated that the cooling break was located between these two bands, as seen in many other GRBs afterglows.

The X-ray light curve of this burst was adequately fit with either a 'doubly broken' or 'smoothly broken' power law model. The 'smoothly broken' power law model provided a good statistical fit to the data but was rejected as it was inconsistent with all of the afterglow models considered. A 'doubly broken' power law model also provided a good fit to the data; the values obtained for the temporal decay slopes and break times were consistent with the canonical light curve model proposed by Nousek et al. (2006), indicating that there is no gross change to the canonical light curve over a large range of z. I conclude that the first break is due to the end of energy injection into the forward shock (Nousek et al., 2006; Zhang et al., 2006) and that the second break is potentially a jet break. There is no confirmation of the expected achromatic nature of this break due to a lack of observations in additional bands at the time. However, the calculated rest frame burst properties are in good agreement with pre-*Swift* era GRBs with proposed jet breaks, provided that the circumburst density was of the order 100 cm^{-3}. The discovery of a break consistent with a jet break is rare in the *Swift* era of observations.

The study of further high redshift bursts is necessarily limited to GRBs with prompt optical spectroscopic follow up observations. The random nature of these events and the limitations on the relevant optical telescope observation time means that a target investigation of these events has limited potential; future studies will necessarily have to occur on an ad hoc basis.

6.2 Line Searches in Swift X-ray Spectra.

The search for emission lines in GRB spectra was motivated by low significance (usually $2 - 3\ \sigma$) Gaussian features reported in the literature in the pre-*Swift* era; often at late times with respect to the GRB trigger. If such features were to be detected they could provide a significant insight into the environment surrounding the GRB and the emission geometry of the burst.

In the past various different approaches were used to determine the significance of potential line features, however, the choice of which statistical methods to use were heavily debated. Chapter 3 compares

three methods (Bayes factor, RS and *ppp*) extant in the literature and discusses their relative advantages and disadvantages, as well as determining the detection limits for each method in spectra with spectral parameters typical of the Swift-era sample. Of the three methods tested the *ppp* method was by far the most rigorous and could be used as a 'stand alone' test. However, it is computationally prohibitive to use this method to test for additional spectral features for every reasonably sampled GRB spectrum obtained. Therefore, in practice, the total number of spectra selected for use with this method must be reduced by other methods; either by basic spectral fitting, the Bayes factor method, the RS method or a combination of these methods. For all three methods the optimum range for emission line detection was found to be $0.4-6$ keV, with line equivalent widths as low as ~ 50 eV detectable in principle from data with only $\sim$1600 counts.

Of the 332 WT mode spectra assessed in chapter 4, only 12 produced possible detections at $\geq 99.90\%$ significance (single trial). These were all located around two energies in the observer frame: 0.7 keV (10/12) and 2.3 keV (2/12). It is my conclusion that all of these features are either due to calibration issues, imperfect bias subtraction at the processing stage or incorrect modelling of the host absorption column (most likely case for the 0.7 keV features), rather than intrinsic GRB emission line detections. The only non-power law emission component I accept as intrinsic is the blackbody component detected in GRB 060218. This work has provided stringent limits on the normalisation of any emission line features present in early time WT observations; whilst it is still possible that such features could be present they must be completely dominated by the underlying afterglow power law component.

In the future this work should be extended to cover spectra occurring at later times, commensurate with the pre-*Swift* era reports. At such times the underlying power law spectral component may not be so dominant therefore it may be easier to detect emission features, if they are present. However, using later time PC mode data means that the average integration time required to get a good SNR spectrum will increase, which means that potentially transient emission features may be missed. To counter this an initial sample of observationally bright bursts should be selected, most likely low z bursts. Furthermore these bursts should have known redshifts so that accurate two absorption component can be applied.

6.3 Precursors and long quiescent times in Swift GRBs.

It has long been hypothesised (Colgate, 1973, 1974) that phase 0 GRB emission is preceded by a transient signal with a different physical origin, and therefore spectral properties, to the rest of the burst. One particular ambiguity in the models proposed so far is the delay between the precursor and phase 0 emission; times range between little as 10 s (Wang & Mészáros, 2007) up to several 100 s (Koshut et al., 1995; Lazzati et al., 2005). A separate study conducted by Nakar & Piran (2002) indicated that there are unusually long intervals of little or no emission during phase 0 that they call *quiescent times* (Q-times, §5.1.3). They stress that such periods are not the same as the delays between precursor and phase 0 emission reported by Koshut et al. (1995), however, it is interesting to note that the timescales discussed in both works bear a striking resemblance.

Thus far precursor definitions have varied widely between different studies in the literature and often depend on the observed energy range and instrument used. Rather than adopt a fully instrumentally based criteria (i.e. emission occurring before a burst 'trigger' etc) in this study I chose to select GRBs with long quiescent times, since quiescent periods indicate a change in central engine activity, which is the essence of the definition of a precursor. In this work I have taken a subsection of Swift GRBs with long Q-times ($>$ 50 s in the observer's reference frame) and known redshifts (with a range between 0.703 and 3.910).

Various pulse spectral, temporal and energetic properties were extracted from the rest frame luminosity light curves for these bursts. No strong evidence was found to suggest that the precursors/early time emission pulses in this sample were spectrally different to the rest of the main emission period over the energy ranges observed by BAT. Pulse properties were used to calculate a series of Spearman Rank and Kendall Tau correlations. Several correlations and anti-correlations were found in the pulse temporal and energetic properties that indicated a common origin for all pulses (as suggested by previous studies), irrespective of which instrument or energy range they are typically observed in. The correlations between pulse properties noted were all consistent with the accretion models proposed by Perna et al. (2006, delayed accretion from a fragmented disk) and Proga & Zhang (2006, accretion moderated by a magnetic barrier). I was not able to confirm the average pulse luminosity light curve as proposed by Lazzati et al. (2008). The gross temporal and spectral characteristics of all of the bursts in this study were found to be consistent with the general GRB sample, though there was a very tentative potential

for different subgroups within the late time afterglow behaviour.

There are two potential avenues for further research arising from this study. The first is developing additional software to aid in the extraction and evaluation of noisy γ-ray light curves, potentially enabling the discovery of precursor emission periods that have been missed by previous investigations. Techniques such as wavelet analysis/transforms (using a base model of a FRED pulse) or further development of Bayesian Block methods are two possible options. The second is broadening the analysis presented in this work to cover all bursts with known redshifts. This would help to resolve whether the (anti-)correlations seen in this work are present in the GRB population as a whole, or whether they are unique to long quiescent time bursts.

BIBLIOGRAPHY

Abbey, T., Carpenter, J., Read, A., et al. 2006, in ESA Special Publication, Vol. 604, The X-ray Universe 2005, ed. A. Wilson, 943–+

Abramovici, A., Althouse, W. E., Drever, R. W. P., et al. 1992, Science, 256, 325

Acernese, F., Amico, P., Alshourbagy, M., et al. 2007, in American Institute of Physics Conference Series, Vol. 924, American Institute of Physics Conference Series, 187–193

Akerlof, C., Balsano, R., Barthelmy, S., et al. 1999, *Nature* , 398, 400

Aloy, M. A., Müller, E., Ibáñez, J. M., Martí, J. M., & MacFadyen, A. 2000, *ApJL* , 531, L119

Amati, L. 2006, *MNRAS* , 372, 233

Amati, L., Frontera, F., Tavani, M., et al. 2002, *A&A* , 390, 81

Amati, L., Frontera, F., Vietri, M., et al. 2000, Science, 290, 953

Anders, E. & Grevesse, N. 1989, Geochimica et Cosmochimica Acta, 53, 197

Andersen, M. I., Hjorth, J., Pedersen, H., et al. 2000, *A&A* , 364, L54

Antonelli, L. A., Piro, L., Vietri, M., et al. 2000, *ApJL* , 545, L39

Arnaud, K. A. 1996a, in ASP Conf. Ser. 101: Astronomical Data Analysis Software and Systems V, ed. G. H. Jacoby & J. Barnes, 17–+

Arnaud, K. A. 1996b, in ASP Conf. Ser. 101: Astronomical Data Analysis Software and Systems V, ed. G. H. Jacoby & J. Barnes, 17–+

Ballantyne, D. R. & Ramirez-Ruiz, E. 2001, *ApJL* , 559, L83

Ballet, J. 1999, *A&AS* , 135, 371

Band, D., Matteson, J., Ford, L., et al. 1993, *ApJ* , 413, 281

Band, D. L., Norris, J. P., & Bonnell, J. T. 2004, *ApJ* , 613, 484

Barthelmy, S. D., Barbier, L. M., Cummings, J. R., et al. 2005a, Space Science Reviews, 120, 143

Barthelmy, S. D., Cannizzo, J. K., Gehrels, N., et al. 2005b, *ApJL* , 635, L133

Belczynski, K., Kalogera, V., & Bulik, T. 2002, *ApJ* , 572, 407

Belczynski, K., Perna, R., Bulik, T., et al. 2006, *ApJ* , 648, 1110

Berger, E. 2006, in American Institute of Physics Conference Series, Vol. 836, Gamma-Ray Bursts in the Swift Era, ed. S. S. Holt, N. Gehrels, & J. A. Nousek, 33–42

Berger, E., Cenko, S. B., Steidel, C., Reddy, N., & Fox, D. B. 2005a, GRB Coordinates Network, 3368, 1

Berger, E., Cowie, L. L., Kulkarni, S. R., et al. 2003a, *ApJ* , 588, 99

Berger, E. & Gladders, M. 2006, GRB Coordinates Network, 5170, 1

Berger, E., Kulkarni, S. R., & Frail, D. A. 2003b, *ApJ* , 590, 379

Berger, E., Kulkarni, S. R., Pooley, G., et al. 2003c, *Nature* , 426, 154

Berger, E., Penprase, B. E., Cenko, S. B., et al. 2006, *ApJ* , 642, 979

Berger, E., Price, P. A., Cenko, S. B., et al. 2005b, *Nature* , 438, 988

Berger, E. & Soderberg, A. M. 2005, GRB Coordinates Network, 4384, 1

Beuermann, K., Hessman, F. V., Reinsch, K., et al. 1999, *A&A* , 352, L26

Blandford, R. D. & Payne, D. G. 1982, *MNRAS* , 199, 883

Blandford, R. D. & Znajek, R. L. 1977, *MNRAS* , 179, 433

Bloom, J. S., Frail, D. A., & Kulkarni, S. R. 2003, *ApJ* , 594, 674

Bloom, J. S., Kulkarni, S. R., & Djorgovski, S. G. 2002a, *AJ* , 123, 1111

Bloom, J. S., Kulkarni, S. R., Price, P. A., et al. 2002b, *ApJL* , 572, L45

Bloom, J. S., Perley, D. A., & Chen, H. W. 2006, GRB Coordinates Network, 5826, 1

Bloom, J. S. & Prochaska, J. X. 2006, in American Institute of Physics Conference Series, Vol. 836, Gamma-Ray Bursts in the Swift Era, ed. S. S. Holt, N. Gehrels, & J. A. Nousek, 473–482

Boella, G., Butler, R. C., Perola, G. C., et al. 1997, *A&AS* , 122, 299

Boër, M. & Gendre, B. 2000, *A&A* , 361, L21

Boggs, S. E., Zoglauer, A., Bellm, E., et al. 2007, *ApJ* , 661, 458

Bradt, H. V., Rothschild, R. E., & Swank, J. H. 1993, *A&AS* , 97, 355

Brainerd, J. J., Paciesas, W. S., Meegan, C. A., & Fishman, G. J. 1994, in AIP Conf. Proc. 307: Gamma-Ray Bursts, ed. G. J. Fishman, 122

Burrows, D. N., Falcone, A., Chincarini, G., et al. 2007, Royal Society of London Philosophical Transactions Series A, 365, 1213

Burrows, D. N., Hill, J. E., Nousek, J. A., et al. 2005a, Space Science Reviews, 120, 165

Burrows, D. N. & Racusin, J. 2007, ArXiv Astrophysics e-prints; astro-ph/0702633

Burrows, D. N., Romano, P., Falcone, A., et al. 2005b, Science, 309, 1833

Butler, N., Ricker, G., Atteia, J.-L., et al. 2005a, GRB Coordinates Network, 3570, 1

Butler, N., Ricker, G., Vanderspek, R., et al. 2005b, *ApJL* , 627, L9

Butler, N. R. 2007, *ApJ* , 656, 1001

Butler, N. R. & Kocevski, D. 2007a, *ApJ* , 663, 407

—. 2007b, *ApJ* , 668, 400

Butler, N. R., Kocevski, D., Bloom, J. S., & Curtis, J. L. 2007, *ApJ* , 671, 656

Campana, S., Beardmore, A. P., Cusumano, G., & Godet, . 2006a, *Swift* XRT CALDB Release Notes, 1

Campana, S., Mangano, V., Blustin, A. J., et al. 2006b, *Nature* , 442, 1008

Campana, S., Romano, P., Covino, S., et al. 2006c, *A&A* , 449, 61

Cavallo, G. & Rees, M. J. 1978, *MNRAS* , 183, 359

Cenko, S. B., Berger, E., & Cohen, J. 2006, GRB Coordinates Network, 4592, 1

Cenko, S. B., Fox, D. B., Penprase, B. E., et al. 2008, *ApJ* , 677, 441

Cenko, S. B., Steidel, C., Reddy, N., & Fox, D. B. 2005, GRB Coordinates Network, 3366, 1

Chapman, R., Priddey, R. S., & Tanvir, N. R. 2008, ArXiv Astrophysics e-prints; astro-ph/0802.0008, 802

Chen, H.-W., Thompson, I., Prochaska, J. X., & Bloom, J. 2005, GRB Coordinates Network Circular, 3709, 1

Chen, W.-X. & Beloborodov, A. M. 2007, *ApJ* , 657, 383

Chen, Y., Ikebe, Y., & Böhringer, H. 2003, *A&A* , 407, 41

Chevalier, R. A. & Li, Z.-Y. 2000, *ApJ* , 536, 195

Chincarini, G., Moretti, A., Romano, P., et al. 2007, *ApJ* , 671, 1903

Christensen, L., Hjorth, J., & Gorosabel, J. 2004, *A&A* , 425, 913

Colgate, S. A. 1968, Canadian Journal of Physics. Proceedings of the 10th International Conference on Cosmic Rays, Calgary, Alberto, June 19-30, 1967, Vol. 46., p.476, 46, 476

Colgate, S. A. 1970, in International Cosmic Ray Conference, Vol. 1, International Cosmic Ray Conference, 353–+

—. 1973, *ApJL* , 181, L53+

—. 1974, *ApJ* , 187, 333

Cordes, J. M., Romani, R. W., & Lundgren, S. C. 1993, *Nature* , 362, 133

Costa, E., Frontera, F., Heise, J., et al. 1997, *Nature* , 387, 783

Covino, S., Malesani, D., Israel, G. L., et al. 2006, *A&A* , 447, L5

Cucchiara, A., Fox, D. B., & Berger, E. 2006, GRB Coordinates Network Circular, 4729, 1

Cusumano, G., Mangano, V., Angelini, L., et al. 2006a, *ApJ* , 639, 316

Cusumano, G., Mangano, V., Chincarini, G., et al. 2007, *A&A* , 462, 73

—. 2006b, *Nature* , 440, 164

Dai, Z. G. 2004, *ApJ* , 606, 1000

Dai, Z. G. & Cheng, K. S. 2001, *ApJL* , 558, L109

Dai, Z. G., Wang, X. Y., Wu, X. F., & Zhang, B. 2006, Science, 311, 1127

Daigne, F. & Mochkovitch, R. 2002, *MNRAS* , 336, 1271

De Grandi, S. & Molendi, S. 1999, *A&A* , 351, L45

De Pasquale, M., Piro, L., Perna, R., et al. 2003, *ApJ* , 592, 1018

de Ugarte Postigo, A., Jelinek, M., Gorosabel, J., et al. 2005, GRB Coordinates Network Circular, 3376, 1

Della Valle, M., Chincarini, G., Panagia, N., et al. 2006a, *Nature* , 444, 1050

Della Valle, M., Malesani, D., Benetti, S., et al. 2003a, *A&A* , 406, L33

Della Valle, M., Malesani, D., Benetti, S., et al. 2004, in American Institute of Physics Conference Series, Vol. 727, Gamma-Ray Bursts: 30 Years of Discovery, ed. E. Fenimore & M. Galassi, 403–407

Della Valle, M., Malesani, D., Benetti, S., Testa, V., & Stella, L. 2003b, *IAU Circular* , 8197, 2

Della Valle, M., Malesani, D., Bloom, J. S., et al. 2006b, *ApJL* , 642, L103

Dessart, L., Burrows, A., Livne, E., & Ott, C. D. 2007, *ApJ* , 669, 585

Di Matteo, T., Perna, R., & Narayan, R. 2002, *ApJ* , 579, 706

Dickey, J. M. & Lockman, F. J. 1990, *ARA&A* , 28, 215

Dickinson, H. & Tamarkin, P. 1965, in Proceedings of the IEEE, volume 53, issue 12

Drenkhahn, G. & Spruit, H. C. 2002, *A&A* , 391, 1141

Dupree, A. K., Falco, E., Prochaska, J. X., Chen, H.-W., & Bloom, J. S. 2006, GRB Coordinates Network Circular, 4969, 1

Eadie, W. T., Drijard, D., James, F. E., Roos, M., & B., S. 1971, Statistical methods in experimental physics (Amsterdam: North-Holland, 1971)

Eichler, D. 1982, *ApJ* , 254, 683

Eichler, D. & Granot, J. 2006, *ApJL* , 641, L5

Eichler, D., Livio, M., Piran, T., & Schramm, D. N. 1989, *Nature* , 340, 126

Evans, P. A., Beardmore, A. P., Page, K. L., et al. 2007, *A&A* , 469, 379

Falcone, A. D., Burrows, D. N., Lazzati, D., et al. 2006, *ApJ* , 641, 1010

Falcone, A. D., Morris, D., Racusin, J., et al. 2007, *ApJ* , 671, 1921

Fan, Y.-Z., Piran, T., & Wei, D.-M. 2008, in American Institute of Physics Conference Series, Vol. 968, American Institute of Physics Conference Series, ed. Y.-F. Yuan, X.-D. Li, & D. Lai, 32–35

Fan, Y. Z. & Wei, D. M. 2005, *MNRAS* , 364, L42

Ferrero, P., Kann, D. A., Zeh, A., et al. 2006, *A&A* , 457, 857

Fishman, G. J. & Meegan, C. A. 1995, *ARA&A* , 33, 415

Fox, D. B., Frail, D. A., Price, P. A., et al. 2005, *Nature* , 437, 845

Frail, D. A., Kulkarni, S. R., Berger, E., & Wieringa, M. H. 2003, *AJ* , 125, 2299

Frail, D. A., Kulkarni, S. R., Nicastro, L., Feroci, M., & Taylor, G. B. 1997, *Nature* , 389, 261

Frail, D. A., Kulkarni, S. R., Sari, R., et al. 2001, *ApJL* , 562, L55

Freeman, P. E., Graziani, C., Lamb, D. Q., et al. 1999, *ApJ* , 524, 753

Frey, R. E. 2007, in American Institute of Physics Conference Series, Vol. 928, American Institute of Physics Conference Series, 11–22

Frontera, F., Amati, L., Zand, J. J. M. i., et al. 2004, *ApJ* , 616, 1078

Fruchter, A. S., Levan, A. J., Strolger, L., et al. 2006, *Nature* , 441, 463

Fryer, C. L. & Heger, A. 2005, *ApJ* , 623, 302

Fryer, C. L. & Woosley, S. E. 1998, *ApJL* , 502, L9+

Fryer, C. L., Woosley, S. E., Herant, M., & Davies, M. B. 1999, *ApJ* , 520, 650

Fugazza, D., D'Avanzo, P., Malesani, D., et al. 2006, GRB Coordinates Network, 5513, 1

Fukugita, M., Shimasaku, K., & Ichikawa, T. 1995, *Publications of the Astronomical Society of the Pacific* , 107, 945

Fynbo, J. P. U., Hjorth, J., Jensen, B. L., et al. 2005, GRB Coordinates Network, 3136, 1

Fynbo, J. P. U., Watson, D., Thöne, C. C., et al. 2006, *Nature* , 444, 1047

Gal-Yam, A., Fox, D. B., Price, P. A., et al. 2006, *Nature* , 444, 1053

Gal-Yam, A., Moon, D.-S., Fox, D. B., et al. 2004, *ApJL* , 609, L59

Galama, T. J., Vreeswijk, P. M., van Paradijs, J., et al. 1998, *Nature* , 395, 670

Galama, T. J. & Wijers, R. A. M. J. 2001, *ApJL* , 549, L209

Garnavich, P. M., Stanek, K. Z., Wyrzykowski, L., et al. 2003, *ApJ* , 582, 924

Gehrels, N. 2008, in American Institute of Physics Conference Series, Vol. 968, American Institute of Physics Conference Series, ed. Y.-F. Yuan, X.-D. Li, & D. Lai, 3–8

Gehrels, N., Cannizzo, J. K., & Norris, J. P. 2007, New Journal of Physics, 9, 37

Gehrels, N., Norris, J. P., Barthelmy, S. D., et al. 2006, *Nature* , 444, 1044

Gehrels, N., Sarazin, C. L., O'Brien, P. T., et al. 2005, *Nature* , 437, 851

Gelman, A., Carlin, J. B., Stern, H. S., & B., R. D. 1995, Bayesian Data Analysis (London: Chapman & Hall)

Gelman, A., Meng, X.-L., & Stern, H. S. 1996, Statistica Sinica, 6, 733

Gendre, B. & Boër, M. 2005, *A&A* , 430, 465

Gendre, B., Galli, A., & Boër, M. 2008, in American Institute of Physics Conference Series, Vol. 1000, American Institute of Physics Conference Series, 72–75

Ghirlanda, G., Ghisellini, G., & Firmani, C. 2005, *MNRAS* , 361, L10

Ghirlanda, G., Ghisellini, G., & Lazzati, D. 2004, *ApJ* , 616, 331

Ghisellini, G. & Celotti, A. 1999, *ApJL* , 511, L93

Goad, M. R., Tagliaferri, G., Page, K. L., et al. 2006, *A&A* , 449, 89

Goad, M. R., Tyler, L. G., Beardmore, A. P., et al. 2007, *A&A* , 476, 1401

Godet, O., Page, K. L., Osborne, J. P., et al. 2006, *A&A* , 452, 819

Goodman, J. 1986, *ApJL* , 308, L47

Gou, L.-J., Fox, D. B., & Mészáros, P. 2007, *ApJ* , 668, 1083

Graham, J. F., Fruchter, A. S., Levan, A. J., et al. 2007, GRB Coordinates Network, 6836, 1

Granot, J., Königl, A., & Piran, T. 2006, *MNRAS* , 370, 1946

Granot, J., Nakar, E., & Piran, T. 2003, *Nature* , 426, 138

Grazian, A., Fernandez-Soto, A., Testa, V., et al. 2006, GRB Coordinates Network Circular, 4545, 1

Gregory, P. C. 2005, Bayesian Logical Data Analysis for the Physical Sciences (Cambridge, UK: Cambridge University Press)

Grupe, D., Gronwall, C., Wang, X.-Y., et al. 2007, *ApJ* , 662, 443

Hakkila, J., Meegan, C. A., Fishman, G. J., et al. 1994a, in American Institute of Physics Conference Series, Vol. 307, Gamma-Ray Bursts, ed. G. J. Fishman, 59–+

Hakkila, J., Meegan, C. A., Pendleton, G. N., et al. 1994b, *ApJ* , 422, 659

Hanlon, L. O., Bennett, K., Collmar, W., et al. 1994, *A&A* , 285, 161

Harrison, F. A., Bloom, J. S., Frail, D. A., et al. 1999, *ApJL* , 523, L121

Hartmann, D. H., The, L.-S., Clayton, D. D., Schnepf, N. G., & Linder, E. V. 1992, in American Institute of Physics Conference Series, Vol. 265, American Institute of Physics Conference Series, ed. W. S. Paciesas & G. J. Fishman, 120–125

Heise, J., in't Zand, J., Kippen, R. M., & Woods, P. M. 2001, in Gamma-ray Bursts in the Afterglow Era, ed. E. Costa, F. Frontera, & J. Hjorth, 16–+

Higdon, J. C. & Lingenfelter, R. E. 1990, *ARA&A* , 28, 401

Hjorth, J., Sollerman, J., Møller, P., et al. 2003, *Nature* , 423, 847

Hjorth, J., Watson, D., Fynbo, J. P. U., et al. 2005, *Nature* , 437, 859

Hohman, D., Henden, A., & Price, A. 2005, GRB Coordinates Network Circular, 3370, 1

Holman, M., Garnavich, P., & Stanek, K. Z. 2005, GRB Coordinates Network Circular, 3716, 1

Homewood, A., Hartmann, D. H., & Wood, M. 2005, GRB Coordinates Network Circular, 3398, 1

Horváth, I. 1998, *ApJ* , 508, 757

Hullinger, D., Barbier, L., Barthelmy, S., et al. 2005, GRB Coordinates Network Circular, 3364, 1

Hurkett, C., Barthelmy, S., Cummings, J., et al. 2005, GRB Coordinates Network Circular, 3360, 1

Hurkett, C. P., Osborne, J. P., Page, K. L., et al. 2006, *MNRAS* , 368, 1101

Hurkett, C. P., Vaughan, S., Osborne, J. P., et al. 2008, *ApJ* , 679, 587

Hurley, K. 2006, Chinese Journal of Astronomy and Astrophysics Supplement, 6, 292

Hurley, K., Boggs, S. E., Smith, D. M., et al. 2005, *Nature* , 434, 1098

Ioka, K., Toma, K., Yamazaki, R., & Nakamura, T. 2006, *A&A* , 458, 7

Jakobsson, P., Fynbo, J. P. U., Ledoux, C., et al. 2006a, *A&A* , 460, L13

Jakobsson, P., Vreeswijk, P., Fynbo, J. P. U., et al. 2006b, GRB Coordinates Network, 5320, 1

Jelinek, M., Castro-Tirado, A. J., Gorosabel, J., et al. 2005, GRB Coordinates Network Circular, 3373, 1

Kass, R. E. & Raftery, A. E. 1995, J. Am. Stat. Ass., 90, 773

Katz, J. I., Piran, T., & Sari, R. 1998, Physical Review Letters, 80, 1580

Kawai, N., Yamada, T., Kosugi, G., Hattori, T., & Aoki, K. 2005, GRB Coordinates Network Circular, 3937, 1

Kelly, P. L., Kirshner, R. P., & Pahre, M. 2008, *ApJ* , 687, 1201

Kendall, M. 1938, Biometrika, 30, 81

Kennea, J. A., Burrows, D. N., Hurkett, C. P., Osbourne, J. P., & Gehrels, N. 2005, GRB Coordinates Network Circular, 3365, 1

King, A., O'Brien, P. T., Goad, M. R., et al. 2005, *ApJL* , 630, L113

King, A., Olsson, E., & Davies, M. B. 2007, *MNRAS* , 374, L34

King, A. R., Pringle, J. E., & Wickramasinghe, D. T. 2001, *MNRAS* , 320, L45

Kippen, R. M. 2000, GRB Coordinates Network Circular, 530, 1

Kippen, R. M., Woods, P. M., Heise, J., et al. 2003, in American Institute of Physics Conference Series, Vol. 662, Gamma-Ray Burst and Afterglow Astronomy 2001: A Workshop Celebrating the First Year of the HETE Mission, ed. G. R. Ricker & R. K. Vanderspek, 244–247

Klebesadel, R. W. 1992a, in Los Alamos Workshop on Gamma-Ray Bursts, p. 161 - 168, 161–168

Klebesadel, R. W. 1992b, The durations of gamma-ray bursts (Gamma-Ray Bursts - Observations, Analyses and Theories), 161–168

Klebesadel, R. W., Strong, I. B., & Olson, R. A. 1973, *ApJL* , 182, L85+

Klotz, A., Boer, M., & Atteia, J.-L. 2005, GRB Coordinates Network Circular, 3403, 1

Kobayashi, S. & Mészáros, P. 2003, *ApJ* , 589, 861

Kobayashi, S. & Zhang, B. 2007, *ApJ* , 655, 973

Kobayashi, S., Zhang, B., Mészáros, P., & Burrows, D. 2007, *ApJ* , 655, 391

Koshut, T. M., Kouveliotou, C., Paciesas, W. S., et al. 1995, *ApJ* , 452, 145

Kouveliotou, C., Meegan, C. A., Fishman, G. J., et al. 1993, *ApJL* , 413, L101

Kulkarni, S. R., Djorgovski, S. G., Odewahn, S. C., et al. 1999a, *Nature* , 398, 389

Kulkarni, S. R., Djorgovski, S. G., Ramaprakash, A. N., et al. 1998a, *Nature* , 393, 35

Kulkarni, S. R., Frail, D. A., Sari, R., et al. 1999b, *ApJL* , 522, L97

Kulkarni, S. R., Frail, D. A., Wieringa, M. H., et al. 1998b, *Nature* , 395, 663

Kumar, P. & Panaitescu, A. 2000, *ApJL* , 541, L51

Kumar, P. & Piran, T. 2000, *ApJ* , 535, 152

Lamb, D. Q. & Reichart, D. E. 2000, *ApJ* , 536, 1

Lazzati, D. 2005, *MNRAS* , 357, 722

Lazzati, D. & Begelman, M. C. 2006, *ApJ* , 641, 972

Lazzati, D., Ghirlanda, G., & Ghisellini, G. 2005, *MNRAS* , 362, L8

Lazzati, D., Perna, R., & Begelman, M. C. 2008, *MNRAS* , 388, L15

Lazzati, D., Rossi, E., Ghisellini, G., & Rees, M. J. 2004, *MNRAS* , 347, L1

Le, T. & Dermer, C. D. 2007, *ApJ* , 661, 394

Le Floc'h, E., Duc, P.-A., Mirabel, I. F., et al. 2003, *A&A* , 400, 499

Ledoux, C., Vreeswijk, P., Smette, A., Jaunsen, A., & Kaufer, A. 2006, GRB Coordinates Network, 5237, 1

Lee, P. M. 1989, Halsted Press (New York)

Lee, W. H. & Ramirez-Ruiz, E. 2007, New Journal of Physics, 9, 17

Levan, A. J., Wynn, G. A., Chapman, R., et al. 2006, *MNRAS* , 368, L1

Levinson, A. 2006, Energy Extraction from a Kerr Black Hole - An Ultimate Power Source in the Universe? (Trends in Black Hole Research), 119–+

Li, Z.-Y. & Chevalier, R. A. 2001, *ApJ* , 551, 940

Liang, E.-W., Racusin, J. L., Zhang, B., Zhang, B.-B., & Burrows, D. N. 2008, *ApJ* , 675, 528

Liang, E. W., Zhang, B., O'Brien, P. T., et al. 2006, *ApJ* , 646, 351

Lipkin, Y. M., Ofek, E. O., Gal-Yam, A., et al. 2004, *ApJ* , 606, 381

Livio, M. & Waxman, E. 2000, *ApJ* , 538, 187

Lloyd-Ronning, N. M. & Ramirez-Ruiz, E. 2002, *ApJ* , 576, 101

Loredo, T. J. 1990, in Maximum-Entropy and Bayesian Methods, Dartmouth., ed. P. Fougere (Dordrecht, The Netherlands: Kluwer Academic Publishers), 81–142

—. 1992, in Statistical Challenges in Modern Astronomy, Springer-Verlag., ed. D. Feigelson & G. Babu (New York: Springer-Verlag), 275–297

Lund, N. 1986, in Presented at the Society of Photo-Optical Instrumentation Engineers (SPIE) Conference, Vol. 597, X-ray instrumentation in astronomy; Proceedings of the Meeting, Cannes, France, December 2-4, 1985 (A87-19722 07-35). Bellingham, WA, Society of Photo-Optical Instrumentation Engineers, 1986, p. 95-100., ed. J. L. Culhane, 95–100

Lyutikov, M. & Usov, V. V. 2000, *ApJL* , 543, L129

MacFadyen, A. I., Ramirez-Ruiz, E., & Zhang, W. 2005, ArXiv Astrophysics e-prints; astro-ph/0510192

MacFadyen, A. I. & Woosley, S. E. 1999, *ApJ* , 524, 262

MacFadyen, A. I., Woosley, S. E., & Heger, A. 2001, *ApJ* , 550, 410

Madau, P. 1995, *ApJ* , 441, 18

Makino, F. 1987, , 25, 223

Malesani, D., D'Avanzo, P., Chincarini, G., et al. 2006, GRB Coordinates Network Circular, 4541, 1

Malesani, D., Tagliaferri, G., Chincarini, G., et al. 2004, *ApJL* , 609, L5

Mao, S. & Paczynski, B. 1992, *ApJL* , 389, L13

Martin, N., Maurice, E., & Lequeux, J. 1989, *A&A* , 215, 219

Masetti, N., Palazzi, E., Pian, E., & Patat, F. 2006, GRB Coordinates Network, 4803, 1

Mason, K. O., Blustin, A. J., Boyd, P., et al. 2006, *ApJ* , 639, 311

McBreen, S., Hanlon, L., McGlynn, S., et al. 2006, *A&A* , 455, 433

Meegan, C. A., Fishman, G. J., Wilson, R. B., et al. 1992, *Nature* , 355, 143

Mészáros, P. 2002, *ARA&A* , 40, 137

—. 2006, Reports of Progress in Physics, 69, 2259

Mészáros, P. & Rees, M. J. 1992a, *MNRAS* , 257, 29P

—. 1992b, *ApJ* , 397, 570

—. 1997, *ApJL* , 482, L29+

—. 2000, *ApJ* , 530, 292

—. 2001, *ApJL* , 556, L37

Mészáros, P., Rees, M. J., & Wijers, R. A. M. J. 1998, *ApJ* , 499, 301

Metzger, M. R., Djorgovski, S. G., Kulkarni, S. R., et al. 1997, *Nature* , 387, 878

Mewe, R., Gronenschild, E. H. B. M., & van den Oord, G. H. J. 1985, *A&AS* , 62, 197

Mirabal, N. & Halpern, J. P. 2006a, GRB Coordinates Network, 4591, 1

—. 2006b, GRB Coordinates Network, 4792, 1

Mirabal, N., Halpern, J. P., An, D., Thorstensen, J. R., & Terndrup, D. M. 2006, *ApJL* , 643, L99

Mizuno, Y., Yamada, S., Koide, S., & Shibata, K. 2004, *ApJ* , 615, 389

Monfardini, A., Kobayashi, S., Guidorzi, C., et al. 2006, *ApJ* , 648, 1125

Moretti, A., Campana, S., Mineo, T., et al. 2005, in UV, X-Ray, and Gamma-Ray Space Instrumentation for Astronomy XIV. Edited by Siegmund, Oswald H. W. Proceedings of the SPIE, Volume 5898, pp. 360-368 (2005)., ed. O. H. W. Siegmund, 360–368

Morrison, R. & McCammon, D. 1983, *ApJ* , 270, 119

Mukherjee, S., Feigelson, E. D., Jogesh Babu, G., et al. 1998, *ApJ* , 508, 314

Murakami, T., Fujii, M., Hayashida, K., et al. 1989, , 41, 405

Murakami, T., Inoue, H., Nishimura, J., van Paradijs, J., & Fenimore, E. E. 1991, *Nature* , 350, 592

Murakami, T., Ogasaka, Y., Yoshida, A., & Fenimore, E. E. 1992, in American Institute of Physics Conference Series, Vol. 265, American Institute of Physics Conference Series, ed. W. S. Paciesas & G. J. Fishman, 28–31

Nakar, E., Gal-Yam, A., Piran, T., & Fox, D. B. 2006, *ApJ* , 640, 849

Nakar, E. & Piran, T. 2002, *MNRAS* , 331, 40

Narayan, R., Paczynski, B., & Piran, T. 1992, *ApJL* , 395, L83

Narayan, R., Piran, T., & Kumar, P. 2001, *ApJ* , 557, 949

Norris, J. P. & Bonnell, J. T. 2006, *ApJ* , 643, 266

Norris, J. P. & Gehrels, N. 2008, in American Institute of Physics Conference Series, Vol. 1000, American Institute of Physics Conference Series, ed. M. Galassi, D. Palmer, & E. Fenimore, 280–283

Norris, J. P., Marani, G. F., & Bonnell, J. T. 2000, *ApJ* , 534, 248

Norris, J. P., Nemiroff, R. J., Kouveliotou, C., et al. 1993, in Bulletin of the American Astronomical Society, Vol. 25, Bulletin of the American Astronomical Society, 1336–+

Nousek, J. A., Kouveliotou, C., Grupe, D., et al. 2006, *ApJ* , 642, 389

Nuclear Test Ban Treaty. 1963, Treaties and Other International Agreements Series #5433, July 26, General Records of the U.S. Government, Record Group 11, National Archives

O'Brien, P. T. & Willingale, R. 2007, Royal Society of London Philosophical Transactions Series A, 365, 1179

O'Brien, P. T., Willingale, R., Osborne, J., et al. 2006, *ApJ* , 647, 1213

Paczynski, B. 1986, *ApJL* , 308, L43

—. 1990, *ApJ* , 363, 218

—. 1991, Acta Astronomica, 41, 257

—. 1998a, *ApJL* , 494, L45+

Paczynski, B. 1998b, in American Institute of Physics Conference Series, Vol. 428, American Institute of Physics Conference Series, ed. C. A. Meegan, R. D. Preece, & T. M. Koshut, 783–+

Paczynski, B. & Xu, G. 1994, *ApJ* , 427, 708

Page, K. L., King, A. R., Levan, A. J., et al. 2006, *ApJL* , 637, L13

Palmer, D. M., Barthelmy, S., Gehrels, N., et al. 2005, *Nature* , 434, 1107

Panaitescu, A. 2005a, *MNRAS* , 363, 1409

—. 2005b, *MNRAS* , 362, 921

—. 2007, *MNRAS* , 379, 331

Panaitescu, A. & Kumar, P. 2001, *ApJL* , 560, L49

—. 2002, *ApJ* , 571, 779

Pandey, S. B., Castro-Tirado, A. J., McBreen, S., et al. 2006, *A&A* , 460, 415

Pe'er, A., Mészáros, P., & Rees, M. J. 2006, *ApJ* , 652, 482

Pei, Y. C. 1992, *ApJ* , 395, 130

Pendleton, G. N., Briggs, M. S., Kippen, R. M., et al. 1999, *ApJ* , 512, 362

Perna, R., Armitage, P. J., & Zhang, B. 2006, *ApJL* , 636, L29

Pian, E., Mazzali, P. A., Masetti, N., et al. 2006, *Nature* , 442, 1011

Piran, T. 1999, , 314, 575

—. 2005, Reviews of Modern Physics, 76, 1143

Piran, T., Kumar, P., Panaitescu, A., & Piro, L. 2001, *ApJL* , 560, L167

Piranomonte, S., D'Elia, V., Fiore, F., et al. 2006, GRB Coordinates Network Circular, 4520, 1

Piro, L., Costa, E., Feroci, M., et al. 1999, *ApJL* , 514, L73

Piro, L., De Pasquale, M., Soffitta, P., et al. 2005, *ApJ* , 623, 314

Piro, L., Garmire, G., Garcia, M., et al. 2000, Science, 290, 955

Popham, R., Woosley, S. E., & Fryer, C. 1999, *ApJ* , 518, 356

Press, W. H., Teukolsky, S. A., Vetterling, W. T., & Flannery, B. P. 1992, Numerical recipes in FORTRAN. The art of scientific computing (Cambridge: University Press, —c1992, 2nd ed.)

Price, P. A., Berger, E., Reichart, D. E., et al. 2002, *ApJL* , 572, L51

Prochaska, J. X., Bloom, J. S., Chen, H.-W., et al. 2006a, *ApJ* , 642, 989

—. 2004, *ApJ* , 611, 200

Prochaska, J. X., Bloom, J. S., Wright, J. T., et al. 2005a, GRB Coordinates Network, 3833, 1

Prochaska, J. X., Chen, H.-W., Bloom, J. S., et al. 2005b, GRB Coordinates Network Circular, 3732, 1

Prochaska, J. X., Foley, R., Tran, H., Bloom, J. S., & Chen, H.-W. 2006b, GRB Coordinates Network, 4593, 1

Proga, D. & Begelman, M. C. 2003, *ApJ* , 592, 767

Proga, D., MacFadyen, A. I., Armitage, P. J., & Begelman, M. C. 2003, *ApJL* , 599, L5

Proga, D. & Zhang, B. 2006, *MNRAS* , 370, L61

Protassov, R., van Dyk, D. A., Connors, A., Kashyap, V. L., & Siemiginowska, A. 2002, *ApJ* , 571, 545

Ramirez-Ruiz, E. 2005, *MNRAS* , 363, L61

Ramirez-Ruiz, E., Celotti, A., & Rees, M. J. 2002a, *MNRAS* , 337, 1349

Ramirez-Ruiz, E., MacFadyen, A. I., & Lazzati, D. 2002b, *MNRAS* , 331, 197

Rees, M. J. & Meszaros, P. 1992, *MNRAS* , 258, 41P

—. 1994, *ApJL* , 430, L93

Rees, M. J. & Mészáros, P. 2000, *ApJL* , 545, L73

—. 2005, *ApJ* , 628, 847

Reeves, J. N., Watson, D., Osborne, J. P., et al. 2002, *Nature* , 416, 512

Reichart, D. E. & Price, P. A. 2002, *ApJ* , 565, 174

Rhoads, J. E. 1999, *ApJ* , 525, 737

Rol, E., Tanvir, N., Levan, A., et al. 2005, GRB Coordinates Network Circular, 3372, 1

Romano, P., Campana, S., Chincarini, G., et al. 2006a, *A&A* , 456, 917

Romano, P., Moretti, A., Banat, P. L., et al. 2006b, *A&A* , 450, 59

Roming, P. W. A., Kennedy, T. E., Mason, K. O., et al. 2005, Space Science Reviews, 120, 95

Roming, P. W. A., Schady, P., Fox, D. B., et al. 2006, *ApJ* , 652, 1416

Rosen, S., Hurkett, C., Holland, S., et al. 2005a, GRB Coordinates Network Circular, 3371, 1

Rosen, S., Hurkett, C., Landsman, W., et al. 2005b, GRB Coordinates Network Circular, 3367, 1

Rossi, E., Lazzati, D., & Rees, M. J. 2002, *MNRAS* , 332, 945

Rosswog, S. 2007, in Revista Mexicana de Astronomia y Astrofisica Conference Series, Vol. 27, Revista Mexicana de Astronomia y Astrofisica, vol. 27, 57–79

Rosswog, S., Ramirez-Ruiz, E., & Davies, M. B. 2003, *MNRAS* , 345, 1077

Rothstein, D. M. & Lovelace, R. V. E. 2008, in American Institute of Physics Conference Series, Vol. 1010, American Institute of Physics Conference Series, 35–39

Ruderman, M. 1975, New York Academy Sciences Annals, 262, 164

Rutledge, R. E. & Sako, M. 2003, *MNRAS* , 339, 600

Sakamoto, T., Barthelmy, S. D., Barbier, L., et al. 2008, *ApJS* , 175, 179

Sakamoto, T., Lamb, D. Q., Kawai, N., et al. 2005, *ApJ* , 629, 311

Sako, M., Harrison, F. A., & Rutledge, R. E. 2005, *ApJ* , 623, 973

Sari, R., Piran, T., & Halpern, J. P. 1999, *ApJL* , 519, L17

Sari, R., Piran, T., & Narayan, R. 1998, *ApJL* , 497, L17+

Sato, G., Yamazaki, R., Ioka, K., et al. 2007, *ApJ* , 657, 359

Sato, R., Kawai, N., Suzuki, M., et al. 2003, *ApJL* , 599, L9

Savage, B. D. & Mathis, J. S. 1979, *ARA&A* , 17, 73

Savaglio, S., Fall, S. M., & Fiore, F. 2003, *ApJ* , 585, 638

Sazonov, S. Y., Sunyaev, R. A., Terekhov, O. V., et al. 1998, *A&AS* , 129, 1

Schlegel, D. J., Finkbeiner, D. P., & Davis, M. 1998, *ApJ* , 500, 525

Schmidt, W. K. H. 1978, *Nature* , 271, 525

Schwartz, G. 1978, Ann. Stat., 6, 461

Shao, L. & Dai, Z. G. 2007, *ApJ* , 660, 1319

Shaviv, N. J. & Dar, A. 1995, *ApJ* , 447, 863

Shemi, A. 1994, *MNRAS* , 269, 1112

Shen, R.-F., Willingale, R., Kumar, P., O'Brien, P. T., & Evans, P. A. 2008, ArXiv Astrophysics e-prints; astro-ph/0806.3541

Sheth, K., Frail, D. A., White, S., et al. 2003, *ApJL* , 595, L33

Shibata, M., Taniguchi, K., & Uryū, K. 2005, , 71, 084021

Singer, S. 1965, in Proceedings of the IEEE, volume 53, issue 12, 1935

Sivia, D. S. 1996, Data Analysis: A Bayesian Tutorial (Oxford Univ. Press (Oxford))

Soderberg, A. M., Berger, E., Kasliwal, M., et al. 2006, *ApJ* , 650, 261

Soderberg, A. M., Kulkarni, S. R., Berger, E., et al. 2004, *Nature* , 430, 648

Sollerman, J., Jaunsen, A. O., Fynbo, J. P. U., et al. 2006, *A&A* , 454, 503

Spergel, D. N., Verde, L., Peiris, H. V., et al. 2003, *ApJS* , 148, 175

Stanek, K. Z., Garnavich, P. M., Holland, S. T., et al. 2002, *IAU Circular* , 7857, 2

Stanek, K. Z., Garnavich, P. M., Nutzman, P. A., et al. 2005, *ApJL* , 626, L5

Stanek, K. Z., Matheson, T., Garnavich, P. M., et al. 2003, *ApJL* , 591, L17

Starling, R. L. C., Vreeswijk, P. M., Ellison, S. L., et al. 2005, *A&A* , 442, L21

Starling, R. L. C., Wijers, R. A. M. J., Wiersema, K., et al. 2007, *ApJ* , 661, 787

Stratta, G., Fiore, F., Antonelli, L. A., Piro, L., & De Pasquale, M. 2004, *ApJ* , 608, 846

Tagliaferri, G., Antonelli, L. A., Chincarini, G., et al. 2005a, *A&A* , 443, L1

Tagliaferri, G., Goad, M., Chincarini, G., et al. 2005b, *Nature* , 436, 985

Tanvir, N. R., Barnard, V. E., Blain, A. W., et al. 2004, *MNRAS* , 352, 1073

Tanvir, N. R., Chapman, R., Levan, A. J., & Priddey, R. S. 2005, *Nature* , 438, 991

Tanvir, N. R., Levan, A. J., Priddey, R. S., Fruchter, A. S., & Hjorth, J. 2006, GRB Coordinates Network, 4602, 1

Tavecchio, F., Ghisellini, G., & Lazzati, D. 2004, *A&A* , 415, 443

Terasawa, T., Tanaka, Y., Takei, Y., et al. 2005, ArXiv Astrophysics e-prints; astro-ph/0502315

Thompson, C. 1994, *MNRAS* , 270, 480

Thompson, T. A., Chang, P., & Quataert, E. 2004, *ApJ* , 611, 380

Tinney, C., Stathakis, R., Cannon, R., et al. 1998, *IAU Circular* , 6896, 1

Tokunaga, A. T. & Vacca, W. D. 2005, *Publications of the Astronomical Society of the Pacific* , 117, 1459

Troja, E., King, A. R., O'Brien, P. T., Lyons, N., & Cusumano, G. 2008, *MNRAS* , L5+

Tyler, L., Page, K., Goad, M., & Osborne, J. 2006, in ASP Conf. Ser. 351: Astronomical Data Analysis Software and Systems XV, ed. C. Gabriel, C. Arviset, D. Ponz, & S. Enrique, 97

Usov, V. V. 1992, *Nature* , 357, 472

Usov, V. V. & Chibisov, G. V. 1975, Soviet Astronomy, 19, 115

van Dyk, D. A., Connors, A., Kashyap, V. L., & Siemiginowska, A. 2001, *ApJ* , 548, 224

van Paradijs, J., Groot, P. J., Galama, T., et al. 1997, *Nature* , 386, 686

Vanderspek, R., Sakamoto, T., Barraud, C., et al. 2004, *ApJ* , 617, 1251

Vaughan, S., Goad, M. R., Beardmore, A. P., et al. 2006, *ApJ* , 638, 920

Vietri, M., Ghisellini, G., Lazzati, D., Fiore, F., & Stella, L. 2001, *ApJL* , 550, L43

Vietri, M. & Stella, L. 1998, *ApJL* , 507, L45

—. 1999, *ApJL* , 527, L43

Villasenor, J. S., Lamb, D. Q., Ricker, G. R., et al. 2005, *Nature* , 437, 855

Vlahakis, N. & Königl, A. 2003a, *ApJ* , 596, 1080

—. 2003b, *ApJ* , 596, 1104

Vreeswijk, P. & Jaunsen, A. 2006, GRB Coordinates Network Circular, 4974, 1

Vreeswijk, P. M., Ellison, S. L., Ledoux, C., et al. 2004, *A&A* , 419, 927

Vreeswijk, P. M., Fruchter, A., Kaper, L., et al. 2001, *ApJ* , 546, 672

Wald, R. M. 1974, , 10, 1680

Wang, X.-Y. & Mészáros, P. 2007, *ApJ* , 670, 1247

Watson, D., Reeves, J. N., Hjorth, J., et al. 2006, *ApJL* , 637, L69

Watson, D., Reeves, J. N., Hjorth, J., Jakobsson, P., & Pedersen, K. 2003, *ApJL* , 595, L29

Watson, D., Reeves, J. N., Osborne, J., et al. 2002, *A&A* , 393, L1

Waxman, E. 1997, *ApJL* , 485, L5

Waxman, E., Kulkarni, S. R., & Frail, D. A. 1998, *ApJ* , 497, 288

Waxman, E. & Mészáros, P. 2003, *ApJ* , 584, 390

Wei, D. M. & Lu, T. 2002, *A&A* , 381, 731

Wessa. 2008, Kendall tau Rank Correlation (v1.0.10)

Wheeler, J. C., Yi, I., Höflich, P., & Wang, L. 2000, *ApJ* , 537, 810

Willingale, R., O'Brien, P. T., Osborne, J. P., et al. 2007, *ApJ* , 662, 1093

Wilms, J., Allen, A., & McCray, R. 2000, *ApJ* , 542, 914

Winkler, C., Bennett, K., Bloemen, H., et al. 1992, *A&A* , 255, L9

Winkler, C., Courvoisier, T. J.-L., Di Cocco, G., et al. 2003, *A&A* , 411, L1

Woosley, S. E. 1993, *ApJ* , 405, 273

Woosley, S. E. & Bloom, J. S. 2006, *ARA&A* , 44, 507

Woosley, S. E. & Weaver, T. A. 1986, *ARA&A* , 24, 205

Yamazaki, R., Toma, K., Ioka, K., & Nakamura, T. 2006, *MNRAS* , 369, 311

Yi, T., Liang, E., Qin, Y., & Lu, R. 2006, *MNRAS* , 367, 1751

Yoshida, A., Namiki, M., Otani, C., et al. 1999, *A&AS* , 138, 433

Zhang, B. 2006, *Nature* , 444, 1010

—. 2007, Chinese Journal of Astronomy and Astrophysics, 7, 1

Zhang, B., Fan, Y. Z., Dyks, J., et al. 2006, *ApJ* , 642, 354

Zhang, B. & Mészáros, P. 2002a, *ApJ* , 571, 876

—. 2002b, *ApJ* , 566, 712

—. 2004, International Journal of Modern Physics A, 19, 2385

Zhang, B., Zhang, B.-B., Liang, E.-W., et al. 2007a, *ApJL* , 655, L25

Zhang, B.-B., Liang, E.-W., & Zhang, B. 2007b, *ApJ* , 666, 1002

Zhang, W. & Fryer, C. L. 2001, *ApJ* , 550, 357